

Preparation of Mannose-derived 2D Supramolecular Polymers and Synthesis of Mannose/Dolichol mimics for Scramblase identification

Inauguraldissertation
der Philosophisch-naturwissenschaftlichen Fakultät
der Universität Bern

vorgelegt von

Giovanni Picca

von Italien

Leiter der Arbeit:

Prof. Dr. Robert Häner

Departement für Chemie und Biochemie der Universität Bern

Preparation of Mannose-derived 2D Supramolecular Polymers and Synthesis of Mannose/Dolichol mimics for Scramblase identification

Inauguraldissertation
der Philosophisch-naturwissenschaftlichen Fakultät
der Universität Bern

vorgelegt von

Giovanni Picca

von Italien

Leiter der Arbeit:

Prof. Dr. Robert Häner

Departement für Chemie und Biochemie der Universität Bern

Bern, 24.09.2020

Der Dekan/Die Dekanin.
Prof. Dr. Zoltán Balogh

ACKNOWLEDGEMENTS

And so, my moment is also here. First of all, I want to thank Prof. Robert Häner for having given me the opportunity to do the PhD in his group, giving me the chance to improve personally and professionally. Furthermore, I would like to thank Prof. Annalisa Guaragna and Prof. Francesca Paradisi for reading and evaluating my work.

My thanks go to the actual and former members of Häner Group: to Simon M. Langenegger and for the fruitful talks and advice; Markus Probst, especially for the time we spent to talk about the “7th art”; my labmate Larysa Markova for the help and suggestions; Mariusz Kownacki for having introduced me to “Bernese life”.

Then, the rest of the group Oleg Khorev, Shi-Xia Liu, Jovana Jevric, Nutchä Bürki, Simon Rothenbühler, Ping Zhou, Oleh Vybornyi, Jan Thiede and Timo Radjenovic: thank you all for having been part of this my professional experience.

A special thought goes to my friends met in these PhD years: Giuseppe Zito, Fulvio Di Lorenzo and Federica Gatto, Georgia Cametti and Daniele Ercolani, Fabio Montisci and Giulia Moretti, Rebecca Scatena and Francesco Bizzotto, Alessandro Mirra, Stefano Racioppi, Matteo Giordani, Alessandro Zana, Michelle Ernst and Lars Gnägi, Cristina Pratelli, Arianna Lanza, Michal Andrzejewski, René Schliemann, Tomasz Poreba, Valentine and Andreas Riedo, Pavel Moreno and Florian Kleemiß. Thanks for the funny and great moments we spent together: these memories will be an important piece of my life.

I would like to thank my family for having always supported my choices.

Finally, a special thank is for my girlfriend Marialda D’Auria. I don’t know if I am able to find the right words to describe your support, I can only say that I have always had (and I hope it will be forever) a special person next to me, a place where I can find a repair in both sunny and stormy days.

And about me... step by step, I keep running!

Giovanni

Keeping moving,
with the past to the back
the focus on the present
and the look at the future

A future like a strong light
that straight in the eyes, it is able to blind
making impossible to see what's awaiting
but with the hope it will be bright

CONTENTS

Part A

INTRODUCTION.....	3
CHAPTER 1	6
1 SUPRAMOLECULAR POLYMERIZATION MECHANISMS.....	6
1.1 ISODESMIC MECHANISM	7
1.2 COOPERATIVE MECHANISM	9
1.3 COOPERATIVE PARAMETER, σ	11
1.4 RING-CHAIN MECHANISM.....	13
2 SUPRAMOLECULAR POLYMERS INTERACTIONS	14
2.1 METAL-LIGAND INTERACTIONS	14
2.2 HOST-GUEST INTERACTION	16
2.3 HYDROGEN BOND	17
2.4 π - π INTERACTION	19
CHAPTER 2	23
1 IMPORTANCE OF WATER	23
2 PAHS IN SUPRAMOLECULAR POLYMERS	25
3 SUPRAMOLECULAR STRUCTURES IN WATER.....	27
4 J- AND H-AGGREGATION.....	28
5 HÄNER GROUP WORK	30
5.1 OLIGOPHOSPHODIESTER SYNTHESIS	31
5.2 DNA AS SCAFFOLD FOR CHROMOPHORE ASSEMBLY	33
5.3 OLIGOARENOTIDES	35
CHAPTER 3	40
1 AIM OF THE THESIS	40
2 PRELIMINARY TESTS	42
3 PYRENE TRIMER (Py ₃)	44
4 STUDY OF Py ₃ Man	47

4.1	UV/VIS ANALYSES OF Py ₃ Man.....	51
4.2	COMPARISON WITH Py ₃ Phos	56
5	AFM ANALYSES.....	60
5.1	Py ₃ Man NANOSTRUCTURES	60
5.2	Py ₃ NANOSTRUCTURES	61
5.3	Py ₃ Man STUDIED AT 0.5°C/MIN AS COOLING RATE	62
5.4	Py ₃ Man STUDIED AT ~7°C/MIN AS COOLING RATE.....	65
5.5	Py ₃ Man STUDIED AT 0.1°C/MIN AS COOLING RATE	66
6	CONSIDERATION ABOUT AGGREGATION	67
7	Py ₃ Phos NANOSTRUCTURES	68
8	STUDIES OF Py ₃ Man WITH NO ETOH: UV/VIS	72
9	STUDIES OF Py ₃ Man WITH NO ETOH: AFM.....	75
10	STUDIES OF Py ₃ But	78
10.1	Py ₃ But IN AQUEOUS SOLUTION WITH ETOH.....	80
10.2	Py ₃ But IN AQUEOUS SOLUTION WITH NO ETOH.....	83
CHAPTER 4		88
1	THE PURPOSE OF FUNCTIONALIZATION	88
2	Py ₃ Man BINDS TO CON A	90
3	CLICK CHEMISTRY OF Py ₃ But IN SOLUTION.....	96
3.1	HPLC ANALYSIS OF THE REACTION WITH THE DYE	99
3.2	HPLC ANALYSIS OF THE REACTION WITH DNA-1	101
4	Py ₃ But LINKING TO DNA-AUNP	104
5	Py ₃ But LINKING TO PEG-AUNP.....	109
6	USE OF TEM FOR Py ₃ But LINKED TO PEG-AUNP	114
CHAPTER 5		119
CONCLUSIONS AND OUTLOOK.....		119
CHAPTER 6		122
EXPERIMENTAL SECTION		122

CHAPTER 1	157
1 INTRODUCTION	157
1.1 BIOSYNTHESIS OF DOLICHOL	158
1.2 O-GLYCOPROTEINS	160
1.3 N-GLYCOPROTEINS	162
1.4 GLYCOSYLPHOSPHATIDYLINOSITOL (GPI) ANCHOR.....	164
1.5 ENDOPLASMIC RETICULUM (ER).....	165
CHAPTER 2	167
1 FLIPPING ACROSS MEMBRANES.....	167
2 SINERGIA	169
3 GOAL OF THE SINERGIA PROJECT	169
3.1 STRATEGIES FOR THE IDENTIFICATION	172
4 AIM OF THE THESIS	175
CHAPTER 3	177
1 SYNTHESIS OF A DOLICHOL MIMIC.....	177
2 USE OF DNA SYNTHESIZER.....	178
3 SYNTHESIS IN SOLUTION	183
3.1 SYNTHETIC STEPS.....	185
CHAPTER 4	190
CONCLUSIONS	190
CHAPTER 5	191
EXPERIMENTAL SECTION	191

Part A

ABSTRACT

Supramolecular polymers are macromolecules obtained by the self-assembly and self-organization of repeating, non-covalently linked units.¹ The structural and functional properties of supramolecular polymers largely depend on the nature of the noncovalent interactions between the individual units. Therefore, the macroscopic properties of the system are strongly dependent on the supramolecular organization and not solely defined by the properties of the molecular components.²

In our research group, we have previously described how a pyrene-trimer (Py₃) self-assembles into nanosheet structures.²

Here, we present the synthesis of functionalized pyrene trimer nanosheets. The functionalizations used are a D-mannose (in the case of Py₃Man) and a butynyl group (in the case of Py₃But), both of them linked to one of the two extremities of pyrene-trimer, through a phosphate group. The self-assembly process is followed by UV/vis analyses, while the formation of sheets is studied by AFM.

In particular, the mannose moiety, in Py₃Man, is selectively linked to Con A, a protein which shows a high affinity with this sugar. The AFM is used to study the presence of Con A bound to the nanosheets surface.

While, the butynyl group, in Py₃But, is used for two approaches: in one, it is linked to a DNA strand bearing an azide, via click chemistry. Then, a complementary strand, linked to gold nanoparticles (AuNP) will hybridizes via base pairing. This approach is studied by AFM.

In the second approach, the butynyl in Py₃But is linked, via click chemistry, to a PEG derivative, bearing an azide group and linked to AuNP. Here, the process is studied by both AFM and TEM.

¹ Aida, T.; Meijer, E. W.; Stupp S. I., **2012**, *Science*, 335, 813–817

² Vybornyi M., Rudnev A. V., Langenegger S. M., Wandlowski T., Calzaferri G., Häner R., **2013**, *Angew. Chem. Int. Ed.*, 52, 11488 –11493

INTRODUCTION

Supramolecular polymers, and their self-organization, are predominant in nature: some of them play an essential role in living beings life, like nucleic acids (DNA and RNA) and proteins.

In the first case, it is possible to observe the presence of nucleobases π - π interaction on two consecutive nucleotides and H-bonds between two single strands, according to Watson-Crick base pairs.

In the case of proteins, their secondary structures are made by an H-bond between the N-H and CO on the peptide chain, generating both α -helices and β -sheets.

In the last decades, supramolecular chemistry has become a research field in huge and strong expansion.

Jean-Marie Lehn (Nobel prize in 1987), one of the pioneer in supramolecular chemistry, conceived the term “chemistry beyond the molecule” in order to describe structures with a high complexity that are the result of the interaction between smaller species via intermolecular forces. They are able to arrange in fascinating structures, through *self-organization* processes, generating well-defined supramolecular scaffold by a self-assembly of their components.¹

The first studies approaching in this field were based on the design of purely organic architectures, obtained by kinetic formation of strong bonds.

Only in recent times, researchers have been addressed their efforts to the planning of structure originated by weak interactions in order to have thermodynamically controlled self-assemblies.²

By merging supramolecular chemistry with polymer science, it is possible to speak of “supramolecular polymers” as a new interdisciplinary research area.

Meijer *et al.* has suggested a definition about this class of compounds:

*Supramolecular polymers are defined as polymeric arrays of monomeric units that are brought together by reversible and highly directional secondary interactions, resulting in polymeric properties in dilute and concentrated solutions, as well as in the bulk. The monomeric units of the supramolecular polymers themselves do not possess a repetition of chemical fragments. The directionality and strength of the supramolecular bonding are important features of systems that can be regarded as polymers and that behave according to well-established theories of polymer physics.*³

This means under specific conditions, it is possible to induce either their assembly or disassembly.

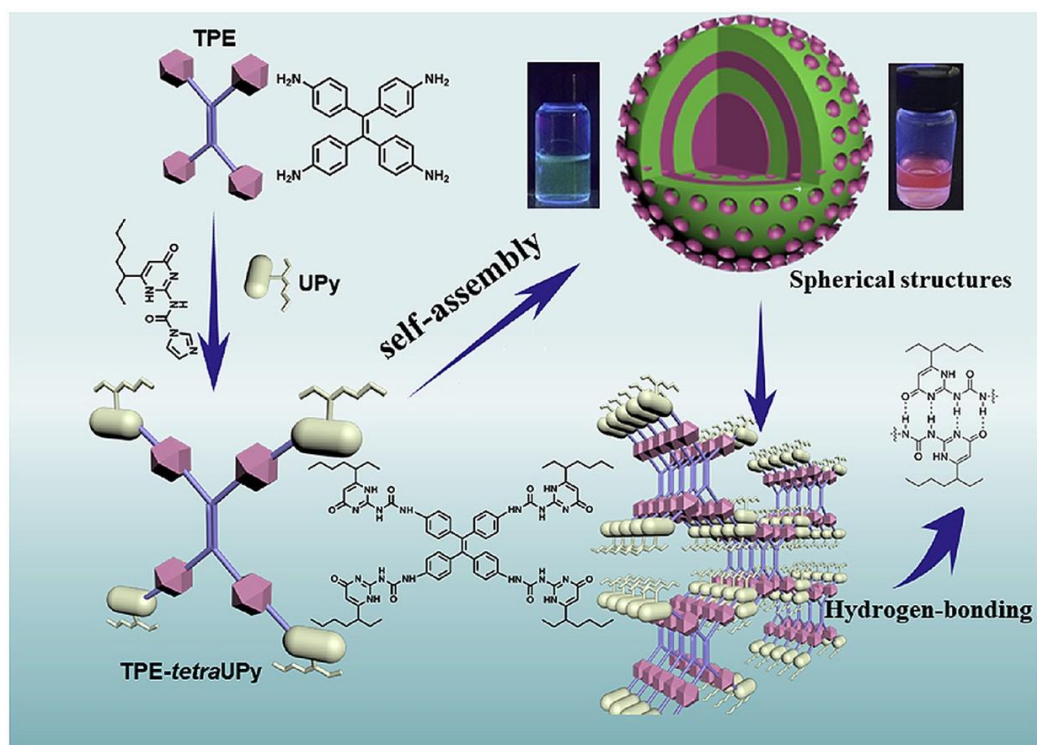


Figure I Representation of the self-assembly driven by weak interaction: H-bond. The self-assembly leads to spherical structures (the picture is taken from ref.⁴)

Of course, standard polymers, which their nature is based on covalent and irreversible bonds, show a much higher robustness, resulting chemically stronger; but on the other hand, supramolecular polymers, whose monomers are held together via weak interactions, and that so leading to less robust materials, display some intriguing properties. The lack of this resistance can make a particular system reversible and responsive,⁵ ensuring they can be used for several applications:

- for electronic devices, in particular for organic light-emitted diodes (OLEDs), which are an efficient light source for liquid-crystal displays, projections displays and spectroscopic imaging.^{6,7} Other examples are organic field-effect transistors (OFETs), organic photovoltaic (OPV) and solar cells.⁸
- self-healing behavior^{9,10} both thermo-¹¹ and light-mediated;¹² this system is made by a network of weak interactions (based on hydrogen bonds, π - π stacking and metal bonds) which are able to recombine. For example, considering a system subjected

to an external force, which generates a damage: it is split in two fragments. These two are able to restore the original supramolecular interactions, regaining the initial structure.¹³

- Biomedical system which can be used as drug delivery systems; in this field, some kind of hydrogels, which have biodegradable properties, can be considered as good candidates for such purposes.¹⁴ Further examples of supramolecular biodegradability and potential biomedical applications are made by *Chen et al.*¹⁵ and *Liu et al.*¹⁶

CHAPTER 1

1 SUPRAMOLECULAR POLYMERIZATION MECHANISMS

Considering a couple of complementary monomers for supramolecular polymers, A and B, it is possible to arrange them in order to have different structures.

They can be settled in different ways: homo-complementary arrangement generating A-A or B-B type homo-polymers; or with an A-B type for having alternating copolymers; other combinations can be ABBA type and so on.

All those combinations can arrange both in linear and (hyper)branched form and the driving force involved are multiple: hydrogen bonds, metal coordination, host-guest interactions and π - π stacking.^{17,18,19}

During the chain growth, there is a step of nucleation and a step of elongation, both of them with their own equilibrium constants, K_n and K_e respectively (**Figure 1.1**).

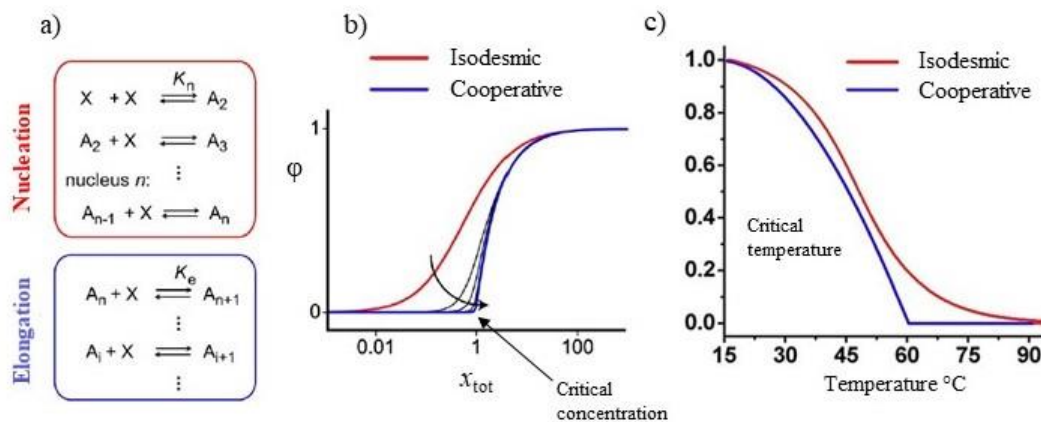


Figure 1.1 a) Equilibrium reactions for nucleation (red) and elongation (blue), from ref.²⁰; b) assembly of monomers depending on to concentration: ϕ as a function of x_{tot} . For isodesmic mechanism the assembly gradually grows; for cooperative, assembly rapidly increases after critical concentration value is reached ($x_{tot} = 1$), adapted from²⁰; c) assembly of monomers depending on to temperature: ϕ as a function of temperature. Here, following the trend from high to low temperature, for isodesmic pathway, the assembly gradually increases, whereas for cooperative there is no assembly until a critical temperature (with nuclei formation), then it quickly raises. Adapted from³⁰

Three major supramolecular polymerization mechanisms are worth to be mentioned: isodesmic, cooperative and ring-chain.

About the first two, *Meijer et al.*²⁰ has described some differences between them, calculating the variation of the degree of aggregation, φ , as a function of x_{tot} .

The latter is a dimensionless value given by the product between the equilibrium constant, K , and the total concentration of monomers C_{tot} (the critical concentrations, which corresponds to K^{-1}):

$$x_{tot} = K \cdot C_{tot} \quad \text{Eq. 1}$$

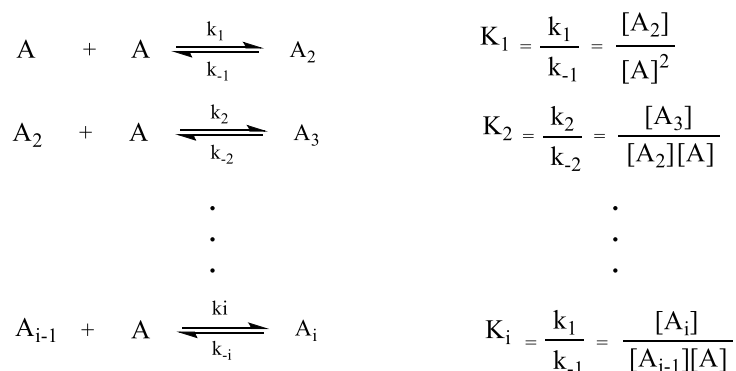
Equilibrium constant depends from the temperature, and for this reasons φ can reach higher values either increasing the concentration or decreasing the temperature.

According to the plot in **Figure 1.1**, for an isodesmic mechanism the degree of aggregation gradually grows at higher values of concentration (or lower values of temperature).^{20,21}

1.1 ISODESMIC MECHANISM

In this kind of model, each monomer is connected, via non-covalent and reversible manner, to the next one in all polymerization phases with no formation of intermediates during the self-assembly process.¹⁹

This is the simplest model of polymerization and the addition of a single monomer to another occurs with the same change of Gibbs free energy and for each binding step; the equilibrium constants (K_i) are the same ($K_1 = K_2 = \dots = K_i$), for all “ i ” fragments (**Scheme 1.1**):



Scheme 1.1 Chemical reactions and relative equilibrium constants (K) for the addition of monomers to a growing chain (i -mer). Adapted from²⁸

Energies involved, for bonds formation, do not depend from the length of the chain, reason why the addition of a monomer to the growing structure occurs with no energetic differences,

leading to a constant decrease in free energy and there is no critical temperature or concentration (**Figure 1.2**).²²

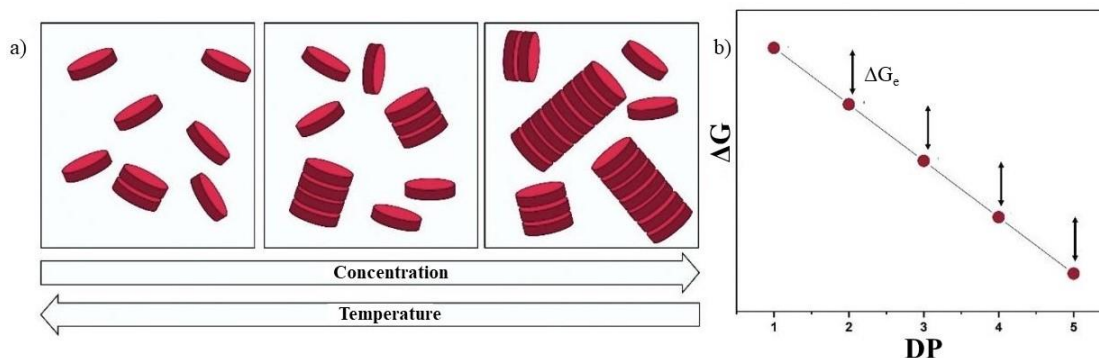


Figure 1.2 a) Schematic representation of isodesmic self-assembly; b) diagram of Gibbs free energy (ΔG^0) as function of the degree of polymerization (DP). Adapted from²²

In this model, the nature of K_i depends from the nature of the monomer and the temperature.²³ The length depends from K_i and monomer concentration.

The isodesmic mechanism is in accordance with Flory's principle of equal reactivity, which says the probability of two functional groups on two different units have been reacted with other groups is the same, even if these two units are unbound.²⁴

The isodesmic approach is also called multistage open association (MSOA). The reactions involved in supramolecular polymerization can follow the scheme of a polycondensation mechanism for standard polymers, but without formation of water as byproduct.

Contrary to molecular polycondensations (based on covalent bonds), which usually possess a very large degree of polymerization (DP), for supramolecular polymers, because of small association constants involved, due to weak and reversible interaction, it is not easy to reach high DP values; even though it's possible to use multiple different weaker interaction in order to increase it.

In these systems, DP follows an approximate law:

$$DP \cong \sqrt{K_i C_{tot}} \quad \text{Eq. 2}$$

In this equation K_i includes also the role of monomer concentration (or monomers in case of different molecules) and so their interaction and the product of their own binding constants (K).^{25,26}

As predictable from **Figure 1.1**, in isodesmic model the aggregation follows a sigmoidal path: aggregation increases with higher values of $x_{tot} = KC_{tot}$.

The same situation is possible building a plot with the weight and number average degree of polymerization (DP_W and DP_N) as function of x_{tot} (**Figure 1.3**).

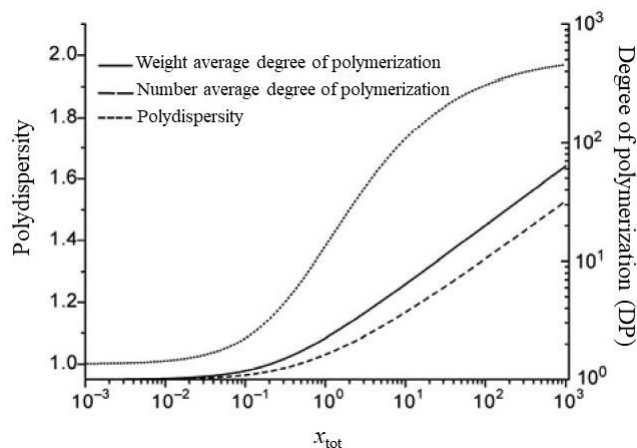
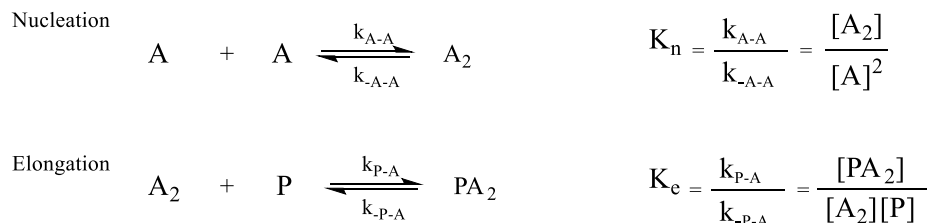


Figure 1.3 Polydispersity, weight and number average degree of polymerization as a function of x_{tot} . Adapted from¹⁹

Where the polydispersity is a measure that describes the dispersion (interpreted as spread) of distributions of diverse molar masses in a polymer and degrees of polymerization (a big polydispersity value means a huge molar mass distribution);²⁷ it is given by the ratio between DP_W/DP_N . In this case is even more obvious that in order to have a system with a high DP, a higher concentration is necessary, or in case of dilute solution, bigger K values are needed.^{19,28}

1.2 COOPERATIVE MECHANISM

Not always the growth of a supramolecular chain occurs in a single step, so with one single equilibrium constant, K_i .



Scheme 1.2 Chemical reactions and relative equilibrium constants (K) for nucleation (K_n) and elongation (K_e). Monomers (A) starts to aggregate in order to form nuclei (A_2); then, they react with other structures (P, monomers or longer). Adapted from²⁸

Indeed, this model can be thought as a two-stage mechanism: nucleation and elongation with $K_e \neq K_n$ (elongation and nucleation constant, respectively) (**Scheme 1.2**).

In the first case, monomers start to aggregate, by either an increasing of concentration or a reduction of temperature, such as in an isodesmic path, with its own K_n , until the formation of a nucleus. This occurs at critical concentration/temperature value ($x_{tot} = 1$), through an unfavorable polymerization process in terms of free energy, so this first part is rather slow.²⁰ As soon as nuclei form, the next addition of monomers to them, for the elongation step, is more feasible since the relative constant K_e is energetically favored (**Figure 1.4a**).

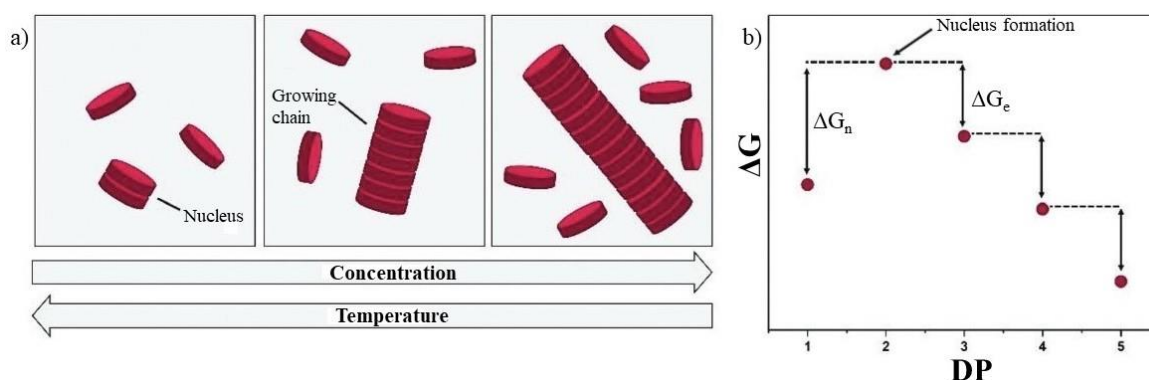


Figure 1.4 a) Schematic representation of cooperative self-assembly; b) diagram of Gibbs free energy (ΔG^0) as function of the degree of polymerization (DP): here nucleation step is energetically unfavorable. Adapted from²²

This elongation step proceeds through another isodesmic pathway and the elongation constant is higher than nucleation constant ($K_e > K_n$).

This model, just as described, is also known as nucleated supramolecular polymerization, where Gibbs free energy increases until a maximum, which corresponds to the nucleation and it occurs at a certain value of x_{tot} ; once this energy barrier is overtaken, the elongation step proceeds with lower ΔG^0 , since it is energetically favored (**Figure 1.4b**).²²

Moreover, there is the case when $K_e < K_n$: anti-cooperative model. Here, the nuclei formation is more favorable than elongation step, leading to the formation of objects with a very narrow size distribution: this means structures with low polydispersity.¹⁹

Finally, it is also interesting distinguish among a homogeneous and heterogeneous nucleation: the first is due to the monomer in solution involved in polymerization, instead the second is caused by some impurities or secondary nucleation of monomers. The latter seems to be very common for many biological supramolecular polymerization.²²

1.3 COOPERATIVE PARAMETER, σ

A good way to understand the difference between isodesmic, cooperativity and anti-cooperative mechanism is described by cooperative parameter, σ , which represents the ratio between K_n and K_e , $\sigma=K_n/K_e$. Cooperative, anti-cooperative and isodesmic model can be compared considering the fraction of aggregation, ϕ , as function of x_{tot} (**Figure 1.5**).

In here, in the cooperative range the formation of polymers occurs when $x_{tot}=1$, so that means after a certain amount of monomers has turned in a nucleus; then, since nucleation is an unfavorable step, it is much easier that monomers can connect to nuclei lengthening the supramolecular chain, rather than bind to other monomers. This is also due to a more favorable elongation step ($K_e>K_n$).

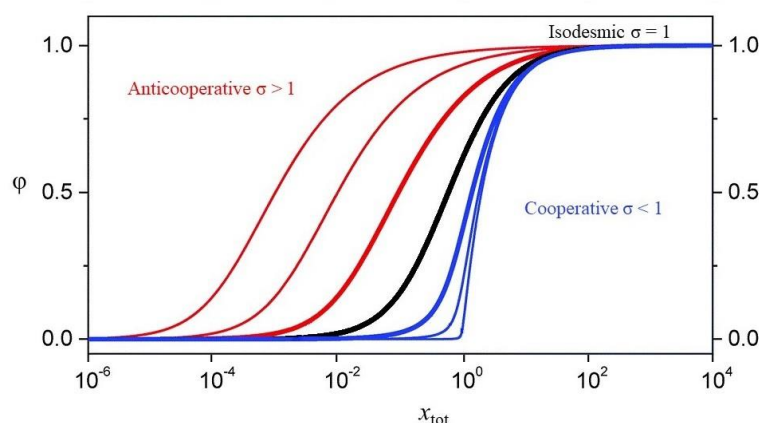


Figure 1.5 Plot of degree of aggregation, ϕ , as a function of x_{tot} , for all three self-assembly mechanism with their own relative σ values. Adapted from²⁹

The phenomenon is more obvious for low values of σ ($\sigma \ll 1$) since the transition at the critical concentration ($x_{tot}=1$) is sharper. Therefore, beyond this value there is a higher concentration of structure with a long chain (**Figure 1.6a**).

For the anti-cooperative model, the situation is different because the elongation step is more unfavorable than nucleation step, so this means that in solution there is just a higher concentration of small objects (**Figure 1.6b**).

Following the trends, increasing K_e , so for smaller values of σ , the system approaches the isodesmic mechanism (where the path follows a sigmoidal curve) which seems an intermediate case between the anti-cooperative and the cooperative supramolecular polymerization.^{29,30}

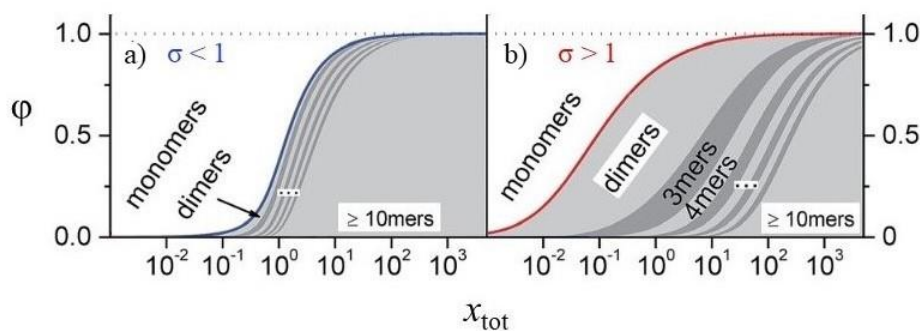


Figure 1.6 Size distribution of oligomers for a) cooperative and b) anti-cooperative mechanisms. Adapted from²⁹

Finally, another conclusion can be made considering the weight fraction as a function of the degree of polymerization (DP).

As shown in **Figure 1.7**, it is possible to have different regions, divided for size distribution: at higher DP values there are structure with longer chain. Going back, there is the region for objects less polymerized (small oligomers), until the region where the predominant species are mainly monomers.

If K_e is assumed to be the same for all three mechanisms, in the case cooperative model there are two regions: at lower DP values, where the monomers start to form nucleus and then couple, in a second step, with other monomers for the elongation phases leading to long chain polymers with higher DP. This is due to $\sigma = K_n/K_e \ll 1$.

Isodesmic and anti-cooperative models are in the region with low/medium DP values where there is the formation of small objects.³¹

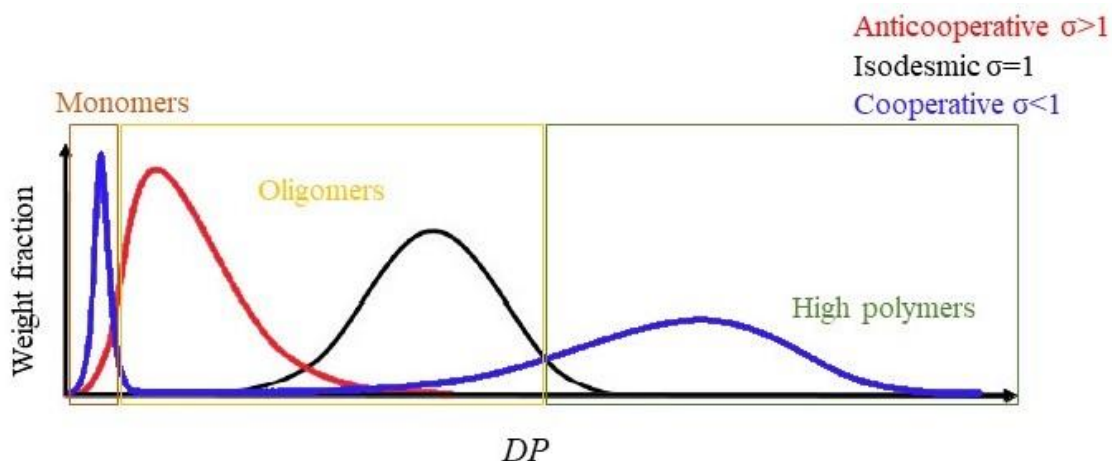


Figure 1.7 Qualitative representation of size distributions of products for isodesmic, cooperative and anti-cooperative supramolecular polymerization mechanisms. Adapted from ref³¹

1.4 RING-CHAIN MECHANISM

The last model is known as ring-chain mechanism: this particular case occurs when two ends of small chains have more probability to link with each other, rather than with monomers in solution, in order to have elongated structures.

This mechanism occurs in covalent polymers as well, but due to the reversible nature of supramolecular polymers, these are in equilibrium with their free counterparts.

Like the cooperative model, there is a concentration value (C_{tot} , critical concentration) beyond which the small objects start to react with monomers leading to longer chain, obtaining supramolecular polymers (**Figure 1.8**).^{32,33}

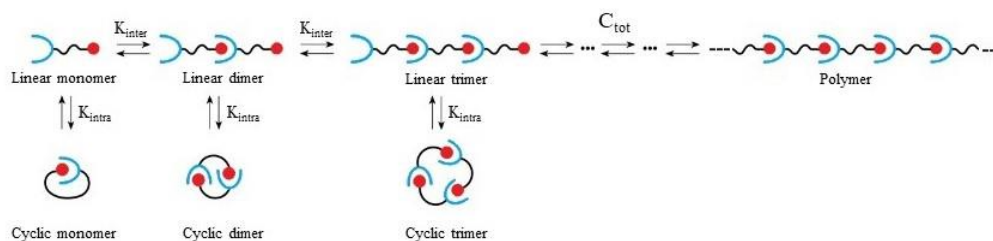


Figure 1.8 At low value of concentration small linear structure are in equilibrium with their ring counterpart. Increasing the temperature only linear form is present. Adapted from³³

If these two extremities belong to same chain, an intramolecular reaction occurs, leading to a ring. The mechanism is reversible with its own K_{intra} , whereas the reaction between two groups from two different structures leads to an intermolecular pathway with K_{inter} as equilibrium constant.

Jacobson and Stockmayer introduced the concept of *effective molarity* (EM) as the ratio between the two constants K_{intra} and K_{inter} :

$$EM = \frac{K_{\text{intra}}}{K_{\text{inter}}} \quad \text{Eq. 3}$$

From this equation, considering strainless cyclic formation, a higher probability for formation of rings is possible in dilute solutions. Since EM is directly proportional to K_{intra} , and in this condition is easier that two reactive groups on the same chain can react with each other. Increasing the concentration, more reactions that are intermolecular occur, leading to formation of bigger cyclic oligomers.^{19,34}

The last assumptions are made below a critical concentration value, where only cyclic objects are present. Above this value, concentration of rings remains constant, and the presence of additional monomers increases the supramolecular acyclic chain (**Figure 1.9**).³⁵

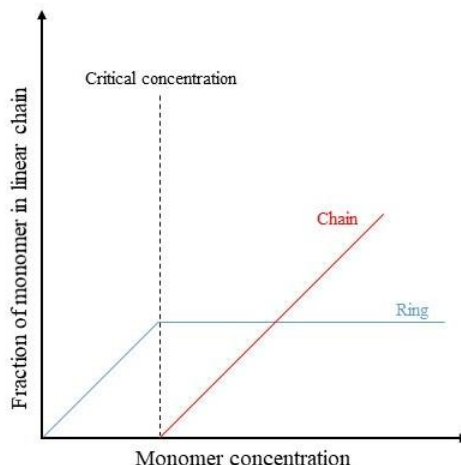


Figure 1.9 Fraction of monomer in linear as a function of monomer concentration. At high concentration values only acyclic structure is formed. Adapted from¹⁹

2 SUPRAMOLECULAR POLYMERS INTERACTIONS

2.1 METAL-LIGAND INTERACTIONS

It is known that organometallic compounds are a branch of coordination chemistry, where the coordination center is a metal and ligands around are organic molecules.

They are used either as reagents or as catalysts in organic synthesis: some example can be organolithium compounds or Grignard reagents about stoichiometric quantities, or in catalytic amount as Ziegler-Natta catalyst, etc.

Even in nature, it is possible found some of these complexes, like porphyrin-derived compounds which is coordinate to either Fe^{2+} or Mg^{2+} , for heme group (in hemoglobin) and chlorophyll respectively; then, vitamin B12, some proteins, etc.

The theory behind this compound is that a ligand has a lone electron pair, which can be donate to an empty orbital of the metal. A ligand can be mono-, di-, tri- (and so on) dentate, according to how many electron pairs it is able to donate; in this case, the ligand is called chelant.

Based on this assumption, using long chains with ligands that are covalently bound, a metal can coordinate to them and based on coordination number it is possible to have linear or branched structure (**Figure 1.10**).³⁶

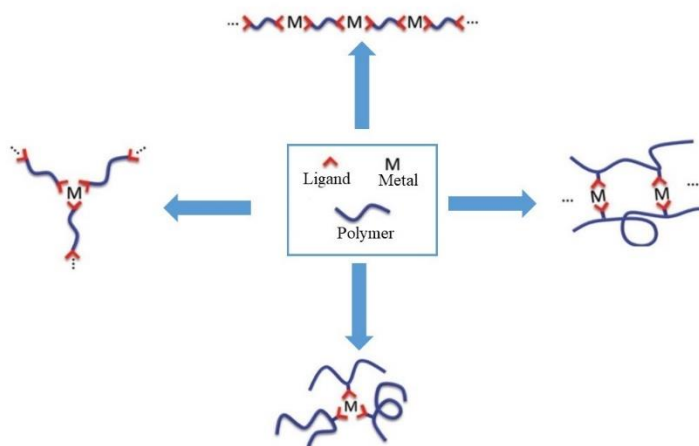


Figure 1.10 Structures based on metal-ligand interaction. Adapted from³⁶

Since the reversible nature of this kind of bonds, high K values are needed in order to have structures with a significant DP.³⁷ Two strategies are used for this purpose: either the use of a ligand with a high affinity with the metal or a chelant (polydentate donor).

Besides ligands nature, the stability of some complexes can depend from the type of metal too, because of a back-donation from metal to ligand through $d-\pi^*$. Irving-William series predicts the order of stability of the first row divalent transition metals: $Mn(II) < Fe(II) < Co(II) < Ni(II) < Cu(II) > Zn(II)$;³⁸ it increases along the row, finding the maximum of the stability in copper.

In literature, it is possible to find different kinds of ligands. It is worth to mention, though, Würtner and Dobrawa: in 2005³⁹, they described how different pyridine derivatives could lead to a strong metal-ligand bond formation. The compounds used as ligands were 1,10-phenantroline and mono-, di- and tridentate pyridine with Zn^{2+} . The last ligand gives the strongest interaction.

In the same publication, they described the work made by other groups with these pyridine derivative structures, using other metals: Ag^+ , Cu^+ , Pd^{2+} , Ru^{2+} , Eu^{3+} .

Metal-ligand interaction can be used for the building of peptide architectures using terpyridine as unnatural ligand (**Figure 1.11**).

Horne *et al.* did this kind of study. They were not able to get long and robust structure, but the system showed potential skills in order to have structures for a wide range of applications.⁴⁰

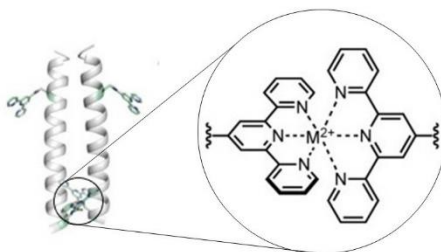


Figure 1.11 Complex between two terpyridines (from two different helices) and a divalent metal. Adapted from⁴⁰

Concluding, this class of interactions combine metals with polymers properties leading to material, which fascinating features: self-healing⁴¹ and shape memory effect⁴², materials that show conductivity, luminescent or photovoltaic properties. Their interest in nanolithography and nanoscience fields, or in catalysis and electrocatalysis; their use as stimuli-responsive materials, which can be used for encapsulating drugs and, then, can be released at a specific location thanks to an external stimuli; they cause interest not only in medicine, but also in bioengineering and nanotechnology.

Last but not least, the fabrication of artificial metalloenzymes used for biological reactions.⁴³

2.2 HOST-GUEST INTERACTION

Host-guest complexes are a class of compound, where a site, host, with a cavity can bind specifically to a guest (**Figure 1.12**).

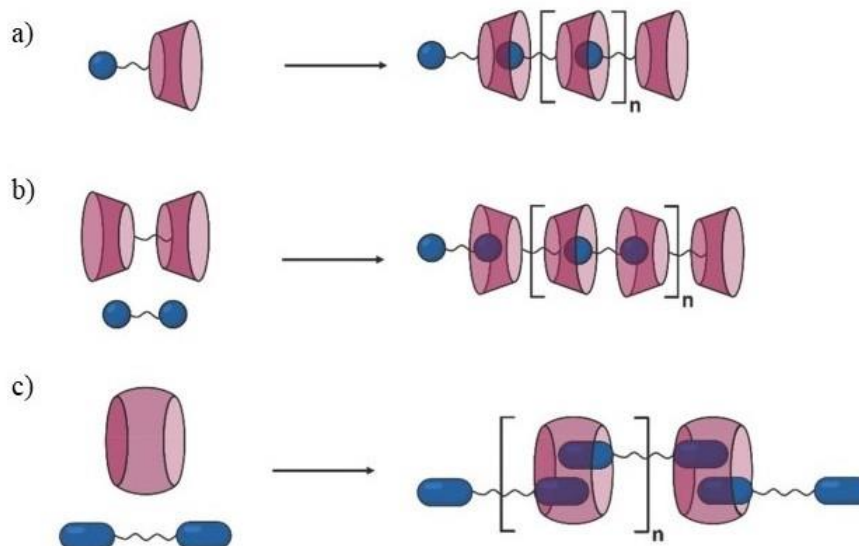


Figure 1.12 Illustration of host (pink)-guest (blue) interaction: a) system with both host and guest sites; b) structures with two either hosts or guests sites; c) host molecule, which is able to interact with two guests. Adapted from²²

This concept can be adapted to supramolecular polymers, generating an architecture with more than one recognition site (both of them can belong to the same structure). In order to have complexes quite robust, these two sites need to have a high specificity, based also on the dimension of the host cavity size, just as the geometry of the two counterparts. Multiple forces are involved for the bound: H-bonds, van der Waals interactions, etc.²²

Many molecules are used as host in this kind of interactions, and those more popular are macrocycles like Calixarenes, Cyclodextrine and Cucurbituril, which are water-soluble (**Figure 1.13**).

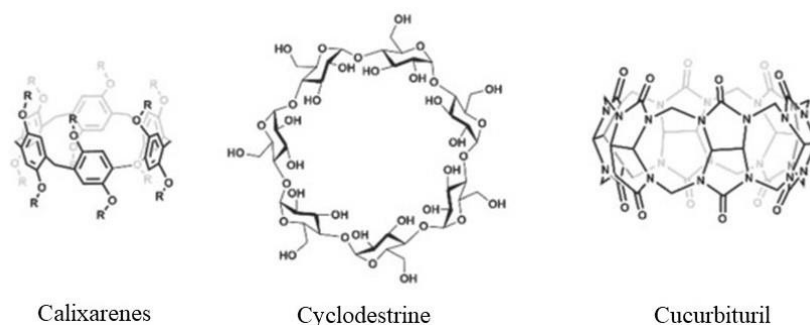


Figure 1.13 Example of water-soluble host system. Adapted from²²

Architectures, that possess the three hosts mentioned above, have found the use in biomedical applications, for example as drug delivery systems.

This approach is used in order to increase water solubility of some drugs: like for some anticancer therapy.

Besides water solubility increase, host-guest system, between macrocycles and drugs, are thought to be cancer targeting.

The structure inside the cavity is protected from chemical reaction, thermal degradation and so on, in biological environment. This system can be absorbed by tumor cell and released in it, because of different cancer cells environment.⁴⁴

2.3 HYDROGEN BOND

It is well known that when a hydrogen atom is bound to an electronegative one (O, N, etc.), the latter attracts to it the cloud of valence electrons. Such situation leaves on the electronegative atom a partial negative charge (δ^-) and on the hydrogen atom a partial positive charge (δ^+).

In such kind of system, hydrogen can be attracted by an electronegative atom and this interaction is called Hydrogen bond (H-bond or HB) (**Figure 1.14**).

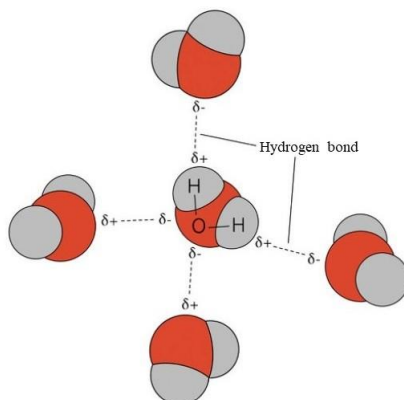


Figure 1.14 Illustration of hydrogen bonds. Adapted from ⁴⁵

Hydrogen bond plays a very important role in nature, especially for supramolecular architectures: one need only consider to DNA and RNA base coupling that, thanks to their directionality property, allow nucleobase recognition inducing stability between the two-coupled strands.

Based on natural compounds, one can think to design supramolecular structures based on the molecular recognition between an H-acceptor (**A**) and an H-donor (**D**).⁴⁶ Taking advantage by the high directionality and specificity of this bond²² and because it is very reactive to variation of external stimuli such as solvent, pH and temperature, this feature can be used to build in supramolecular chemistry in order to obtain structures with fascinating properties⁴⁷, like self-healing compounds.

It is possible to build a site, which bears multiple hydrogen bonds.⁴⁸ In such motifs, there is an increase of strength and directionality; but the strength of this interaction depends, not only by the numbers of **A** and **D**, but by their arrangement as well.

When a hydrogen bond is formed, the two structures are pretty close to each other. The donor or the acceptor are in proximity to the neighbor of its counterpart, creating a secondary interaction, which can be either attractive or repulsive.

Secondary attractive interactions increase the association constant value (K_a), generating a stronger bond, so this means for a triple hydrogen bond system the best combination is **AAA-DDD** (**Figure 1.15**).

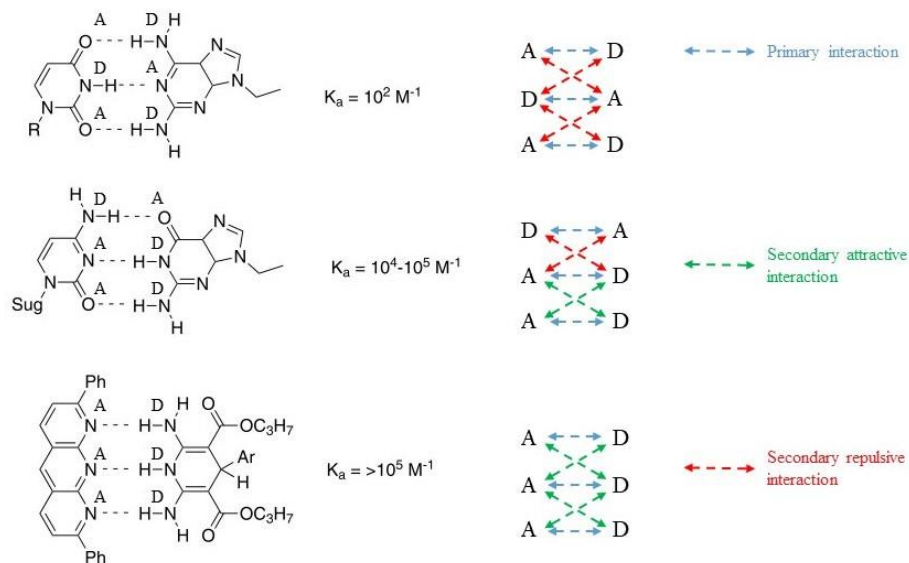


Figure 1.15 Secondary attractive and repulsive interactions influence association constant (K_a). Adapted from⁴⁹

The same assumption can be made with other kind of motifs, like quadruple hydrogen bond.⁴⁹ One of the first use of this interaction in supramolecular chemistry was made by Lehn *et al*, using uracil a 2,6-diaminopyridine for the formation of liquid crystals, through a triple hydrogen bond interaction.⁵⁰ Other uses are as shape memory^{51,52} and self-healing materials.⁵³

2.4 π - π INTERACTION

The term π - π interaction (or π - π stacking) refers to a non-covalent interaction between two aromatic molecules. Although this phenomenon is not still so clear, some consideration can be made in order to understand how some of aromatic rings can interact with each other. Thinking to a benzene dimer, the first picture, which comes in mind is a face-to-face stacking. This is the less stable interaction (**Figure 1.16**).

It is known that the aromatic electron cloud stays below and above the plane since the electrons are delocalized on the entire structure. As a consequence, π -electron density creates a quadrupole moment, where the negative charge is in the middle of the ring and the positive stays at the edge. The two molecules involved can arrange in different ways in order to have the right quadrupole-quadrupole orientation.

Thinking to a face-to-face interaction, this generates a repulsion between the two moieties of a hypothetical dimer.⁵⁴

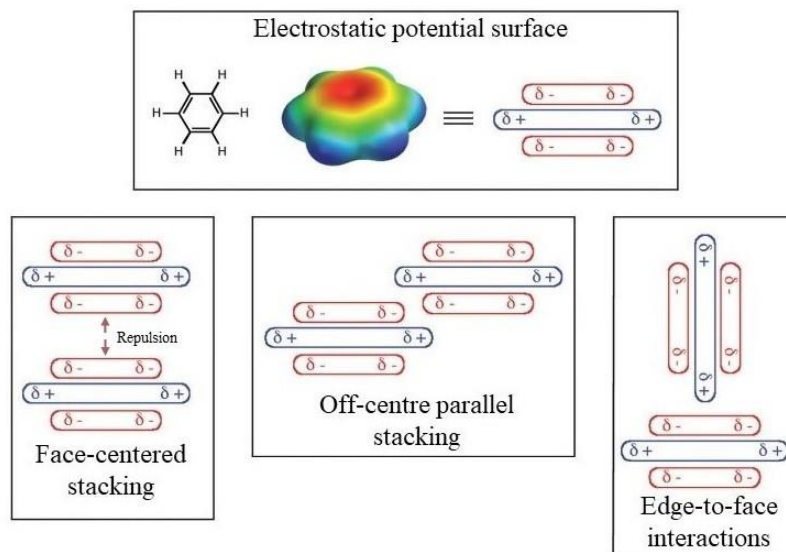


Figure 1.16 Electrostatic aromatic interactions: formation of a quadrupole moment (top) and arrangement of two molecule in order to have the right orientation (bottom). Adapted from⁵⁴

A more stable situation can be obtained by two assets: edge-to-face and off-centered parallel stacking, where an interaction between different charge is possible (**Figure 1.17**).

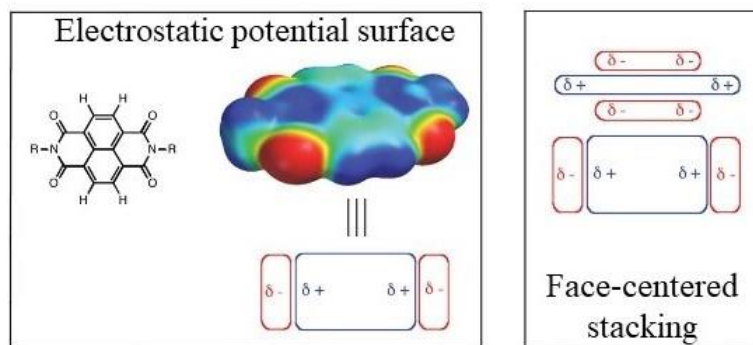


Figure 1.17 EWGs attract electronic clouds inverting quadrupole moment direction (left); this situation allows a face-centered stacking interaction with a benzene (right). Adapted from⁵⁴

Electron withdrawing groups (EWG), as either heteroatoms or external groups, can influence the electronic clouds, modifying the charge distribution, generating a positive charged area in the core of the structure, with the electronic distribution around EWGs. In this way, when it interacts with a benzene-like π -electron density, a face-centered stacking is favored.⁵⁴

In the latter case, EWGs are exactly on the opposite side of the molecule, leading to a situation where the overall dipole moment is null.

Taking the case of either a benzene with few substituent groups or a heterocyclic aromatic ring, there is the generation of a dipole leading to other kind of interactions: dipole-dipole, dipole-quadrupole. This complicates a bit more the situation because for minimizing the repulsion the two molecules have to rotate in order to find the right orientation for a good dipole-dipole interaction.⁵⁵

This interaction plays an important role for DNA double helix stabilization. As already discussed above, H-bond is very important for stability and nucleobase recognition for the pairing of the two strands. The presence of π -stacking in DNA was already known and it was common opinion that their energetic contribution to the strands stability was very little.

Recently, quantum chemical calculations have demonstrated that energetic contributions given by this stacking are comparable to those from H-bonding. The two interaction are related to each other, because it has also been shown, by evaluation of molecular electrostatic potentials, intrastrand stacking improves H-bonding capability of nucleobases.

Furthermore, stabilization is due to both an intra- and an interstrand π -interaction as depicted in **Figure 1.18**.⁵⁶

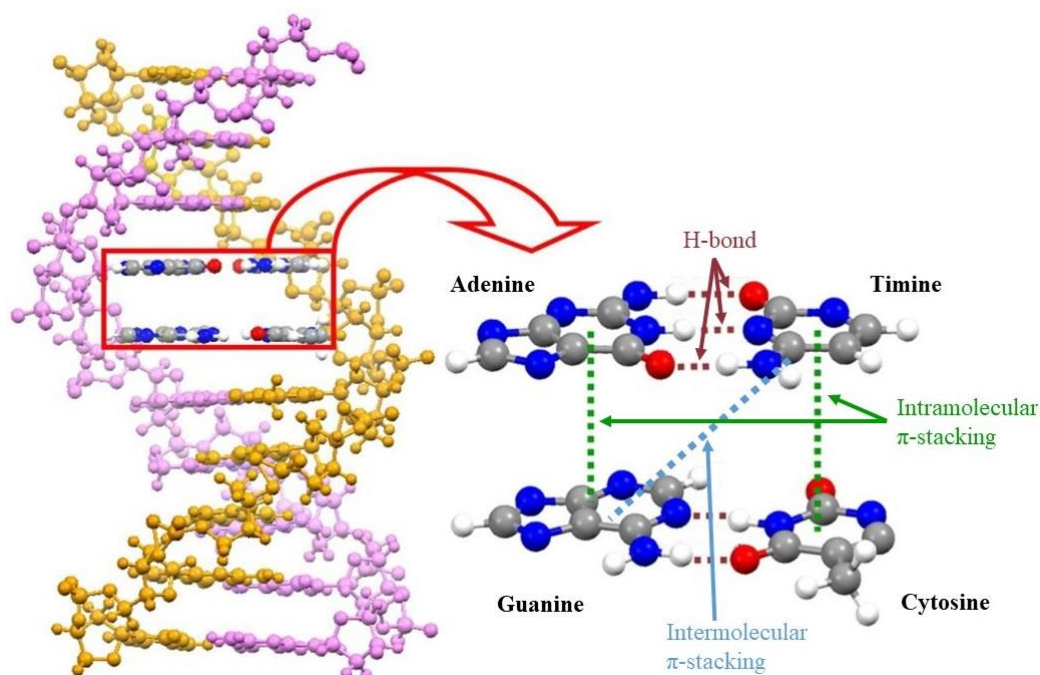


Figure 1.18 Interactions involved in base pairing: besides hydrogen bonds, intra- and intermolecular π -stacking are very important because they contribute to the stabilization of DNA double helix. Adapted from ref.⁵⁶

Supramolecular polymers based on π - π stacking have found many applications. Liu *et al.* have published their use for bioapplications. Structures based on this interaction have been

detected as potential tools for DNA sequencing, controlled drug release, fabrications of sensors. They are also used for electrochemical energy storage, catalysis and electrocatalysis. The use of this π -stacking-based supramolecular polymers is still in an initial stage, but they have shown a great potential for being used in a huge variety of fields.⁵⁷

CHAPTER 2

1 IMPORTANCE OF WATER

Water is an essential component for life. It covers 71% of Earth's surface; it plays crucial roles for biological mechanism and biological cells are made up of about the half with water. Nowadays, it is known that water molecule has not a linear structure but bent: this is due to the fact that hybridization of molecular orbitals of oxygen is sp^3 . This leads to a tetrahedral geometry, where two sp^3 orbital share their lonely electron with the $1s$ orbital of two H atoms, whereas the other two sp^3 orbitals stay with a lone pairs (**Figure 2.1a**). Furthermore, the latter two orbitals repulse with each other generating a tiny structural deformation to the geometry with the consequence that the angle between the two O-H is 104.5° instead of 109° , typical of tetrahedrons.

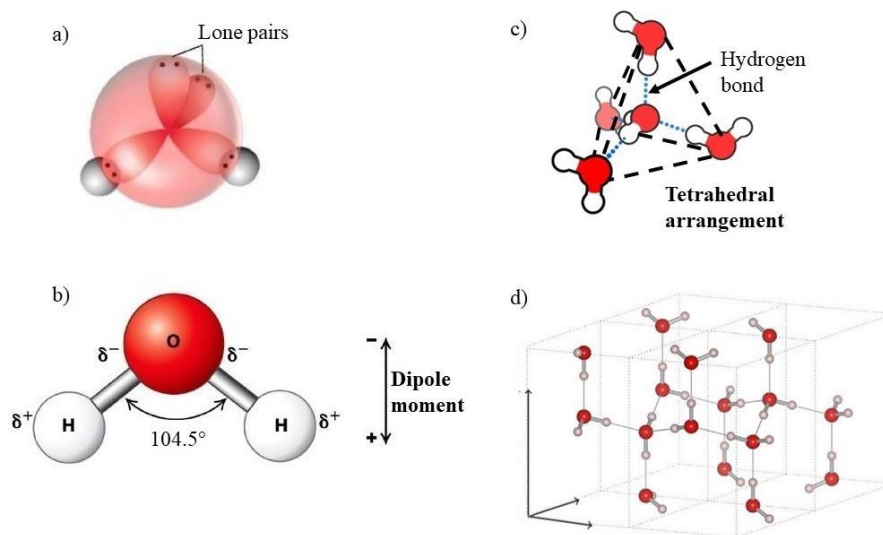


Figure 2.1 a) Tetrahedral geometry of water due to sp^3 hybridization; b) angle between the O-H bonds is 104.5° and the presence δ^+ (on hydrogen atoms) and δ^- (on oxygen atom), which generate a dipole moment. Adapted from ref.⁵⁹; c) tetrahedral arrangement of water due to hydrogen bonds. Adapted from ref.⁶⁰; d) structure of ice in a six-membered arrangement, due to tetrahedral geometry of hydrogen-bonded network. Adapted from ref.⁵⁸

Because of a higher electronegativity of oxygen, electrons stay closer to it, generating a partial negative charge (δ^-), while a partial positive charge (δ^+) stay on hydrogens. This effect has as consequence the generation of a dipole moment of magnitude 1.85D (**Figure 2.1b**).

This particular situation leading to the generation of a particular class of interaction, which is very important in chemistry and biology: hydrogen bonds.

Hydrogens, with their δ^+ , point toward the lone pair of oxygens (δ^-) of other two water molecules, and this situation leads an arrangement which results in a tetrahedral geometry (**Figure 2.1c**).^{59,60}

It is well known the fact that freezing water has a lower density than liquid state. In pure liquid water, hydrogen bonds have a lifetime of about 1ps on average. In solid state, water molecules are arranged in a rigidly imposed manner. Hydrogen bonds are coordinated in tetrahedral geometry, where each molecules has six possible orientations.

As result, water molecules bind each other in a six-membered ring arrangement, with a lot of empty space between the molecules (**Figure 2.1d**). When ice melts, the network of hydrogen bonds is free to move and the distance between molecules decreases.^{60,61}

The fact water is a liquid at room temperature and pressure is due to its capacity to form a network of hydrogen bonds (in a tetrahedral arrangement), which give to the molecules a great cohesion with each other.⁶⁰

Based on the expression “like dissolves like”, water is able to dissolve polar molecules and ions. For these species, it is possible to speak of hydrophilicity (hydrophile, from *hydros*, which means “water” and *philia* “friendship”; so something that shows affinity with water). In case of ions, water can surround solutes avoiding their aggregation; in particular coulombic interactions involved orientate water molecules with oxygen atoms towards cations and hydrogen atoms toward anions.⁶¹

On the other hand, non-polar molecules and/or structures are hydrophobic species (hydrophobe, from *hydros* “water” and *phobos* “fear”, so something which has no affinity with water) and, in this case, studies are focused on the hydrophobic effect.

Hydrophobic effect can be described as the case where non-polar species tend to aggregate in order to avoid the contact with water,⁶² and it is very important in chemistry and biology. Behavior of hydrophobic solutes in water is not very clear yet, but some consideration can be made. First, the hydrophobic effect is considered to be of entropic origin.

Now, considering a small hydrophobic solute: when it is added to water, the H bonded network surrounds these small molecules, with no dramatic changes. This arrangement reduces water molecules mobility, because surrounding the solute; they are in a more ordered state, leading to a system entropy decrease.

At this point, these hydrophobic species start to aggregate, increasing the occupied volume, leading to an H bond network breaking, where water between these solute molecules is released in the bulk, with an entropy increase as a consequence (**Figure 2.2**).⁶³

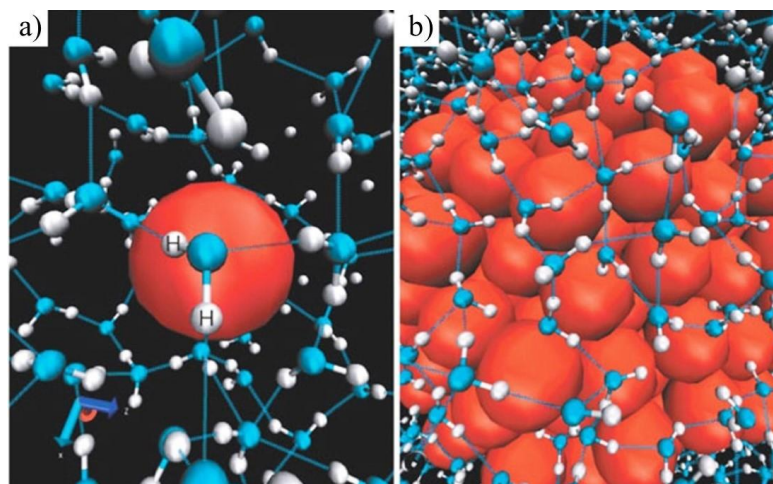


Figure 2.2 a) H bond network accommodates small hydrophobic molecules with no any breakage; b) hydrophobic molecules aggregate, breaking H bond network: water molecules between solutes are released in the bulk. Taken from ref.⁶³

Hydrophobic effect plays an essential role in protein folding. In order to minimize the hydrophobic interface, proteins aggregate leading to a self-assembly with a strong association between the hydrophobic units.⁶⁴

Finally, the addition of an organic cosolvent or the presence of electrical charges can have dramatic consequences on the robustness of hydrophobic effect, making it weaker, enabling reversible construction and destruction of self-assembled systems.⁶³

2 PAHS IN SUPRAMOLECULAR POLYMERS

Polycyclic aromatic hydrocarbons (PAH) are a class of compound made up of two or more fused benzene rings and contain only carbon and hydrogen atoms. The most simple PAH is naphthalene consisting of two fused benzene rings.

These compounds are also commonly observed in the space and scientists think they formed with stars and exoplanets after Big Bang.⁶⁵

PAHs are very abundant in the environment because of pollution, which has a high concentration of these compounds.

They came from oil processing (drilling, transport, combustion), but also urban and industrial wastes, cars, fumes from factories or as product of combustion of organic compounds: for example, it is possible to find a high concentration of them after a recent forest fire. Unfortunately, they are spread worldwide and it is known they are toxic, carcinogenic and mutagenic.⁶⁶ Solubility of PAHs can be expressed in terms of hydrophobicity. In particular, their hydrophobic behavior increases with their molecular weight and alkyl side groups. Moreover, these compounds can be very dangerous, because they tend to bioaccumulate due to hydrophobicity.⁶⁷

Instead, the term heterocyclic PAHs refers to those compounds with an endocyclic heteroatom (**Figure 2.3**).

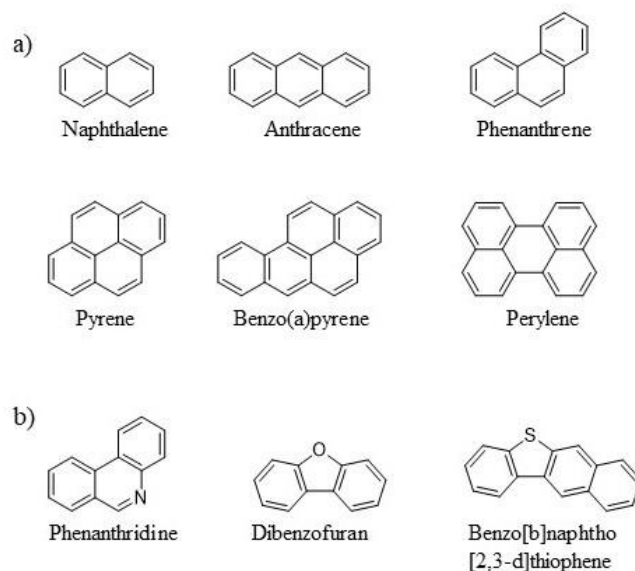


Figure 2.3 Example of some a) PAHs and b) heterocyclic PAHs structures.

Due to their large π -conjugated structure, the gap HOMO-LUMO is reduced. Due to a self-assembly driven by π - π interactions,⁶⁸ PAHs are compounds, which can be used as supramolecular polymers.

In fact, they show optoelectronic properties, which can be used for light-emitting diodes, photovoltaic cells and field-effect transistors:⁶⁹ like in the case of liquid crystals (LCs) (**Figure 2.4**).

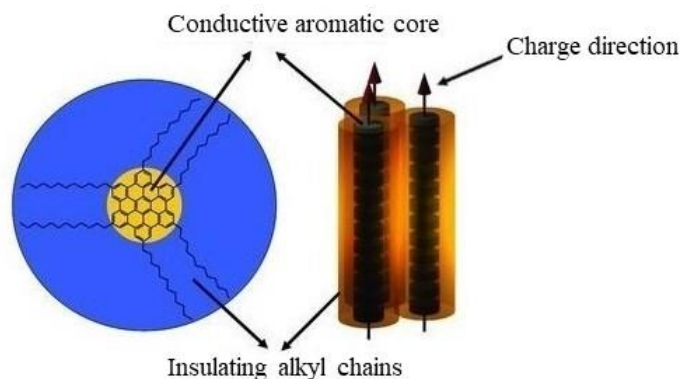


Figure 2.4 LCs discotic structure: alkyl chains insulating the aromatic core, leading to a charge transport (arrow in columns) across the column. Taken from⁷⁰

LCs are considered a new generation of organic semiconductors since their charge carrier transport properties are due to an extended π orbital overlap.⁷⁰

Because of a rigid aromatic core, PAHs in LCs can settle in a discotic architecture with a good stability and a high supramolecular order.

Alkyl chains, bound to the aromatic core, have the dual function to modulate solubility of PAHs and insulate the adjacent piles. This leads to a one-dimensional charge migration. In fact, conductivity across the axis of the column is higher than a perpendicular mobility.⁷⁰

3 SUPRAMOLECULAR STRUCTURES IN WATER

Many solvents have been used for studying supramolecular polymers self-assembly based mostly on π - π interactions due to large π conjugated structure of PAHs.

Indeed, they also show self-aggregation properties in aqueous phase, as both PAHs and heterocyclic PAHs.

Self-aggregation of PAHs, and their functionalization, in aqueous phase, is due to the interactions between aromatic molecules, influenced by hydrophobic effect.

Like the case of perylene diimide (PDI), which possesses a perylene as PAH core. In fact, in order to reduce hydrophobic surface, the aggregation results in the stacking between aromatic structures, held by π - π interactions,⁷¹ leading to architectures, which have some interesting properties.

These materials can be robust and with a well-defined structured order⁶³, like, for example, Rybtchinski and Krieg showed.⁶⁴

They studied self-aggregation of a system, which uses PDI as hydrophobic core, anchored to polyethylene glycol (PEG) as hydrophilic shell, in a mixture water/THF 4:1 (**Figure 2.5**).

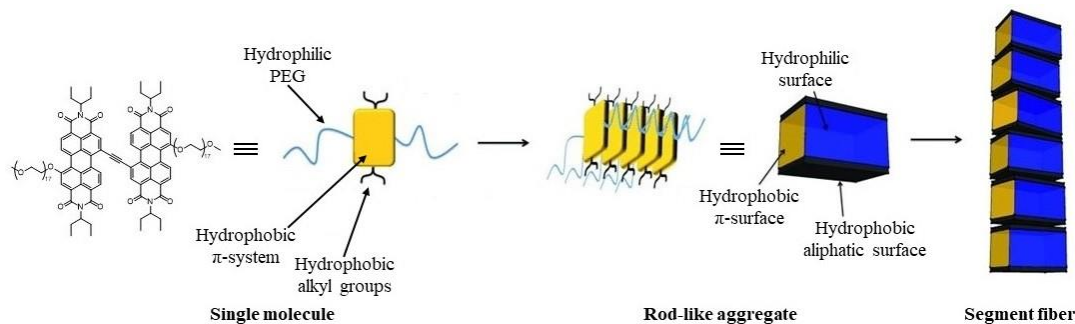


Figure 2.5 Self-assembly starts from π - π interactions of PDI aromatic core with formation of small rod-like aggregates; then, further aggregation leads to fibers. Adapted from⁶⁴

In the beginning, there is the formation of small rod-like aggregated, driven by π - π interactions; these π -stacked structures have an aliphatic surface which is exposed to the aqueous medium with the consequence of a further aggregation between the hydrophobic region of these aggregates, obtaining a fiber-like structure.

4 J- AND H-AGGREGATION

Thanks to π conjugated motif, supramolecular polymers based on an aromatic core (like PAHs or heterocyclic PAHs) absorb light in UV/vis or near IR range. This facilitates the study of their characteristics and investigation about their aggregation.

It is possible to discriminate the kind of their stacking motif: this stacking can arrange with J-, H-type⁶³ or oblique aggregation.⁷²

These types of aggregation show a certain absorption band change compared with the monomers: in particular, J-aggregate is shifted toward longer wavelengths (red-shifted) of the absorption spectrum, speaking of a bathochromic shift.

In particular, J-aggregation was discovered, independently, by Jelley⁷³ and Scheibe⁷⁴, in their study of cyanine dye aggregates in aqueous solutions.

In fact, the compounds, which arrange with formation of this band, are known as J-aggregates, where the “J” denotes Jelley, and Scheibe aggregates, according to the names of their inventors.⁷⁵

On the other hand, H-aggregate shows a hypsochromic shift, showing a less narrow band at shorter wavelengths of the spectrum (blue-shifted).

These shifts, in the absorption spectrum, are explained by exciton theory, which considers a monomer as a transition dipole moment (μ). Considering the easiest case where two monomers aggregate, the excitonic state of the aggregates is split in two levels (S_1 and S_2), based on the interaction of the two transition dipole moments (**Figure 2.6**).^{76,77}

For H-aggregates, the dimers orientation consists in a face-to-face alignment (sandwich-like). The excited state splits in two states: one with a lower energetic level (S_1), in which the transition dipole moments orientation is antiparallel and another with a higher energetic level (S_2), where transition dipole moments are in a parallel orientation.

For J-aggregates, the centers of the two dimers are shifted, arranging in an end-to-end orientation. In this case the excited states splits in a lower energetic level (S_1) with a parallel transition dipole moment orientation, while in the higher energetic level (S_2) transition dipole moment orientation is antiparallel.⁷⁸

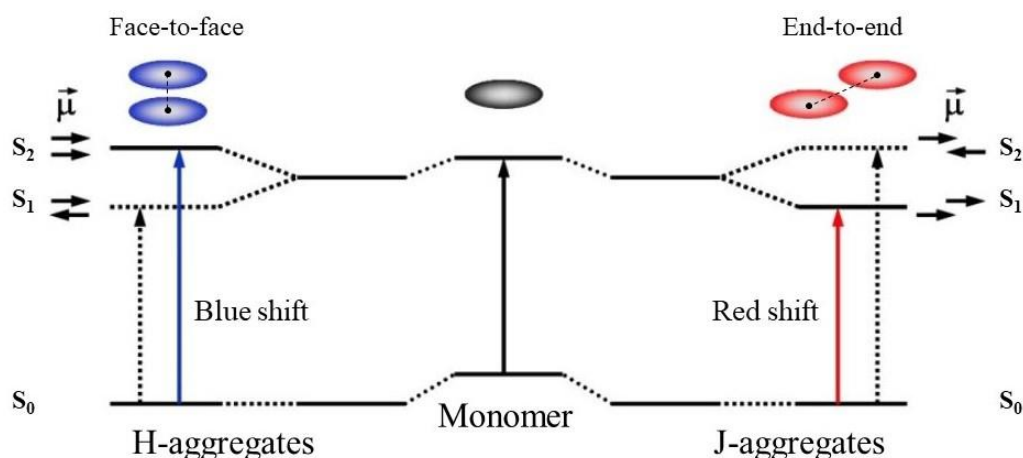


Figure 2.6 Energy diagram for H- and J-aggregates. In the first case the two monomers aggregate in a face-to face fashion, while for J-aggregates in an end-to-end. The excitonic state, for both aggregations, is split in two energetically different states (S_1 and S_2) with their transition dipole moments orientation (parallel and antiparallel). Adapted from⁷⁶

The reason why each excited energy state corresponds to a certain orientation of the transition dipole moments is that in a face-to-face arrangement (H-type), when the two transition dipole moments are parallel, they repulse each other since the same charges are spatially close, leading to a higher energy state.

On the other hand, in a situation where they are antiparallel, they attract each other obtaining a lower energy state.²⁰

The same consideration can be made with the end-to-end arrangement (J-type): in here, a parallel orientation of the transition dipole moment is in a lower state because in this case

different charges are in proximity, leading to a more favorable situation. Antiparallel orientation leads to an opposite situation, with the result of a higher energy state.²⁰

Finally, in order for a transition is allowed the transition moment dipole has to be greater than zero.

In this way, for H-aggregate, the allowed transition from ground state to the higher level of excited state ($S_0 \rightarrow S_2$), exhibits a blue shift (hypsochromic shift)

Instead, for J-aggregate, the transition occurs from the ground state to the lower level of excited state ($S_0 \rightarrow S_1$) with a red shift (bathochromic shift) compared to the monomer.^{77,78}

The last type of aggregation is in between H- and J-orientation: oblique aggregation (**Figure 2.7**). Oblique aggregation shows split broad bands^{72,79} and the transition dipole moments are at a certain angle between H- or J-configuration.

Transition from ground to excited state is allowed for both the higher and lower energy levels of the excited state, since, in both cases, a non-zero total transition dipole moment is obtained.⁸⁰

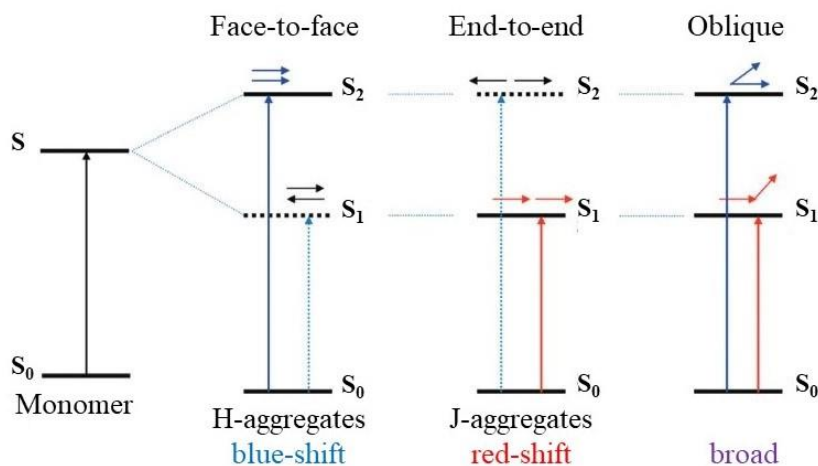


Figure 2.7 Comparison between model of transition dipole moment interactions in H-, J- and oblique aggregates. Solid line arrows indicate allowed transition from ground to one of the level of excited states. For oblique aggregation, both transitions are allowed because transition dipole moments is greater than zero. Adapted from⁷²

5 HÄNER GROUP WORK

The research field of Häner group aims to the design and synthesis of supramolecular polymers and their self-assembly in aqueous media.

In particular, chromophores (pyrene, phenanthrene, PDI, etc.) are used as building blocks for the study of supramolecular interactions. They are linked, by a phosphodiester bond, to either DNA short strands or other polycyclic aromatic structures.

The aggregation of such architectures is followed by spectroscopic and fluorescence analyses, while AFM furnishes a direct observation of the kind of nanostructure formed.

5.1 OLIGOPHOSPHODIESTER SYNTHESIS

Nowadays, oligonucleotide synthesis is carried out through an automated process with the use of a DNA synthesizer, obtaining structures with the desired sequence, via phosphoramidite synthesis.

It is possible to synthesize well-defined structures using monomers (or building block) different from nucleotides, bound each other through a phosphate bridge, leading to oligophosphodiester derivatives (**Figure 2.8**).

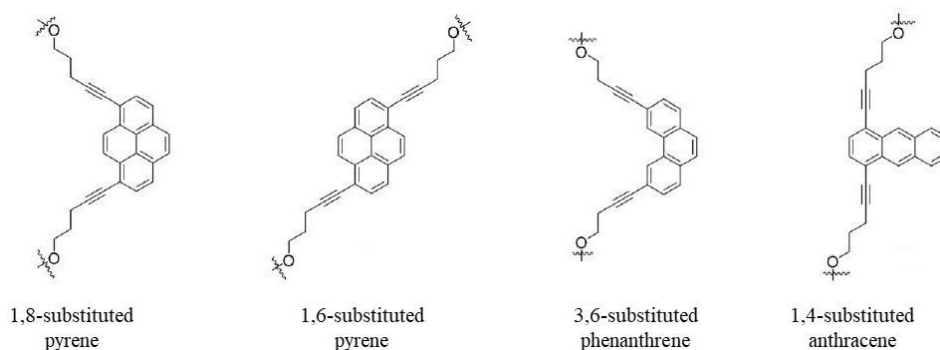
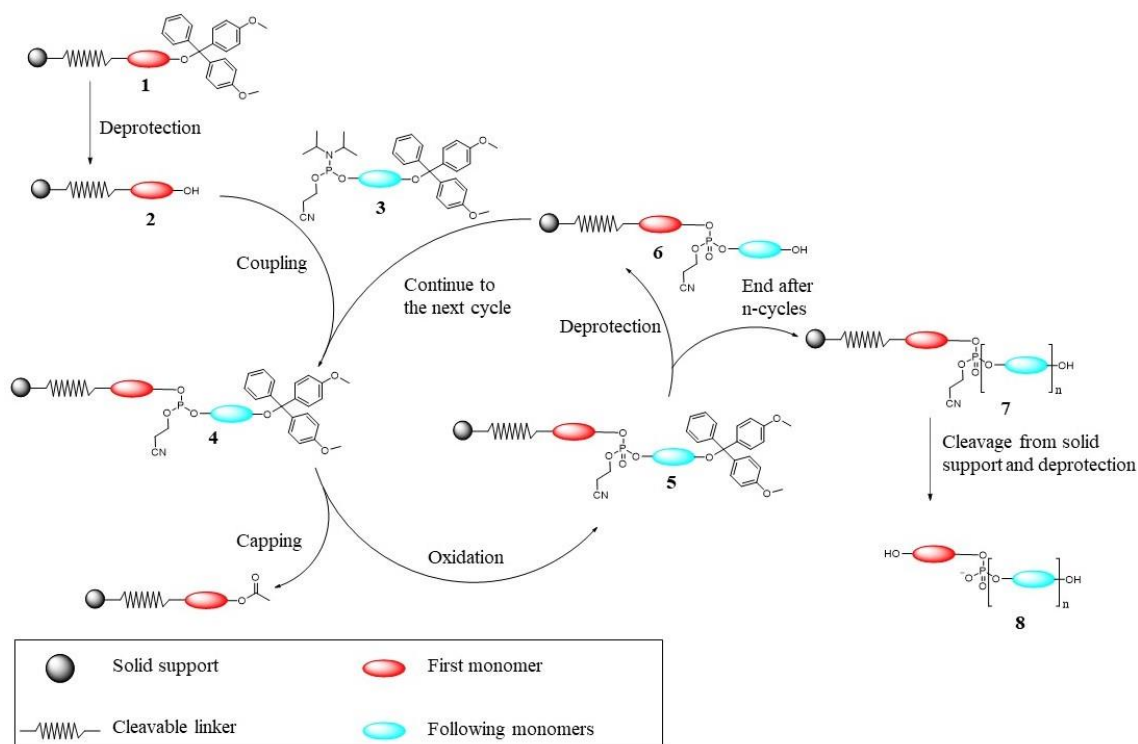


Figure 2.8 Some building blocks used for phosphoramidite synthesis. The two oxygens are linked to a phosphate group, which is linked to another building block: the same molecule, nucleotides, etc. Adapted from ref.⁸¹

This chemical group is important for structural consideration, indeed, the presence of phosphate group increases water solubility and supplies additional tools for self-assembly control (ionic strength, pH).⁸¹

The process for this approach is the solid phase synthesis, in which several steps are needed for the coupling of a single unit.

In **Scheme 2.1**, solid phase phosphoramidite synthesis is depicted. First, the two hydroxyl groups of building blocks (**3**) are functionalized: one with a 2-cyanoethyl N,N-diisopropylphosphoramidite group (CEP) and the other one is protected with an acid-labile dimethoxytrityl (DMT).



Scheme 2.1 Solid phase synthesis for preparation of phosphodiester linked oligomers. Actually, this approach is used for DNA synthesis, but with the right functionalization, other kind of monomer can be added. In picture, first and following monomers can be the same.

The first step starts with deprotection (DMT cleavage) of the monomer anchored to the solid support (**1**), leading to formation of a free hydroxyl function (**2**). This detritylation reaction is made in acidic conditions, using a solution of trichloroacetic acid (TCA) at 3% in dichloromethane (DCM). Next step is a coupling reaction: a solution containing **3** is added. Before the reaction starts, the monomer is treated with 4,5-dicyanoimidazole (DCI). The role of DCI is to activate phosphoramidite group, leading to the formation of a protonated, as intermediate specie. The latter, thus, can react with the free OH in **2**.

Before the oxidation step begins, an additional step is carried out, known as capping. Since not all deprotected monomers are coupled, in order to avoid side product, the unreacted monomers (with OH still free), anchored to the solid support, are “blocked” with an acetyl group, being, thus, unable to take part in next coupling reactions. For capping two solutions are used: one, which contains acetic anhydride and lutidine (Cap A), while the second has N-methylimidazole as catalyst (Cap B). After this step, reaction goes on with oxidation of phosphite (P(III)) to phosphate (P(V)), using a solution of iodine (I_2 , 0.02M) in a mixture of tetrahydrofuran/water/pyridine (66/12/22 v/v/v). This oxidation step leads to formation of **5**, where the phosphate is still protected with the 2-cyanoethyl group.

At this point, after that monomers are coupled, DMT, which belonged to **3**, is cleaved (with 3% TCA in DCM, as described above), setting free the hydroxyl group of the last added monomer of the growing chain (**6**).

The latter can take part to the next cycle in order to elongate the structure or, after n-desired cycles, the obtained n-mer (**7**) is cleaved from solid support using a solution of 2M ammonia in methanol (2M NH₃ in MeOH).

In this condition, 2-cyanoethyl is cleaved from phosphate as well, with formation of the phosphodiester-linked oligomer (**8**).^{82,83}

5.2 DNA AS SCAFFOLD FOR CHROMOPHORE ASSEMBLY

PAHs (like pyrene, anthracene, phenanthrene, PDI, etc.), covalently attached to DNA, are often used. DNA plays the role of scaffold to control the arrangement, of these molecules, for the study of their interactions in solution.^{84,90}

Thanks to their extended π -system, they have the tendency to aggregate through π - π interactions, facilitating the stacking and intercalation with DNA conjugates, allowing the formation of architectures with electronic properties, which can be used for optical and electronic devices or diagnostic application.^{85,86}

Such constructions can be used as light-harvesting antennae: a system where the excitation energy is transferred from multiple donor molecules to a few or one acceptor.⁸⁷

For example, considering a system made up with DNA double helix as supramolecular scaffold, which assists the formation of an array of π -stacked phenanthrenes and pyrene (Figure 2.9).

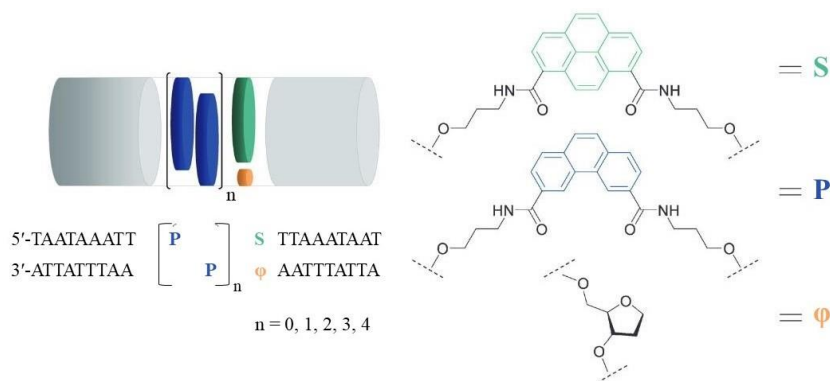


Figure 2.9 DNA double helix (grey cylinders) assists π -stacked phenanthrenes (blue) and pyrene (green) (on each end of the phenanthrenes stack) formation. Taken from ref.⁸⁸

Phenanthrenes are stacked in the center of DNA duplex, with one pyrene to one of the two extremities of phenanthrene stack. In addition, an abasic site is added opposite to pyrene, in order to avoid the formation of positional isomers.

UV/vis absorption spectra reveal a band with a maximum around 320nm originated from phenanthrene, the absorbance increased linearly with the number of the molecules.

Fluorescence studies have showed the formation of an exciplex between pyrene and one of the phenanthrenes, with an emission wavelengths at 450nm formed after excitation of phenanthrene at 320nm (**Figure 2.10**).⁸⁸

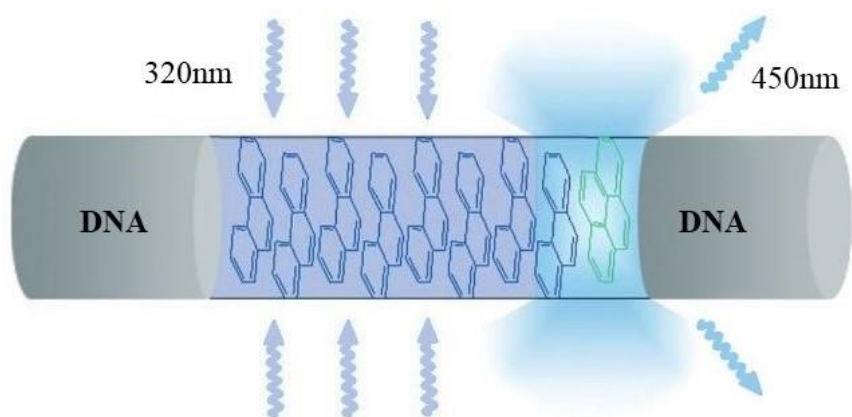


Figure 2.10 Light-harvesting antenna, with π -stacked phenanthrene as energy-collecting donor (purple block) and phenanthrene-pyrene exciplex as energy acceptor (blue block). Adapted from⁸⁸

In conclusion, this light-harvesting antenna model is formed by a π -stacked phenanthrene motif, which acts as energy-collecting donor and the exciplex (phenanthrene-pyrene) as energy acceptor.⁸⁸

Another example, of chromophore interaction assisted by DNA base pairing, is the formation of a DNA three-way junction (3WJ). The latter is formed by a core of π -stacked chromophores, from which three complementary oligonucleotides are branched.

In these architectures, self-assembly of non-nucleosidic chromophores is stable and based on the type of chromophore combinations used, the structures show different spectroscopic behaviors.⁸⁹ An interesting use for DNA-3WJ is as light-harvesting antenna system.

In **Figure 2.11**, it is showed oligonucleotide sequences, containing phenanthrene, pyrene, PDI and cyanine. In here, phenanthrene molecules, which are linked to two different oligonucleotide strands ((a) and (b)), are π -stacked in the core of the structures.

In other strands, pyrene, phenanthrenes, and cyanine are linked in the middle of the sequence ((c) – (g)).

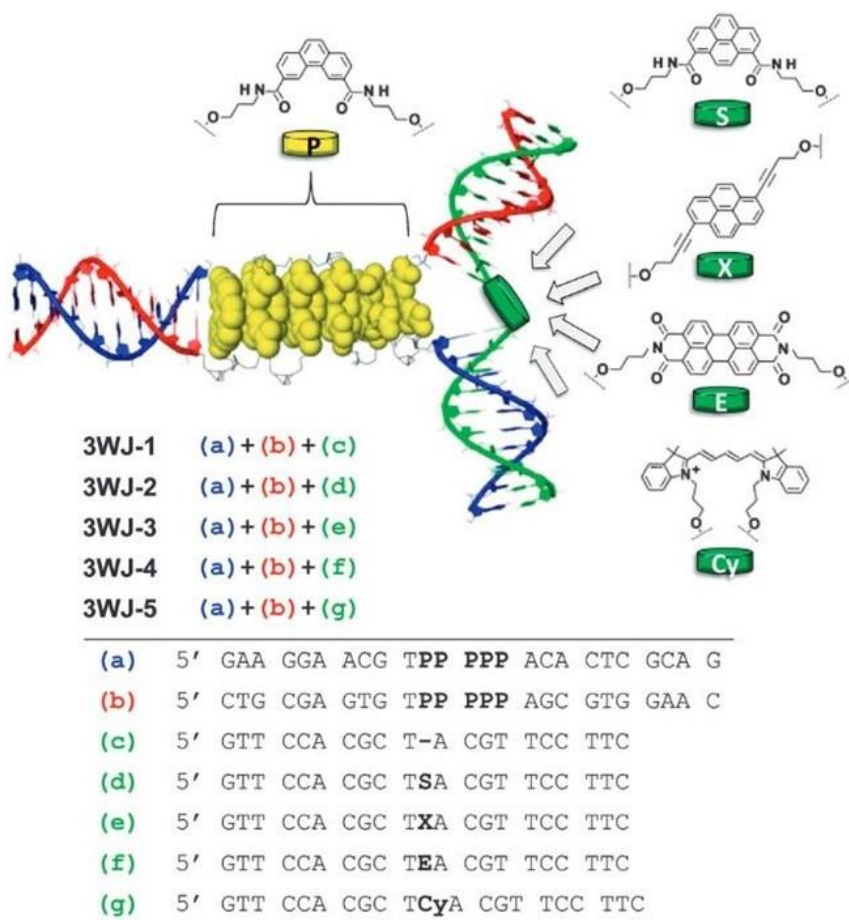


Figure 2.11 Representation of different arrangement of 3WJ. The chromophores used are indicated with letters: **P** = 3,6-disubstituted phenanthrene; **S** and **X** = 1,8- and 1,6-disubstituted pyrene respectively; **E** = PDI; **Cy** = cyanine. Taken from ref.⁹⁰

In this work, phenanthrene core is the donor: energy is transferred from the core to the acceptor in the third strand. In particular, it was observed that in the case of pyrene there is the formation of an exciplex fluorescence and for cyanine typical fluorescence of the molecule. PDI, instead, acts as a quencher.⁹⁰

5.3 OLIGOARENOTIDES

The oligoarenotides are a class of compound made by repeating aromatic molecules (arene) units linked with each other by a phosphodiester group. Because their similarity with oligonucleotides, the term oligoarenotides is used.⁹¹

Atomic force microscopy (AFM) is used for the studies of such architectures (**Figure 2.12**).

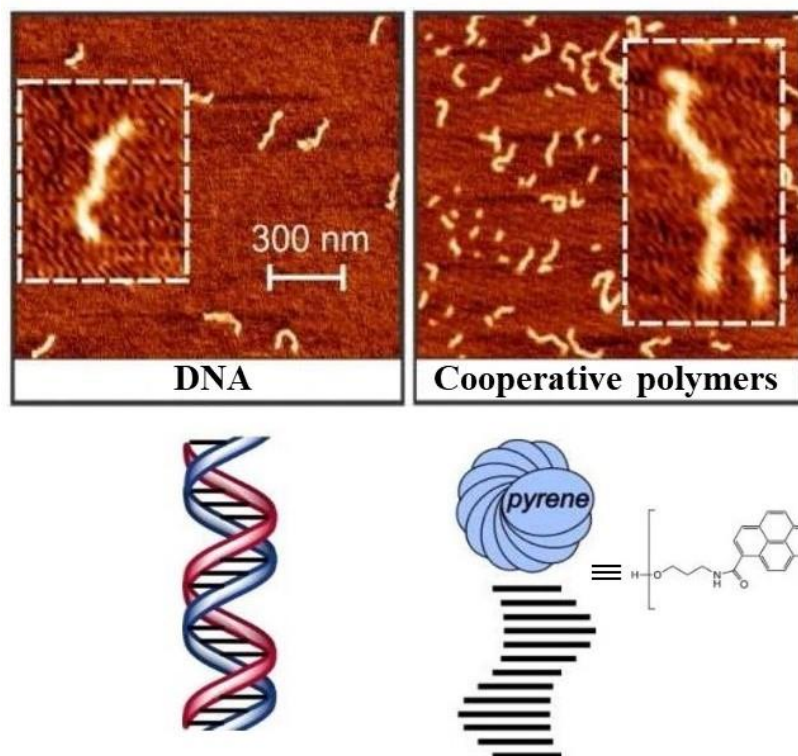


Figure 2.12 AFM pictures, where structure similarity between a 600 bp DNA (on the left) fragment and a pyrene-like heptamer (on the right) is showed. Conditions: $7\mu\text{M}$, 10mM sodium phosphate buffer pH 7.0 and 1M NaCl. Adapted from ref.⁹²

In **Figure 2.12** is showed an example of similarity, in terms of observed nanostructures, between DNA double strand and an oligoarenotide, where the self-assembly was induced in certain aqueous phase conditions.

A system made up with pyrene heptamer linked via phosphate (pyrene-like heptamer, Py_7) has showed a cooperative self-assembly with high similarity of 600 bp DNA fragment.

The aggregation in aqueous medium, for both oligomers, was induced by cooling a solution of $7\mu\text{M}$ of both sample, with 10mM sodium phosphate buffer pH 7.0 and 1M NaCl. High ionic strength of NaCl is needed for the aggregation of hydrophobic pyrene units; in fact, there is no aggregation in the absence of the salt.

In conclusion, intrinsic properties of Py_7 leads to a one-dimensional polymer with a high homogeneous width, making such kind of oligomers potential candidates for the development of new self-pairing systems.⁹²

Another interesting use of pyrene, in an oligoarenotides system, is the synthesis of a pyrene trimer linked via phosphate, capable to self-aggregate in 2D structural motif.

Spectroscopic studies, made on 1,6-dialkynyl substituted pyrene trimer (Py_3), has showed temperature-dependent aggregation behavior revealed by the formation of J- and H-type aggregation (**Figure 2.13**).⁹³

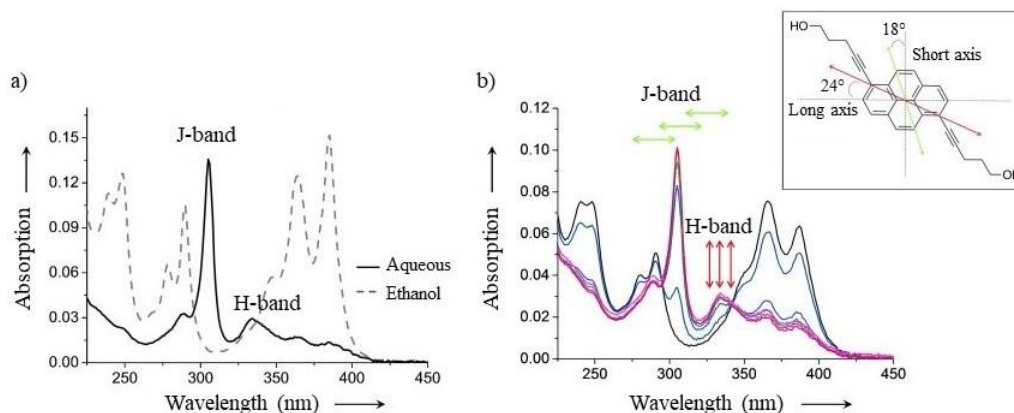


Figure 2.13 UV/vis spectra of Py_3 . a) UV/vis spectra comparison between $1\mu\text{M}$ of Py_3 in ethanol (dashed line) and in aqueous medium (10mM sodium phosphate buffer pH 7.2, 10mM NaCl, 10 vol% ethanol) at 20°C ; b) temperature dependent UV/vis spectra in aqueous medium: at 80°C (black line) the system is completely disassembled and at 20°C (red line) the system is assembled showing formation of J- and H-band, with their own transition dipole moment orientation; lines with different colors represent the equilibration, measured within 20 min at 20°C .

Inset: orientation of transition dipole moments, twisted by 24° relative to the long axis and 18° relative to the short one, due to the substituents in 1 and 6 position. Adapted from⁹³

Self-assembly process, in water solution, occurs following a cooperative model path. In ethanol at 20°C , Py_3 is disassembled; whereas, in aqueous medium (10mM sodium phosphate buffer pH 7.2, 10mM NaCl, 10% ethanol) self-aggregation of pyrene molecules is observed at the same temperature. Small amount of ethanol is required to ensure the reversibility of aggregation process.

In particular, a temperature-dependent process is observed. As showed in **Figure 2.13**, at 80°C there is no aggregation between pyrene molecules.

In fact looking at the spectra there is no evidence of J- and H-bands, showing a similarity with the trend of the solution measured in pure ethanol.

Cooling the solution down to 20°C , the trends changes with the formation of a long bathochromic-shifted peak, typical for J-aggregation and a small hypsochromic-shifted peak, which indicates an H- aggregation.⁹³

The aggregation path can be understood better looking at **Figure 2.14**, where a graph of UV/vis absorption as a function of temperature is showed.

This plot is measured at three different wavelengths (305nm, 365nm and 385nm), starting from 80°C to 20°C.

Moreover, the wavelength at 305nm corresponds to J-band. The aggregation proceeds according to a cooperation model: at 80°C, the system is disassembled.

Cooling down the solution, the curves undergo a change in their absorption at ~73°C.

This value corresponds to the critical temperature (T_c , see chapter 1): here, there is the formation of nuclei. Lowering the temperature, more Py_3 structures join to nuclei for the elongation step.⁹³

In **Figure 2.14**, the curve, which corresponds to the absorption at 305nm, shows a different path, in contrast to those at 365nm and 385nm. This is due to the formation of J-band at 305nm, which occurs at low temperatures and indicates the aggregation of the system.

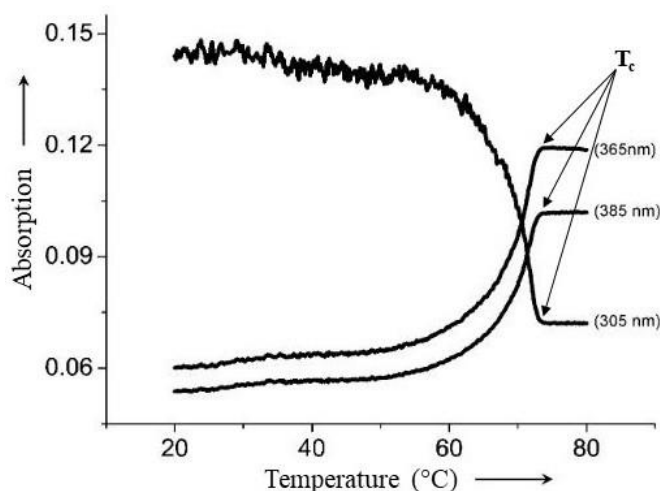


Figure 2.14 UV/vis absorption as a function of the temperature. The system, disassembled at 80°C, starts to aggregate lowering the temperature. There is an initial nuclei formation ($T_c \sim 73^\circ\text{C}$) and then the elongation step.

AFM studies confirmed the aggregation for this structure and with the combination of UV/vis analyses, some valuation can be made (**Figure 2.15**).

As showed by AFM, Py_3 aggregates with formation of nanosheets. The trimer in water at higher temperature is present as random coils. Then, cooling down the solution, there is the formation of nuclei at $\sim 73^\circ\text{C}$, followed by addition of further Py_3 structures for the elongation step. Py units, inside the trimer, interact in a staircase-like manner (inset in **Figure 2.15**), which corresponds to the appropriate transition dipole moments alignment.⁹³

The latter causes the appearance of J-band due to a parallel orientation of transition dipole moments ($S_0 \rightarrow S_1$). Instead, an antiparallel orientation of transition dipole moments ($S_0 \rightarrow S_2$) generates H-band, as described in this chapter.

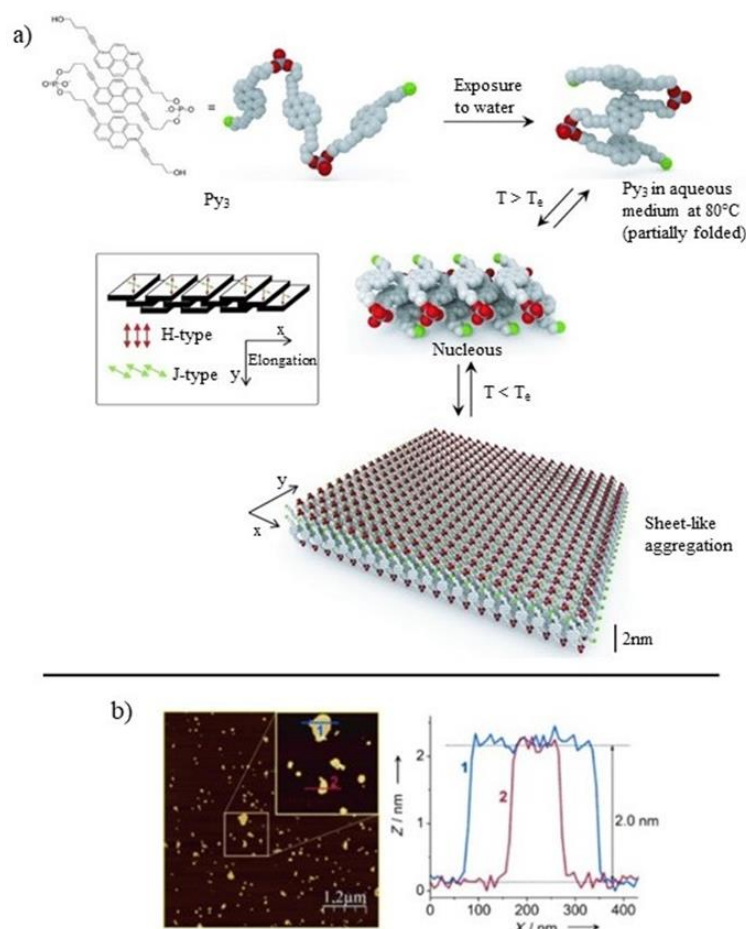


Figure 2.15 Pyrene-like trimer sheets formation: a) self-assembly according to a cooperative mechanism, with the initial formation of a nucleus at critical temperature (T_c), followed by elongation step, which leads to formation of the sheet; b) AFM picture, which shows nanosheet structures with 2nm width (cross section next to the picture). Adapted from⁹³

CHAPTER 3

1 AIM OF THE THESIS

In our group, we study short oligomers, based on π -conjugated structures, linked via phosphate group, and their self-assembly driven by π - π interactions in aqueous medium. A few of low molecular weight PAHs are used as oligomers core, like anthracene, phenanthrene and pyrene.

In particular, pyrene and its derivatives, forms excimers, which are used to detect environmental parameters (pressure, temperature, pH) or molecule, like gases, organic compounds, metals. Furthermore, the link of pyrene to hydrophilic polymers, changes the properties of the latter. Nowadays, pyrene is used by scientist in many research areas, for the preparation of many derivatives.⁹⁴

Our group uses this molecule for the synthesis of many compounds; for example, it was linked to nucleotides in short DNA sequences,^{90,95} or other PAH structures (like phenanthrene).⁸⁸ Studies based on phosphodiester-linked pyrene trimer proved the ability of this structure to form supramolecular aggregate with a sheet-like motif, in aqueous media⁹³ (see chapter 2).

The aim of this thesis is to study pyrene-like trimer functionalized, which were able to self-aggregate with the formation of nanosheets. The functionalizations used were a mannose (for Py₃Man) and a butynyl (for Py₃But), linked via phosphate groups (**Figure 3.1a** and **Figure 3.1b**, respectively). The idea for the choice of these two molecules was due for their possibility to interact, selectively, with external architectures.

In particular, about Py₃Man, after its supramolecular nanostructure formation, mannose moiety will bind to Concanavalin A, which is a protein able to bind to D-mannose and D-glucose. Instead, Py₃But will be used for two approaches, both of them based on the use of click chemistry. In the first case, a DNA strand (DNA-1), bearing an azide group, will be covalently linked to the supramolecular aggregate, via click chemistry.

On the other hand, a complementary DNA strand (DNA-2) bound to gold nanoparticles will bind via base pairing to DNA-1.

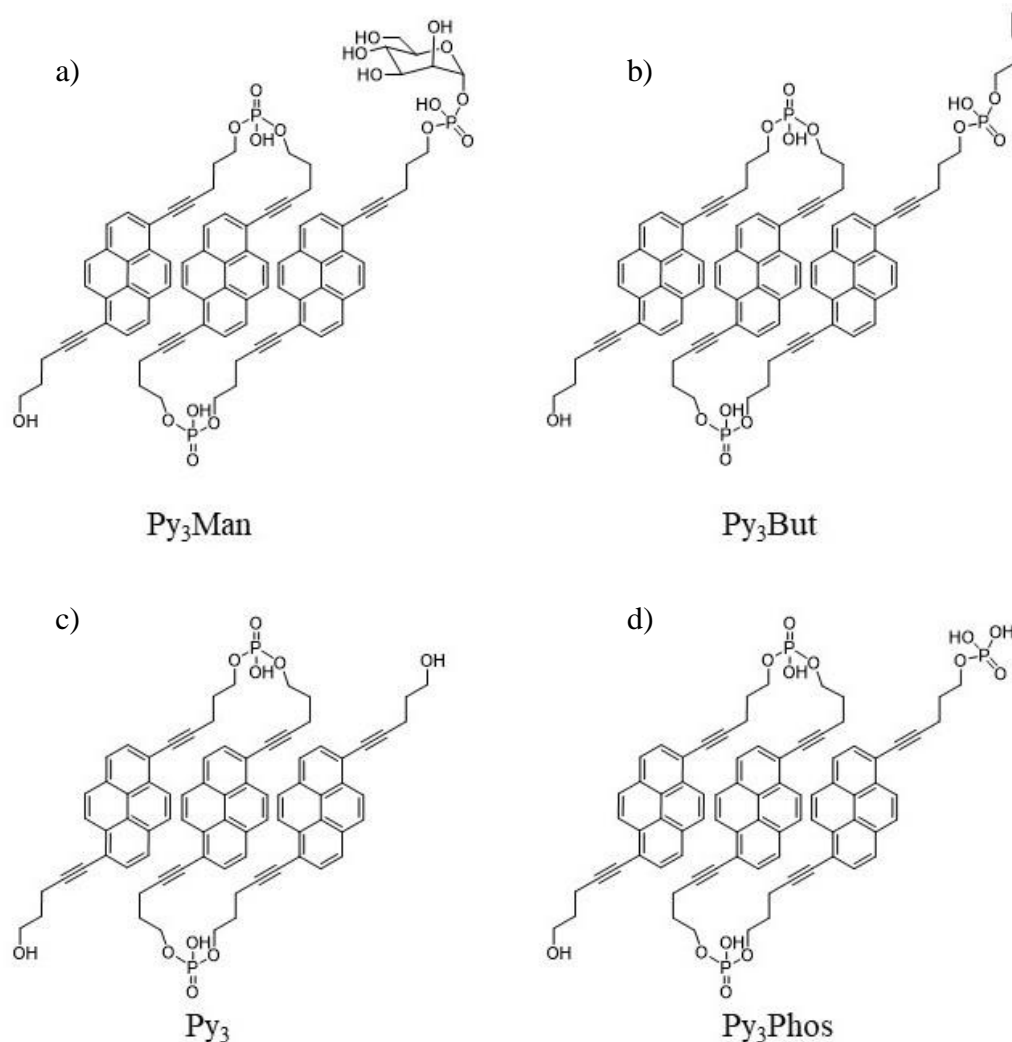


Figure 3.1 Structure of pyrene trimers studied here: Py₃Man (a) and Py₃But (b) as object of study. Py₃ (c) and Py₃Phos (d) are used as control.

The other approach is based on the use of polyethylene glycol (PEG) derivative. In here, PEG carries a thiol group, which links to gold nanoparticles, and an azide group, which will react with the triple bond moiety linked to the pyrene trimer.

The first set of analyses are aimed to the study of aggregation of Py₃Man and Py₃But in aqueous medium. Whereas, a second set of experiments is focused on the link with Concanavalin A in the case of Py₃Man and click chemistry in the case of Py₃But.

The aggregation studies are made with the use of UV/vis spectrometry, in order to follow the self-assembly of these compounds, and AFM to see which kind of nanostructure the self-assembly leads to.

Furthermore, two additional structures are synthesized as control (**Figure 3.1c** and **Figure 3.1d**): pyrene trimer (Py_3), already studied in ref.⁹³ and a pyrene trimer linked to a phosphate group (Py_3Phos).

In this way, for example, if Concanavalin A links to mannose moiety of Py_3Man , the same experiment will be done with Py_3 and Py_3Phos , which act as control molecules.

Instead, the control for the tests made with Py_3But will be made using PEG derivatives, linked to gold nanoparticles, with no azide.

Moreover, one can understand how the addition of mannose and butynyl can influence the supramolecular aggregation.

In this chapter is illustrated the studies about the self-assembly of all four pyrene trimers.

2 PRELIMINARY TESTS

As depicted in chapter 2, Py_3 was already studied in our group. It was proved that Py_3 in aqueous solution with 10mM sodium phosphate buffer pH=7.2 and 10% of ethanol (EtOH) and 10mM NaCl, was involved in a self-assembly process.^{93,96}

These previous studies on Py_3 were conducted at UV, showing that the trimer was aggregated at 20°C, with formation of nanosheet structures, as found at AFM.

Whereas, in EtOH and in aqueous solution at 75°C, there was no aggregation and the UV spectrum, relative to both conditions, were pretty similar (see chapter 2).

Here, all trimers are studied in two different aqueous solutions: the first is in 10mM sodium phosphate buffer pH=7.2 and 10% EtOH, while the second is in only 10mM sodium phosphate buffer pH=7.2.

The first UV/vis analyses were made in EtOH and in aqueous solution (described above) at 75°C, showing no aggregation (**Figure 3.2**).

In all four trimers, the UV/vis curves, both in EtOH and in solution at 75°C, are similar, with the same kinds of the maxima of absorption and with their relative positions. That means that the systems are disassembled in these conditions.

For a better understanding of the experiments, the UV/vis analyses of $1\mu\text{M}$ of the compounds in aqueous solution made with 10mM sodium phosphate buffer $\text{pH}=7.2$ and 10% EtOH are first showed

Then, the same experiments are made in aqueous solution with 10mM sodium phosphate buffer $\text{pH} = 7.2$, without EtOH.

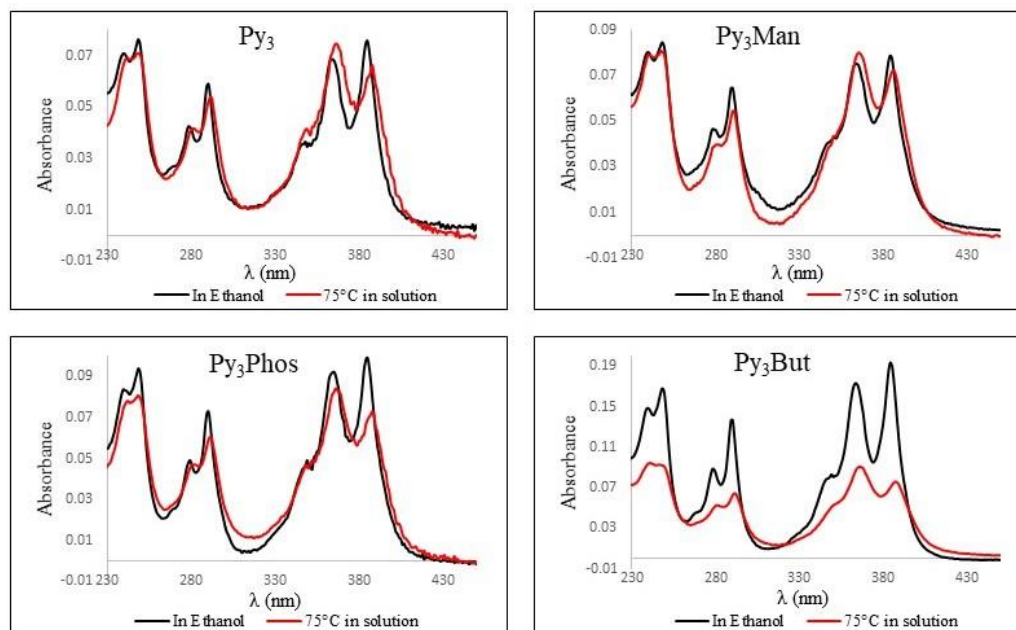


Figure 3.2 UV/vis trends of $1\mu\text{M}$ of all four trimers, in EtOH and in aqueous solution at 75°C . Previous studies⁹³ conducted on Py_3 showed that in EtOH and in aqueous solution at high temperature (in that case the temperature was 80°C , here 75°C is used) the trimer is not self-assembled. Moreover, the intensity of absorption in Py_3But is due to a different concentration: in EtOH the concentration is $\sim 2\mu\text{M}$, while in aqueous solution is $1\mu\text{M}$.

Furthermore, at first, a comparison between Py_3 , Py_3Man and Py_3Phos is illustrated, because the first approach aimed to the study of Py_3Man and subsequent link with Concanavalin A. In order to understand how a functionalization could influence the aggregation, these three trimers were synthesized and, then, studied in parallel.

Py_3But was synthesized for a second approach aimed to the use of gold nanoparticles and studied with no comparison with the other trimers.

3 PYRENE TRIMER (Py₃)

As already mentioned above, the aim of this thesis is to synthesize functionalized nanosheets (based on Py₃ systems). Studies on Py₃ system in our group showed the formation of nanosheets (as observed at AFM), after the solution was cooled at 0.1°C/min in presence of 10mM of NaCl.^{93,96}

In order to understand if a sugar phosphodiester-linked to the structure can influence the aggregation, Py₃ was studied in the same condition used for Py₃Man studies, which is an aqueous solution of 10mM sodium phosphate buffer pH = 7.2 and 10% EtOH.

As showed in **Figure 3.3**, UV/vis curve of Py₃ shows a different behavior at different temperatures: at 75°C, it is disassembled; but cooling the solution down to 20°C, it is aggregated, with the formation of both J- and H-band. The path from higher to lower temperatures does not occur randomly. In order to have reproducible analyses, the cooling block of spectrophotometer goes from 75°C to 20°C in ~8 minutes, so it is possible to calculate a cooling rate of ~7°C/min

The H-band originates from S₀→S₂ transition, which leads to the formation of a small and blue-shifted peak at 335nm, with a face-to-face orientation of transition dipole moments. Instead, the J-band is due to a S₀→S₁ transition, with the formation of a big and sharp red-shifted peak at 305nm, and the transition dipole moments arrange in an end-to-end orientation.

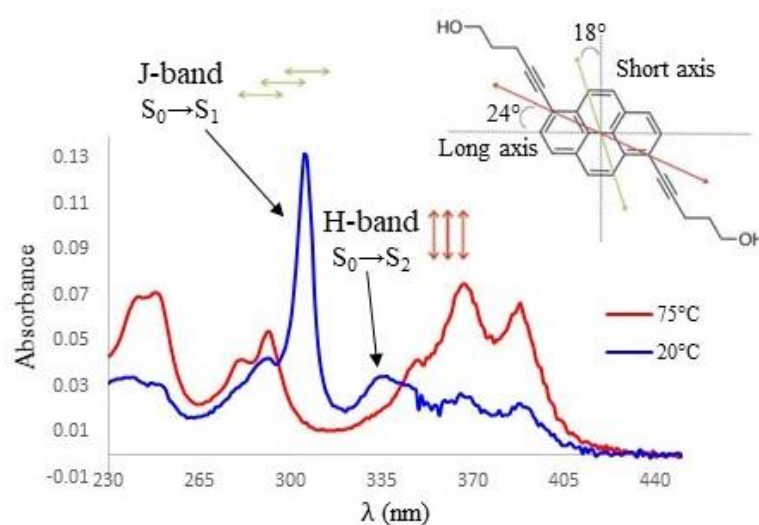


Figure 3.3 UV/vis absorption of 1 μ M Py₃ in aqueous solution with EtOH. At 75°C (red line), the system is disassembled, while at 20°C (blue line) it is aggregated. The J- and H-bands depend by their transition dipole moments orientation. The inset is taken from ref.⁹³

The presence of substituents, in position 1 and 6 of pyrene, leads to a rotation of the transition dipole moments: 18° relative to the short axis and 24° relative to the long one⁹³ (inset in **Figure 3.3**)⁹³. Furthermore, at 20°C , the intensity of the two maxima, in the range between 350nm and 400nm , is much more reduced.

It is possible to calculate a ratio as: absorbance at 75°C /absorbance at 20°C = ~ 2.92 . This value can give an idea of the loss of the value of the absorbance at lower temperature. In fact, the absorbance at 75°C is almost three times bigger than that at 20°C .

UV/vis temperature dependent analyses can give more information about the aggregation in this solution, with a cooling/heating rate of $0.1^\circ\text{C}/\text{min}$ (**Figure 3.4**).

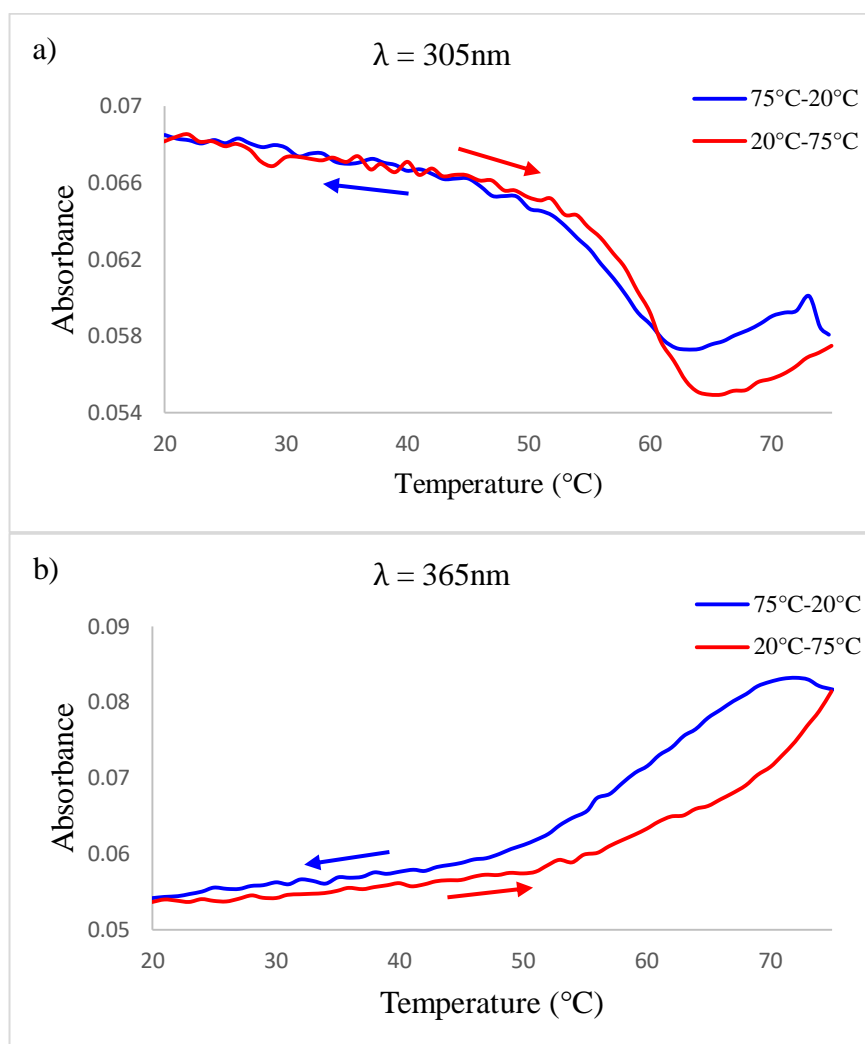


Figure 3.4 UV/vis cooling (blue) and heating (red) curves, of Py₃, measured at $0.1^\circ\text{C}/\text{min}$ as cooling rate, at: a) 305nm and b) 365nm . The formation of nuclei starts at is at $\sim 70^\circ\text{C}$ (T_c). Py₃ is measured with a concentration of $1\mu\text{M}$ in a solution with 10mM sodium phosphate buffer and 10% EtOH.

The measure is pretty simple: at the chosen wavelength, the solution from 75°C degrees is cooled down to 20°C with a cooling rate of 0.1°C/min. Then, a second run goes in the opposite way, warming the solution up again to 75°C, at the same rate.

The analysis was made at 305nm, which corresponds to the J-band wavelength, while the choice of 365nm is due to the fact that at this wavelength there is a bigger change of the corresponding absorption intensity. Wavelength at 335nm (H-band) is not chosen because its intensity is quite small.

In this analysis, it is clear that supramolecular aggregation of Py₃ occurs according with a cooperative model (see chapter 1).

In fact, at 75°C the molecules are dissolved. Then, cooling down the solution there is a first formation of nuclei (at critical temperature, T_c).

In this case, that happens at ~70°C: at this value of temperature, the UV curves have a huge change of the absorbance.

The trend at 305nm increases (**Figure 3.4a**). This is obvious because J-band appears as a long peak at 20°C; while at 365nm (**Figure 3.4b**), the trend is the opposite, because the maximum at this wavelength has a loss of intensity when the temperature decreases.

Anyway, the formation of nuclei at the critical temperature is followed by an elongation step, with the self-assembly in some nanostructures.

A similar result can be obtained measuring the heating/cooling at 0.5°C/min as cooling rate (**Figure 3.5**), in the same conditions.

The two curves look like pretty similar to those measured at 0.1°C/min with T_c value at ~70°C. Also in this case, the plot of absorbance as a function of the temperature is measured in correspondence of J-band (at 305nm) and at 365nm. It is also interesting to note how the system, in this kind of analysis (both at 0.1°C/min and 0.5°C/min as cooling rates), is reversible.

In fact, in the cooling step, the two curves (in each analysis) start to a certain value of the absorbance (at 75°C) and, then, they end with another one at 20°C. In the heating step, there is a reverse path where the curves come back to the values of the absorbance at the beginning of the experiment (in terms of absorbance, at 75°C: lower value at 305nm and higher value at 365nm).

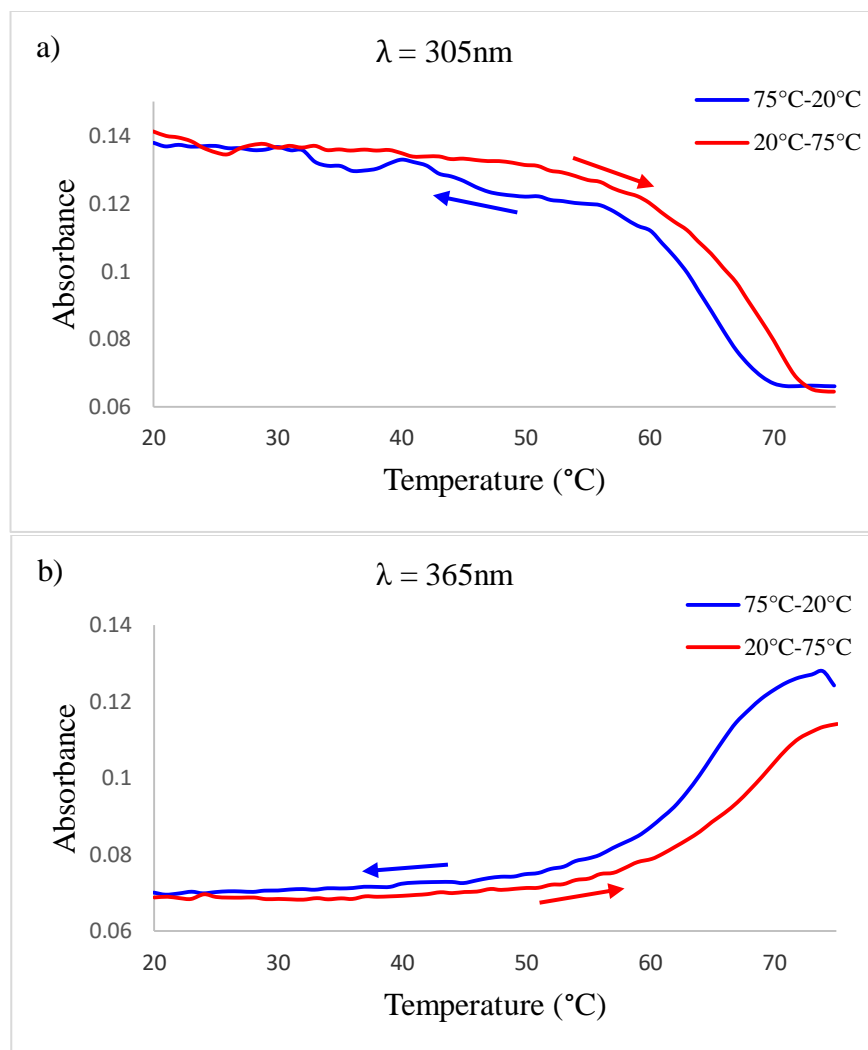


Figure 3.5 UV/vis cooling (blue) and heating (red) curves of Py₃ measured at 0.5°C/min as cooling rate, at: a) 305nm and b) 365nm. Also in this case T_c is at ~70°C. Measured in aqueous solution with 10% of EtOH.

The same UV/vis analyses were made on Py₃Man, as well. In this way, in this first studies, it is possible to understand how the presence of the functionalization can influence the aggregation.

4 STUDY OF Py₃Man

The first functionalization was the addition of α -D-Mannose (Man) to one of the two extremities of pyrene trimer (Py₃), leading to Py₃Man synthesis.

Preparation of the trimer is made via phosphoramidite synthesis (described in chapter 2).

In experimental section, the synthetic procedures, of each building block, are described. Just for an idea, molecules used for preparation of the product Py₃Man are showed in **Figure 3.6**.

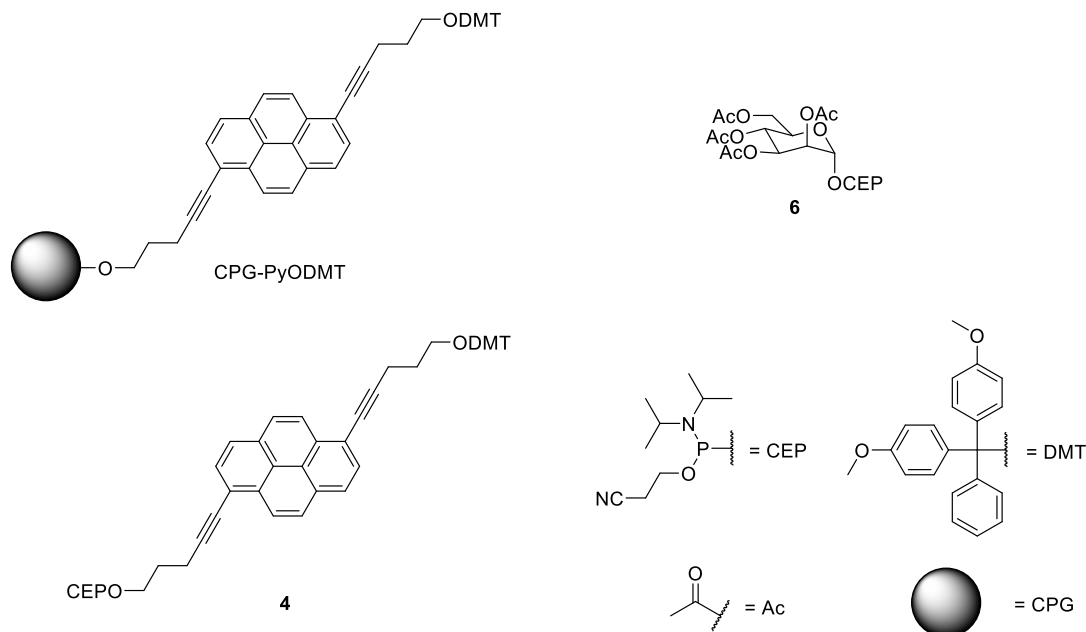
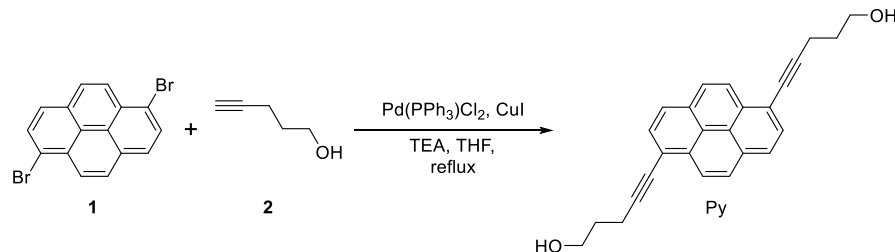


Figure 3.6 Monomers used in phosphoramidite synthesis. The synthesis is starts using a solid support linked to a pyrene (CPG-PyODMT), which is the first pyrene of Py₃Man. Then, two **4** molecules and one **6** are coupled.

These building blocks need to be synthesized, starting from commercially available molecules, which are subjected to organic chemistry modifications, as described below. According to literature,⁹³ the first step is the synthesis of Py starting from 1,6-dibromopyrene (**1**), which is coupled to 4-pentyn-1-ol (**2**) through Sonogashira coupling, leading to the formation of the corresponding product (**Scheme 1**).

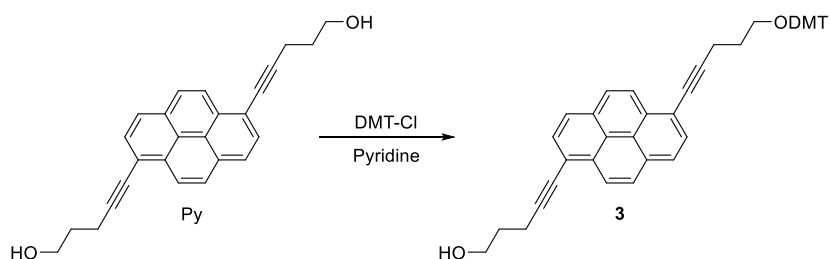


Scheme 3.1 Reaction scheme of Sonogashira coupling between 1,6-dibromopyrene (**1**) and 4-pentyn-1-ol (**2**) with formation of Py.

In order to be clear, the term Py refers here to pyrene which ends with two hydroxyl groups, while Py₃ (and similar) is used to indicate three pyrene (Py) molecules linked to each other via phosphate group.

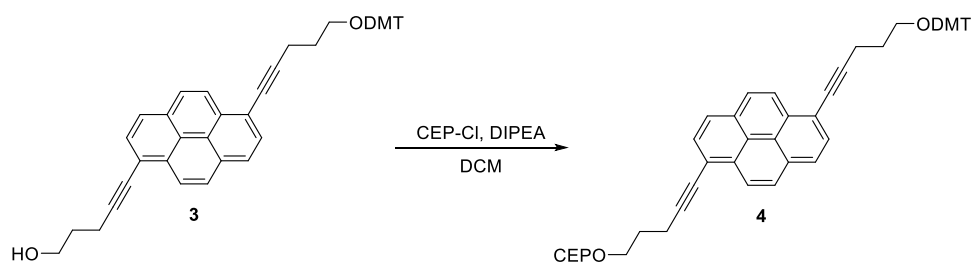
Sonogashira coupling is transition metal-catalyzed coupling, with formation of a bond between sp²-C and sp-C atoms, using as precursor aryl or alkenyl halides and terminal alkynes^{97,98} (in this case, the substrate is an aryl dihalide).

The next step is the protection of one of the two hydroxyl functions of Py with 4,4'-dimethoxytrityl chloride (DMT-Cl) (**Scheme 3.2**). The reaction is made in pyridine with 1 eq of DMT-Cl, in order to minimize the formation of the di-protected compound as byproduct.



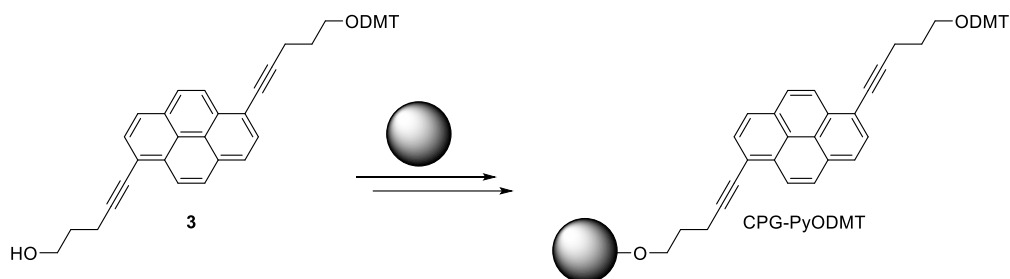
Scheme 3.2 Scheme of mono protection reaction with DMT, leading to formation of **3**.

Compound **3** is used for two different reaction paths: in the first case, the free hydroxyl group reacts with 2-Cyanoethyl N,N-diisopropylchlorophosphoramidite (CEP-Cl), with the presence of N,N-diisopropylethylamine (DIPEA) in excess, leading to formation of **4** (**Scheme 3.3**).



Scheme 3.3 Reaction scheme of **3** with CEP-Cl, leading to formation of **4**.

Compound **4** is used in phosphoramidite synthesis for the preparation of Py₃Man, with the use of synthesizer. In second case, **3** is anchored to a solid support. For this strategy, CPG (controlled pore glass) is used as solid support (grey sphere in **Figure 3.4**).⁹³

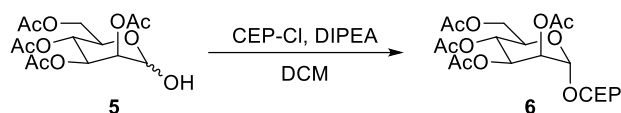


Scheme 3.4 In a few steps, **3** is anchored to solid support (indicated with grey sphere) leading to CPG-PyODMT.

Last monomer was obtained by adding CEP to the anomeric position of α -D-mannose (**Scheme 3.5**).

For this reaction, the commercially available 2,3,4,6-tetra-O-acetyl-D-mannopyranose (**5**) was used.

This reaction, performed at ambient temperature, led to formation of α -anomer.⁹⁹



Scheme 3.5 Reaction scheme of CEP coupling of anomeric position of **5**. The product obtained is the α -anomer **6**.

After their preparation, all monomers were coupled via phosphoramidite synthesis using the DNA synthesizer.

The synthesized product (Py₃Man) was still anchored to solid support and both phosphate and mannose were still protected with a cyanoethyl and acetate groups, respectively.

Therefore, the pyrene trimer with mannose linked to CPG, is suspended in a solution of methylamine (33% in ethanol) and NH₃ (25-30% in H₂O) 50/50 for 15 min at ambient temperature, then for 15 min at 65°C.

In this way, the trimer is cleaved from solid support and at same time the deprotection of both phosphate (with cyanoethyl group removal) and mannose (with acetyl groups removal) occurred.

The obtained Py₃Man is purified by HPLC and the product (**Figure 3.7**) is confirmed by mass spectrometry (MS).

About the other two trimers, Py₃ was synthesized according to procedure⁹³, while Py₃Phos was found as byproduct during the synthesis of Py₃Man.

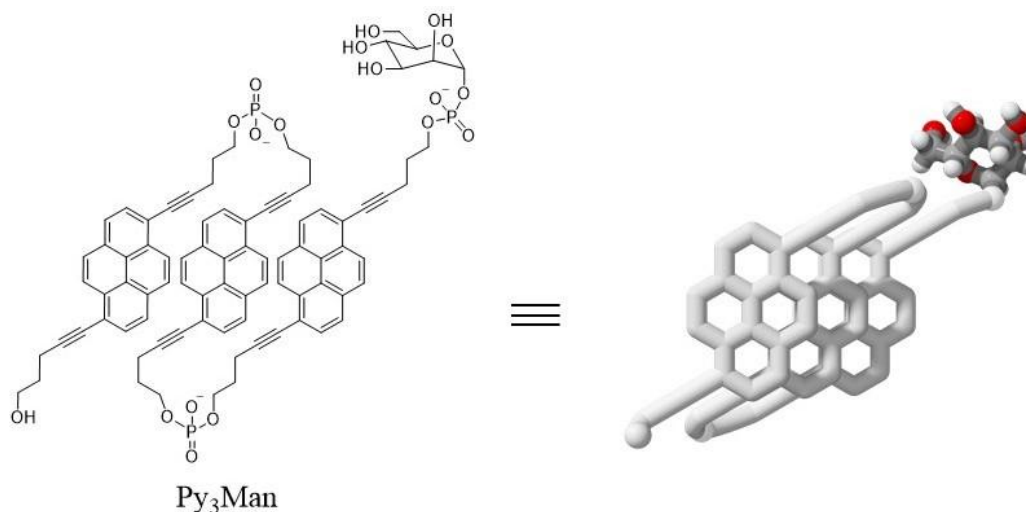


Figure 3.7 Structure of Py₃Man: the three Py molecules and mannose are linked via phosphodiester.

4.1 UV/VIS ANALYSES OF Py₃Man

Repetita iuvant: UV/vis analyses are carried out with 1 μ M of Py₃Man in an aqueous solution made by 10mM sodium phosphate buffer pH = 7.2 and 10% of ethanol (EtOH). As already described above, at 75°C the UV/vis spectra indicates that the trimers are not aggregated, and so Py₃Man as well (**Figure 3.4**).

In fact, repeating the same analyses made with Py₃, cooling the solution down at 20°C ($\sim 7^\circ\text{C}/\text{min}$), UV/vis spectra change showing the formation of two new bands. But, in this case, the aggregation is not immediate: in fact, the change of the trend occurs within 40 minutes, showing, the appearance of a bigger bathochromically shifted band at 305nm, which corresponds to J-type aggregation ($S_0 \rightarrow S_1$ transition). While a smaller band, at 335nm, with a hypsochromic shift, corresponds to H-type aggregation ($S_0 \rightarrow S_2$ transition). Moreover, the two maxima between 350nm and 400nm have a loss of intensity with a ratio of: absorbance at 75°C/absorbance at 20°C = ~ 1.3 , much lower than the one found with Py₃ (which was ~ 2.92). From these first analyses, it is clear the system aggregates in aqueous solution, showing a temperature dependent path.

In **Figure 3.4a**, the first measurement at 20°C (yellow curve) shows no change in the trend with the one previously measured at 75°C (red curve). Keeping the solution at 20°C,

further measurements were made every 10 minutes and in any of each, there was a small change of the trend with the appearance of J-band and a small H-band. After 40 minutes, no further changes occurred (**Figure 3.4b**).

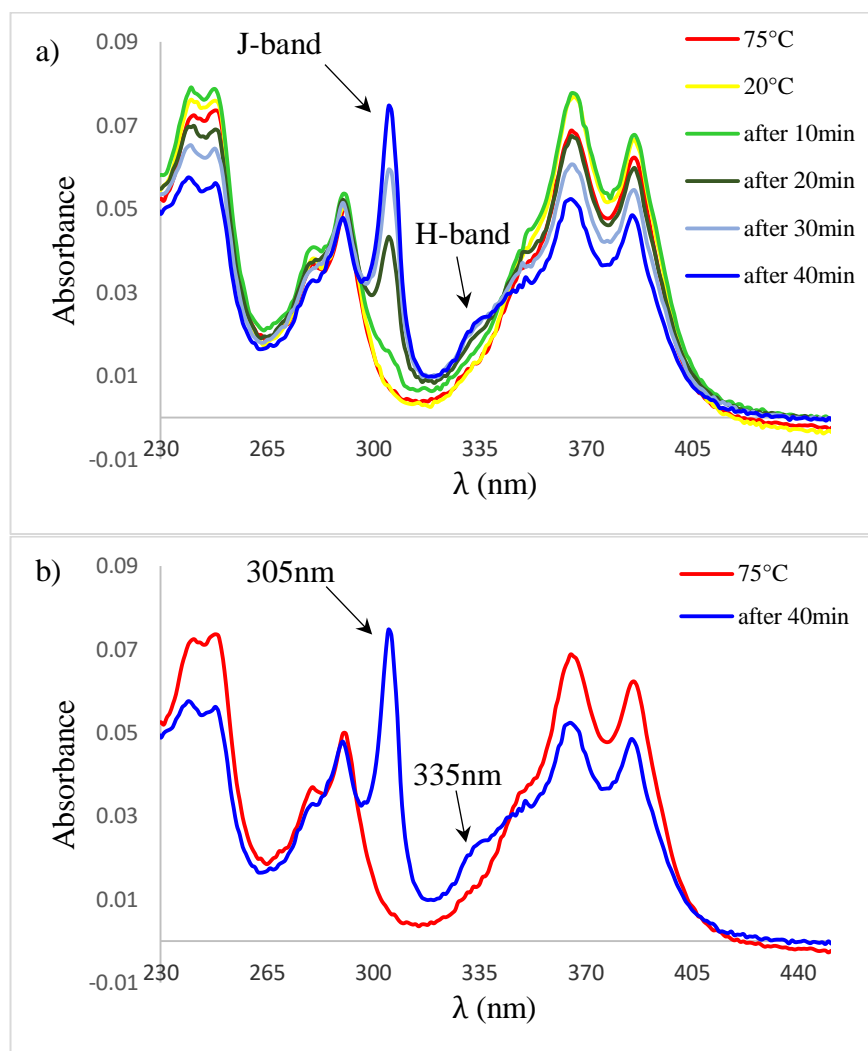


Figure 3.4 Formation of J- and H-bands within 40 minutes at 20°C. On the top (a), when the solution from 75°C (red line) is cooled down to 20°C (yellow line), the two curves are the same. Making UV measurements every 10 minutes, the trend changes. It is possible to note the appearance of H-band at 335nm and the J-band at 305nm, which become bigger until a maximum after 40 minutes (dark blue line). On the bottom (b), only the two trends at 75°C and 20°C after 40 minutes are showed.

The second step was to monitor the absorbance as a function of the temperature, using 0.1°C/min as cooling rate (**Figure 3.5**).

In this way, it is possible to make further consideration about the process of supramolecular polymerization.

Also here, the absorbance is monitored at 305nm (**Figure 3.5a**), which corresponds to J-band, and at 365nm (**Figure 3.5b**).

The first difference, with the same UV/vis analysis made with Py₃, is that the ending point (at 20°C) of the cooling curve (blue) and the starting point of the heating curve (red) do not match. This is because a complete aggregation occurs at 20°C after 40 minutes (as described above).

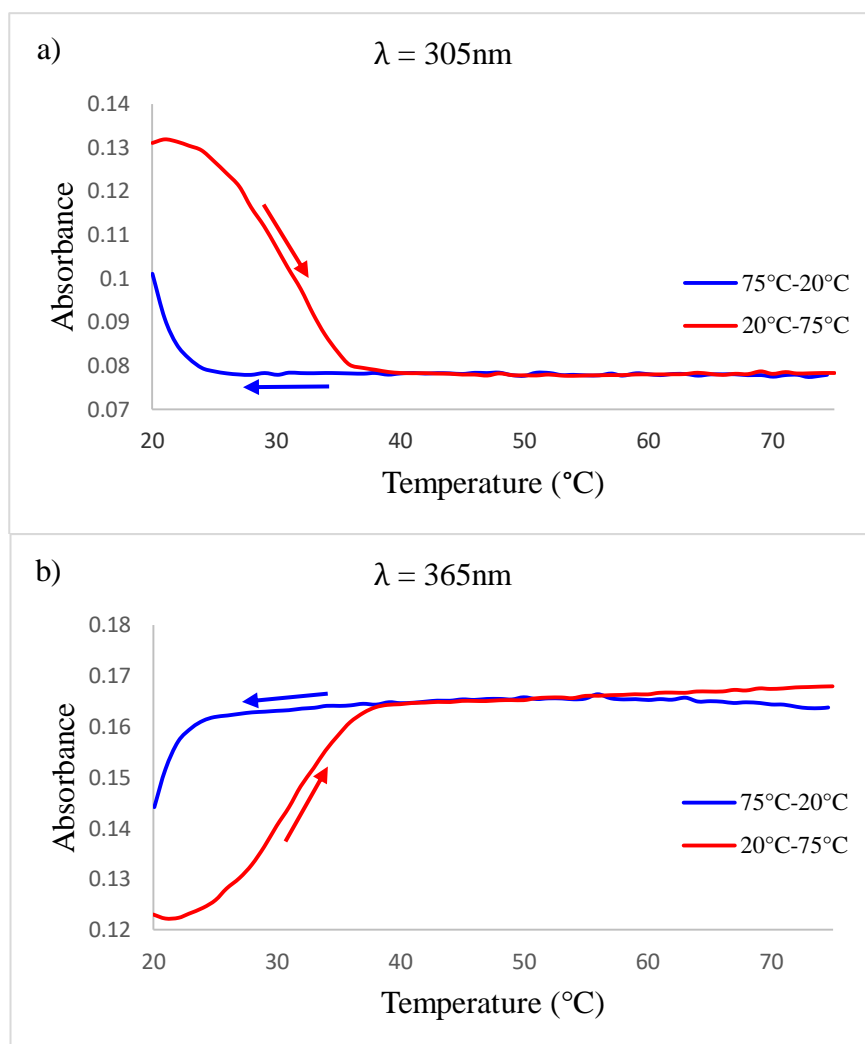


Figure 3.5 UV/vis cooling (blue) and heating (red) curves of Py₃Man measured: a) in correspondence of J-band at 305nm and (b) at 365nm. The plot is measured as the absorbance as a function of the temperature. Temperature gradient: 0.1°C/min. Conditions: 1 μ M of Py₃Man, 10mM sodium phosphate buffer pH = 7.2, 10% EtOH.

In fact, at the end of every run, the system is held at the corresponding temperature, for 40 minutes. In the heating run, it is possible to see that when the solution reaches again to 75°C, the curve has the same intensity of the first analysis.

Two interesting aspects can be observed: the first is the reversibility of the process, since the curves at 75°C have the same intensity. The other one, which is very interesting, is that, in the case of Py₃Man, the system shows a consistent hysteresis of ~10°C.

In **Figure 3.6**, a comparison between the UV/vis spectra of Py₃Man and Py₃ is showed. In here, the analyses are made at 0.1°C/min, measured at 305nm.

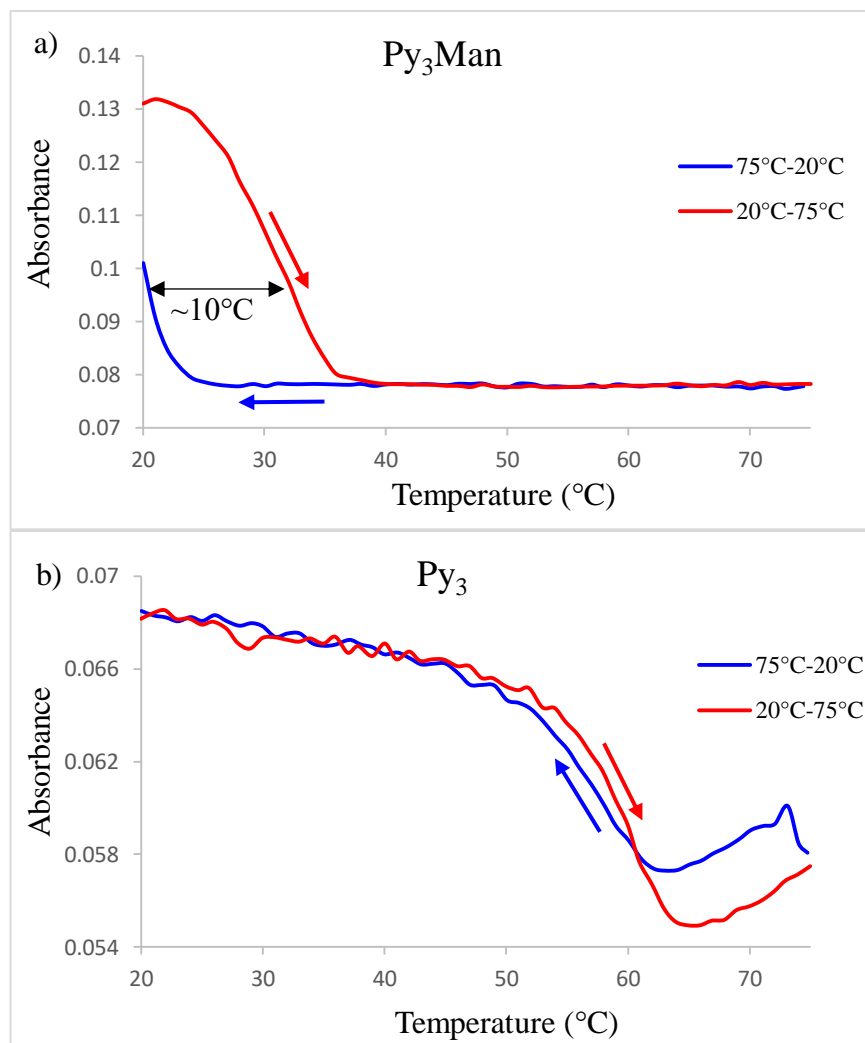


Figure 3.6 Comparison heating/cooling spectra (at 0.1°C/min) of Py₃Man and Py₃. In the first case, a bigger hysteresis (~10°C) is present. The two spectra are those measured at 305nm, but the same difference is valid for those made at 365nm.

As mentioned by Krieg *et al.*,¹⁰⁰ the hysteresis is the result of a large kinetic effect. Some self-assembled structures have a high kinetic stability. Measuring the aggregation at certain heating and cooling rates, it is possible to observe hysteresis as consequence of a large kinetic barrier in the assembly/disassembly process.¹⁰¹

Furthermore, and very important, the T_c value of Py_3Man is $\sim 24^\circ\text{C}$, much smaller than the one of Py_3 , which occurs at $\sim 70^\circ\text{C}$. Therefore, in this case, the formation of nuclei starts at very low temperature and the subsequent elongation step needs time, in order to have a complete aggregation to supramolecular polymer, at 20°C . This hypothesis can probably justify the reason why a complete change of UV/vis spectrum (absorbance as a function of wavelength) occurs in 40 minutes. A similar result is obtained using as cooling rate $0.5^\circ\text{C}/\text{min}$ (**Figure 3.7**). In fact, also in this case, the two ending and starting points at 20°C do not match and also here the solution is kept at this temperature for 40 minutes.

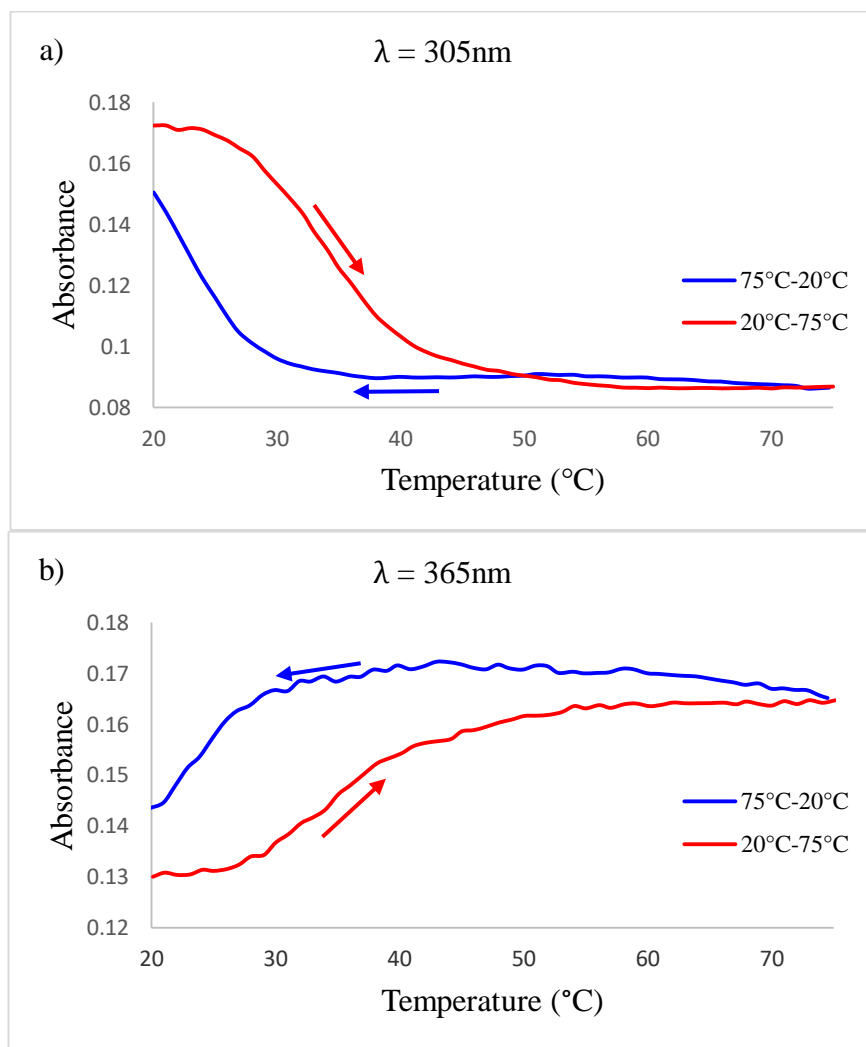


Figure 3.7 UV/vis cooling (blue) and heating (red) curves of Py_3Man measured at $0.5^\circ\text{C}/\text{min}$ as cooling rate.

A way to try to have the same ending/starting point was to cool the solution to lower temperature values, but it was not feasible, because at low temperature condensation could form on the walls of the cuvettes, giving a wrong result.

In any case, it is possible to note that T_c value is located at $\sim 28^\circ\text{C}$. At these temperatures (T_c), there is the formation of nuclei, followed by the elongation step with the addition of further trimer molecules, as described by cooperative model.

4.2 COMPARISON WITH Py_3Phos

Py_3Phos can be thought as an intermediate architecture between Py_3Man and Py_3 , since it is made by a phosphate group linked to one of the two extremities of Py_3 .

The study of Py_3Phos has also the aim to understand if one phosphate group can influence the aggregation. Using the aqueous conditions: the first approach was to see the behavior at higher and lower temperature (**Figure 3.8**).

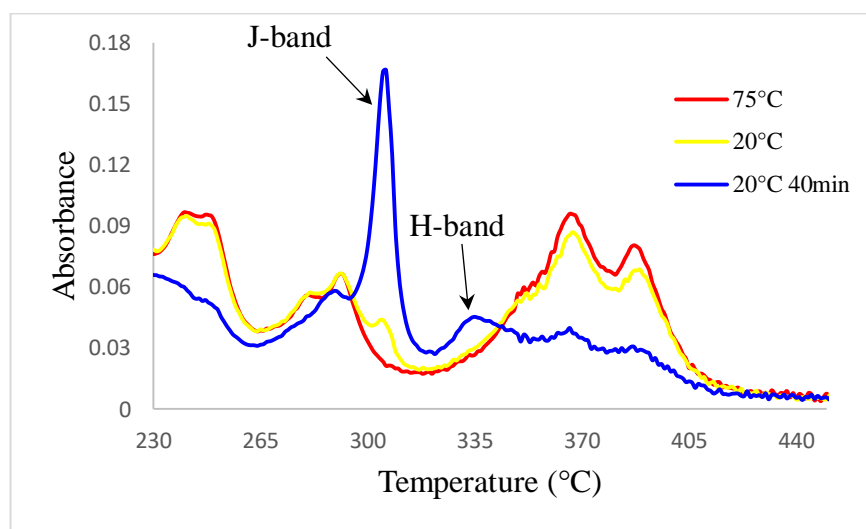


Figure 3.8 UV/vis absorption of Py_3Phos in aqueous solution with 10mM phosphate buffer and 10% EtOH. The system is completely aggregated in 40 minutes with the development of J- and H-band (305nm and 335nm respectively).

Py_3Phos shows a path, which seems to be something between the other two trimers described above. Also here, the system is disassembled at 75°C , but cooling the solution down to 20°C (at $\sim 7^\circ\text{C}/\text{min}$), a small J-band is already present, which reaches the maximum in 40 minutes.

An interesting aspect is the H-band: it is similar to the one obtained with Py₃ and so bigger than the one in the case of Py₃Man. The same consideration can be made with the decrease of the intensity of the two maximum in the region between 350nm and 400nm, like in Py₃, with a ratio of absorbance at 75°C/absorbance at 20°C = ~2.56.

Heating/cooling UV/vis analyses gave more information about the aggregation (**Figure 3.9**). As already did with the other two trimers, starting from 75°C, solution is cooled down at 20°C with a rate of 0.1°C/min.

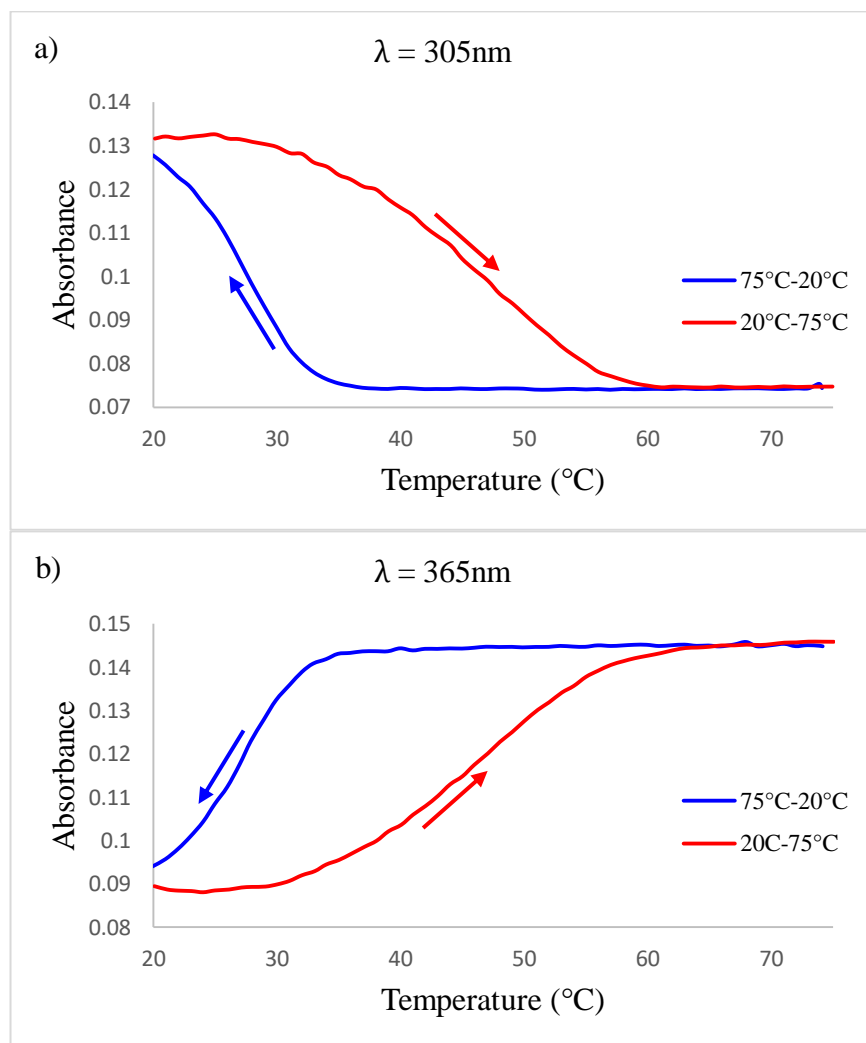


Figure 3.9 UV/vis cooling (blue) and heating (red) curves of Py₃Phos measured at 0.1°C/min as cooling rate, at: a) 305nm and b) 365nm. In this case, T_c is at ~35°C. Measured in aqueous solution with 10mM phosphate buffer and 10% EtOH.

Following the cooling rate, nuclei formation starts at ~34°C, much higher than the one found with Py₃Man (with 10°C of difference). This aspect can explain why, in the

previous experiment, when the solution was cooled down to 20°C, a small J-band was already formed, reaching the maximum of intensity in 40 minutes. It is easy to think that at 20°C, the elongation step was already started and some small supramolecular polymers were already present in solution. As further prove, at 20°C self-assembly was not fully complete, the ending and starting points, at 20°C, do not match for the two runs, even though the gap is small. The presence of phosphate shows two interesting changes: the aggregation starts at ~35°C, a higher value of temperature than the one found for Py₃Man, with a difference of almost 10°C. Then, a bigger hysteresis is showed, leading to the assumption that the different aggregation paths in Py₃Man and Py₃Phos, compared to Py₃, are due to phosphate group. However, the same heating/cooling analysis was made using a temperature gradient of 0.5°C/min (**Figure 3.10**).

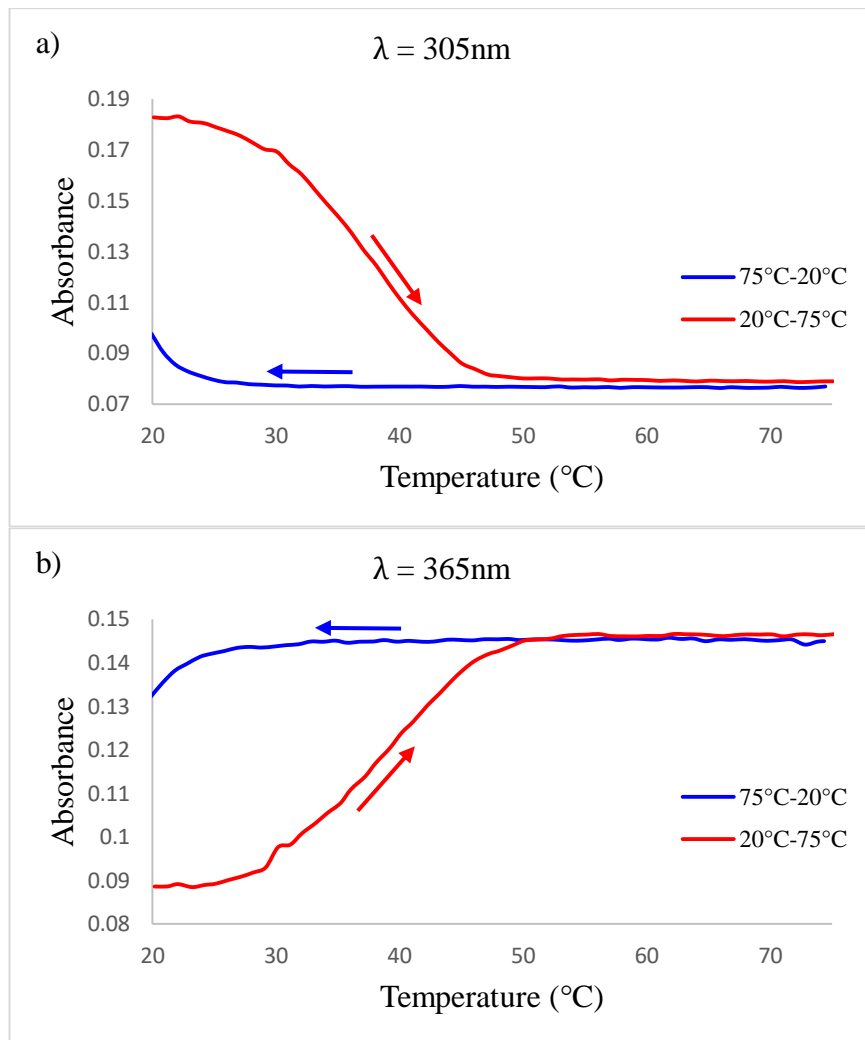


Figure 3.10 UV/vis cooling (blue) and heating (red) curves of Py₃Phos measured at 0.5°C/min as cooling rate, at: a) 305nm and b) 365nm. In this case, T_c is at ~23°C.

While the other two trimers showed a similar behavior during the cooling/heating analysis at both 0.1°C/min and 0.5°C/min, in the latter case, Py₃Phos shows a different situation. When the temperature changes with a rate of 0.5°C/min, the system starts to aggregate at ~23°C, much lower than the value found with the cooling rate at 0.1°C/min.

Furthermore, there is a huge difference between the ending and starting point at 20°C, even bigger than the one found in the case of Py₃Man.

Finding an explanation is not so easy: the only thing, which can be said, is that some kinetic effect is involved during nuclei formation and subsequent elongation.

Finally, with this last test, it has been showed the influence given by single phosphate group linked. By the comparison of Py₃ with Py₃Man and Py₃Phos, data have showed that aggregation temperature dramatically reduces when one phosphate and a phosphodiester-linked mannose are bound. In particular, it seems the highest contribution to the reduction of aggregation temperature (when nuclei formation starts) is given by the phosphate group.

A difference between Py₃Man, Py₃Phos and Py₃ is that in the first two cases, there are three phosphate groups, while in the third one only two, for the same number of pyrene molecules.

This additional phosphate increases the number of the negative charges in the entire structure of Py₃Man and Py₃Phos, compared to Py₃. For this reason, probably, the formation of nuclei starts at lower temperature. In water, due to hydrophobicity of pyrenes, the structures aggregate driven by hydrophobic effect (see chapter 2). The additional negative charges (carried by phosphates) in Py₃Man and Py₃Phos can repulse each other when two molecules approach, hampering the initial formation of nuclei at higher temperatures. In absolute EtOH, all trimers showed no aggregation, because pyrene molecules are more soluble in this solvent and the solvation of the aromatic structures hampers the hydrophobic interactions.

5 AFM ANALYSES

In order to understand the nanostructure formed by Py₃Man, the easiest way is to look by direct observation.

Atomic Force Microscopy (AFM) is a valid tool for this purpose. The analysis is made placing a drop of solution, with aggregated polymers, onto the surface of mica.

The advantage to use mica (natural muscovite) is due to the fact that it has a flat surface at the atomic level, making it a valid substrate for AFM analyses. Moreover, mica is quite hydrophilic with a negatively charged surface.¹⁰² For the structures studied here, a modification is needed. In fact, the use of AFM for investigation of DNA and protein-DNA complexes employs functionalized mica, in order to increase the affinity between the negative mica surface and DNA.¹⁰³

The approach used for the study of Py₃Man at AFM follows a protocol described in ref.¹⁰³, where mica is functionalized with 3-Aminopropyltriethoxy silane (APTES). Pyrene units of trimers described in this thesis, like for the DNA, are held to each other by a phosphate group (which is negative).

The modification with APTES (APTES-mica) turns the surface of mica from negative to positive, making an electrostatic interaction between the phosphate (in trimer) and amino (on APTES-mica) groups possible.

5.1 Py₃Man NANOSTRUCTURES

UV/vis analyses have shown a temperature-dependent behavior of the self-assembly of the structure. It has been depicted that the trimers are disassembled at 75°C and assembled at 20°C, with an initial formation of nuclei at T_c, followed by the elongation step, according to the cooperative model.

Self-aggregated structures have their own morphology, which can be observed at AFM. After UV/vis analysis, ~30µL of solution are deposited on an APTES modified mica surface for about 3 minutes. Then, the solution is washed away with 1mL of MilliQ water and dried with argon.

Solutions after all UV/vis experiments were measured at AFM. Since different kind of UV/vis analyses were made, the set of experiments can be divided in:

- 1) cooling from 75°C to 20°C with 0.5°C/min as cooling rate;
- 2) cooling from 75°C to 20°C with ~7°C/min as cooling rate;
- 3) cooling from 75°C to 20°C with 0.1°C/min as cooling rate.

5.2 Py₃ NANOSTRUCTURES

Py₃ was already studied in our group and in these previous works, it was showed (by AFM analyses) that the structure aggregated with formation of tubes and sheets.^{93,96}

In here, since the conditions used for aggregation were made with no NaCl, the only time that some objects were found was after the solution was cooled at ~7°C/min (**Figure 3.11**).

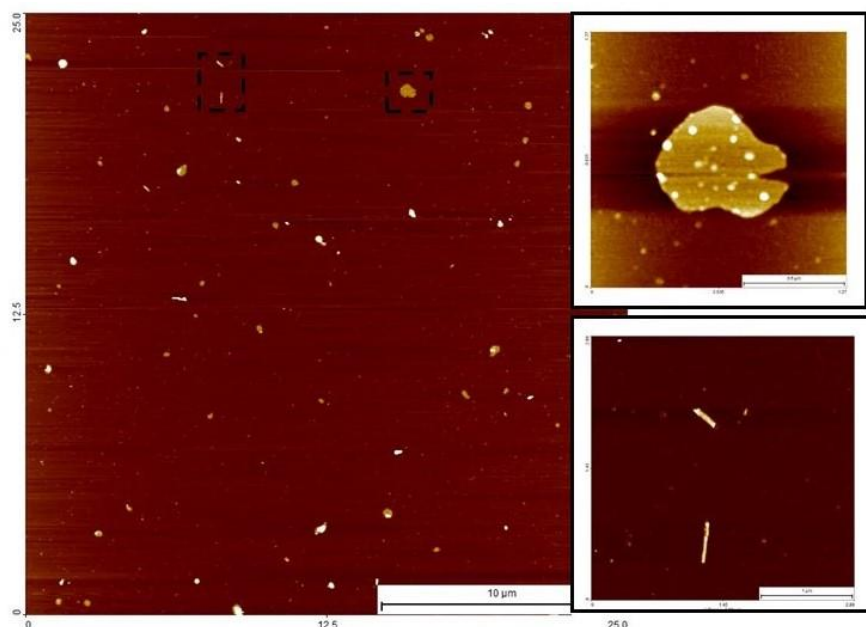


Figure 3.11 AFM scan of a solution of Py₃ cooled at ~7°C/min. There is the coexistence of sheets and tubes.

The reasons why in the other two experiments (0.5°C/min and 0.1°C/min as cooling rates) nothing was found was due to the fact that the aggregation led to very big structures. This causes a much more diluted solution, which makes very hard to find in solution some objects to be measured at AFM.

The structures found are sheets and a few of tubes. In this case, there was no need to wait 40 minutes, since T_c had very high value and at 20°C , the system was already aggregated. About the shape of the sheets, it was similar to those found for Py_3Man , but with a height of $\sim 2.0\text{nm}$ and the presence of the dots on the sheet surface (**Figure 3.12a**).

About the tubes, (**Figure 3.12b**), the shape is obvious because the cross section along the surface is pretty smooth with the height almost the double ($\sim 5\text{nm}$). Whereas, cross section, measured diagonally to the surface, shows a round trend.

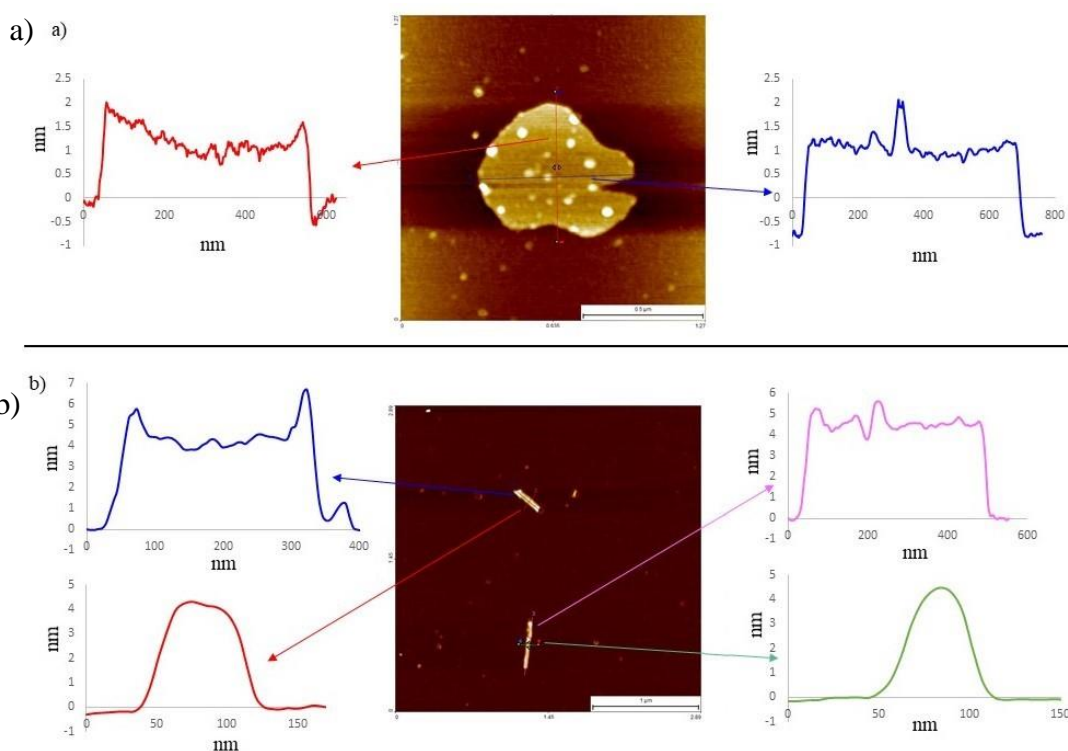


Figure 3.12 Cross section of nanosheet (a) and tubes (b). Nanosheet is similar to one found for Py_3Man and also in this case there is the presence of small aggregated structures on its surface. Tubes have a height almost the double of the surface and cross section shows a round trend when it is measured diagonally to the structure. For the plots: x-axis = width; y-axes = height.

5.3 Py_3Man STUDIED AT $0.5^\circ\text{C}/\text{MIN}$ AS COOLING RATE

Starting from Py_3Man , after having cooled the solution at $0.5^\circ\text{C}/\text{min}$, AFM analysis shows that the system aggregates with formation of nanosheets.

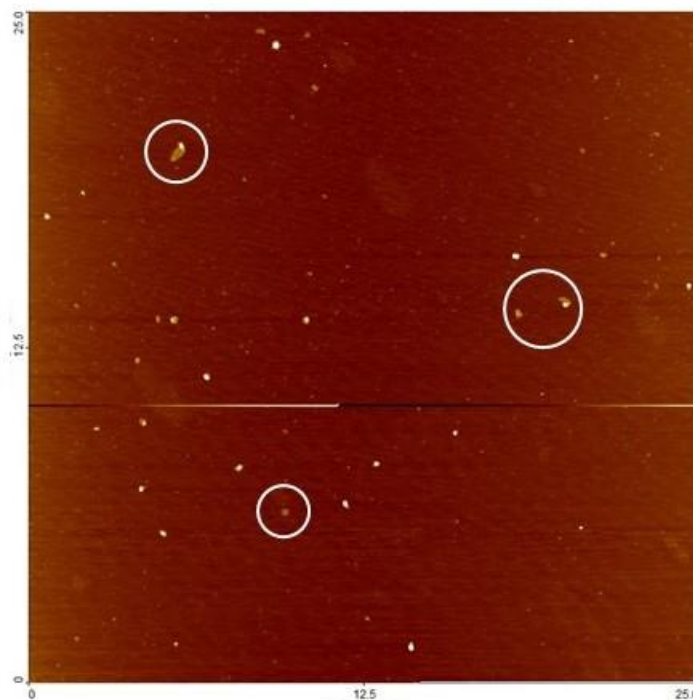


Figure 3.13 AFM picture ($25\mu\text{m}\times 25\mu\text{m}$) with deposition of nanosheet-like structures (white circles). Only three examples are highlighted, but it is possible to note others.

In **Figure 3.13**, some of them are highlighted in white circles, but it is possible to note a few more. In order to have a better idea about the characteristics of these nanostructures, in **Figure 3.14a**, it is showed the enlargement of one of them.

The fact these nanostructures have a sheet shape is more understandable studying the cross section, thus obtaining information about length, width and thickness (**Figure 3.14b**). Looking at the appearance of this nanostructure, it is possible to note the presence of small aggregated structures on the surface (in the picture they appear as white spots).

In **Figure 3.14b**, cross section has been measured in different part of the sheet.

The measure of the area of the nanosheet, free of small aggregated structures, is indicated with the red arrow, which calculates a height of $\sim 2.5\text{nm}$.

Instead, with the blue arrow is measured the cross section, which indicates the length of the structure.

The white part seems to be part the sheet folded on itself and this hypothesis is supported by the fact that, in cross section, every higher “step” is a multiple of 2.5nm .

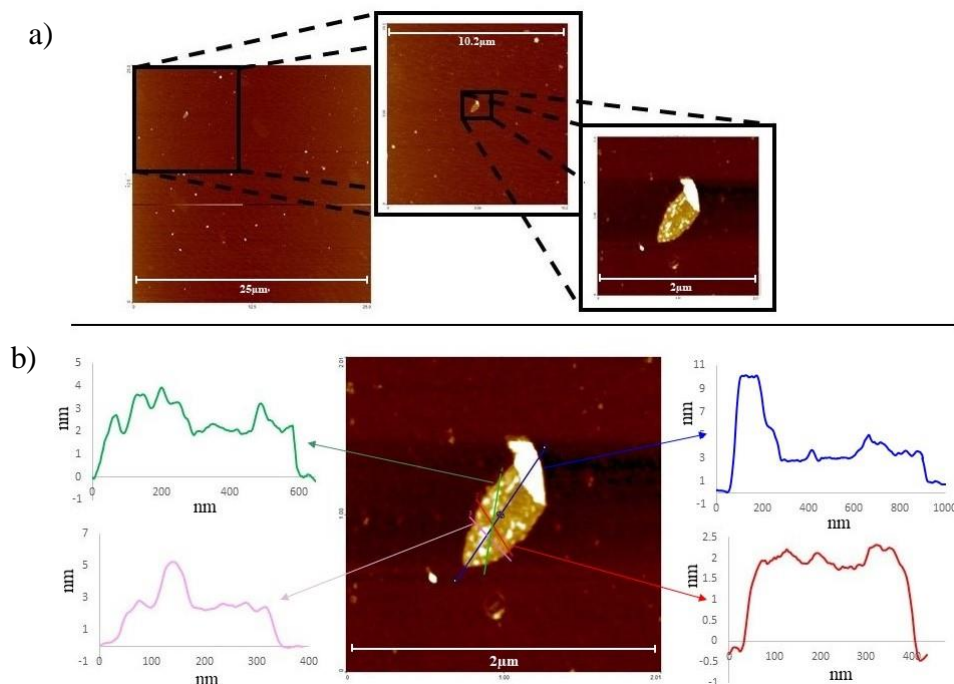


Figure 3.14 Formation of sheets on mica surface: a) an area is enlarged, showing the objects more detailed; b) cross section of the zoomed nanosheet. For the plots: x-axis = width; y-axis = height.

The origin of these small aggregated structures, on the surface of the nanosheet, is not so clear. The easiest conclusion is they are some tiny aggregated trimers, which simply deposit on the main surface and, for this reason, the cross section measurement gives a value as multiple of 2.5 nm. The fact nanosheets have a height of 2.5 nm can be reasonably explained, considering the height of 1,6-substituted pyrene, which was calculated with a value of $2.0 \text{ nm} \pm 0.1 \text{ nm}$.⁹³

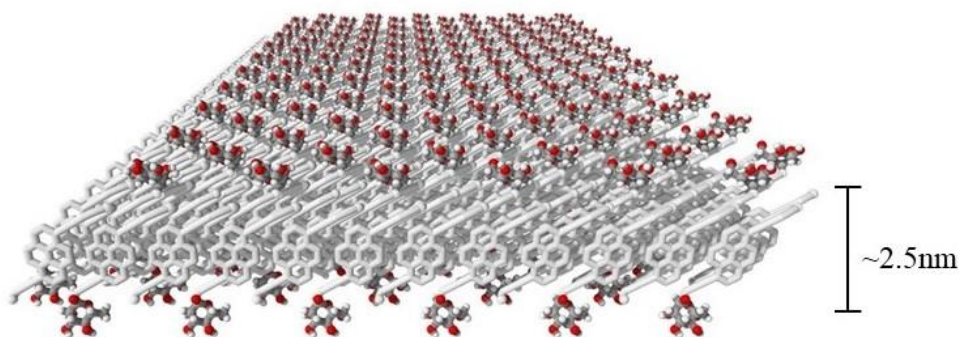


Figure 3.15 Pyrene units of Py₃Man arranged in a nanosheet structure. Pyrene units aggregate in order to reduce the hydrophobic surface in contact with water, while phosphates and mannose are exposed to water.

In **Figure 3.15**, it is shown a cartoon of a Py₃Man nanosheet in order to make clearer how pyrene units are arranged in a nanosheet motif. The reason why in this case they are

0.5nm higher than the structure found for Py₃, is probably due to the presence of phosphate and mannose.

Pyrene aggregate forming a hydrophobic core, in order to minimize the contact with water. Instead, all phosphate groups and mannose, due their polarity, are exposed to the aqueous environment.

5.4 Py₃Man STUDIED AT ~7°C/MIN AS COOLING RATE

About AFM analysis of the solution cooled at ~7°C/min as, also in this case Py₃Man aggregates in nanosheets structures (**Figure 3.16**). As described previously, in this condition, Py₃Man needs additional 40 minutes for aggregation, when the solution is cooled down to 20°C, from 75°C. The solution was kept at this temperature in the block of UV spectrometer for 40 minutes, then a drop was deposited on modified mica, for 3 minutes. After that, the solution was washed away with 1mL of MilliQ water, dried with argon and, then, analyzed to AFM.

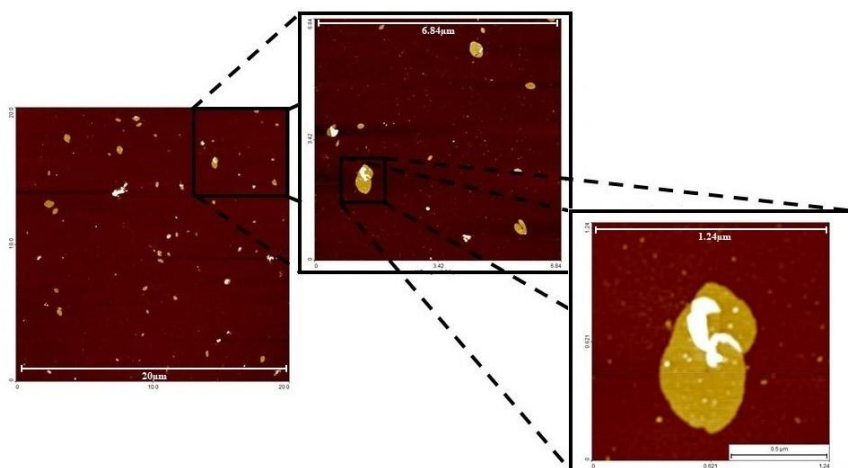


Figure 3.16 AFM picture of Py₃Man after aggregation induced cooling the solution at ~7°C/min. The first AFM scan is taken in a larger range (20µm*20µm). Then, desired areas were zoomed in order to have a more detailed view.

Py₃Man nanosheets are pretty spread on mica surface. Some are completely flat and others are folded on themselves, like the most zoomed one.

In order to get more information from these structures, height and length of nanosheets are measured (**Figure 3.17**).

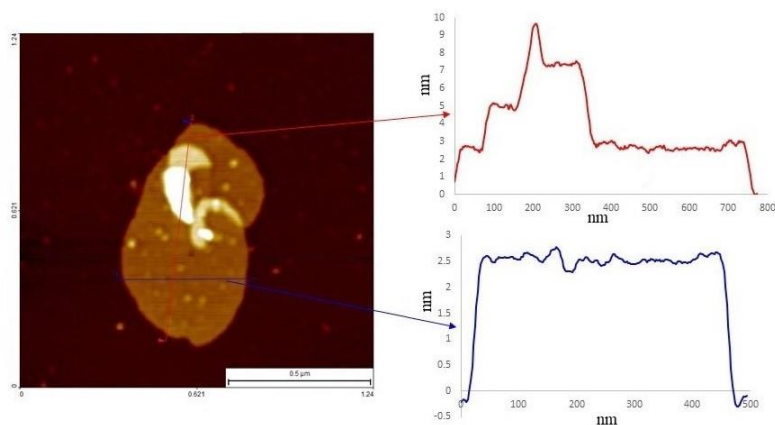


Figure 3.17 Cross section of a nanosheet. The darker part of the surface is the thinnest with a height of ~ 2.5 nm (blue arrow). Red arrow goes across the highest spots of the surface and they are again all multiple of 2.5 nm. For the plots: x-axis = width; y-axis = height.

The surface of the sheet is pretty smooth (blue arrow) with a height of ~ 2.5 nm. On the sheets, as showed in **Figure 3.17**, there is the presence of higher spots (less than the previous case) and looking at the cross section (red arrow), the height increases as multiple of 2.5 nm. This gives the idea either smaller sheets deposited on the surface of the bigger sheet or in some part, the nanostructure is folded.

5.5 Py₃Man STUDIED AT 0.1°C/MIN AS COOLING RATE

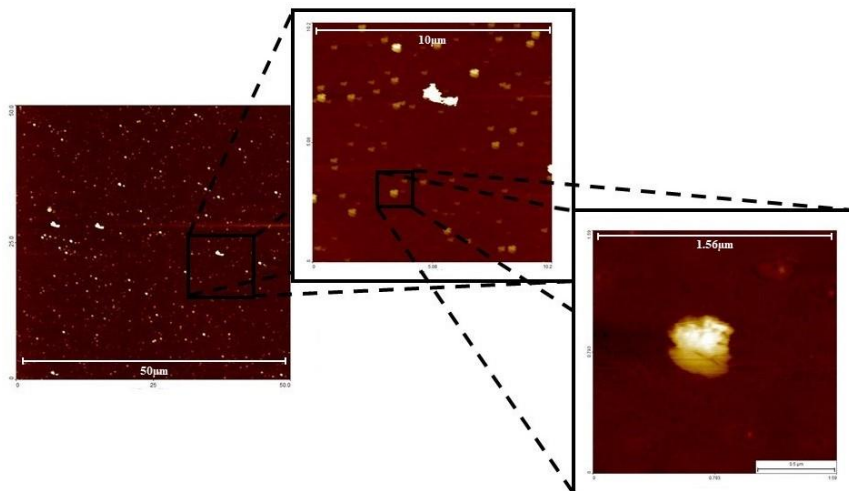


Figure 3.18 AFM picture of Py₃Man after having cooled the solution at 0.1°C/min. White objects are the results of an over-aggregation of the trimer. The one in the zoomed picture (on the right) gives a better definition of this round-shaped structures formation.

The situation is different in case of heating/cooling analysis at $0.1^{\circ}\text{C}/\text{min}$. In this case, the system aggregates with formation of round-shaped nanostructures (**Figure 3.18**). These round-shaped objects are quite diffused on mica surface. Their characteristics is better understood studying the cross-section of the shape (**Figure 3.19**). The cross section shows a round-shape motif with a height of 7nm.

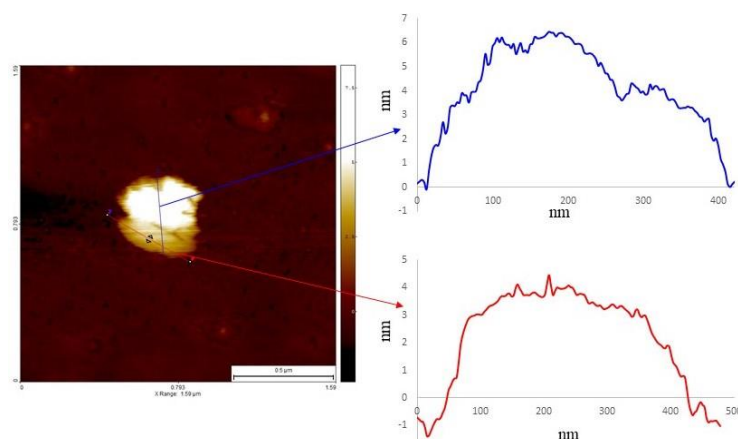


Figure 3.19 Cross section of the nanostructure. The shape in this case is not flat, it is round with a maximum height of $\sim 7\text{nm}$. For the plots: x-axis = width; y-axes = height.

6 CONSIDERATION ABOUT AGGREGATION

Once the kind of nanostructure is established by AFM analysis, it is clearer what happens to aggregation when the solution is cooled down to lower temperatures (**Figure 3.20**).

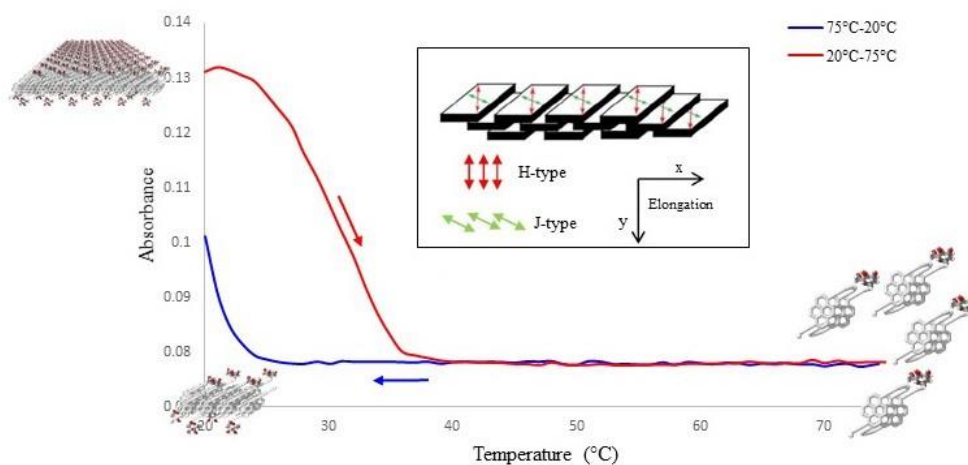


Figure 3.20 Schematic representation of aggregation path. At 75°C , all trimers are in solution as random coil. Cooling down the temperature, when it reaches T_c value, there is the initial formation of a nucleus, followed by elongation step with formation of nanosheet. For sheet-like aggregation, the trimers arrange like showed in the inset. Only inset is taken from⁹³

The idea behind aggregation path is that at higher temperature, the trimers are in solution as random coil. When the temperature goes to lower values, there is an initial formation of a nucleus, which happens at nucleation temperature (T_c). The latter, depending of the kind of system, is different for each case, as showed in the previous sections.

Once nuclei are formed, according to the cooperative model, further pyrene trimer units bind in the elongation phase and subsequent nanosheet formation. In the case of sheet-like aggregation, pyrene units arrange in staircase-like motif, in this way the interaction of the transition dipole moments generates H- and J-bands. As already discussed above and in chapter 2, H-band originates from $S_0 \rightarrow S_2$ transition, with a face-to-face orientation of transition dipole moments (red arrows in the inset in **Figure 3.20**), which generates the formation of a small and blue-shifted peak at 335nm. Instead, J-band is due to a $S_0 \rightarrow S_1$ transition, with an end-to-end orientation of transition dipole moments (green arrows in the inset in **Figure 3.20**), which leads to the formation of a big and sharp red-shifted peak at 305nm.

7 Py₃Phos NANOSTRUCTURES

Py₃Phos has showed different structures depending on the conditions used for inducing aggregation. In particular cooling the solution down at 0.5°C/min (**Figure 3.21**), it aggregates forming strange structures.

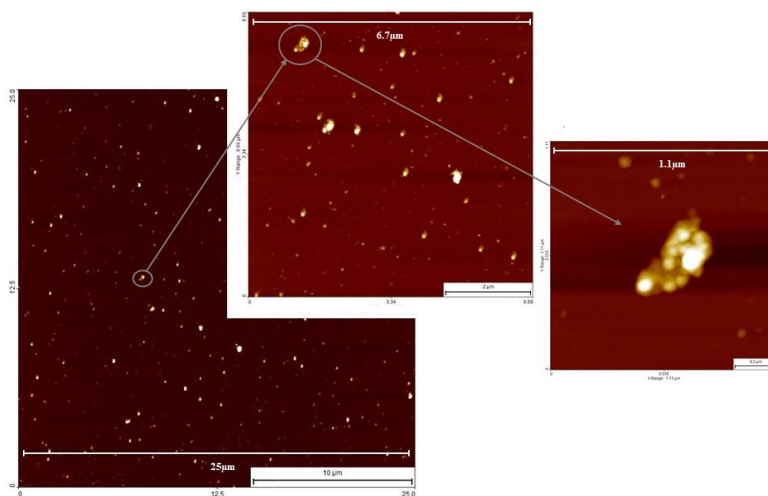


Figure 3.21 AFM image of the solution of Py₃Phos cooled at 0.5°C/min. There is the formation of structures similar to those found for Py₃Man cooled at 0.1°C/min.

From a first look, the objects found seem to be similar to those found for the solution of Py_3Man cooled at $0.1^\circ\text{C}/\text{min}$, but their shape is not perfectly round. They appear elongated, such as a sheet-like shape with an uneven cross section (**Figure 3.22**).

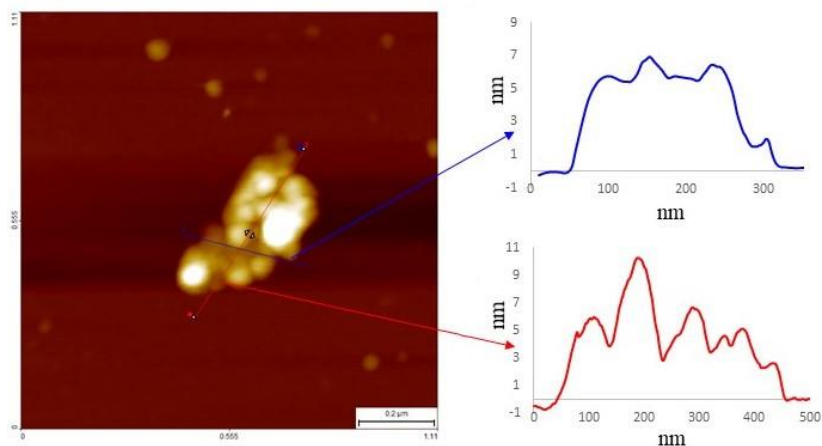


Figure 3.22 Cross section of structure found for a solution of Py_3Phos cooled at $0.5^\circ\text{C}/\text{min}$. Even though the structure is not round, the minimum height (blue arrow) is the same for the solution of Py_3Man cooled at $0.1^\circ\text{C}/\text{min}$. For the plots: x-axis = width; y-axis = height.

It is not so easy calculate the cross section with a minimum height since the structure is not regular: it seems a lot of round-shaped objects joined to a bigger structure. An attempt was made with the measure indicate by blue arrow, giving a height of $\sim 7\text{nm}$ (again there is a similarity with the solution of Py_3Man cooled at $0.1^\circ\text{C}/\text{min}$).

Instead, the red arrow shows an irregular surface with a maximum of more or less 11nm . The solutions of Py_3Phos cooled at $\sim 7^\circ\text{C}/\text{min}$ (**Figure 3.23**) shows an aggregation with formation of nanosheets.

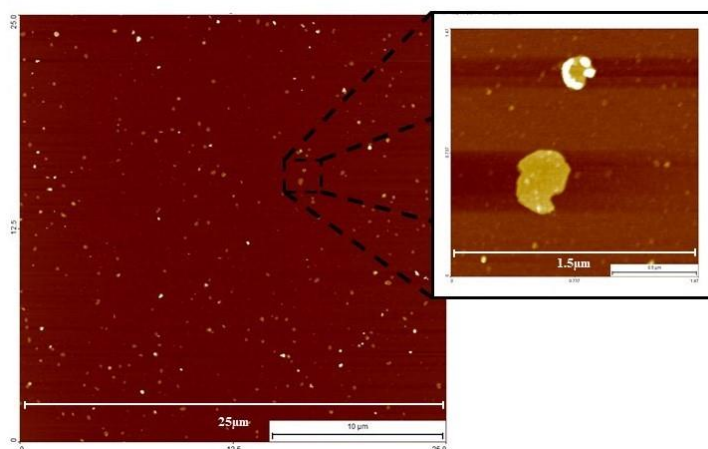


Figure 3.23 AFM picture of Py_3Phos solution cooled at $\sim 7^\circ\text{C}/\text{min}$, with formation of sheets spread enough on mica surface.

In this condition, the trimer aggregates with the formation of sheets. It is possible to note a lot of these sheets on mica surface and their shape seem to be pretty regular as confirmed by the cross section of one of those (**Figure 3.24**).

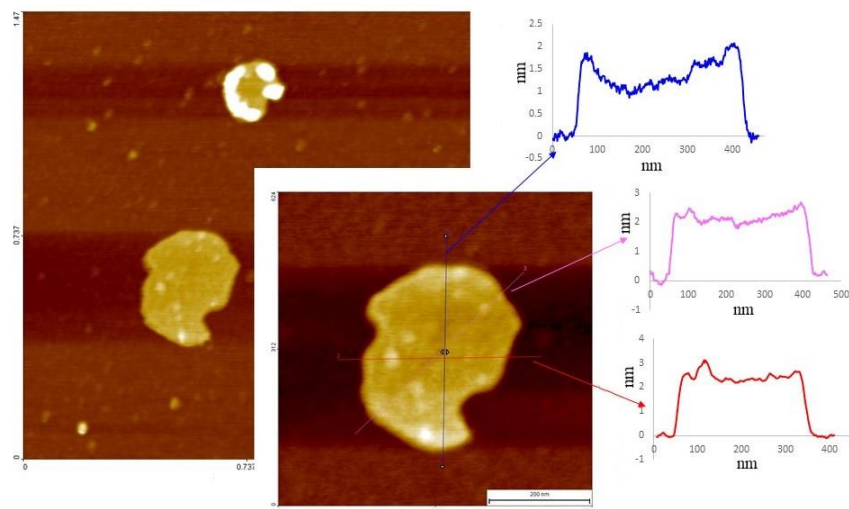


Figure 3.24 Cross section of Py3Phos after having cooled the solution at $\sim 7^\circ\text{C}/\text{min}$. The surface is pretty smooth with a height of $\sim 2.5\text{nm}$. For the plots: x-axis = width; y-axes = height.

The sheet surface is pretty regular with a height of $\sim 2.0\text{nm}$. They seem to be smaller than those found for Py₃Man in the same conditions.

Instead, the measurement obtained with the cooling rate of $0.1^\circ\text{C}/\text{min}$, as perceivable from **Figure 3.25**, there are not so many nanostructures on mica surface.

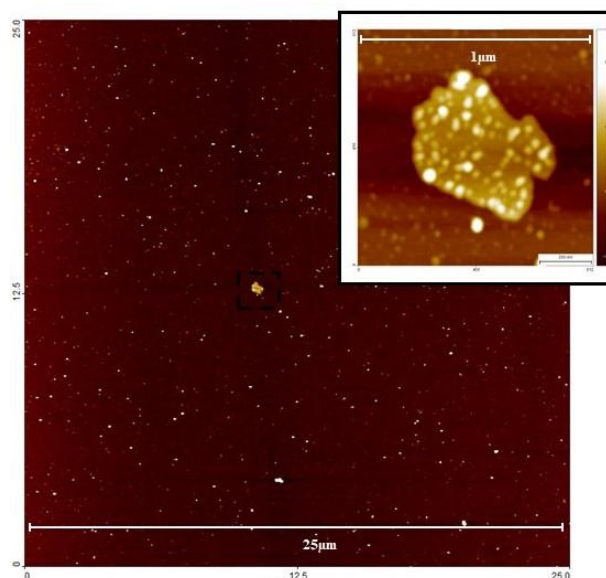


Figure 3.25 AFM picture of Py3Phos after having cooled the solution at $0.1^\circ\text{C}/\text{min}$, with formation of few sheets on mica surface.

The reason why the sheets (**Figure 3.26**) found in this analysis are not so spread on mica surface, it is likely due to the precipitation of these nanostructures in solution, which make very difficult their analysis.

Moreover, there is the presence of a lot of smaller aggregated structures on the nanosheet surface.

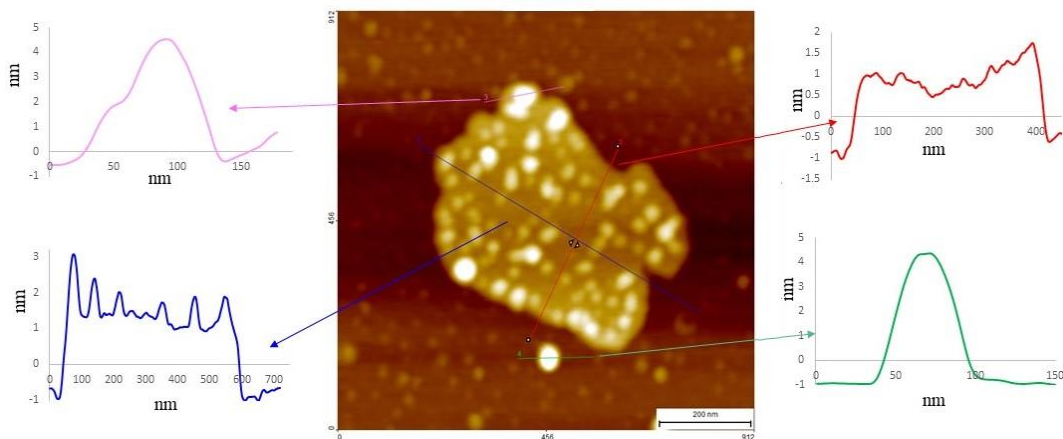


Figure 3.26 Cross section of Py_3Phos cooling the solution at $0.1^\circ\text{C}/\text{min}$. The sheet has a lot of white dots on its surface. Also in this case the height of the surface, free from dots, is $\sim 2.5\text{nm}$ (red arrow). For the plots: x-axis = width; y-axis = height.

Like in other cases, cross section shows the main surface of the sheet has a height of $\sim 2.0\text{nm}$ and the presence of these smaller aggregated structure, increases the height of the double. Moreover, cross section indicated with green arrow shows that they look like small spheres.

In conclusion, one can think that in these conditions, the trimer can aggregate as both smaller and bigger sheets and the first aggregated structures can just deposit on the second ones. The same conclusions can be used to explain the presence of the same objects on the surface of the sheets obtained with Py_3 and Py_3Man .

8 STUDIES OF Py₃Man WITH NO EtOH: UV/VIS

As mentioned in chapter 2, cosolvent can have dramatic consequence on self-assembly process.⁶³ This is the case of EtOH used at 10%, as discussed in the previous sections.

In any case, the experiments discussed above were made with no EtOH, using only water with 10mM sodium phosphate buffer pH = 7.2.

About Py₃Man, AFM showed the formation of nanosheets as aggregation product, while the study of Py₃ was not possible without EtOH because the system was always aggregated: both at high and low temperatures. It seems that the use of EtOH as cosolvent, for Py₃, is very important to induce disassembly.

This because pyrene unities are more soluble in EtOH and the presence of this solvent influence the self-assembly, leading that the aggregation to start to lower temperature values. Increasing the amount of EtOH, there is the decrease of T_c: as showed in the beginning of this chapter in pure EtOH the pyrene trimers structures were all disassembled. Using different combination of water and EtOH, it can be possible to modulate the value of the temperature of nuclei formation.

It is easy to think at this point that by using higher amount of EtOH there is a decrease of T_c, while by increasing water quantity the opposite effect is obtained.

In fact, UV analyses showed a trend with a very low intensity, due probably to a precipitation of aggregated structures, with no differences at both 75°C and 20°C.

Anyway, the first UV/vis analysis of Py₃Man is made going from 75°C to 20°C with ~7°C/min as cooling rate, showing some differences in aggregation path (**Figure 3.27**).

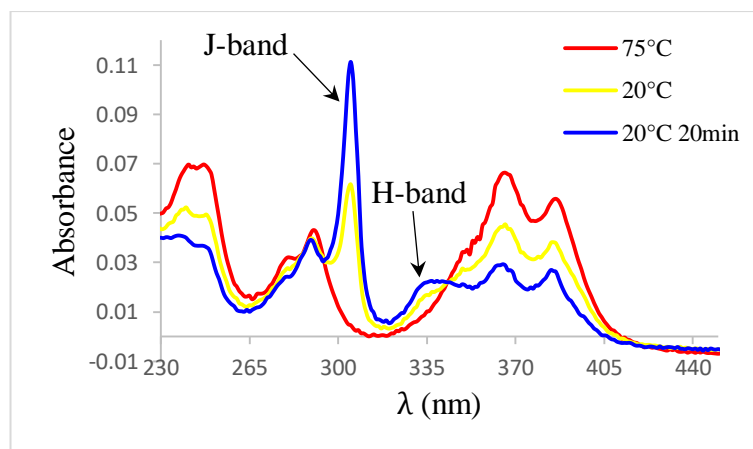


Figure 3.27 UV/vis analysis of Py₃Man in the solution without EtOH. The system shows small J- and H-bands at 20°C. The two bands reach the maximum of intensity already after 20min.

The absence of EtOH induces the trimer to be partially aggregate already at 20°C with the consequence of a fully aggregation after 20 minutes.

Measures of the absorbance, at 10 minutes intervals, show that the aggregation has already started at 30°C (**Figure 3.28**).

Looking at UV trend, at 30°C there is the formation of J-band (with tiny H-band), giving the idea (in this case) aggregation starts to a temperature included between 30°C and 40°C. The trend changes with lower temperatures, reaching the maximum intensity after being waiting for additional 20 minutes at 20°C.

Moreover, the two maximum, in the range between 350nm and 400nm are less intense than the case of EtOH in solution and even H-band seems to be bigger.

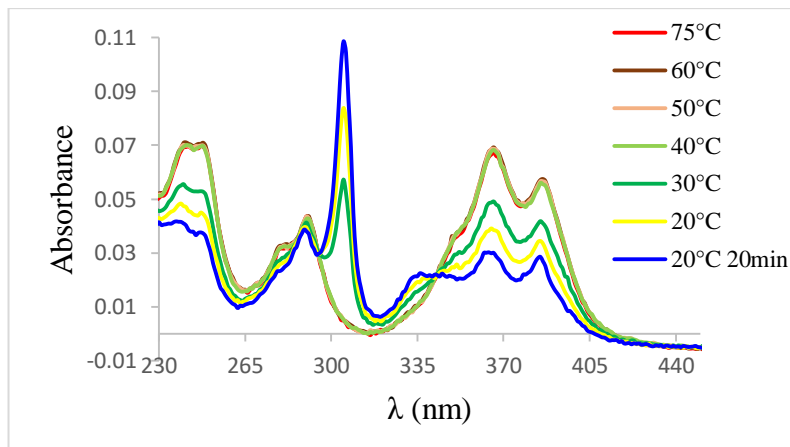


Figure 3.28 UV/vis measured at intervals of 10 minutes. At 30°C (green arrow), J-band is already formed, sign of an already started elongation phase.

A better understanding of aggregation route is to measure, again, the absorbance as a function of the temperature at 305nm (J-band) and 365nm (**Figure 3.29**), using 0.1°C/min as cooling rate.

In this analysis, trimer starts to aggregate at temperature of ~45°C, while with a cooling rate of ~7°C/min, the aggregation seems to start between 30°C and 40°C.

This characteristic can be due to the fact that the low cooling/heating rate keeps Py₃Man longer to a determine temperature and this induces that the formation of nuclei can already start at higher temperatures (~45°C in this case).

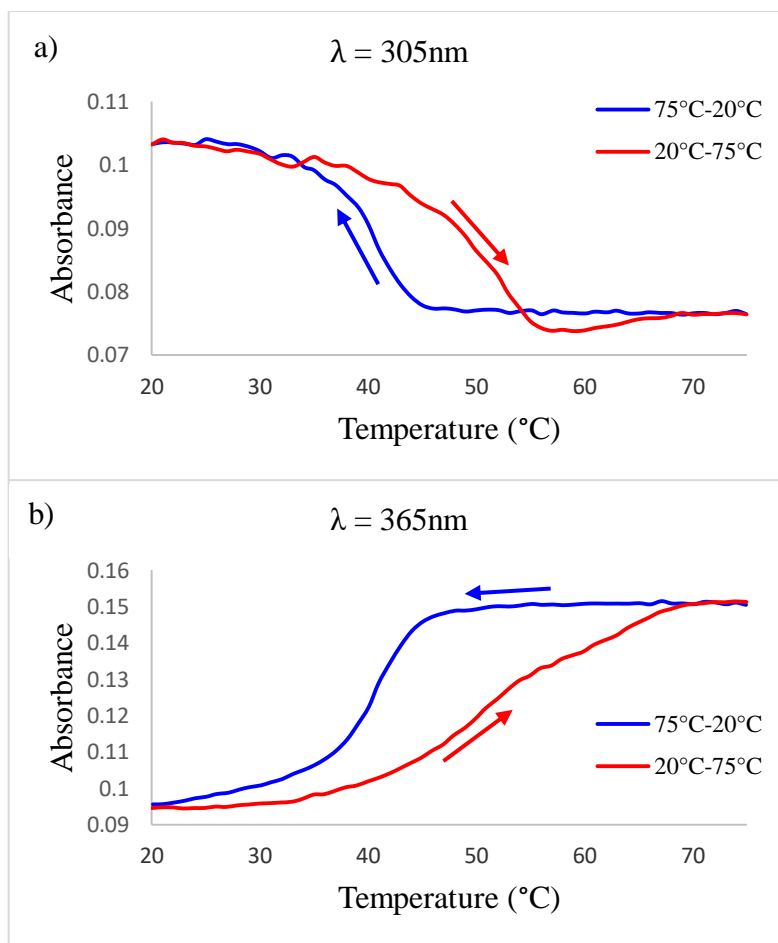


Figure 3.29 UV/vis cooling (blue) and heating (red) curves of Py₃Man measured at 0.1°C/min as cooling rate at: a) 305nm and b) 365nm.

The situation looks like different when the temperature gradient used is 0.5°C/min (**Figure 3.30**).

According to the first analysis made with the cooling gradient $\sim 7^\circ\text{C}/\text{min}$, in the case of rate at 0.5°C/min, the trimer starts to aggregate at a temperature just above of $\sim 33^\circ\text{C}$.

Also in this case, there is the presence of a hysteresis and ending/starting point at 20°C is not the same. This just gives the idea that the elongation step has already started but not all molecules were bound for the nanosheet formation at this temperature gradient.

Finally, the lack of EtOH as cosolvent shifts T_c values at higher temperature. Considering 0.1°C/min as cooling rate, in presence of EtOH, T_c is $\sim 24^\circ\text{C}$, while without this cosolvent T_c is $\sim 45^\circ\text{C}$. The experiments made with 0.5°C showed that T_c is $\sim 28^\circ\text{C}$ with EtOH, whereas without it T_c is $\sim 33^\circ\text{C}$.

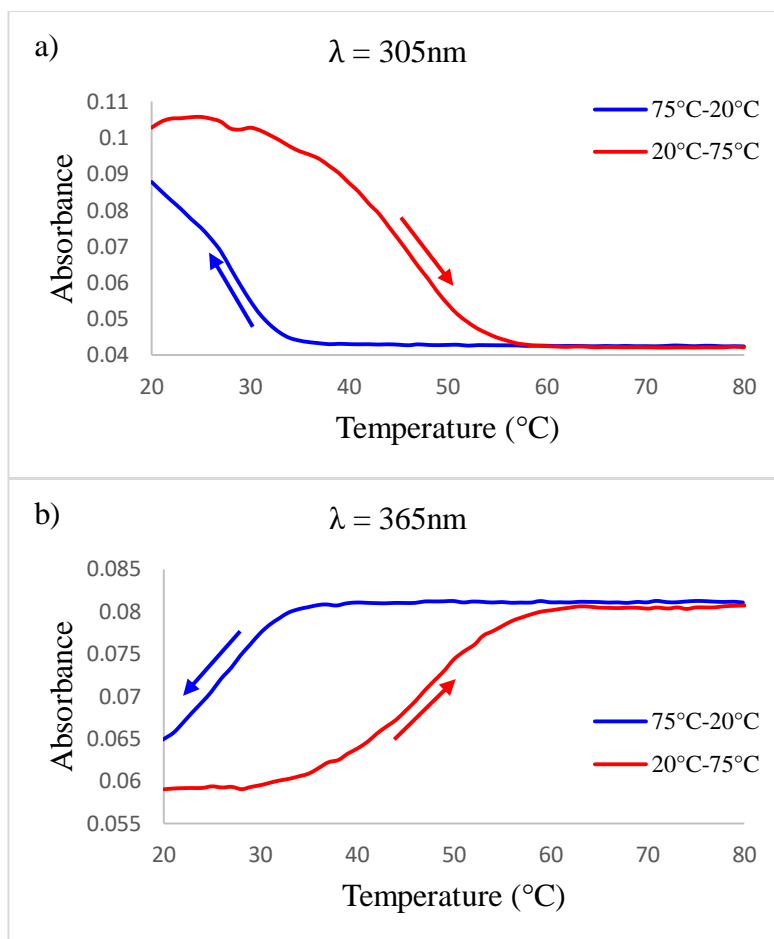


Figure 3.30 UV/vis cooling (blue) and heating (red) curves of Py₃Man measured at 0.5°C/min as cooling rate at: a) 305nm and b) 365nm.

In conclusion, EtOH in the solution decreases the aggregation temperature values, because it has a higher affinity with the pyrenes unities in the trimers.

This leads to a higher solubility of the structures, which shifts the nuclei formation temperatures to lower values. This seems to influence, somehow, on the hysteresis of the structure. In fact, the experiments made without EtOH showed a bigger hysteresis.

9 STUDIES OF Py₃Man WITH NO ETOH: AFM

Also here, AFM was used for looking the kind of structure made after UV/vis analyses. Starting from self-assembly induced with $\sim 7^\circ\text{C}/\text{min}$ as temperature gradient: Py₃Man aggregates with formation of nanosheets (**Figure 3.31**).

Also in this case, the sheets are spread all over the mica with a very smooth surface with the same size.

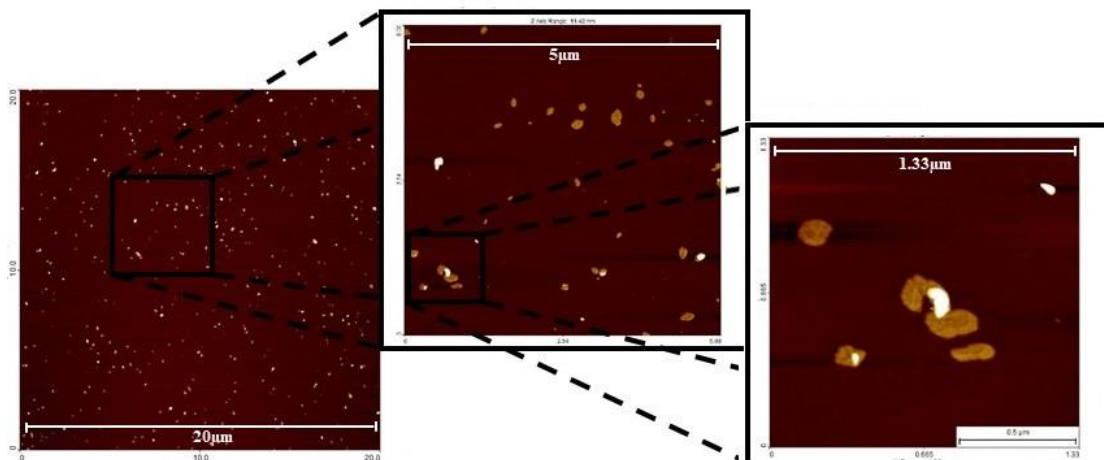


Figure 3.31 AFM picture of Py_3Man in aqueous medium without EtOH. The solution is cooled down with no specific temperature gradient. The aggregation leads to formation of nanosheets.

A better understanding of the characteristics of these sheets is given by cross section.

The surface of these sheets is pretty smooth, with the height of $\sim 2.5\text{nm}$ (**Figure 3.32**), as already found for Py_3Man in solution with EtOH.

The more height part on the surface is due to some smaller sheets deposited on the bigger one. In fact, looking at the cross sections, in particular the one indicated with the pink arrow, it is possible to note the height grows as multiple of 2.5nm .

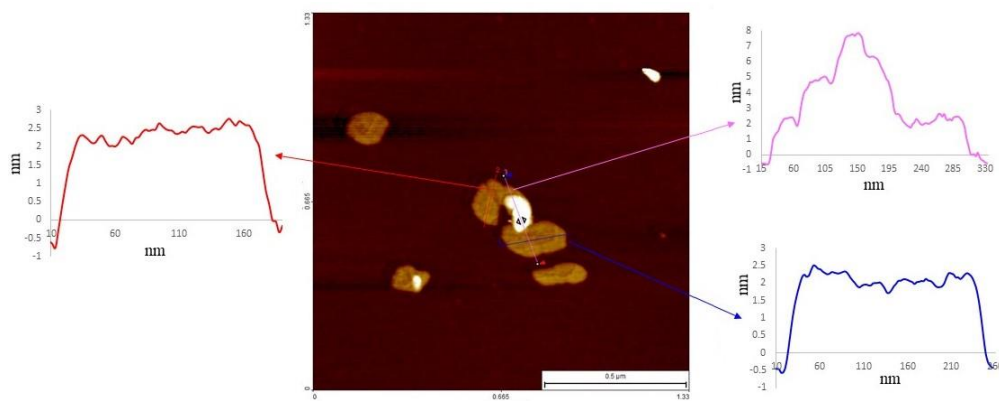


Figure 3.32 Cross section of nanosheets. There is no presence of white spots this time. The white part seems to be due to some other smaller sheet deposited on the surface of a bigger one (pink arrow). For the plots: x-axis = width; y-axis = height.

As regards the analysis made with $0.1^\circ\text{C}/\text{min}$ as cooling rate, Py_3Man aggregates again with formation of sheets (**Figure 3.33a**). In this case, a very small population on mica

surface is present. As already discussed, this is maybe due to a formation of big structure, which makes the solution very diluted, and it is very complicated collect solution with enough material.

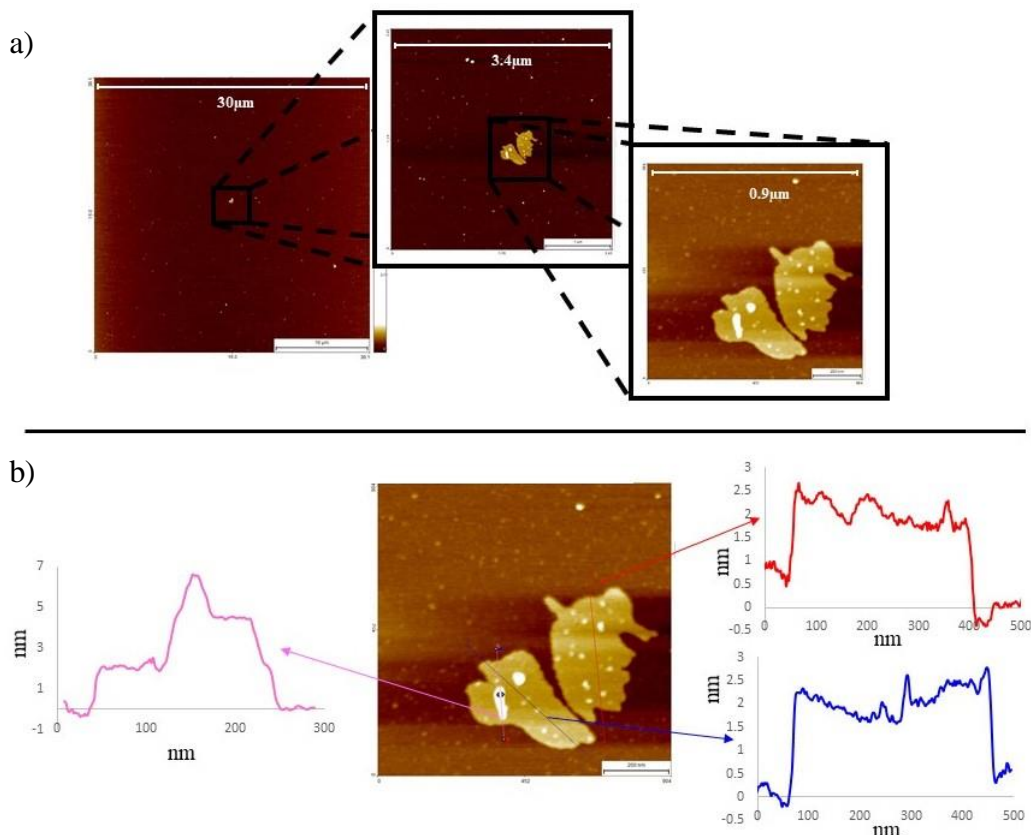


Figure 3.33 AFM picture of Py_3Man in aqueous medium without EtOH, from 75°C to 20°C with $0.1^\circ\text{C}/\text{min}$ as cooling rate: a) a scan of a larger area of the mica with presence of a few nanostructures; b) cross section of the sheets. For the plots: x-axis = width; y-axis = height.

In **Figure 3.33b**, cross section shows some details of the sheets. They look like those found in other cases, with a height of 2.5 nm. In here, there is again the presence of small dots, which increases the height of multiple of 2.5 nm.

Finally, the last measurement is made cooling and heating the solution with a temperature gradient of $0.5^\circ\text{C}/\text{min}$ (**Figure 3.34**).

In **Figure 3.34a** it is showed that, in this case, there are more sheets on mica surface, whereas in **Figure 3.34b** is showed the cross section, where the sheet has again a height of $\sim 2.5\text{nm}$. Also in this case, smaller structure are deposited on the bigger surface, just as in other cases seen previously.

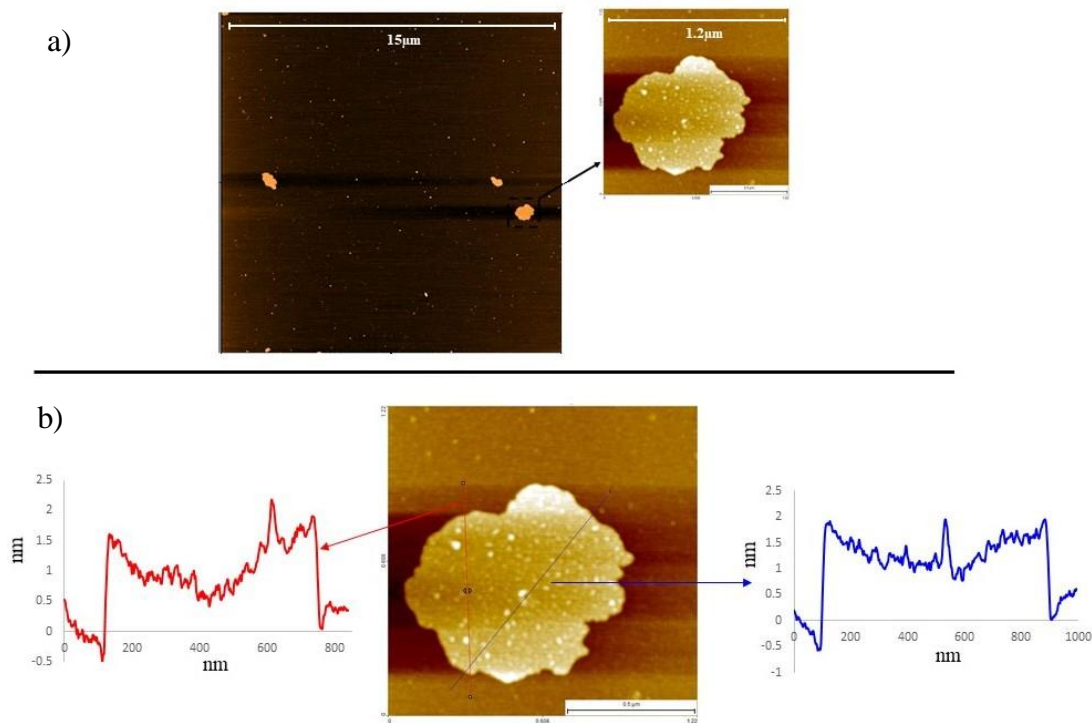


Figure 3.34 AFM picture of Py₃Man in aqueous medium without EtOH, with 0.5°C/min as temperature gradient: a) there are more objects on mica surface; b) cross section of the sheets shows the same characteristics as the other cases. For the plots: x-axis = width; y-axes = height.

Despite of the rate of heating/cooling analyses, in this solution with no EtOH, Py₃Man has showed the formation of nanosheets, in all three cases.

Whereas, in presence of EtOH, only with the rate of 0.1°C/min, the aggregation led to the formation of a round-shaped structure with a height of ~7nm.

In conclusion, all these experiments prove that Py₃Man has a different behavior than Py₃, since it can be subjected to assembly/disassembly effects with no need of EtOH in solution.

10 STUDIES OF Py₃But

Another kind of functionalization is the addition of a triple bond linked via phosphate to pyrene trimer (**Figure 3.35**).

As already described, Py₃But will be used for two approaches: in one, a DNA strand bearing an azide group will be covalently bound through click chemistry. Then, a

complementary DNA strand linked to gold nanoparticles will be coupled through base pairing.

In the other approach, gold nanoparticles are linked to a PEG derivative, which bears an azide group. This will react via click chemistry with Py₃But.

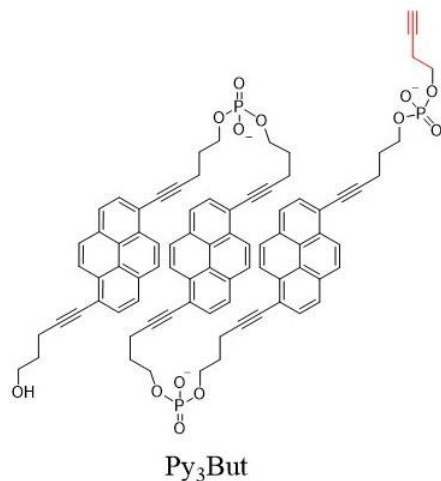
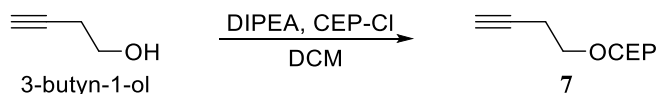


Figure 3.35 Structure of Py₃But: the three Py molecules and the butynyl moiety are linked via a phosphodiester link.

The synthesis of this compound is made with synthesizer, in the same condition described for Py₃Man. Preparation of monomer as butynyl source is described in **Scheme 3.6**.



Scheme 3.6 Synthetic step of preparation butynyl 2-cyanoethyl diisopropylphosphoramidite (**7**), starting from 3-butynol.

The procedure for the synthesis of butynyl 2-cyanoethyl diisopropylphosphoramidite (**7**) is the same used for preparation of **4** and **6**.

Once the compound is obtained, it is linked to Py₃ via phosphoramidite chemistry (see chapter 2), leading to the desired structure: Py₃But.

The study made on Py₃But were made in an aqueous solution made with 10mM of sodium phosphate buffer pH=7.2 with both 10% of EtOH and without.

The aggregation is followed by UV/vis analyses and the structure is confirmed at AFM, but only after the cooling/heating with 0.5°C/min as temperature gradient.

10.1 Py₃But IN AQUEOUS SOLUTION WITH ETOH

The first UV/vis analysis, for checking changes of UV trends at higher and lower temperatures, was made with the cooling/heating rate at $\sim 7^\circ\text{C}/\text{min}$ in 10mM sodium phosphate buffer and 10% EtOH (**Figure 3.36**).

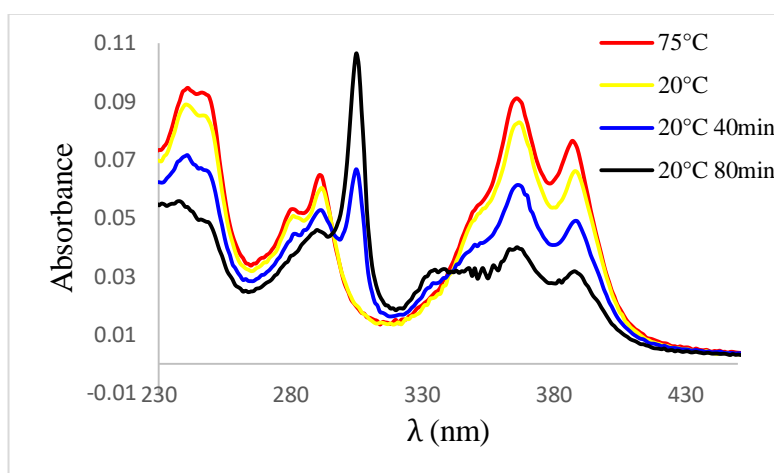


Figure 3.36 UV/vis from 75°C to 20°C . In this condition (10mM sodium phosphate buffer pH = 7.2 and 10% EtOH) the trimer take more time to reach a fully aggregation (80 minutes).

Aggregation of Py₃But is very slow in these conditions. In fact, the fully aggregation is reached after 80 minutes.

The fact that the structure aggregates differently, from the other molecules studied so far, is even more evident measuring the aggregation behavior with $0.5^\circ\text{C}/\text{min}$ as gradient temperature (**Figure 3.37**).

Heating/cooling analyses, with absorbance as a function of the temperature at 305nm and 365nm, show the aggregation starts at very low temperature, at $\sim 21^\circ\text{C}$.

At this point, it is easy to explain why all molecules are aggregated after 80 minutes: the critical temperature value is at $\sim 21^\circ\text{C}$, while the solution is cooled until 20°C .

Since the elongation step occurs after the formation of nuclei, it is easy to think that if the solution is kept to a temperature much lower to the value of the formation of nuclei, the elongation phase will be faster.

In this case, the analysis ends to a value (20°C) very close the critical temperature ($\sim 21^\circ\text{C}$) and, in this condition, a total aggregation requires more time.

Anyway, also in this case a hysteresis is present, which can be comparable to the one found for Py₃Man in the same conditions.

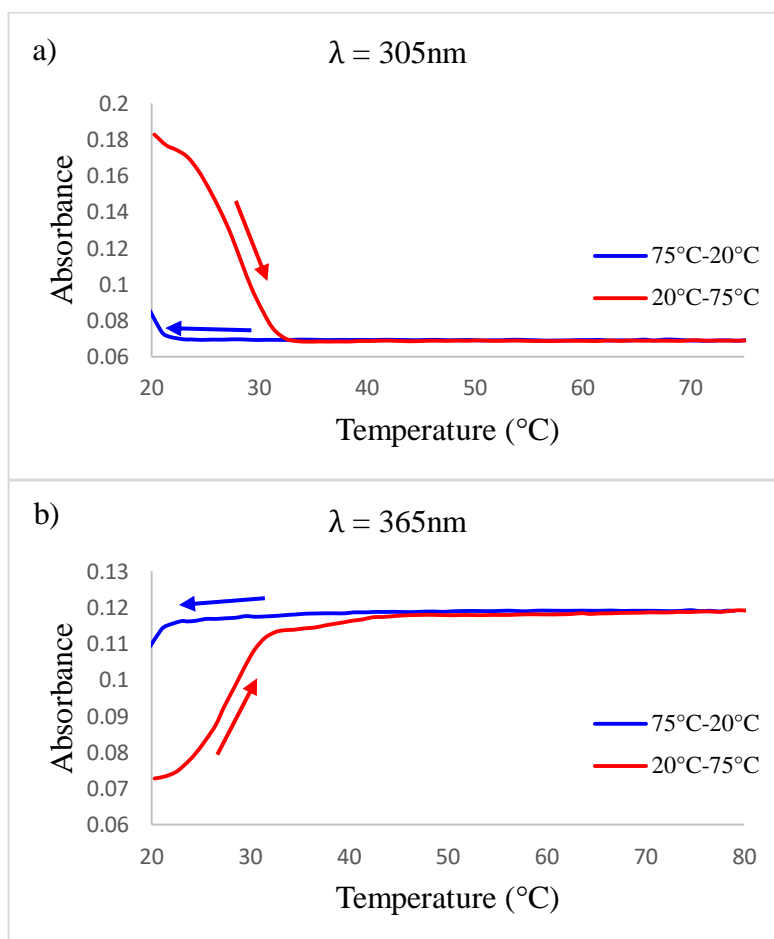


Figure 3.37 UV/vis cooling (blue) and heating (red) curves of Py₃But measured at 0.5 $^{\circ}\text{C}/\text{min}$ as cooling rate at: a) 305nm and b) 365nm

As regards the AFM analysis of Py₃But, the deposition of the solution on mica was made at room temperature, knowing that it was higher than T_c . Since the heating curve changed in absorbance in a range of $\sim 10^{\circ}\text{C}$, the system had to be still assembled, allowing the analysis.

In any case, the nanostructure found looked like fibers, even though few sheets are present (**Figure 3.38**).

Looking at AFM image, there is a pretty big population of aggregated structures on mica surface and fibers are much more abundant than sheets (indicated in white circles).

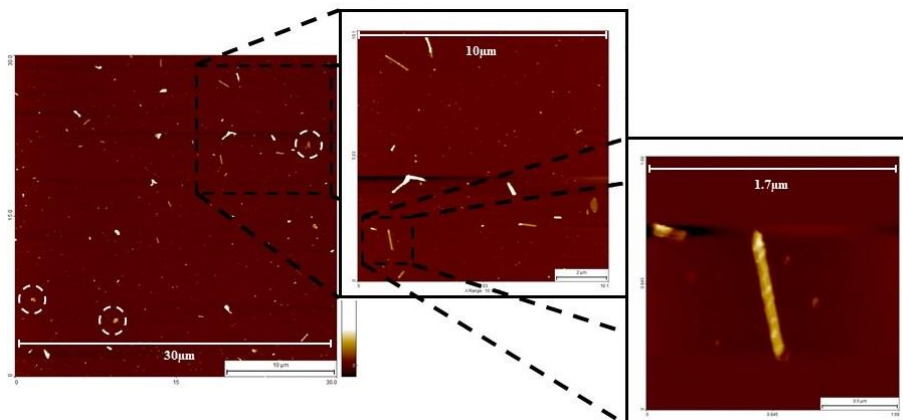


Figure 3.38 AFM picture of Py_3But in aqueous medium + EtOH, with $0.5^\circ\text{C}/\text{min}$ as temperature gradient with formation of fibers and a few sheets.

The fact that the product of aggregation is fibers rather than tubes, it is clearer looking at the cross section (**Figure 3.39**).

The cross section along the surface shows an uneven motif (for tubes cross section is smoother) and the measure diagonally to the structure gives a round shape with the height of $\sim 6\text{nm}$.

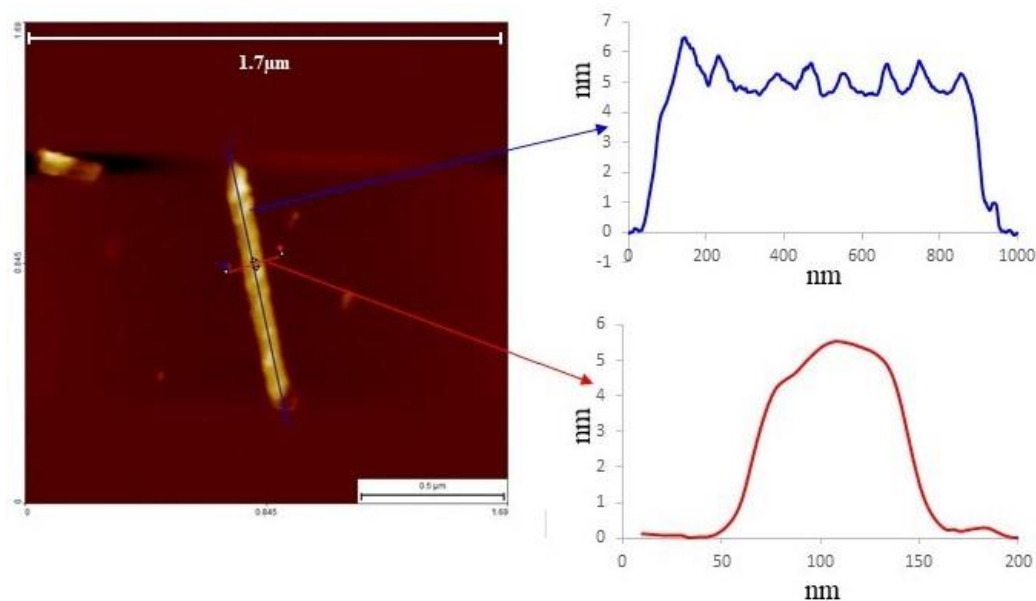


Figure 3.39 Cross section of a fiber. The surface along the fiber is uneven, while measuring diagonally the structure, the shape is round.

For the plots: x-axis = width; y-axes = height.

10.2 Py₃But IN AQUEOUS SOLUTION WITH NO EtOH

The situation is completely different when Py₃But is studied in aqueous solution without EtOH (**Figure 3.40**).

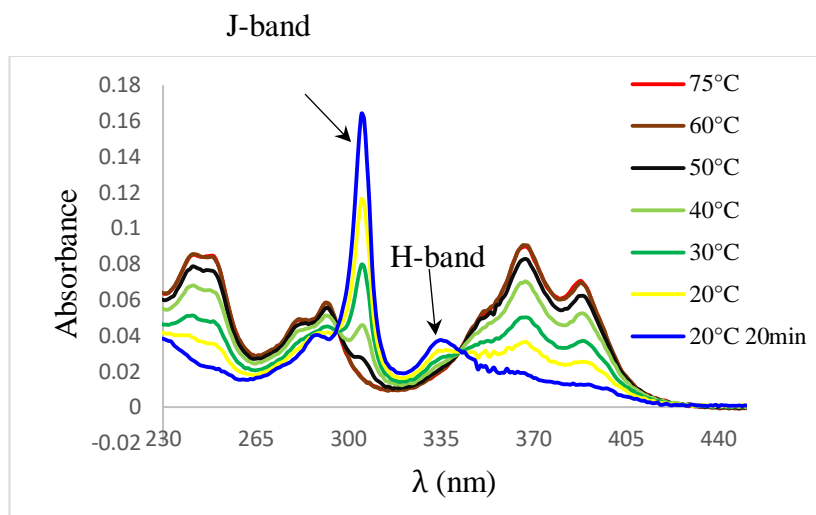


Figure 3.40 UV/vis measured at intervals of 10 minutes. The aggregation starts already at temperature of $\sim 50^{\circ}\text{C}$ (black curve).

Already in UV/vis experiment made with a temperature gradient of $\sim 7^{\circ}\text{C}/\text{min}$, it is possible to note that the aggregation starts at temperature much higher than in the case with EtOH.

As seen in the previous experiments, the absence of EtOH induces the aggregation at a temperature much higher.

In here, as showed in **Figure 3.40**, the aggregation seems to be already started at 50°C , with the formation of a small J-band.

By reducing the temperature at 10°C intervals, there is a gradual change in the respective curves. At 20°C the system is not fully aggregated; in fact, waiting further 20 minutes, at this temperature, J- and H-band reach their maximum intensity.

Furthermore, the two peaks in the range between 350nm and 400nm completely disappear: the curve is almost flat.

A better understanding about the aggregation is given by UV/vis analysis cooling/heating the solution with $0.5^{\circ}\text{C}/\text{min}$ as temperature gradient (**Figure 3.41**).

The measurements are made choosing the wavelength corresponding to the J-band (305nm) and 360nm.

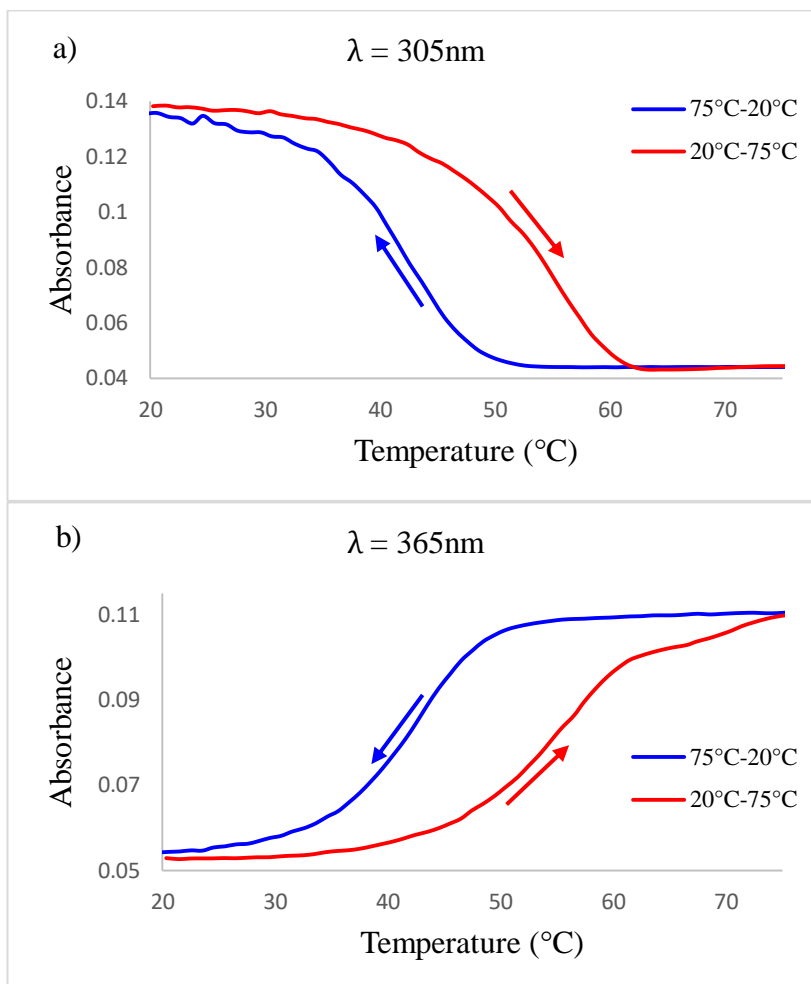


Figure 3.41 UV/vis cooling (blue) and heating (red) curves measured at 0.5°C/min as cooling rate at: a) 305nm and b) 365nm

According to cooling/heating analysis, Py₃But aggregates starting from a temperature of ~50°C, with the presence of hysteresis.

Not only aggregation temperature changes, but also AFM shows that the trimer aggregates with formation of sheets (**Figure 3.42**).

There are not so many on mica surface, but in any case, they have the same characteristics of those found with the other structures described so far: height of ~2.5nm and presence of smaller nanostructures deposited on the nanosheet surface.

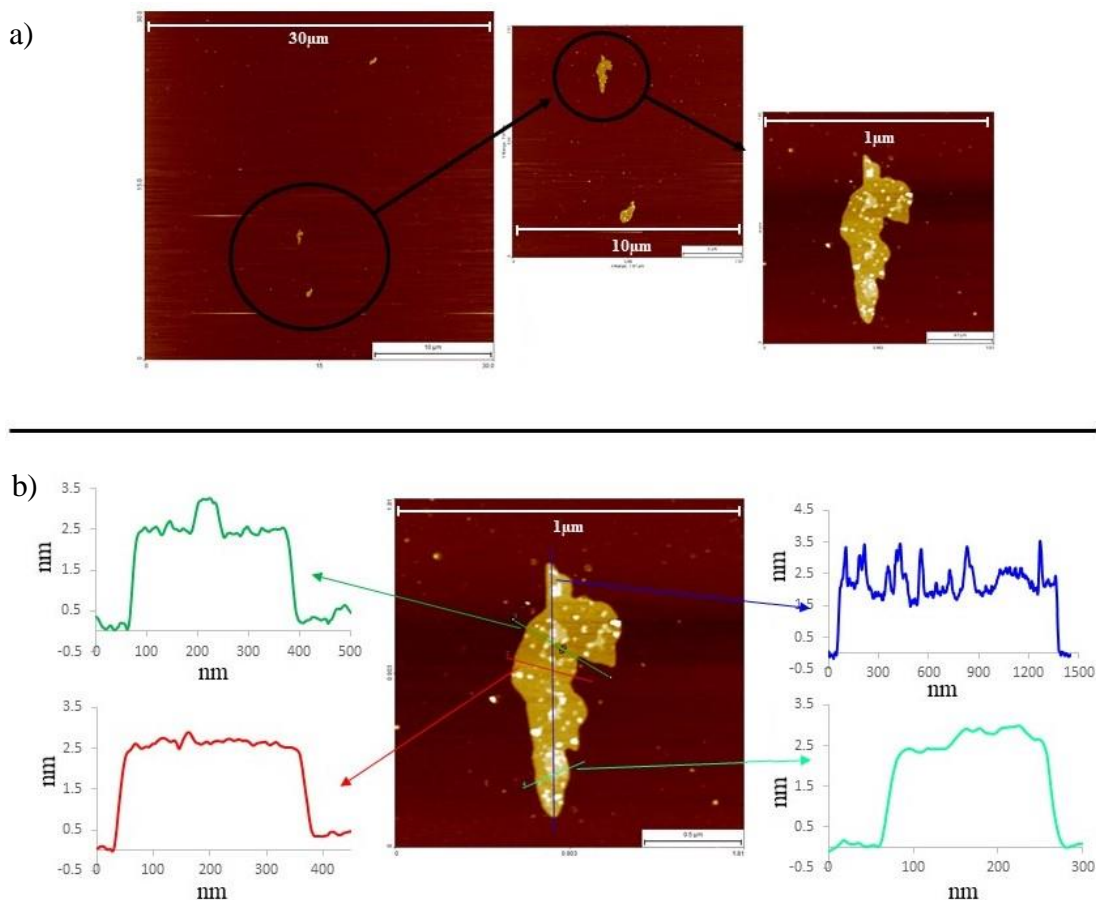


Figure 3.42 AFM pictures of Py₃But after cooling/heating with 0.5°C/min as temperature gradient. The system aggregates with formation of sheets (a). They have the same characteristics found for Py₃Man, which are a height of ~2.5 nm and white dots and small sheets deposited on main surface. For the plots: x-axis = width; y-axes = height.

Finally, in this last experiment, it is very interesting to note as the lack of EtOH leads to a high shift of the temperature of nuclei formation value (~21°C with EtOH vs ~50°C without EtOH).

Just as for pyrene, butynyl group has a higher affinity with EtOH than water. Since a higher solubility decreases the temperature for nuclei formation, probably, the fact butynyl is more soluble in the organic solvent can make more difficult the supramolecular aggregation at higher temperatures.

Moreover, the change regards also the kind of structure formed: the presence of EtOH seems to lead to the formation of fibers, whereas in aqueous solution without this cosolvent there is the formation of nanosheets.

In conclusion, the formation of functionalized sheets (in almost all cases nanosheets were formed), based on a pyrene trimer (Py_3) is showed. As already discussed above Py_3 was already known for its aggregation in nanosheets structures in certain conditions.⁹³

In here, the addition of a both mannose and butynyl groups, linked through a phosphate bridge, leads to a huge decrease of the nucleation temperature.

The analyses, made in aqueous solution with 10mM sodium phosphate buffer pH = 7.2, with the heating/cooling rates at 0.1°C/min and 0.5°C/min in presence of 10 % EtOH, showed two differences between Py_3 and its functionalized compounds. For the latter, the nucleation temperature values (summarized in **Table 1**) were much lower than those of Py_3 and they showed a hysteresis in all cases.

Aqueous solution with 10mM sodium phosphate buffer pH = 7.2 and 10% EtOH				
	Py_3	Py_3Man	Py_3Phos	Py_3But
0.1°C/min	~70°C	~24°C	~35°C	--
0.5 °C/min	~70°C	~28°C	~23°C	~21°C

Table 1 Summary of the nucleation temperatures found at UV/vis heating/cooling analyses of the structures studied at 0.1°C/min and 0.5°C/min. Py_3But was studied only at 0.5°C/min.

From these analyses, the presence of phosphate has most likely given the highest contribution to those differences compared to Py_3 . Probably the presence of the phosphate increases the solubility in water, leading as result to a lower temperature for nuclei formation. About the hysteresis, it is not clear which are the mechanisms involved, but the UV/vis analyses showed that it was bigger in the case of Py_3Phos .

The studies made in the aqueous solutions, but without EtOH (summarized in **Table 2**) showed how the lack of this organic solvent can effect on the aggregation temperatures.

Aqueous solution with 10mM sodium phosphate buffer pH = 7.2		
	Py_3Man	Py_3But
0.1°C/min	~45°C	--
0.5 °C/min	~33°C	~50°C

Table 2 Summary of the nucleation temperatures found at UV/vis heating/cooling analyses of Py_3Man studied at 0.1°C/min and 0.5°C/min and Py_3But at 0.5°C/min.

This can be explained considering the affinity of pyrene unities with EtOH. In an aqueous solution without EtOH, the structures studied are less soluble and this leads to the pyrenes to aggregate at higher temperature than the case of solutions where this organic solvent was used at 10%.

Again, the presence of the phosphate (linked to both mannose and butynyl) increased the solubility of the entire structures, making possible the self-assembly/disassembly processes in the range of temperature between 20°C and 75°C.

In fact, in this condition, Py₃ appeared every time aggregated at both 20°C and 75°C due to its low solubility.

By making a comparison of Py₃Man and Py₃But studied in solutions with and without EtOH, the hysteresis is similar. This gives only the idea that EtOH has no effect to it, but why it is observed is, so far, not understood yet.

CHAPTER 4

1 THE PURPOSE OF FUNCTIONALIZATION

In this chapter, the purpose of the functionalizations, depicted in the last chapter, will be explained. Their role was to bind, selectively, to specific macromolecules or structures, after that Py₃Man and Py₃But self-assembled in nanosheet structures.

In particular, in Py₃Man, mannose moiety was used as bonding site for Concanavalin A (Con A), a protein which has a high affinity to mannose and glucose residues.

After the formation of the sheets on mica, confirmed by AFM, a solution containing the protein is poured on the surface of mica in the same area where sheets are present and studied (**Figure 4.1**), allowing the bond, which will be confirmed at AFM.

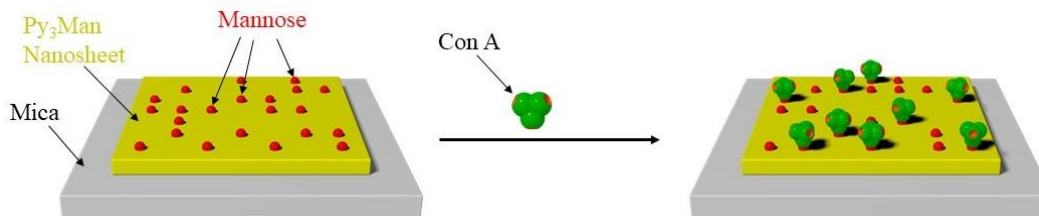


Figure 4.1 Representation of the approach with Con A: after the formation of nanosheets, a solution containing Con A is deposited on mica where sheets are present.

Whereas, in Py₃But, butynyl was used for two different approaches: in both cases, click chemistry and gold nanoparticles (AuNP) were used.

In the first approach, after the formation of sheets, a DNA strand bearing an azide (DNA-1) is linked to butynyl moiety via click chemistry. Then, a complementary DNA strand, containing a thiol group (DNA-2), is first linked to AuNP and, then, it will couple to DNA-1, via base pairing. Also in this case, AFM is used to check the nanosheets on mica surface. The solution containing DNA-1 and the reagents for click chemistry is poured on mica, in the area with sheets. Then, another solution with DNA-2 is poured on mica (on the same area with sheets) and studied at AFM (**Figure 4.2**).

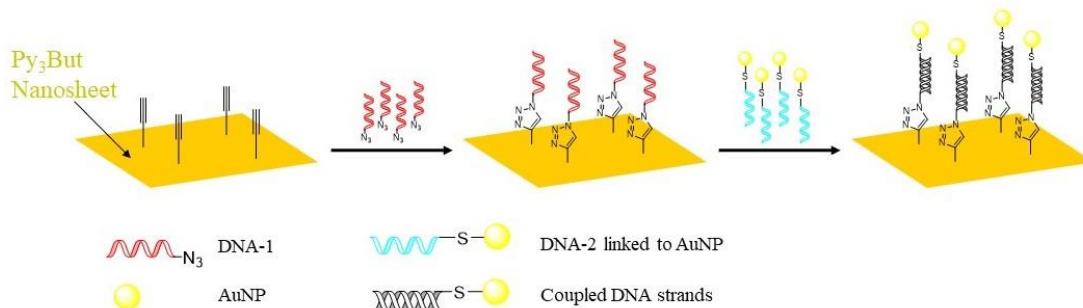


Figure 4.2 Click chemistry between the butynyl moieties of a Py₃But nanosheet and the azide in DNA-1. After this first step, DNA-2 linked to AuNP couples to DNA-1 via base pairing.

The second approach is based on the use of a PEG derivative, bearing an azido and a thiol group at the two extremities of the structure.

The thiol group is linked to AuNP, obtaining the corresponding product; then the latter is dissolved in a solution containing the reagents for click chemistry in order to allow the link with the butynyl moieties of Py₃But after the sheet formation (**Figure 4.3**).

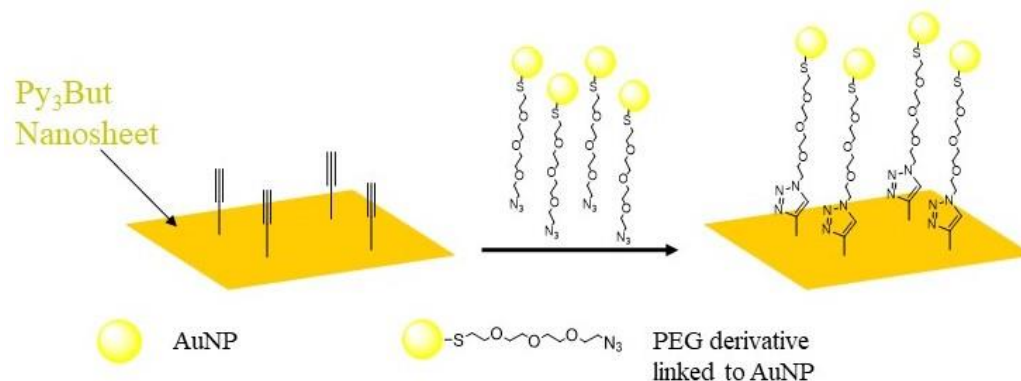


Figure 4.3 Click chemistry between a PEG derivative linked to AuNP and the butynyl moiety of Py₃But nanosheet.

In the experiments involving click chemistry and AuNP, in order to be sure the two approaches worked, a preliminary test was made in solution, using a dye bearing an azide. In a solution containing the reagents for the click chemistry and the dye-azide, an aliquot of the solution with Py₃But nanosheets was added (after the self-assembly of the trimer). The reaction progress was checked at HPLC at different reaction times.

The same was made with DNA-1 strand, before the approach with AuNP was carried out.

2 Py₃Man BINDS TO CON A

Starting from the role of mannose, in Py₃Man, it was used for its affinity with a protein: Concanavalin A (Con A)

Con A is a lectin isolated from *Canavalia ensiformis* (Jack bean), which has demonstrated a binding specificity to α -D-mannose and α -D-glucose moieties.

This protein (**Figure 4.4**) is used for carbohydrate studies, glycoprotein purification, cell membrane studies, etc.

It has a tetrameric structure at pH 7 or greater, consisting of 4 subunits with equal molecular masses of 26kDa.

While, at lower pH values (pH 4.5–5.5), Con A converts to a dimeric structure. Each monomer, regardless of pH or molecular structure, contains two metal ions (Ca^{2+} and Mn^{2+}) binding sites.

The presence of these metal ions is very important; indeed, they must be bound to these sites in order to allow the binding with the sugar.¹⁰⁴

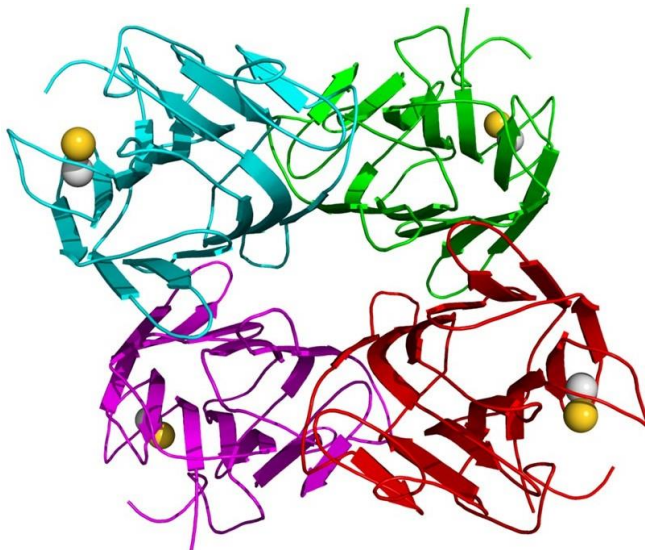


Figure 4.4 Structure of Con A in tetrameric form. The four monomers are colored in green, red, magenta and cyan, while the two spheres are calcium (in gold) and manganese (grey) cations.¹⁰⁵

In order to be used, a stock solution of 10 μ M of Con A was prepared. The protein was dissolved in 10mM sodium phosphate buffer pH = 7.2 with 0.1mM CaCl_2 and 0.1mM MnCl_2 (the conditions were partially taken from¹⁰⁴).

The idea behind the use of Py₃Man was to develop the affinity of Con A with the mannose residue on the trimer. This kind of experiment was made at AFM.

The two structures of Py₃ and Py₃Phos were synthesized just as control. In aqueous medium, with or without EtOH, Py₃Man aggregates with formation of nanosheets, in one of the conditions described in Chapter 3.

About 30µL of the solution, containing the 1µM of trimer, are deposited on mica (APTES modified) surface for 3 minutes. Then, the solution was washed with 1mL of MilliQ water, dried with argon and measured at AFM.

After the AFM analysis, a solution with 0.2µM Con A in 10mM sodium phosphate buffer pH = 7.2 was prepared and a volume of 30µL was poured on the same area of mica where sheets were present, for 30 seconds.

After that, the drop with Con A is washed away, dried with argon and the mica was analyzed at AFM.

In order for the same spot is measured and, thus, the same nanostructure can be observed after Con A deposition, the Kinematic Sample Holder (KSH) was installed in AFM instrument.

The principle of KSH is very simple as showed in **Figure 4.5**.

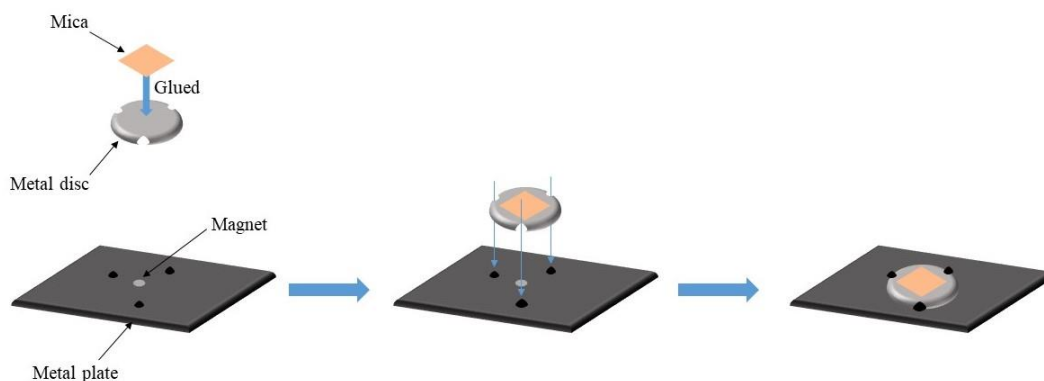


Figure 4.5 Kinematic Sample Holder (KSH) use: mica is glued on a metal disc, which maintained on metal plate thanks to a small magnet in a fixed position.

Basically, mica is glued on metal disc, which is fixed on a metal plate (screwed to the AFM instrument) thanks to the presence of a small magnet. In this way, metal disc stays fixed during the analysis and, after, it can be easily removed. Furthermore, the presence of three small balls constrain the metal disc to be placed in the same way, allowing the user to scan the same area every time the metal disc is removed and repositioned on the

metal plate. In this way, it is possible to find the nanostructure at AFM, deposit the solution containing the Con A and observe again the same objects but with the opportune modification. Unfortunately, Con A totally covered the mica surface (**Figure 4.6**).

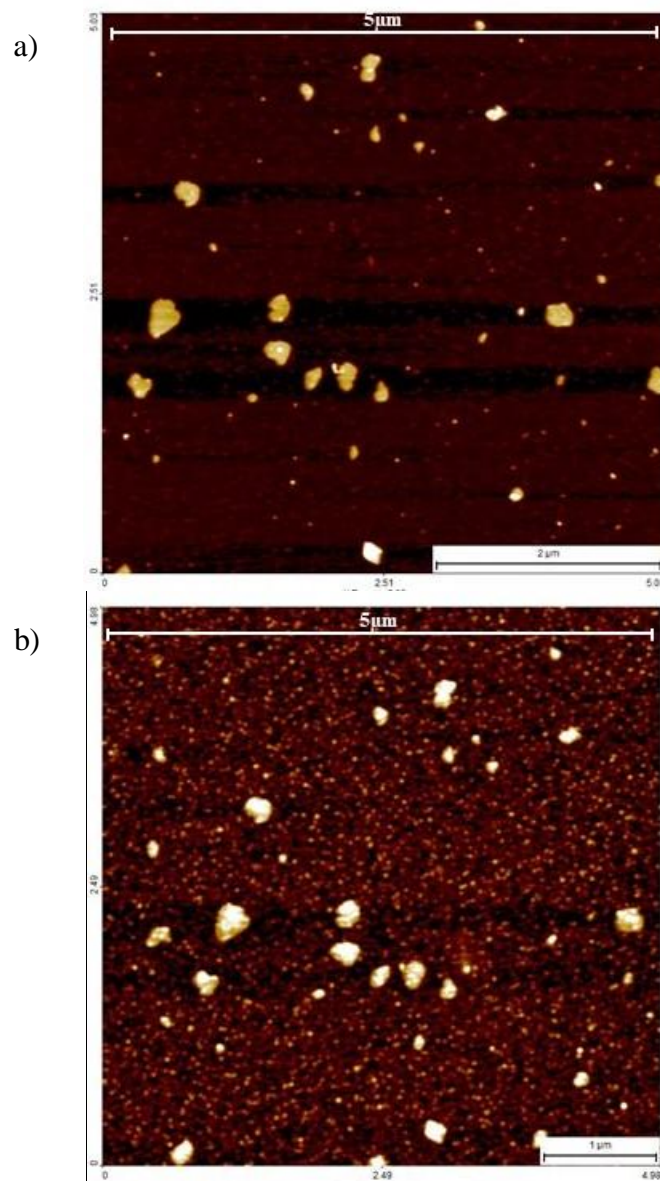


Figure 4.6 Comparison between: mica surface covered by Py₃Man nanosheets (a) and the same after addition of Con A solution (b). In the latter case, protein covers everything (both sheets and mica surface), as it is possible to note from small spheres on the background.

In **Figure 4.6a**, AFM picture of nanosheets of Py₃Man is showed. The nanosheets aggregation was made in aqueous solution without EtOH (the solution is cooled down at 0.5°C/min). The characteristics are described in Chapter 3, it is worth to remember that their shape can be different, but the height is ~2.5nm. After the AFM measurement, the

solution with Con A is deposited on mica for 30 seconds, the solution is washed away and, then, the mica is measured again at AFM.

As showed in **Figure 4.6b**, Con A covers everything. This can be noticed looking at the surface between the sheets, where the surface shows very rough because of the presence of small spheres. For a better understanding, the cross section, of the same sheets, shows how the surface looks like before and after the addition of Con A (**Figure 4.7**).

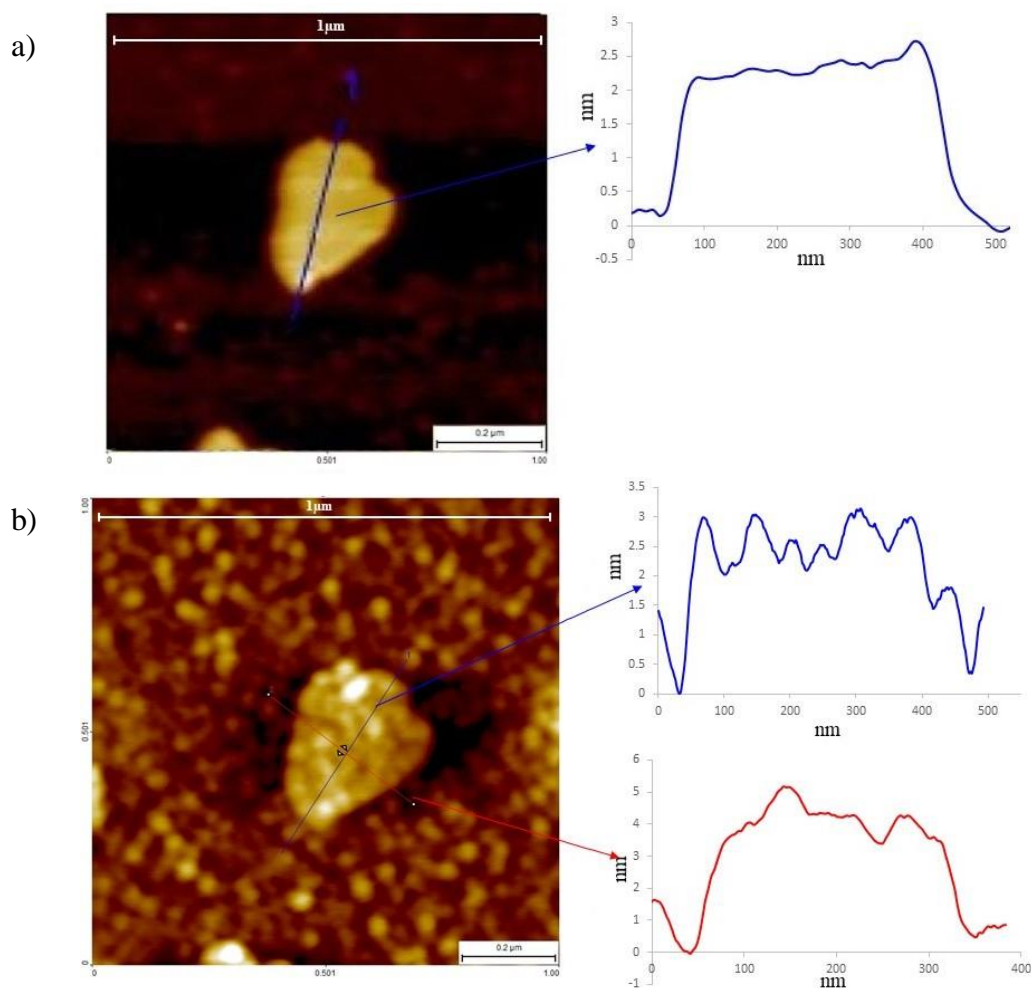


Figure 4.7 AFM picture of an enlargement of a nanosheets. The picture on the top (a) has a pretty smooth cross section. On the bottom (b), small spheres cover everything (mica and sheet area). The cross sections show a pretty rough trend with a higher value of the height.

The nanosheet, showed in **Figure 4.7a**, have a pretty smooth surface with a height of ~ 2.5 nm. Whereas, the structure in **Figure 4.7b** appears with a value of the height between 1 nm and 2.5 nm as prove that something is deposited on the top of the surface.

This increase of the height does not surprise when only $0.2\mu\text{M}$ of Con A are measured at AFM.

In fact, leaving the solution on mica for 30 seconds, a situation where the surface is completely covered by the protein is observed, showing a cross section quite rough with a maximum height of $\sim 2.5\text{nm}$ (**Figure 4.8**).

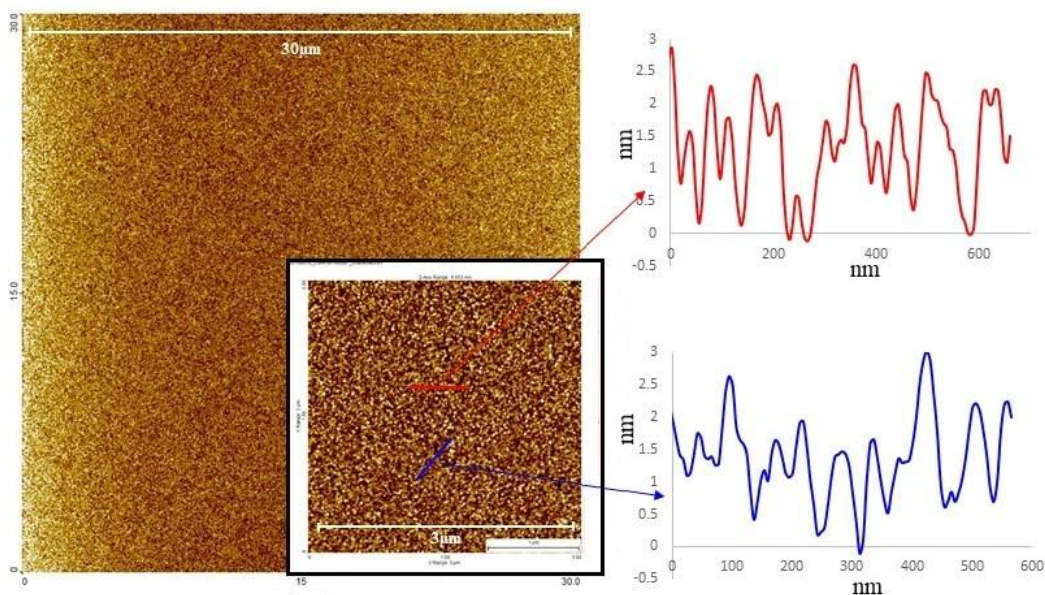


Figure 4.8 AFM picture of Con A ($0.2\mu\text{M}$). Mica surface is completely covered by the protein showing small spheres with a height of $\sim 2.5\text{nm}$.

Finally, a control experiment was made using Py_3 . The idea was to have sheets not linked to Con A because of the lack of mannose, even considering the affinity of the protein with mica (**Figure 4.9**).

But unfortunately, also in this case there was no difference, having a situation pretty similar to the one showed above. The nanosheet of Py_3 (**Figure 4.9a**) was obtained in aqueous solution with 10% of EtOH after the solution was cooled down from 75°C to 20°C , at $\sim 7^\circ\text{C}/\text{min}$. Also in this case, a solution of $0.2\mu\text{M}$ of Con A was poured on mica surface for 30 seconds.

From **Figure 4.9b**, it is possible to note how Con A covers everything, with the presence of the spheres on both mica and sheets surface. From these experiments, it is obvious that Con A binds to mica and it deposits on nanosheets, making impossible to understand the link with mannose. A different approach could be the use of unmodified mica, but in these conditions the trimers does not bind to its surface.

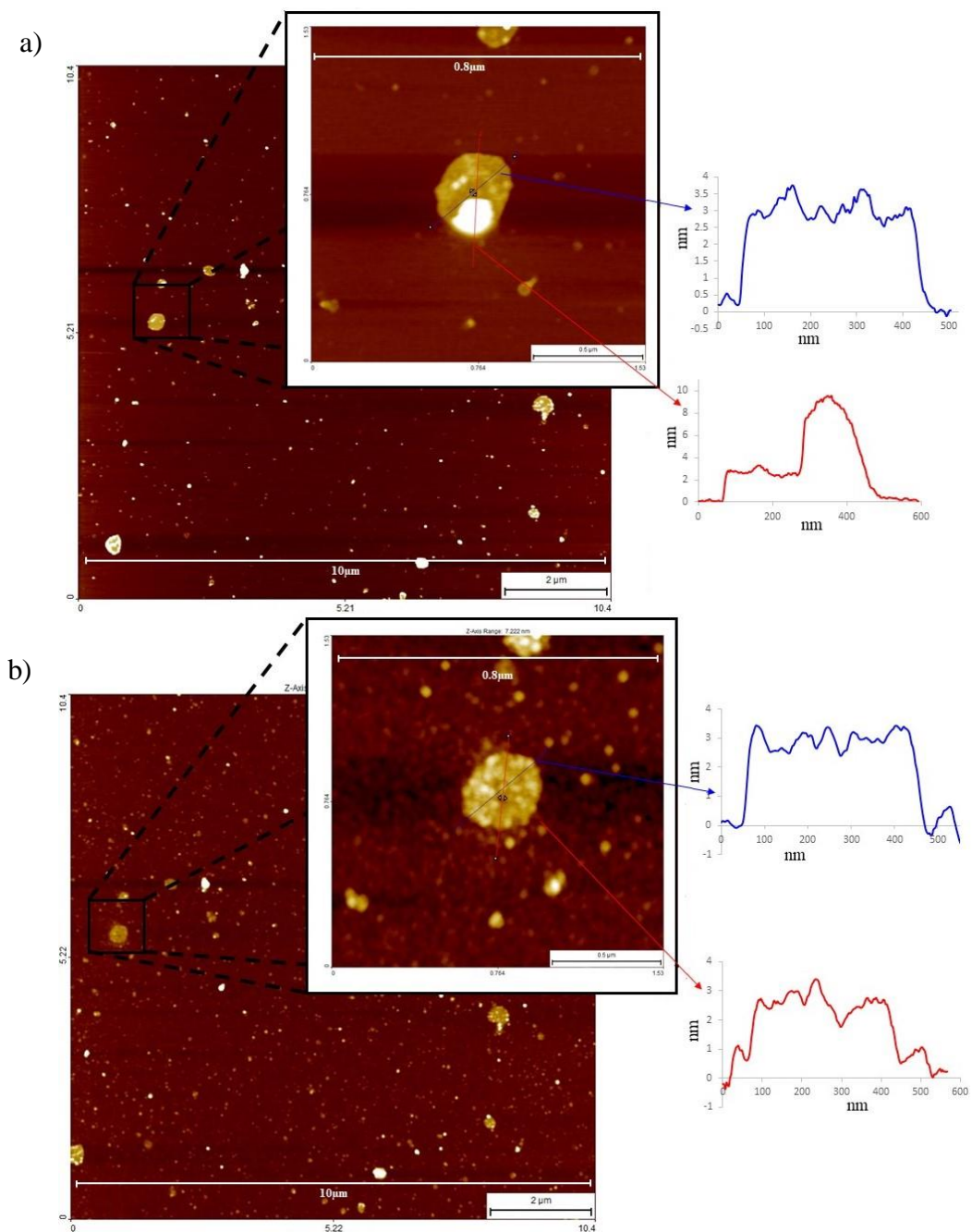


Figure 4.9 AFM picture of Py₃ nanosheets (a). On the same of the sheets, a solution of Con A is deposited (b), which covers both nanosheets than mica surface.

This because, as described in chapter 3, mica surface is negatively charged, so there is a repulsion with the phosphates in the trimers. Another approach is to use a divalent cation e.g. Ni²⁺.

This divalent cation can bind to the negative mica surface and to the phosphate groups in the trimers, allowing a deposition of the nanostructures.

In conclusion, the fact that Con A binds on mica surface, even for a very short time (only 30 seconds), represents a huge limit for this kind of studies.

Probably, the link is due to the presence of some amino acid, like glutamic acid and aspartic acid, in the amino acid sequence of Con A.¹⁰⁶ Since the pH of stock solution of Con A was 7.2, the side chain of these two amino acids could be deprotonated, since at physiological pH (7.4), their side chains are negatively charged.^{107,108}

3 CLICK CHEMISTRY OF Py₃But IN SOLUTION

As already described above, Py₃But was used for two approaches base on the use of click chemistry and AuNP.

In order to have an idea about the reaction conditions of the click chemistry, a test with the use of a dye bearing an azide (Azide-fluor 488 was used, **Figure 4.10**) was first made. The progress of the reaction was monitored by HPLC.

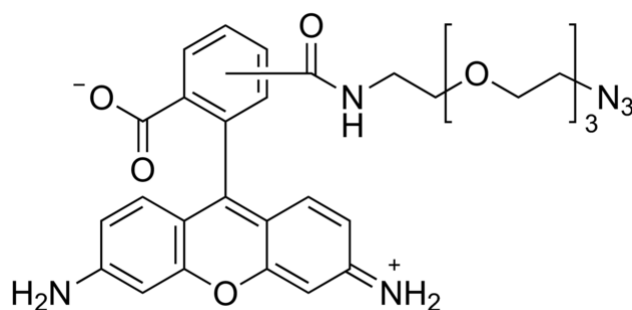


Figure 4.10 Azide-fluor 488 structure. The compound was bought as an isomeric mixture.

The HPLC trace was measured at 365nm. At this wavelength, pyrene has a ϵ_{365} value of $35000 \text{ M}^{-1}\text{cm}^{-1}$ (a value of 105000 is taken, because of the three pyrene in Py₃But).⁹³

At this point, it was necessary to calculate the dye contribute at 365nm, by calculating the relative ϵ_{365} value.

For this purpose, a solution of $\sim 20\mu\text{M}$ of Azide-fluor 488 was measured at UV, in water, obtaining the spectrum showed in **Figure 4.11**.

From literature¹⁰⁹, the value of ϵ , at 496nm, is $\epsilon_{496} = 74000 \text{ M}^{-1}\text{cm}^{-1}$. In this way, using the Lambert-Beer's law, it is possible to calculate ϵ at 365nm: $\epsilon_{365} = 1676 \text{ M}^{-1}\text{cm}^{-1}$.

It is obvious that the contribution of the dye at 365nm is very low. In fact, at 365nm the ratio: ϵ_{365} of the dye/ ϵ_{365} of Py₃But = ~0.02.

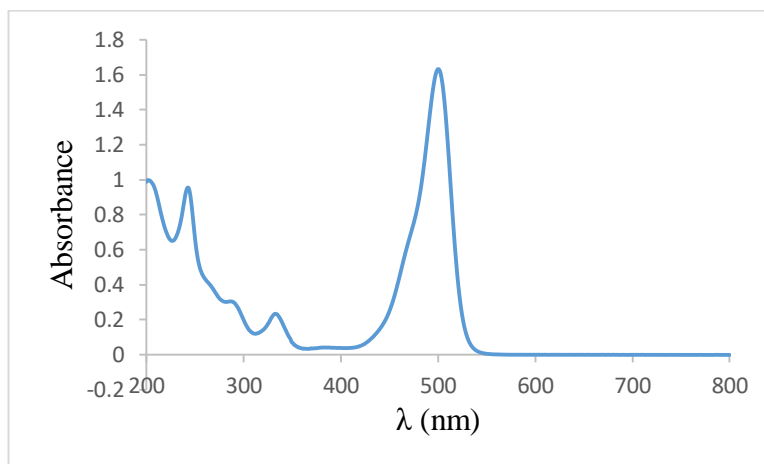


Figure 4.11 UV spectrum of Azide-fluor 488 in water. The value of ϵ_{496} is $74000 \text{ M}^{-1}\text{cm}^{-1}$, while the calculate value of ϵ_{365} is $1676 \text{ M}^{-1}\text{cm}^{-1}$.

Before to proceed with the reaction, $1\mu\text{M}$ of Py₃But was induced to self-assemble in aqueous solution, with formation of nanosheets, by cooling down the solution from 75°C to 20°C , at $0.5^\circ\text{C}/\text{min}$.

To the solution with these nanostructures, $10\mu\text{M}$ of the dye were added, at ambient temperature, and then injected to the HPLC (**Figure 4.12**).

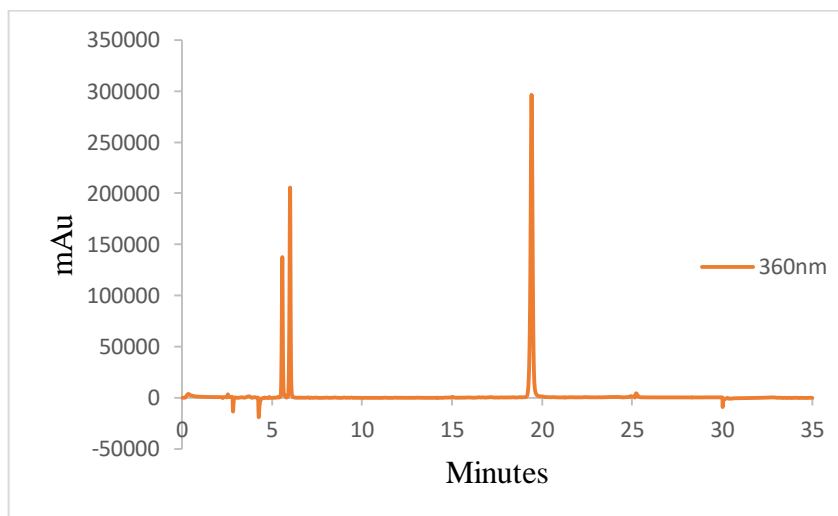


Figure 4.12 HPLC trace, measured at 365nm, of a solution containing $10\mu\text{M}$ of the isomeric mixture of Azide-fluor 488 (the two peaks at ~6 minutes) and $1\mu\text{M}$ of Py₃But at ~20 minutes.

The two solvents used were: Solvent A 0.05 triethylammonium acetate (TEEA) 0.05M pH=7; Solvent B ACN (for HPLC grade).

The program used (with a flow of 1mL/min and a temperature of 50°C) was: Solvent B [%] (tR [min]) = 20 (0); 35 (2); 65 (16); 80 (18); 100 (22); 100 (27); 20 (30), obtaining the trace showed in **Figure 4.12**.

The peak relative to Py₃But is the one at ~20 minutes (checked by mass spectrometry), while the dye shows two peaks at ~6 minutes, because an isomeric mixture was used.

After having made these preliminary tests, in order to have an idea of the contribution of the dye at 365nm and the positions of the peaks of Py₃But and the dye to HPLC, the next step was the click chemistry of these two structures.

This click chemistry reaction uses Cu(I) as catalyst; in fact, the procedure is known as copper-catalyzed azide-alkyne cycloaddition (CuAAC).¹¹⁰

For this reaction, the source of Cu(I) was CuSO₄; since, in solution copper is divalent, it is reduced *in situ* using a huge excess of sodium ascorbate (NaAsc).

Furthermore, to the reaction the ligand Tris(3-hydroxypropyltriazolylmethyl)amine (THPTA) was added in excess.

Finn *et al.*¹¹¹ suggested that the role of THPTA is to intercept and quickly reduce the reactive species of the oxygen. These species are generated by the reduction of the O₂ (dissolved in the aqueous medium), driven by ascorbate.

The ligand THPTA acts as sacrificial reductant and the use of 5 equivalent (relative to copper) does not compromise, very much, the reaction rate.

In all tests, based on click chemistry, described in this chapter, a stock solution containing both CuSO₄ and THPTA in a ratio 1:5 was used (CuSO₄/THPTA = 1:5), since the ligand was used in a concentration 5 times more than the one of CuSO₄.

THPTA has two functions: acceleration of the reaction by maintaining the Cu(I) oxidation state of copper and protection of biomolecules from oxidative damage during the labeling reaction.^{110,112}

The stock solutions of the dye-azide and CuSO₄-THPTA (1:5) were prepared and added in the desired amount for the reaction. Instead, the NaAsc solution was every time freshly made.

3.1 HPLC ANALYSIS OF THE REACTION WITH THE DYE

The reaction between the dye and the nanosheets of Py_3But in click conditions was made at different reaction times and, then, checked at HPLC in order to have information about the yield.

The formation of sheets was made using $1\mu\text{M}$ of Py_3But in the aqueous solution (10mM sodium phosphate buffer $\text{pH} = 7.2$), cooling the solution from 75°C to 20°C , at $0.5^\circ\text{C}/\text{min}$. Then, the other components were added, from their relative stock solutions, calculating the following concentrations: dye-azide = $10\mu\text{M}$, $\text{CuSO}_4\text{-THPTA}$ (1:5) = $20\mu\text{M}$ and $100\mu\text{M}$ respectively and $\text{NaAsc} = 1\text{mM}$, at ambient temperature.

The yields were calculated at different reaction times, by making a ratio between the area of the two peaks relative to the product at ~ 15 minutes and the peak relative to Py_3But at ~ 20 minutes (**Figure 4.14**).

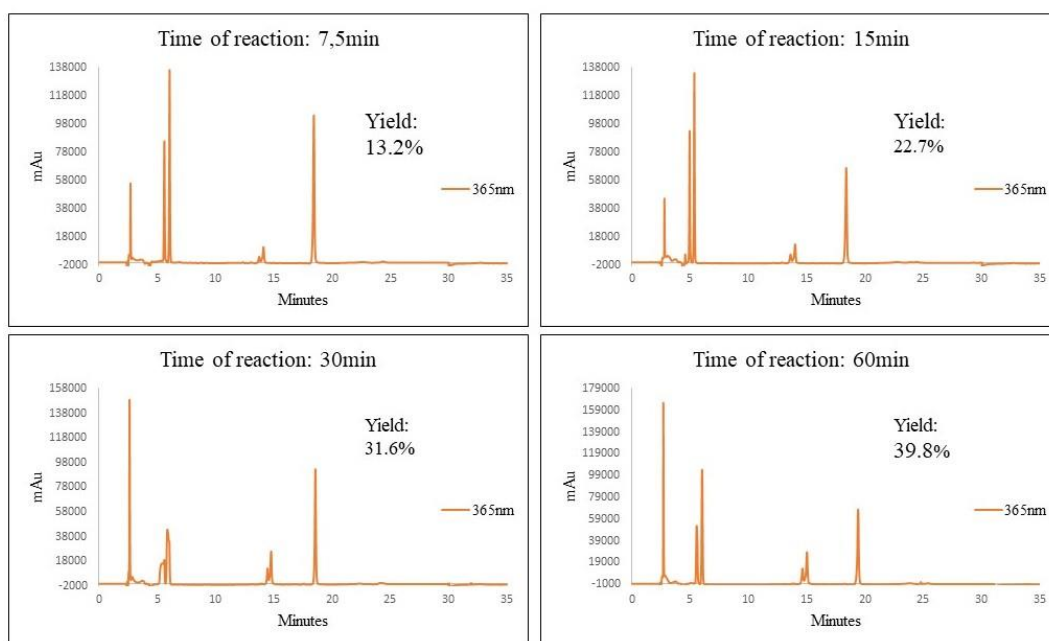


Figure 4.14 HPLC traces of the reaction of click chemistry between Py_3But nanosheets and the Azide-fluor 488, at different reaction times.

The fact that there are two peaks (~ 15 minutes) is due to isomeric mixture of the dye.

The reaction after 60 minutes shows a yield of 39.8%. Making a plot of the yield (% Reacted) as a function of the time of reaction (minutes), it is possible to have an idea about the evolution of the reaction (**Figure 4.15**).

Minutes	% Reacted
0	0
7.5	13.2
15	22.7
30	31.6
60	39.8

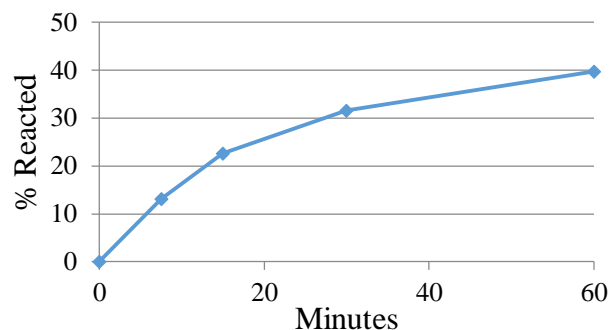


Figure 4.15 Plot of the yield (% Reacted) as a function of the reaction time (minutes), of Py₃But (after nanosheets aggregation) and the dye.

Following the curve, the reaction looks like to proceed pretty well, indeed after 7 minutes and 30 second, the 13.2% of Py₃But has reacted.

After 15 minutes, the yield is almost the double, then, the fact the reaction seems to slow down, it is clear because at 30 minutes the % of the product obtained is much less than the value expected.

Finally, after 60 minutes the reaction is over with a 39.8% of yield. The fact that not all Py₃But reacts is due to the initial formation of sheets.

Probably, when a first dye is linked to the butynyl of a nanosheet, it can covers part of the surface, hampering the reaction between the butynyl close to it and another dye-azide.

Therefore, the situation is a nanosheets with part of butynyl groups, which have reacted with Azide-fluor 488, and free butynyl groups, which are inaccessible, because spatially covered by the dye.

To support this theory is a similar experiment made without the formation of the sheets.

In solution, Py₃But and Azide-fluor 488 were mixed in solution using the same concentrations and adding the same reagents, for the click chemistry, as described above. Also in this case, the reaction was checked at HPLC (**Figure 4.16**).

In this case already after 30 minutes the reaction was complete and all Py₃But reacted with dye.

At this point, it is logic to think that when the pyrene trimer is aggregated in a different manner of the sheets found at AFM. In this case, butynyl moieties are more exposed for the reaction with the dye.

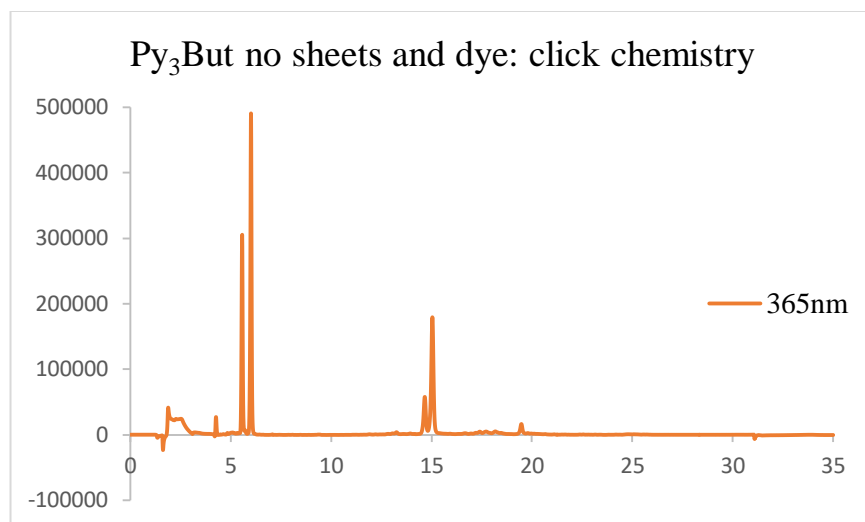


Figure 4.16 Click chemistry reaction between Py₃But without nanosheets formation and Azide-fluor 488. After 30 minutes all Py₃But has reacted.

It is possible to conclude that, the self-assembled nanostructure is formed by an ordered position of the components: this means pyrene molecules aggregate with formation of sheet. While, the butynyl groups are located on the top and, probably, on the bottom of the sheets surface, with a certain distance between them.

When a dye molecule links to one of them, it can cover the butynyl moieties nearby, hampering their reaction with other dye molecules.

So, the surface of the nanosheets has areas covered by dyes, which hide some areas making the other unreacted butynyls nearby inaccessible.

Moreover, these reactions were made at ambient temperature. Tests made at higher temperatures could not be done because the nanosheets disassemble.

3.2 HPLC ANALYSIS OF THE REACTION WITH DNA-1

The same analysis, with the use of click chemistry, with Py₃But after the formation of sheets, was made using a 3' N₃ modified DNA strand (DNA-1).

Also in this case, after the sheets formation, in aqueous solution, cooling the temperature down from 75°C to 20°C, at 0.5°C/min, DNA-1 and the other reagents for click chemistry were after added.

The conditions were the same used for the click chemistry with the dye, discussed above.

The only difference is that this time the reaction was checked at different reaction times to HPLC at 365nm, using the same solutions and the same program for the reaction between Py₃But and the dye.

In **Figure 4.13**, it is showed the HPLC trace of 1μM of Py₃But and 10μM of DNA-1 (the sequence is showed in the inset of **Figure 4.13**), without click chemistry reagents.

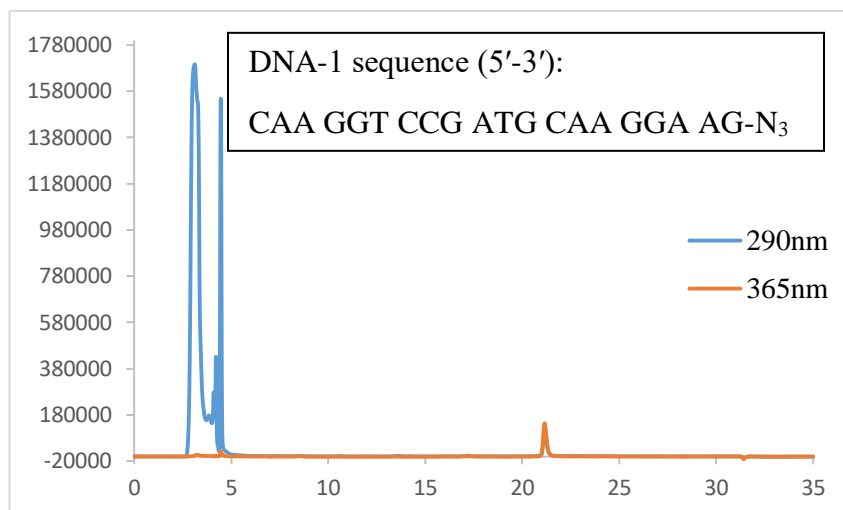


Figure 4.13 HPLC traces, measured at 290nm and 365nm, of a solution containing 10μM of DNA-1 (the two peaks at ~3 and 5 minutes) and 1μM of Py₃But at ~20 minutes. DNA-1 can be detected only at 290nm.

The HPLC is measured at 290nm and 365nm. The DNA strand is revealed only at 290nm while Py₃But mostly at 365nm.

The peaks at 295nm, in a range within 5 minutes, is a bit suspicious since sometimes impurities are found, due probably to the eluents used.

Moreover, the intensity of the peaks is also much bigger than the one relative to Py₃But at 365nm. For this reason, the path of the reaction is checked only at 365nm.

In here, the click reaction between Py₃But and DNA-1 was made at longer reaction times than the ones used for the dye, using the same conditions and the same reagents with the relative concentrations.

The values of the yields of this reaction were low (**Figure 4.17**). Py₃But and DNA-1 were let to react for a maximum of 20 hours, at ambient temperature.

Also in here, the yield were obtained by calculating the ratio between the peak relative to the product at ~9 minutes and Py₃But at ~20 minutes.

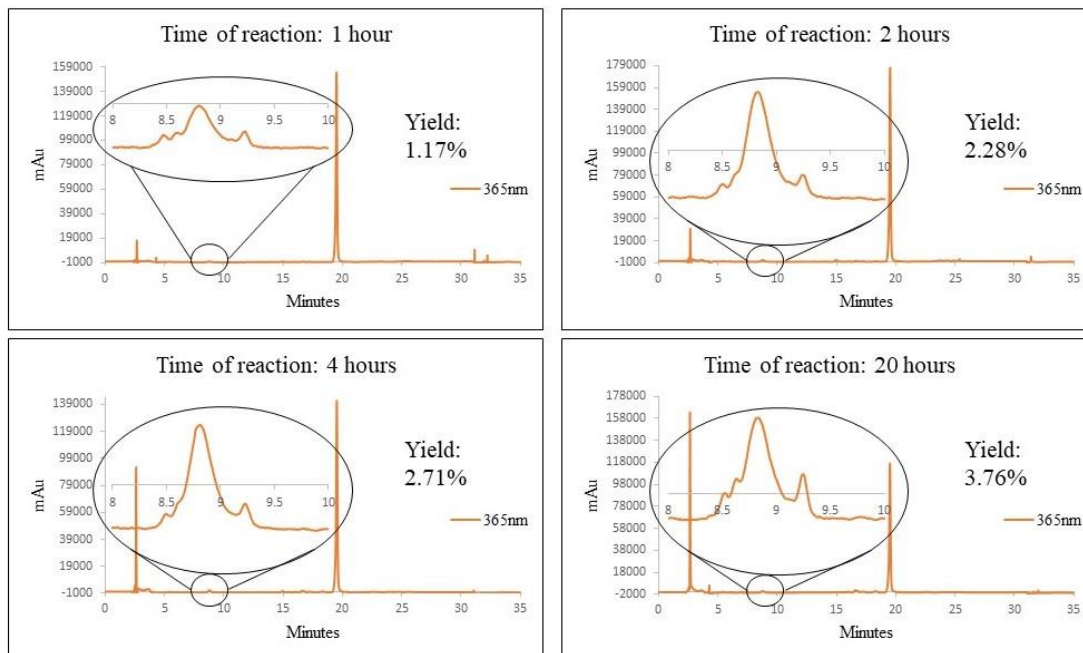


Figure 4.17 HPLC traces of the reaction of click chemistry between Py₃But nanosheets and DNA-1, at different reaction times.

The reaction, after 20 hours, shows a yield of 3.76%. Also in this case, a plot of the yield (% Reacted) as a function of the time of reaction (hours) was made (**Figure 4.18**).

The yields of the reactions are very low. After 1 hour, only the 1.17% of Py₃But has reacted with DNA-1, whereas after 2 hours the yield doubles and then it increase very slowly until a maximum of 3.76% after 20 hours.

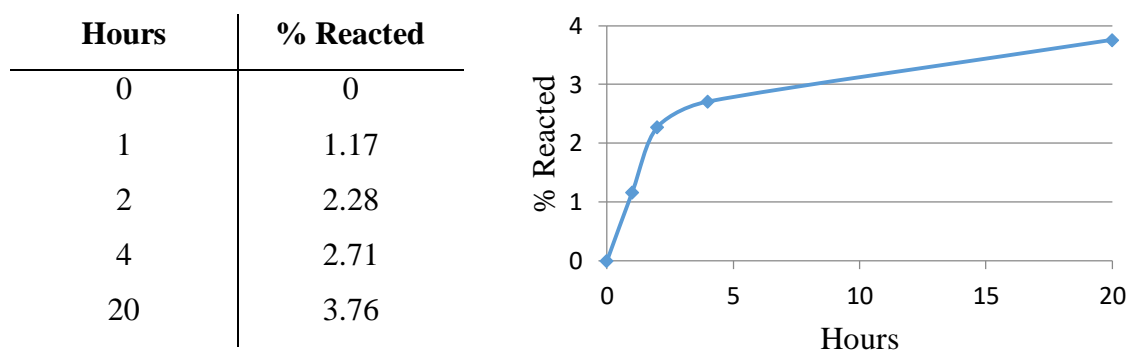


Figure 4.18 Plot of the yield (% Reacted) as a function of the reaction time (minutes), of Py₃But (after nanosheets aggregation) and DNA-1.

These lower values can be justified using the same consideration made with the case of the dye. The only difference is that DNA strand is a longer structure: in fact, when a first

DNA strand is linked to the sheet, it can hamper the reaction between a nearby butynyl moiety and another DNA strand.

So, in summary, when the reaction starts all butynyl are accessible. The first DNA strands, which bind, due to the flexibility of the chain, can “cover” the near butynyl groups. Because DNA-1 is longer than the dye, it is possible that more butynyls are “covered” by a single oligomer strand, leading to a very low reaction yields.

Despite the low percentage of the DNA-1 linked to the nanosheet, this reaction was used for the next step with AuNP linked to a complementary DNA strand (DNA-2).

4 Py₃But LINKING TO DNA-AuNP

As already depicted above, Py₃But was used for two different approaches, both of them based on the use of gold nanoparticles (AuNP). The DNA strands, used in this section, are commercially available.

In one case, a 3' azide modified DNA (DNA-1) single strand is bound to Py₃But via click reaction, after sheets formation, while a complementary 3' thiol modified DNA single strand (DNA-2) is linked to AuNP (**Scheme 4.1**). The purpose is to link AuNP to the sheets using the DNA base pairing.

The synthesis of AuNP was made following the procedure published by Liu *et al.*¹¹³ (see experimental section).

In here, the procedure leads to formation of nanoparticles with a size of ~5nm, stabilized by bis(*p*-sulfonato-phenyl)phenylphosphine dehydrate dipotassium salt (BSPP).

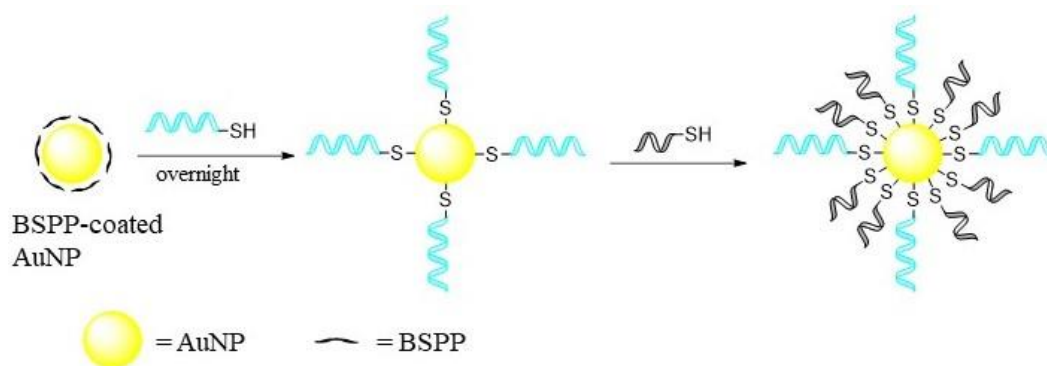
The latter solution was used for preparing a mixture AuNP-DNA-2 in a ratio 1:17, respectively.




Very simply, an aliquot of AuNP-BSPP solution was diluted with a solution of DNA-2, in the right amount for obtaining the desired ratio.

The two were shaken overnight at room temperature. Then, the solution was purified by centrifugation and the precipitate was redissolved in a solution containing the DNA-3, in a concentration 100 times more than DNA-2. This last step was made in order to cover entirely AuNP surface.

The DNA-1 sequence was used for click reaction with Py₃But after nanosheets formation.

Also this experiment was made with the use of KSH.



DNA sequence (5'-3')	
 (DNA-1)	CAA GGT CCG ATG CAA GGA AG-N ₃
 (DNA-2)	GTT CCA GGC TAC GTT CCT TGT TTT TT-SH
 (DNA-3)	TTT TTT-SH

Scheme 4.1 Schematic representation of DNA-2 coated AuNP. The sequence DNA-2 was dissolved in solution with DNA-BSPP in a concentration 17 times more. The DNA-1 sequence was linked to Py₃But via click chemistry.

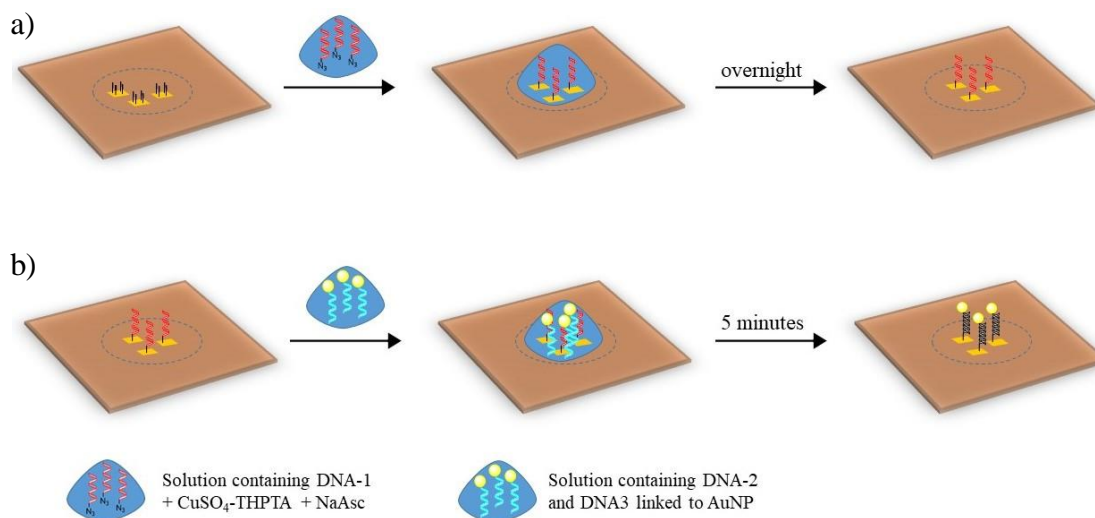
As already described in the previous sections, the aggregation of Py₃But (1 μM) was made in aqueous medium, cooling the solution from 75°C to 20°C, with 0.5°C/min as temperature gradient. The nanostructures (nanosheets) obtained were observed at AFM, using KSH.

After that the sheets were found at AFM, 1 mL of a solution containing the reagents for click chemistry was prepared (DNA-1 = 10 μM, CuSO₄-THPTA (1:5) = 20 μM and 100 μM, respectively and NaAsc = 1 mM).

An aliquot (~30 μL) of this solution was poured on mica, covering the area where sheets were deposited, leaving it overnight (**Scheme 4.2a**).

Then, the mica was washed with MilliQ water and dried with Argon. Then, another solution (~30 μL), containing AuNP linked to DNA-2 and DNA-3, was poured on the same area on mica surface for 5 minutes, in order to induce the base pairing between the two DNA complementary strands (**Scheme 4.2b**).

The amount of AuNP used is the 1% compared to the concentration of DNA-1.



Scheme 4.2 Schematic representation of click reaction on sheets (a): the solution with all reagents for click chemistry was left overnight. Then (b), a solution with 1% of AuNP (compared to DNA-1 concentration) is left for 5 minutes, in order to allow the base pairing between the two complementary strands.

Then, AFM was used to observe a potential change of the sheets found before the click reaction, as a result of the base pairing step (**Figure 4.19**).

Unfortunately, it was not so clear if the two DNA strands coupled according to base pairing, since AuNP covered all mica surface.

In fact, in **Figure 4.19a**, it is showed the first analysis, when the nanostructure was observed at AFM. In here, the surface of mica is flat, showing the classical sheet with a smooth surface.

Whereas, in **Figure 4.19b**, it is possible to note a different situation. At a first looking, the shape of the nanosheet is not changed, just as the height, which remains more or less similar. What changes, instead, is the surface of the nanostructure, because the cross section is very rough. Surprisingly, mica surface has almost the same height of the sheet, with a cross section very uneven. This gives the idea, that AuNP linked to DNAs covered the surface.

Since the concentration of DNA-1 is 10 times more than that of Py₃But, the phosphate groups of the oligomer can link to the positively charged APTES-modified mica surface. While, the click chemistry reaction, between them, leads to a maximum of the 3.76%, as yield, probably, when the AuNP are added, DNA-2 can couple with DNA-1 both on mica and the sheet surface, via base-pairing. The result is the situation showed in **Figure 4.19**.

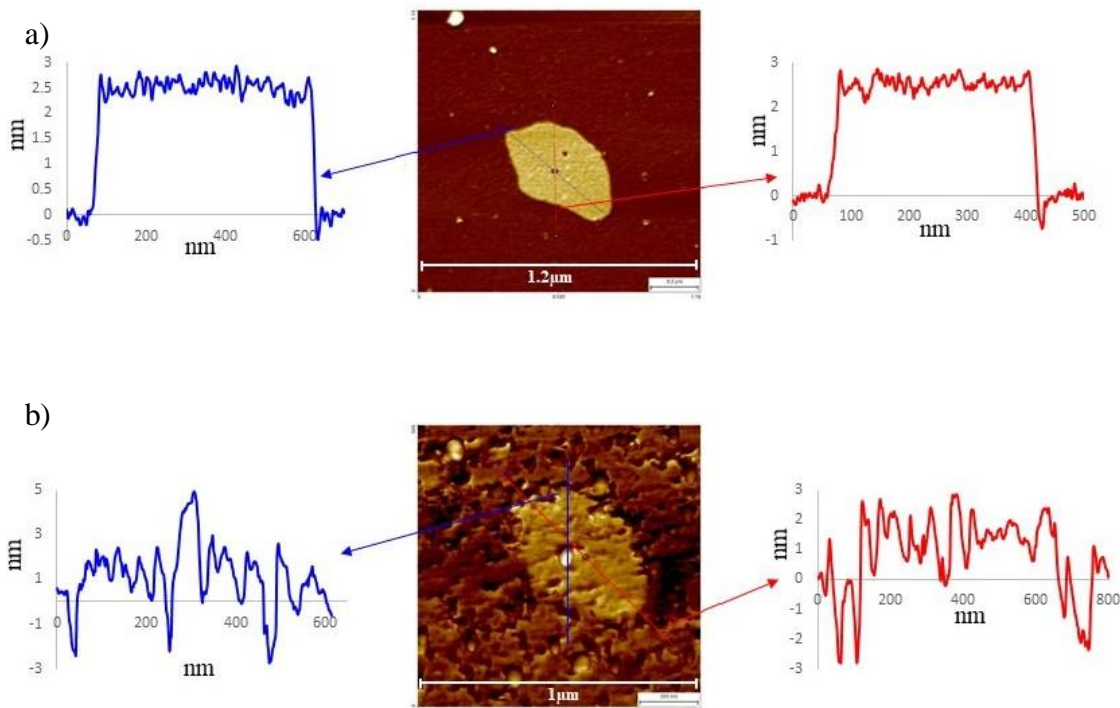


Figure 4.19 AFM pictures of Py₃But sheet (a) and the same sheet after the click reaction of DNA-1 and subsequent base pairing with the complementary DNA-2 strand linked to AuNP.

In any case, because the situation is not so clear, it is impossible to judge the success of the experiment.

Finally, a last experiment, made as control, used the same nucleotides sequence of DNA-1 but with no azide group (DNA-0).

The purpose was to avoid the bond of DNA-0 strand on nanosheets, in this way there was no base pairing with DNA-2 linked to AuNP.

The experiment was made in the same manner of the previous one: Py₃But nanosheets were observed at AFM with the use of KSH. Also in this case, a solution containing DNA-0 (without azide), with a concentration 10 times more than the one used for Py₃But, and the reagents for click chemistry was deposited on mica, overnight.

Then, the solution with 1% of AuNP covered by DNA-2 and DNA-3 was poured on the same area where the sheets were present, for 5 minutes, and analyzed at AFM. Looking at **Figure 4.20**, also in this case mica surface looks quite rough. Even though the sheet surface seems smooth, but the picture does not give enough details to make a right conclusion.

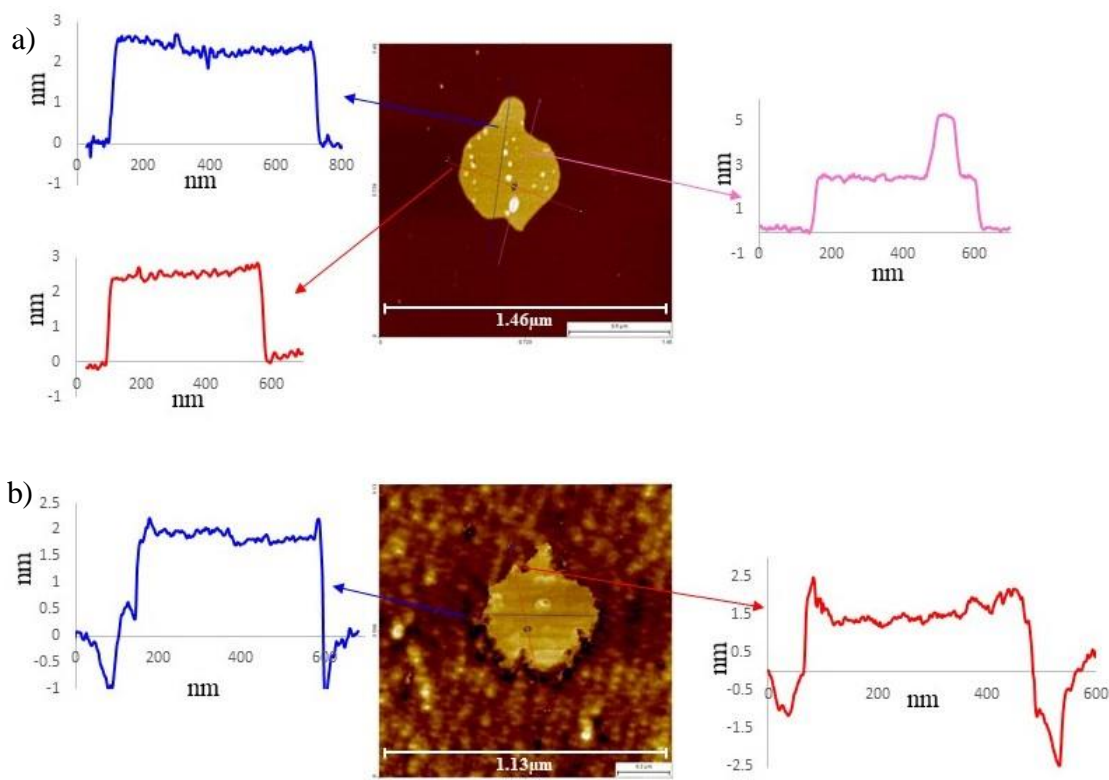


Figure 4.20 AFM pictures of Py₃But sheet (a) and the same sheet after the deposition of a solution containing DNA-0 and subsequent base pairing with the complementary DNA-2 strand linked to AuNP.

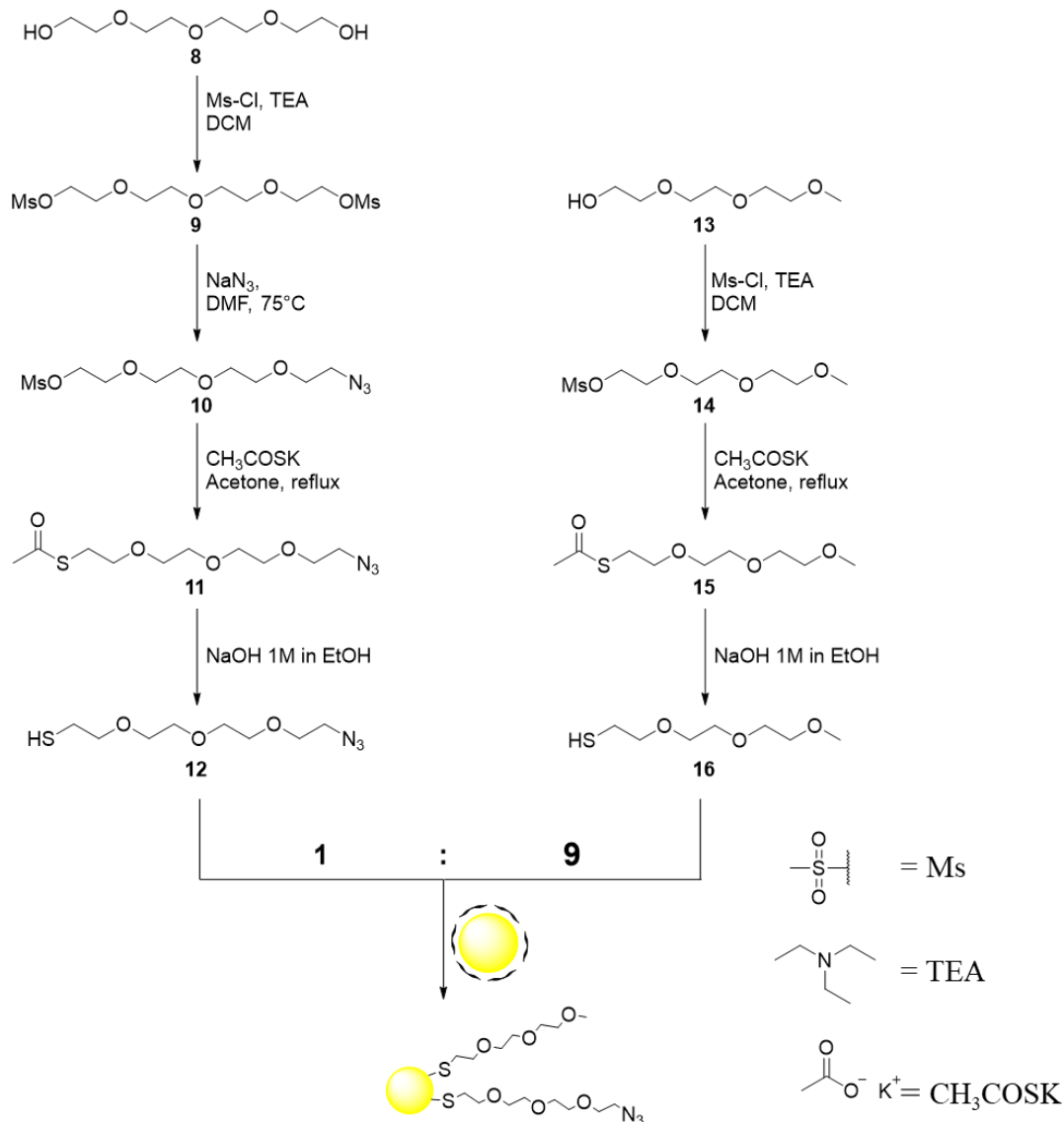
Also in this case, it is possible to think that in the first step of the experiment, DNA-0 can link to the APTES-mica, when its solution (with the reagents for click chemistry) is poured on the same area of the nanosheets. In the second step, AuNP-DNA-2 solution is deposited, in order to let the two DNA strands couple via base pairing.

Because of the link between the two oligomers, AuNP stay on mica surface (appearing pretty rough), while the sheet seems to still keep a smooth cross section.

Unfortunately, the fact that gold nanoparticles are found on the mica surface makes pretty hard to give an idea about the success of the experiment. This because, even though in the second experiment the surface of the sheet is still smooth, there are a lot of AuNP on mica. This does not exclude that they can also deposit on the nanosheets.

5 Py₃But LINKING TO PEG-AUNP

In this last set of experiments, AuNP are linked to a mixture of polyethylene glycols derivative (**Scheme 4.3**).



Scheme 4.3 Schematic representation of procedures for synthesis of **12** and **16**. The two molecules, in the end, were mixed in a ratio of 1:9, using, in terms of concentration, the 3% of AuNP (synthesized in the same way as explained in the previous section). For practical reason only two molecules are linked to AuNP, but the reader can imagine a totally covered surface.

In this way, it was thought that the link between the DNA strands and the APTES-modified mica could be avoided.

As starting materials, two polyethylene glycol (PEG) derivatives were used: in particular, tetraethylene glycol (**8**) and triethylene glycol methyl ether (**13**).

In the case of **8**, the two external hydroxyl groups were substituted with an azide and a thiol group, with formation of **12**.

While, regarding **13**, the only OH present in the molecule was converted in a thiol function. The synthetic procedure was based on the ref.¹¹⁴ with the only difference that in this case OHs were coupled to a mesyl (Ms), in the first step of the syntheses.

Briefly: the two OHs, in **8**, were converted in mesylate, since it is a better leaving group, obtaining **9**. Then, the reaction with 1 equivalent of sodium azide leads to **10**. The other mesylate function is substituted with a thioacetate (using potassium thioacetate, CH₃COSK), with formation of **11**. Finally, the reduction of thioacetate gives the desired product **12**.

The same synthetic steps are made starting from **13**, in order to obtain **16**, but without the step for the addition of azide.

Once the two products were obtained, they were dissolved in a small volume of water obtaining a mixture containing 0.1mM of **12** and 0.9mM of **16**.

To this mixture, 1 μ M of AuNP covered by BSPP (where the preparation is explained in the last section) was added.

This solution was shaken overnight. Then, it was purified via centrifugation, the precipitate was redissolved in water and the concentration checked at 520nm,¹¹³ obtaining AuNP covered by PEG derivatives.

For the experiment, also in this case, KSH was used; the sheets with Py₃But were formed in aqueous medium, cooling down the solution at 0.5°C/min.

Then, click reaction was made in two different reaction times. The reagents and the conditions are the same used in the previous section, but this time AuNP were covered with PEG derivatives (still the 1%).

After the formation of the sheets (**Figure 4.21a**), on the same area, an aliquot of solution, containing all the components, is left for 10 minutes. Then, this solution was washed away, the mica was dried with argon and, then, scanned at AFM (**Figure 4.21b**).

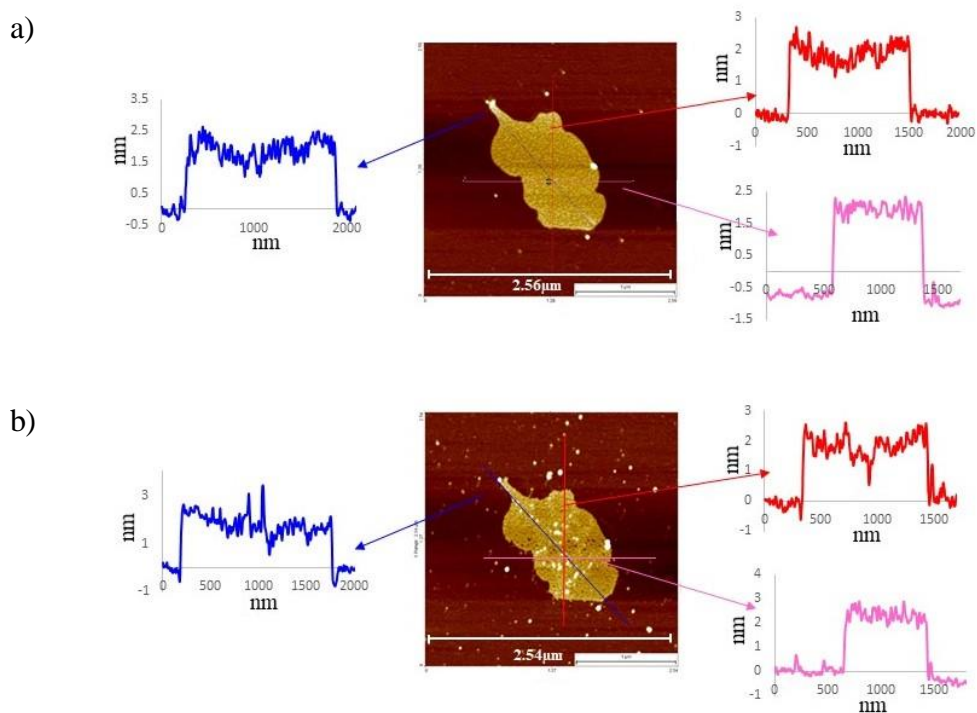


Figure 4.21 AFM pictures of Py₃But sheet (a) and the same sheet after the deposition of a solution containing AuNP covered by PEG derivatives (b), for 10 minutes.

The sheet seems to be covered by some objects but in any case, the same are present on mica surface as well. Moreover, some holes are present on sheet surface, giving the idea that something was linked to the sheet and the washing phase, of the drop of solution (containing AuNP and click chemistry reagents), took off pieces of the nanostructure.

A further experiment was made with a prolonged reaction time: 30 minutes (**Figure 4.22**). As usual, after the formation of sheets (**Figure 4.22a**) and the cross section measurement, a drop with AuNP and click chemistry reagents is left on mica for 30 minutes (**Figure 4.22b**).

In here, the situation seems to be even worse, because mica surface is covered by many more particles, just as the sheet. In fact, the cross sections of the sheet has a rougher trend, with the same height.

The fact that the surface of the sheet is rough gives no conclusions about a link, via click chemistry, with the azide group of the PEG derivative, because the height of the nanostructure does not increase.

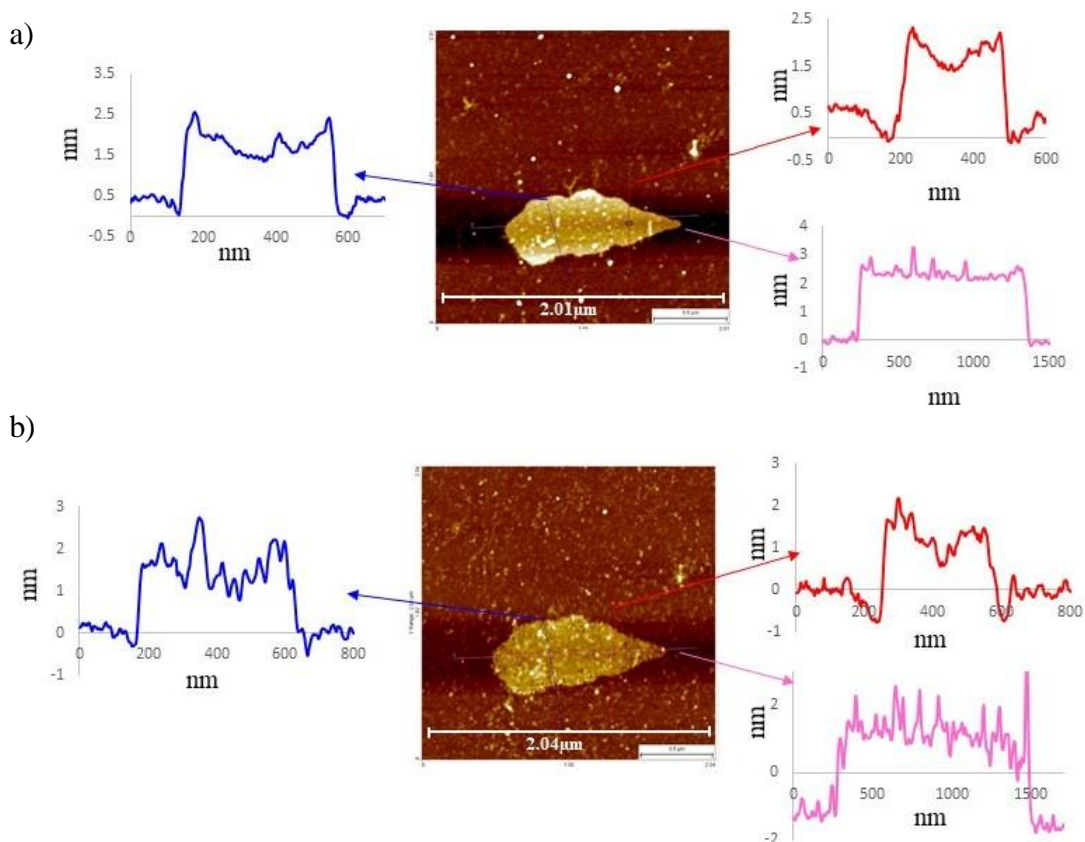


Figure 4.22 AFM pictures of Py₃But sheet (a) and the same sheet after the deposition of a solution containing AuNP covered by PEG derivatives (b), for 30 minutes.

About the presence of the AuNP on mica surface, they can link to the APTES-modified mica.¹¹⁵ This makes more complicated any kind of analysis at AFM of gold nanoparticles, with the use of APTES-modified mica.

As already described, the modification of mica, in order to have a positive charged surface, is essential to allow the bond with this type of supramolecular structures.

Also here, a sort of experimental control was made (**Figure 4.23**), using gold nanoparticles covered by only PEG derivative without azide (**16**).

This AuNP, linked to **16**, was obtained in the same way described above for the particles with azide. In this case a solution of 1 mM of **16** was prepared, 1 μM of AuNP covered by BSPP was added.

After the formation of Py₃But nanosheets and their observation at AFM, with the use of KSH (**Figure 4.23a**), a solution containing AuNP covered by **16** and the reagent for click chemistry was deposited on mica, for 30 minutes (**Figure 4.23b**). The amounts used were the same of those described above.

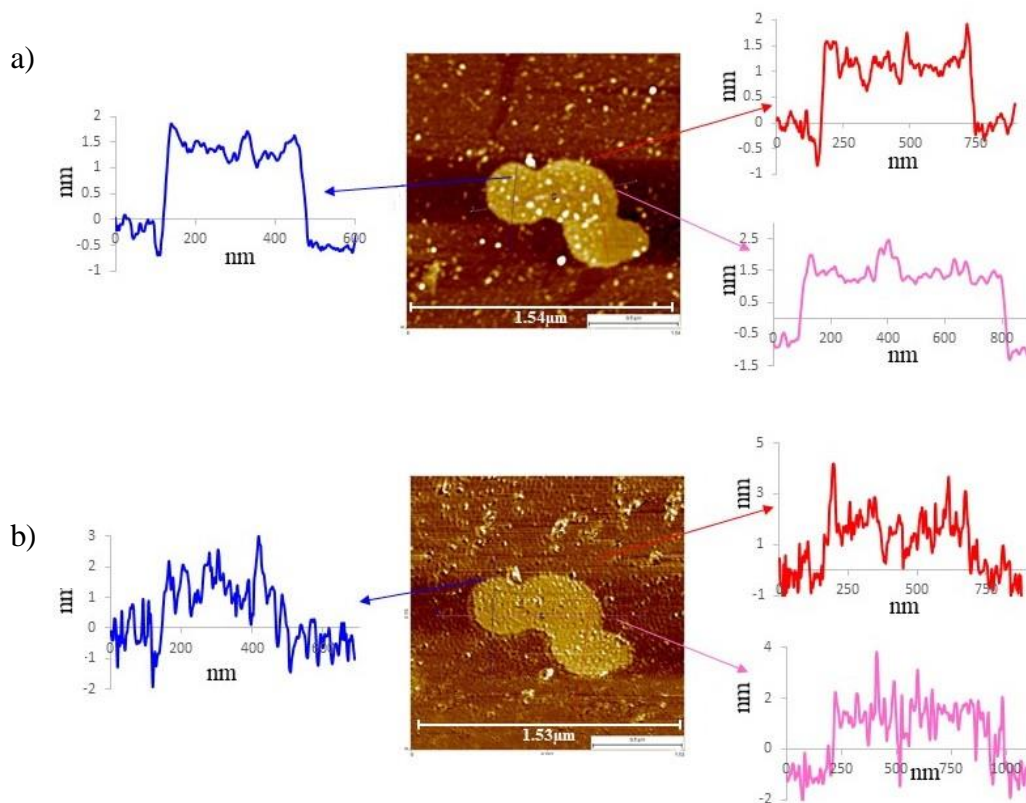


Figure 4.23 AFM pictures of Py₃But sheet (a) and the same sheet after the deposition of a solution containing AuNP covered by PEG derivative (**16**) without azide (b), for 30 minutes.

Also in this case, the situation is not so easy to be described. In fact, AuNP cover again both mica and sheets. Also here the surface of the sheet becomes rougher, after the treatment.

The fact that AuNP were completely covered by PEG derivatives gave the illusion that their bond with mica surface could be avoided. This did not happen and the only thing sure is the limit of AFM for this kind of structure and conditions.

In conclusion, also in this case, it is not possible to evaluate the bond between the PEG derivative, bearing an azide and linked to AuNP, via click chemistry.

Indeed, since they bind to mica surface, it is hard to understand whether or not the butynyl function on Py₃But reacts with the azide.

Furthermore, the size of the sheets, showed in this section, does not increase. This is due probably to the fact that since the AuNP cover everything, they form a new layer on mica surface and the AFM instrument is not able to reveal the difference.

6 USE OF TEM FOR Py₃But LINKED TO PEG-AUNP

Because the limitation of the analysis made with AFM, due to the bond of AuNP to the mica surface, another try was made with TEM.

The analysis made with Transmission Electron Microscopy (TEM) was made using a copper grid covered by a holey carbon film.

After the formation of Py₃But nanosheets as described above, a small aliquot (5 μ L) of the nanosheets was poured on the grid for 5 minutes. Then, the drop was blotted with filter paper, in order to remove surface water.

After that, 5 μ L of an aqueous solution of uranyl acetate (0.8%) was deposited on the grid for 30 seconds and, then, the water was removed with filter paper and, finally, analyzed at TEM (**Figure 4.24**).

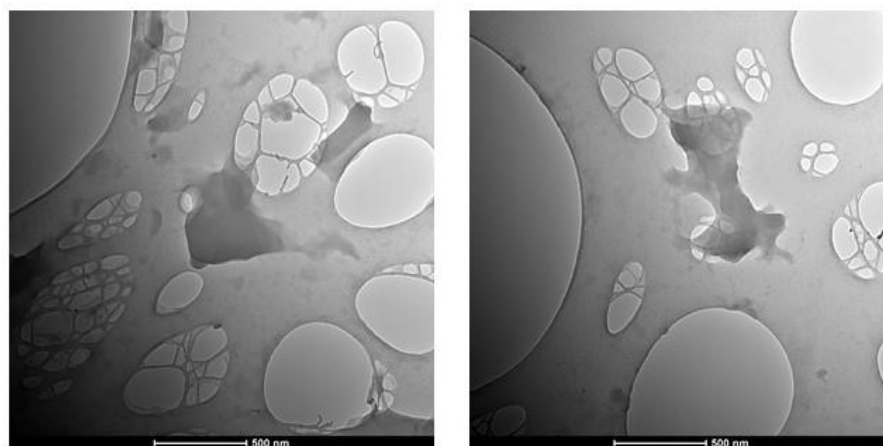


Figure 4.24 TEM pictures of Py₃But nanosheets after the solution (10mM sodium phosphate buffer pH = 7.2) was cooled at 0.5°C/min, from 75°C to 20°C.

The uranyl acetate was used to stain the sheets in order to make them darker and be better visible for the analysis.

In any case, the sheets found have the same size of those found at AFM. Unfortunately, the TEM did not allow to measure the height of the structures.

Since in this kind of analysis there is no way to measure a same position when the grid is removed from the instrument (with AFM this was possible with the use of the Kinematic

Sample Holder), the click reaction is made in solution after the formation of the nanostructures.

The nanosheets were formed in the same way described above. Then a solution containing the reagents for click chemistry (with the same amounts described in the previous section) and the 3% AuNP covered by **12** and **16** (compared to the concentration of Py₃But) were added.

The reaction was left at ambient temperature for 30 minutes and, then, also in this case, 5 μL were poured on the grid, for about 5 minutes. After that, the solution was bottled with filter paper and analyzed at TEM (**Figure 4.25**).

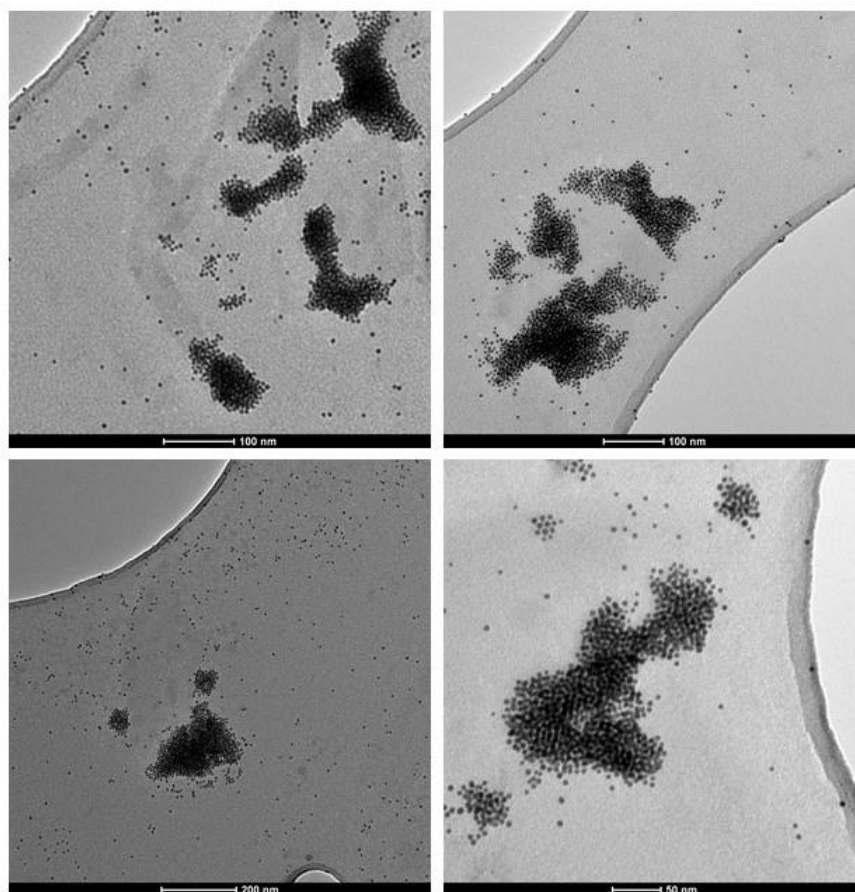


Figure 4.25 Different TEM pictures of Py₃But nanosheets and AuNP covered by **12** and **16**, after they have reacted for 30 minutes, in click reaction conditions. The size is maximum 200nm.

In this step, uranyl acetate was not used, because AuNP were visible at TEM, appearing as black dots. It is possible to note some AuNP, seems to aggregate in a specific shape, staying close to each other, while others are spread randomly on the grid. In some case, for example the image on top left in **Figure 4.25**, some structures seem to be not covered

by AuNP: they are showed as areas a bit darker than the background. This gives the idea than some supramolecular structure are not fully linked to gold nanoparticles.

Finally, the size of the (covered) sheets seems to be smaller than that found at AFM. This can due to the fact that the reaction was made in solution, and not for deposition after the sheets formation on the grid. Probably, in this way the sheets could be just ripped up in smaller structures.

The last experiment was made with AuNP covered only by PEG derivative without azide, **16** (Figure 4.26).

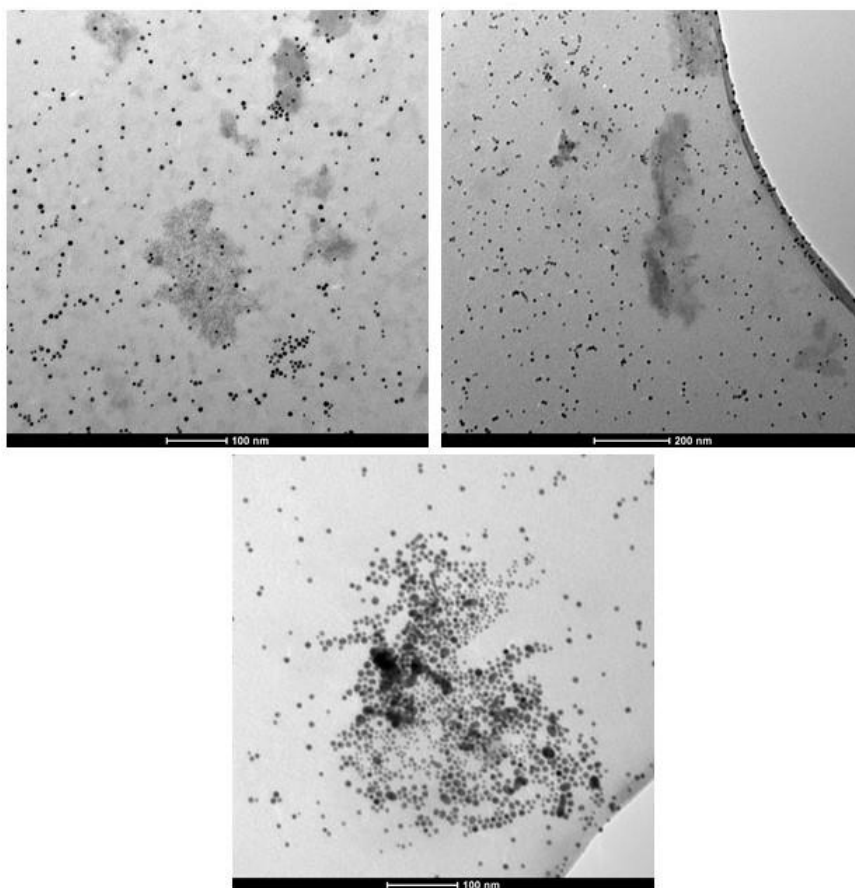


Figure 4.26 Different TEM pictures of Py₃But nanosheets and AuNP covered by only **16**, after they were left in solution for 30 minutes, in click reaction conditions.

In here, AuNPs were found spread quite often in different part of the grid, where in the same area some sheets were present (dark grey colored part).

In any case, a situation where gold nanoparticles appeared grouped was found, but differently from the experiment with the azide, in here the population of AuNPs seems to

be smaller. The experiment made with TEM showed a different situation compared the one measured with AFM.

The only difference is the execution of the experiment: in fact, in the case with AFM, thanks to the use of the Kinematic Sample Holder, there is first the deposition of the sheets on mica. Then, after the analysis, a drop containing AuNPs linked to azide (or without azide, in the case of the control) and the solution with the reagents for click chemistry is poured on the same area where these nanostructures were found.

The situation was not clear because of the “affinity” of AuNPs with APTES-modified mica, which cover everything, making impossible to judge if PEG derivatives linked to butynyl moieties, via click chemistry.

On the other hand, for TEM, after the formation of the nanosheets, AuNPs were linked to PEG derivatives with the azide in solution, and then everything was poured on the grid.

TEM analysis showed a clearer situation: the gold nanoparticles, after the click reaction, were grouped in a shape, which reminds that of the nanosheets. As already described above, the size was different, but this can be associated to the fact that in solution, the presence of gold nanoparticles ripped the sheets.

The situation is different when AuNPs without azide are used. They are spread on the surface of the grid, and when some of them are grouped, their population seems to be smaller than the one observed for the case of AuNP with azide.

In conclusion, after that the formation of functionalized sheets was obtained (as described in chapter 3), the next step was to use the functionalization for the selective bonds.

In the case of Py₃Man, mannose moiety had to selectively link to Con A. Unfortunately, the protein entirely covered both the mica surface and nanosheets on it, making impossible to conclude if mannose linked to Con A.

Probably, the reason why Con A covered the mica surface was due to the fact that the side chains of aspartic and glutamic acid residues were deprotonated at the pH of the solution where the protein was stored (the stock solution at pH 7.2).

Since, the surface of mica was positively charged, because it was modified with APTES, the deposition was due to the attraction between the negative charges in aspartate and glutamate and the positive charge on APTES-modified mica surface.

Maybe there was a link between the mannose moiety and Con A as well, but unfortunately, it was not possible to proving it.

In the case of Py₃But, the functionalized sheets were used for two approaches: in the first one, they were linked to a DNA strand bearing an azide (DNA-1) via click chemistry.

Then, a second DNA strand (DNA-2) linked to AuNP, was coupled to DNA-1 by base pairing. The measurement at AFM showed that AuNP covered entirely the mica surface. In here, probably, DNA-1 can link to mica surface in the same way of the pyrene trimers (due to the presence of phosphate groups). Considering it was used 10 times more than Py₃But, it could be that part of the DNA-1 could have reacted with the butynyl via click chemistry, but the others just linked to the mica surface.

In this way, DNA-2 linked to AuNP coupled, via base pairing, to the complementary strand both on mica and sheets surface, making impossible to describe the result of the experiment.

There is also a possibility that AuNP linked to the mica surface, as showed in the second approach. In this case AuNP were linked to a PEG derivative bearing an azide (**12**). Also in this case AuNP covered the entire mica surface, and no conclusion could be made.

A last experiment was made with TEM, where, first, the Py₃But nanosheet were made and then, in the same solution, AuNP linked to **12** were added.

In this case, it was possible to note that gold nanoparticles aggregated in a shape similar to the sheets.

The control experiment, using AuNP linked to PEG derivatives without azide (**16**), showed the presence of a lot of AuNP spread around the grid. On the same area some nanosheets were present too.

In other area there were the formation of a group of AuNP, but the amount of nanoparticles were smaller than the one found in the case with PEG bearing the azide.

CHAPTER 5

CONCLUSIONS AND OUTLOOK

The synthesis of functionalized pyrene-trimer, able to self-assemble in a nanosheet motif, has been described. The role of mannose was to bind selectively to a Con A, while the butynyl was linked to structures bearing an azide, via click chemistry.

In chapter 3, the aggregation of Py₃Man and Py₃But was followed by UV/vis analyses, while AFM showed that these structures aggregated with the formation of nanosheets. In here, the behavior of Py₃Man was compared with the Py₃ (already studied in our group) and Py₃Phos.

From UV/vis analyses, it was found that the functionalized pyrene-trimers showed a lower aggregation temperature than Py₃. Probably this is due to the presence of an additional phosphate group, in Py₃Man, Py₃Phos and Py₃But, which increases the number of the negative charges. In water, the aggregation of the pyrene unities is driven by the hydrophobic effect. The additional negative charges repulse each other when two molecules approach and this effect can hamper the initial nuclei formation at higher temperatures. Furthermore, another difference, due to the presence of this additional phosphate, in the functionalized structures, is the presence of the hysteresis. The latter is due to a large kinetic barrier during the assembly/disassembly process.

In chapter 4, the purpose of the functionalization was described. The mannose moiety, in Py₃Man, was used as bonding site for the Con A, which has a high affinity with this sugar. After the study of the Py₃Man nanosheets at AFM, Con A was added in order to be linked to the mannose, which is supposed to stay on the nanosheets surface.

Unfortunately, Con A binds on mica surface covering everything (sheets included), making impossible to judge the success of the experiment. Probably, this was due to the presence of aspartic and glutamic acid (in the amino acid sequence of the protein), which have the side chains deprotonated because at the pH (7.2) of the stock solution of Con A.

Since the mica, used for AFM analyses, was APTES-modified and, so, the surface was positively charged, the protein linked on the surface.

The butynyl group, in Py₃But, was used in the two approaches based on the use of the click chemistry.

A set of experiment, in order to have an idea about the conditions for the reaction, was first made. In here after the formation of Py₃But nanosheets, a dye bearing an azide was added to the solution, with the click reagents. The reaction was made at different reaction times and checked at HPLC. A similar experiment was made with a DNA-1 strand, which bore an azide group. In both cases, there was not a complete reaction of the butynyl group on the nanosheets surface. This was due, probably, to the fact that the structures with the azide, after the click reaction, covered the butynyl groups nearby, hampering their reaction with other azide groups. The fact that DNA-1 strand showed lower percentage of the reaction with nanosheets was due to its bigger size, which covered a larger area of the sheets where it was linked on.

In any case, the first approach was studied at AFM: after the formation of the nanosheets, a solution containing DNA-1 and the reagents for the click chemistry was added. This strand, which bore an azide group, was linked to the butynyl via click chemistry. Then, a solution of complementary DNA-2 strand, bound to AuNP, was hybridized via base pairing. The AFM analysis showed that the AuNP covered the mica surface. Probably, their presence was due to the fact that DNA-1 linked on mica surface, because of the phosphate groups in the nucleic acid sequence. So the base pairing occurred with DNA-1 strand bound both to the mica and on the sheets surface. It can also be that AuNP are able to link to the mica, as showed in the second approach. In any case, it was not possible to explain the result of the experiment.

In the second approach, after the formation of Py₃But nanosheets a solution with PEG derivative bearing an azide, and reagent for click chemistry, was added. The study at AFM showed, also in this case, the mica surface was completely covered by AuNP, making impossible to understand if the approach worked.

A last experiment was made with use of TEM. After the formation of the sheets, AuNP linked to PEG derivative bearing an azide, with reagents for click chemistry were added in the solution with the aggregated Py₃But. At TEM, the AuNP were found aggregated in

a shape that reminded the nanosheets. Some other AuNP were found spread around these aggregated nanoparticles.

In a similar experiment, PEG derivatives linked to AuNP, but without the azide were used. The conditions were the same described above. In this case, AuNP were mostly spread on the surface of the grid and in the same area, there was also the presence of nanosheets. Moreover, some aggregated AuNP were found but the population of these nanoparticles was smaller.

The use of TEM showed that the azide in PEG derivatives reacted with the butynyl on the nanosheets surface, leading to a situation where the aggregated supramolecular structures were covered by AuNP.

In conclusion, AFM was not the best instrument to analyze the role of the functionalizations. In fact, both Con A than AuNP linked to the mica surface.

A way to solve the problem of the experiments made with Py₃Man and Con A, in order to avoid the absorption on the mica surface, could be to change the pH between 4.5 and 5.5. At this pH value, Con A is in a dimeric form (as described in chapter 4), but the side chains of aspartic and glutamic acid are still protonated and maybe they do not bind to the surface of mica.

Finally, TEM can be used also to analyze Py₃But linked to DNA strands. In this case, after the formation of the sheets, DNA-1 and click reagents are added to the solution for the click chemistry reaction. Then, the unreacted DNA-1 can be separated by those linked to the sheets by dialysis. In this way, a solution with only DNA-1 linked to nanosheets is present. After that, the DNA-2 linked to AuNP can be hybridized to DNA-1 strands, which are bound to the Py₃But nanosheets.

CHAPTER 6

EXPERIMENTAL SECTION

Abbreviations

ACN	Acetonitrile
APTES	(3-Aminopropyl)triethoxysilane
DCM	Dichloromethane
DIPEA	N,N-diisopropylethylamine
DMAP	4-dimethylaminopyridine
DMF	Dimethylformamide
EtOAc	Ethyl acetate
EtOH	Ethanol
Hex	Hexane
LCAA-CPG	Long chain alkylamine controlled pore glass
MeOH	Methanol
Na ₂ SO ₄	Sodium sulfate
TEA	Triethylamine
THF	Tetrahydrofuran

MATERIALS

All chemical reagents and solvents were purchased from Aldrich and TCI, the CPG solid support from LCG Genomics and DNA strands from Microsynth.

For AFM analysis, the mica plates were purchased from Plano GmbH. The holey carbon film on 300 Mesh Copper Grid, used for TEM, from Agar Scientific.

UV/VIS MEASUREMENTS

UV/vis spectra were collected using Varian Cary-100 Bio-UV/vis spectrophotometer equipped with a Varian Cary-block temperature controller. The temperature from 75°C was cooled down to 20°C in ~7 minutes. Heating/cooling cycles were recorded with 0.1°C/min and 0.5°C/min.

For the analyses, quartz cuvettes, with an optical path length of 1cm were used.

ATOMIC FORCE MICROSCOPY (AFM) MEASUREMENTS

AFM images were acquired with a Nanosurf FlexAFM using Tap190Al-G cantilevers from BudgetSensors (resonance frequency \approx 190 kHz, force constant = 48 N/m).

They were recorded at rt in air in tapping mode.

Mica (1cm x 1cm) used for analysis was modified with APTES according to procedure:¹⁰³ in order to “clean” mica sheets, a layer was removed with scotch tape. Then, they were fixed on the top of a desiccator with the tape.

The desiccator was purged with argon for 20 minutes. After that, two plastic caps were used: one was filled with 30 μ L of APTES and the other one with 10 μ L of DIPEA.

The desiccator was closed and the chemicals were allowed to evaporate overnight. Then, the two caps were removed and the desiccator was again purged with argon for 20 minutes.

Mica sheets were ready to be used. On their surface, 30 μ L of sample solution were poured for the necessary time required by the analysis. After that, the drop was washed away with 1mL of MilliQ water and dried with argon.

TRANSMISSION ELECTRON MICROSCOPY (TEM) MEASUREMENTS

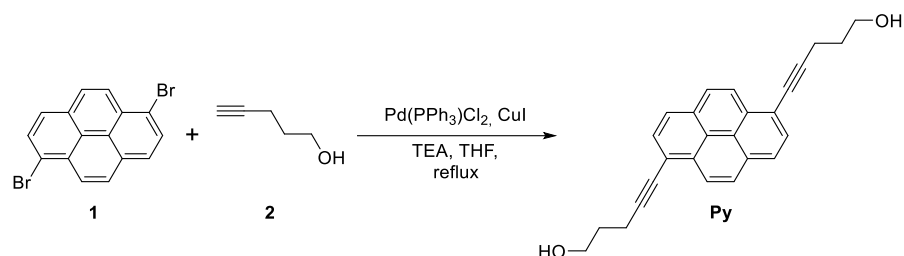
TEM images were acquired on a FEI Tecnai Spirit device, using an operating voltage of 80kV. The samples were analyzed by depositing 5 μ L of the solution on a holey carbon film on 300 Mesh Copper Grid, for 5 minutes. After that, the solution was blotted with filter paper. Then, a washing step was made twice: 5 μ L of MilliQ water were poured on the grid for 30 seconds and then removed with filter paper.

In one case (when click chemistry was not made), 5 μ L of an aqueous solution of 0.8% of uranyl acetate was poured on the grid for 30 seconds and, then, washed.

SYNTHETIC STEPS

All synthetic steps regarding pyrene are taken from⁹³

Synthesis of Py

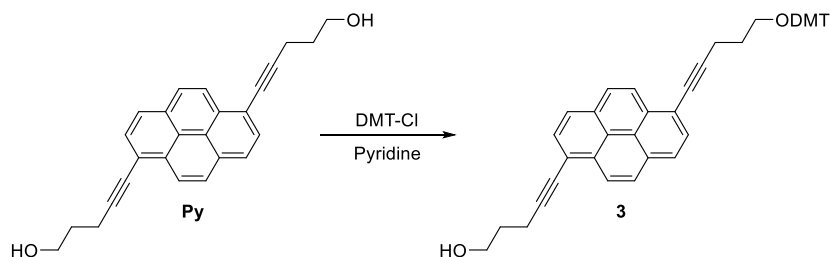


The commercially available 1,6-dibromopyrene (**1**) (500 mg, 1.387 mmol), bis(triphenylphosphine) palladium(II)chloride (24 mg, 0.035 mmol, 0.025 eq) and copper(I) iodide (4 mg, 0.018 mmol, 0.013 eq) were suspended in THF (13 mL) and refluxed under argon. Then, triethylamine (8 mL) and 4-pentyn-1-ol (**2**) (0.5 mL, 5.548 mmol, 4 eq) were added. The mixture was refluxed and stirred overnight. Then, after having cooled to room temperature, the suspension was filtered through celite, the filtrate was evaporated to dryness, re-dissolved in DCM and washed with brine two times. The organic phase was dried with Na₂SO₄ and purified by column chromatography (DCM/MeOH 97:3), obtaining **Py** as a yellow solid (380 mg, 75%).

The data corresponds to those published in⁹³

¹H NMR (300 MHz, DMSO-*d*₆) δ 8.50 (d, *J* = 9.1 Hz, 2H), 8.29 (d, *J* = 8.5 Hz, 4H), 8.13 (d, *J* = 8.0 Hz, 2H), 4.64 (t, *J* = 5.2 Hz, 2H), 3.66 (q, *J* = 6.2 Hz, 4H), 2.72 (t, *J* = 7.1 Hz, 4H), 1.93 – 1.76 (m, 4H).

Synthesis of 3

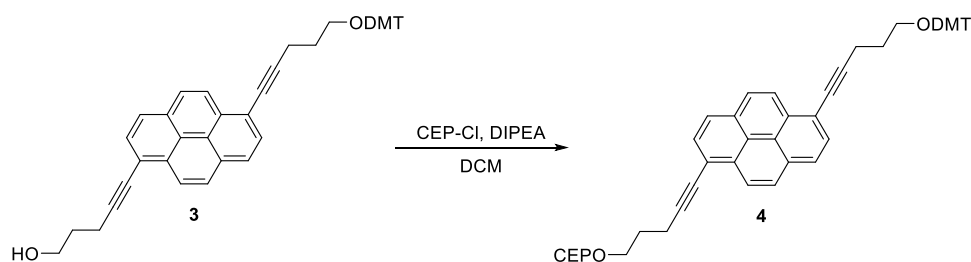


Solid 4,4'-dimethoxytrityl chloride (DMT-Cl) (345 mg, 1.018 mmol, 1 eq) was added to a solution of **Py** (375 mg, 1.023 mmol) in pyridine (7 mL), under argon, and at rt. The mixture was stirred overnight. Then, the solvent was evaporated and the residue was dissolved in DCM and washed with 10% citric acid solution. Then, the organic phase is re-washed with brine, dried with Na₂SO₄, and purified by column chromatography (DCM/MeOH/TEA 97/2/1) obtaining **3** as a yellow foam (292 mg, 43%).

The data corresponds to those published in⁹³

¹H NMR (300 MHz, Chloroform-*d*) δ 8.53 (d, *J* = 9.1 Hz, 1H), 8.44 (d, *J* = 9.1 Hz, 1H), 8.08 (t, *J* = 5.3 Hz, 4H), 8.03 – 7.92 (m, 2H), 7.50 (d, *J* = 7.1 Hz, 2H), 7.38 (d, *J* = 8.9 Hz, 4H), 7.32 – 7.23 (m, 3H), 7.23 – 7.11 (m, 1H), 6.79 (d, *J* = 8.9 Hz, 4H), 3.96 (t, *J* = 6.2 Hz, 2H), 3.67 (s, 6H), 3.37 (t, *J* = 6.1 Hz, 2H), 2.89 – 2.72 (m, 4H), 2.13 – 2.00 (m, 4H).

Synthesis of 4



Compound **3** (292 mg, 0.437 mmol) was dissolved in DCM (12 mL), followed by *N,N*-diisopropylethylamine (DIPEA) (114 μ L, 1.311 mmol, 3 eq) at rt under argon. In a pear-shaped flask, 2-Cyanoethyl *N,N*-diisopropylchlorophosphoramidite (CEP-Cl) (134 mg, 0.568 mmol, 1.3 eq) was dissolved in DCM (3 mL) under argon at rt and the mixture was left under stirring for 15 minutes. Then, the latter was transferred via cannula to the solution with **3**. The mixture was stirred for an additional hour. After that, the solvent was evaporated and the crude was purified by column chromatography (Hex/EtOAc/TEA 50/49/1) obtaining **4** (160 mg, 42%) as a yellow foam.

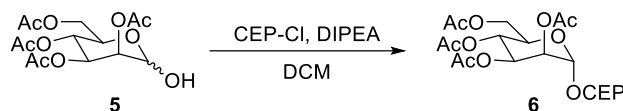
The data corresponds to those published in⁹³

¹H NMR (300 MHz, Chloroform-*d*) δ 8.55 (d, *J* = 9.1 Hz, 1H), 8.44 (d, *J* = 9.0 Hz, 1H), 8.15 – 8.04 (m, 4H), 8.00 (t, *J* = 10.6, 8.5 Hz, 2H), 7.50 (d, *J* = 7.1 Hz, 2H), 7.38 (d, *J* =

8.9 Hz, 4H), 7.27 (d, $J = 1.7$ Hz, 3H), 7.23 – 7.13 (m, 1H), 6.79 (d, $J = 8.9$ Hz, 4H), 4.05 – 3.79 (m, 4H), 3.67 (s and m, 8H), 3.36 (t, $J = 6.1$ Hz, 2H), 2.88 – 2.72 (m, 4H), 2.65 (t, $J = 6.5$ Hz, 2H), 2.14 – 1.97 (m, 4H), 1.25 – 1.18 (m, 12H).

^{31}P NMR (121 MHz, Chloroform-*d*) δ 147.84.

Synthesis of 6



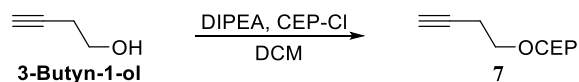
The commercially available **5** (500 mg, 1.435 mmol) was dissolved in anhydrous DCM (2 mL) with DIPEA (0.375 mL, 2.153 mmol, 1.5 eq). Then, CEP-Cl (408 mg, 1.722 mmol, 1.2 eq) was added and the reaction mixture was stirred for 30 minutes at rt under argon. The crude product was directly purified by column chromatography, using a mixture of Hex/EtOAc/TEA (50/50/1) as eluent. The fractions containing the product were combined and the solvents were removed on a rotary evaporator to give the product **6** (0.76 g = 1.39 mmol, 96% yield) as a colorless syrup. $R_f = 0.71$ (Hex/EtOAc/TEA 50/49/1).

^1H NMR (Chloroform-*d*, 300 MHz): δ (ppm) 5.39 – 5.34 (m, 1H), 5.33 – 5.28 (m, 1H), 5.28 – 5.20 (m, 1H), 5.19 – 5.01 (m, 1H), 4.29 (td, $J=12.4, 4.9$ Hz, 1H), 4.21 – 4.05 (m, 2H), 3.95 – 3.77 (m, 2H), 3.77 – 3.44 (m, 2H), 2.66 (td, $J=6.3, 3.8$ Hz, 2H), 2.16 (s, 3H), 2.10 – 2.04 (m, 7H), 1.99 (s, 3H), 1.24 – 1.16 (m, 12H).

^{13}C NMR (DMSO-*d*₆, 101 MHz): δ (ppm) 170.6, 170.5, 170.3, 170.2, 170.2, 170.1, 170.0, 119.3, 119.3, 92.9, 92.7, 92.6, 92.4, 70.2, 70.1, 70.0, 69.9, 69.5, 69.1, 68.8, 68.8, 65.7, 65.6, 62.5, 62.4, 59.4, 59.3, 59.2, 59.1, 55.3, 43.7, 43.7, 43.6, 43.5, 24.7, 24.6, 24.6, 21.0, 20.9, 20.9, 20.9, 20.8, 20.8, 20.3, 20.3, 20.2, 14.5.

^{31}P NMR (CDCl₃, 121 MHz): δ (ppm) 151.81, 149.61.

Synthesis of 7



The commercially available **3-Butyn-1-ol** (100 mg, 1.410 mmol) was dissolved in DCM (8 mL), followed by DIPEA (368 μL , 2.115 mmol, 1.5 eq) at rt under argon. In a pear-

shaped flask, CEP-Cl (435 mg, 1.833 mmol, 1.3 eq) was dissolved in DCM (3 mL) under argon at rt and the mixture was left under stirring for 15 minutes. Then, the latter was transferred via cannula to the solution with **3-Butyn-1-ol**. The mixture was stirred for an additional hour. After that, the solvent was evaporated and the crude was purified over column chromatography (Hex/EtOAc/TEA 50/50/1) obtaining **7** as a colorless oil.

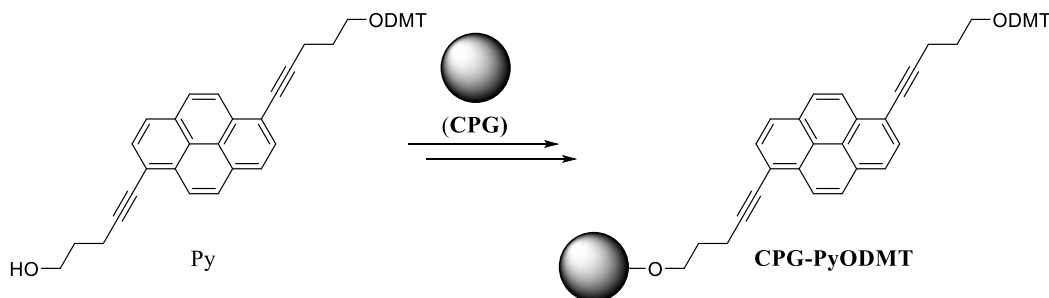
^1H NMR (300 MHz, Chloroform-*d*) δ 3.92 – 3.53 (m, 6H), 2.64 (t, *J* = 6.5 Hz, 2H), 2.48 (dd, *J* = 2.6, 0.7 Hz, 2H), 1.97 (t, *J* = 2.7 Hz, 1H), 1.17 (dd, *J* = 6.8, 2.0 Hz, 12H).

^{13}C NMR (75 MHz, CDCl_3) δ 117.6, 81.0, 69.6, 61.7, 61.5, 58.7, 58.4, 43.2, 43.0, 24.7, 24.6, 24.6, 24.5, 21.5, 21.4, 20.4, 20.3.

^{31}P NMR (121 MHz, CDCl_3) δ 148.11.

HR-MS (NSI): calc. *m/z* for $[\text{C}_{13}\text{H}_{23}\text{O}_2\text{N}_2\text{P}]$ 270.15, found: 270.1492.

Pyrene modified solid support (CPG-PyODMT)¹¹⁶



Compound **3** (33 mg, 0.050 mmol) was dissolved in DCM (0.25 mL). Then, succinic anhydride (5 mg, 0.050 mmol, 1eq) and DMAP (9.16 mg, 0.075 mmol, 1.5 eq) were added. The reaction mixture was stirred for 4h at rt and then transferred into a separation funnel. The organic phase was washed once with 10% citric acid and once with brine and then dried with Na_2SO_4 ; the solvent was removed in vacuo. Afterwards, the residue was dissolved in ACN.

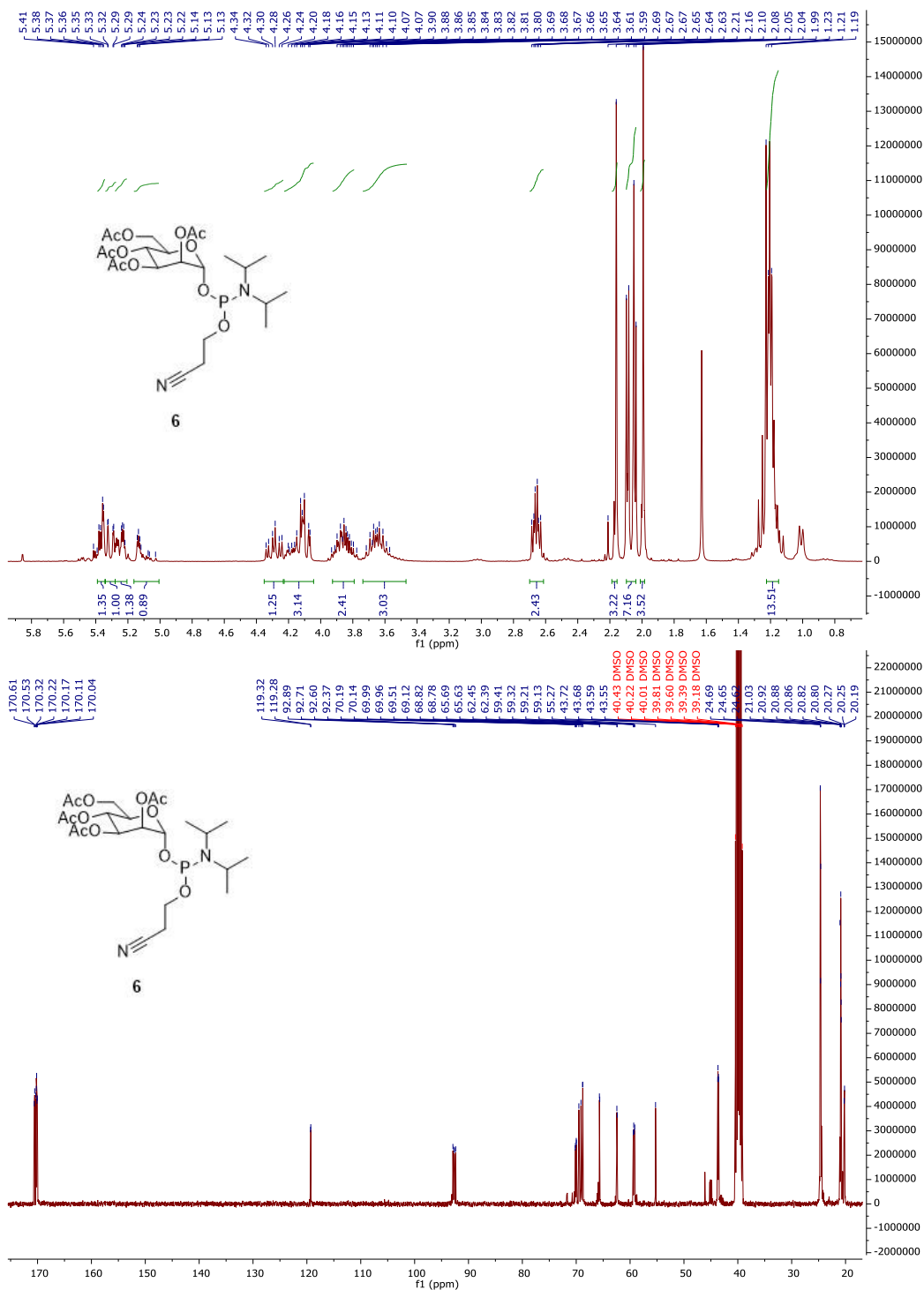
Then, 2 mL (0.015 mmol of ester) of this solution were transferred into a round bottom flask. LCAA-CPG (500Å, 300 mg) was added, followed by BOP ((Benzotriazol-1-yloxy)tris(dimethylamino)phosphonium hexafluorophosphate) (13.3 mg, 0.030 mmol) and *N*-methylimidazol (5 μL , 0.060 mmol).

The suspension was stirred for 20h. After that, the solid support was filtered and washed with DCM. A solution of pyridine and acetic anhydride (3:1, 2.4mL) was prepared, to

which were added DMAP (30 mg) and the solid support. After 2 h of stirring, the solid support was filtered and washed with DCM.

Determination of loading: a small sample of solid support (2.3 mg) was treated with 10 mL of 3% trichloroacetic acid in DCM. The absorption was measured at 498 nm. For the calculation of the loading, the absorption coefficient $\epsilon = 70000$ for DMT cations was used.

NMR SPECTRA

Figure 5.1 ^1H NMR (top) and ^{13}C NMR (bottom) of compound 6

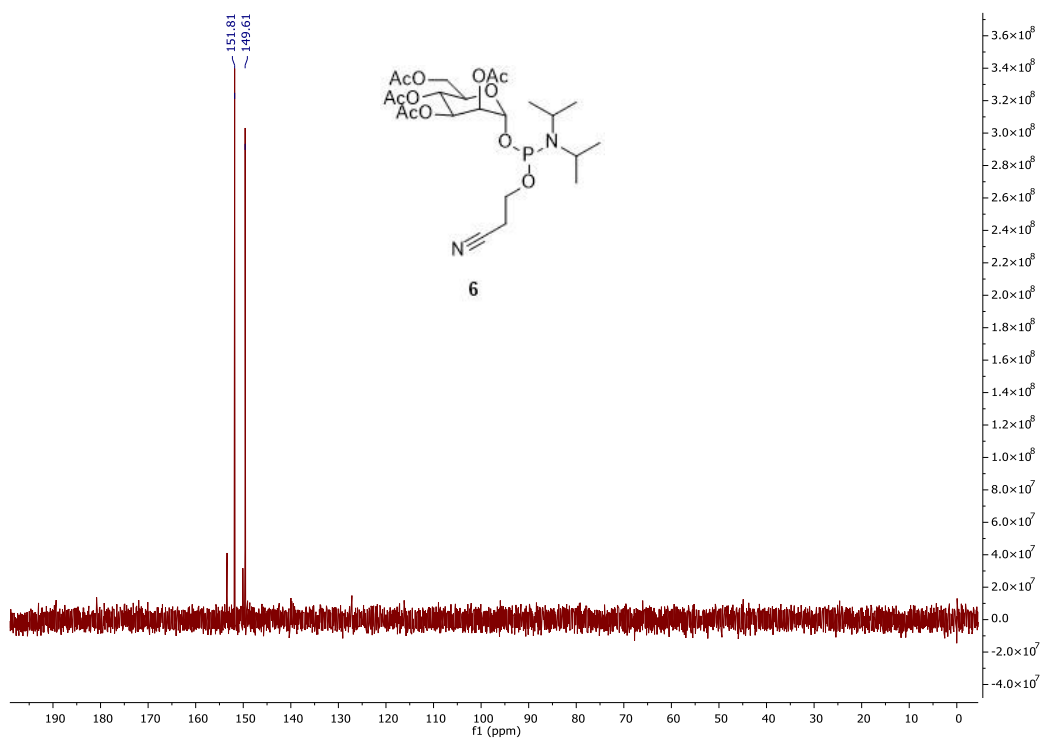


Figure 5.2 ^{31}P NMR of compound **6**

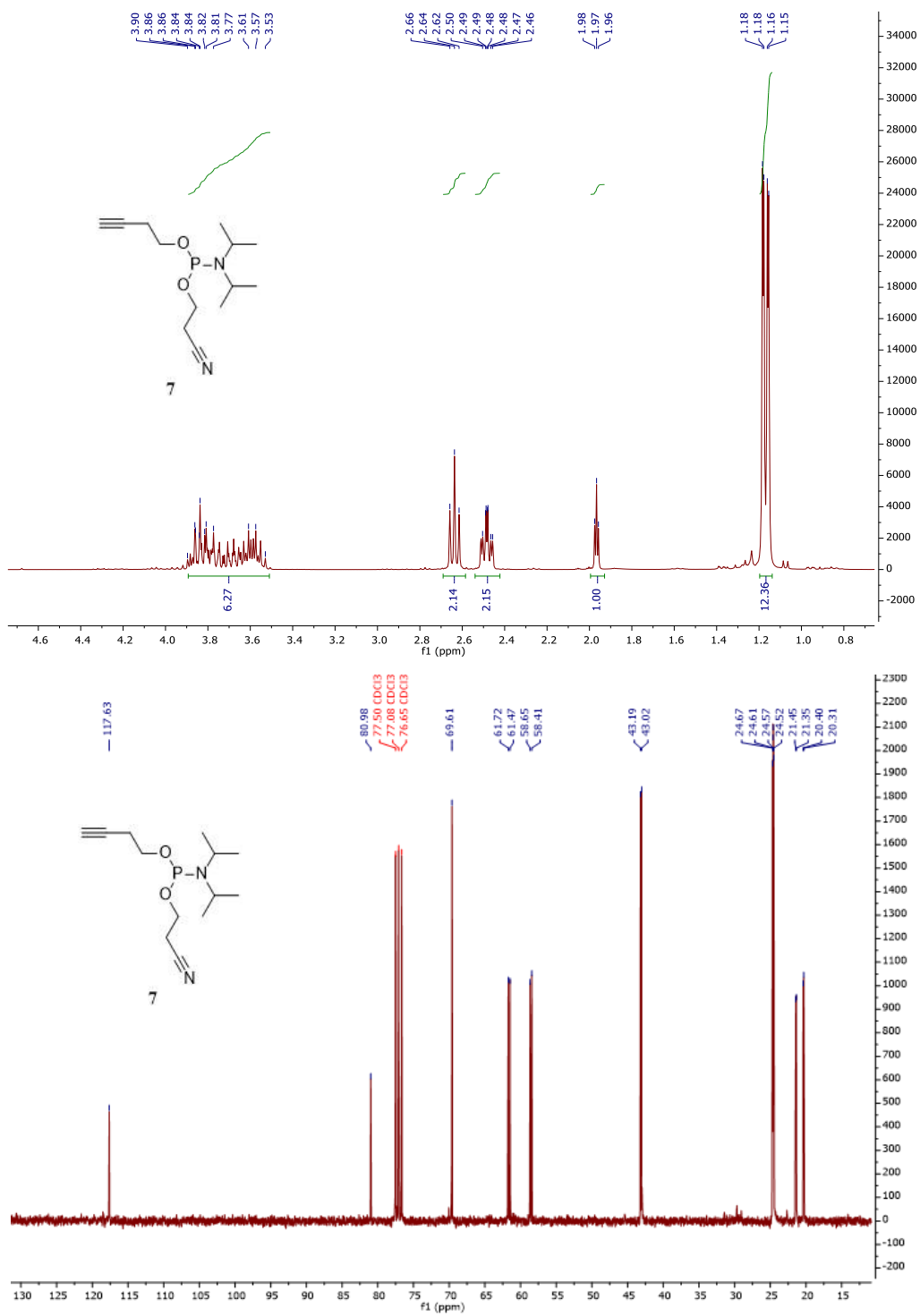


Figure 5.3 ^1H NMR (top) and ^{13}C NMR (bottom) of compound 7

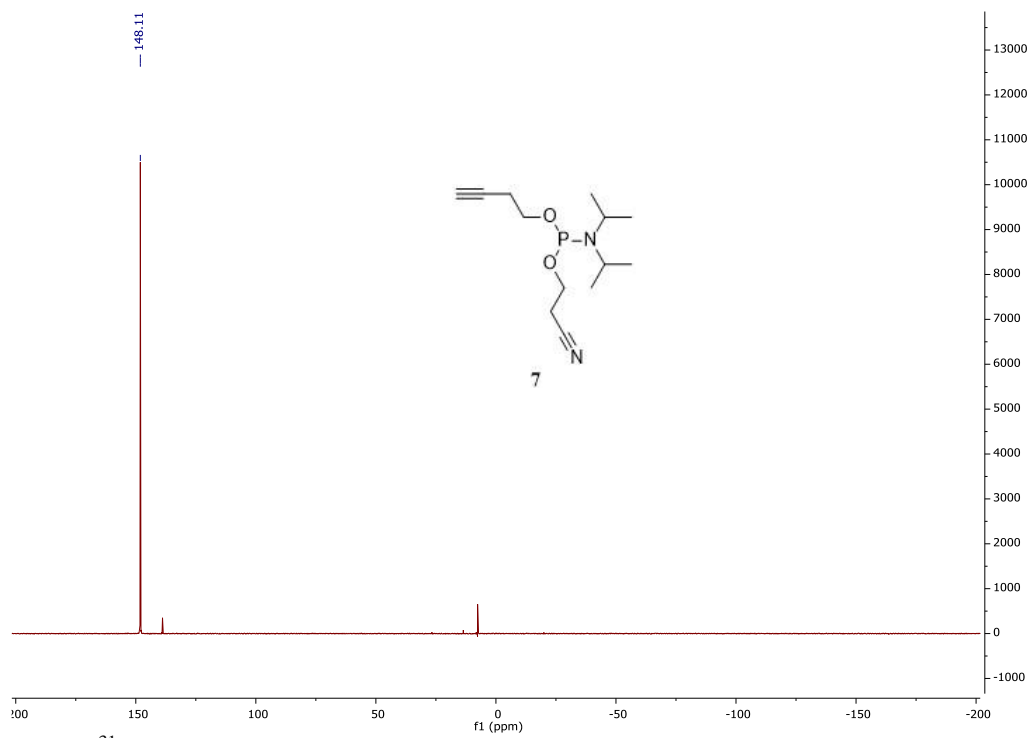
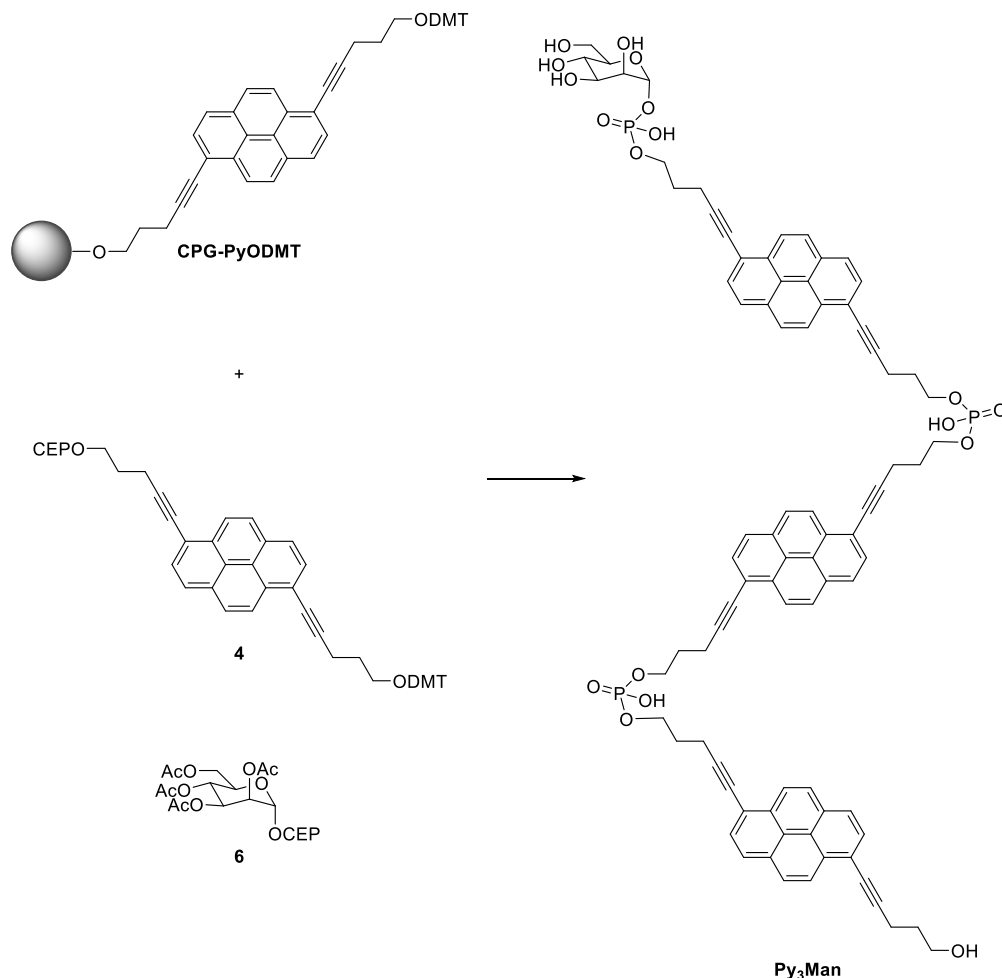


Figure 5.4 ^{31}P NMR of compound 7

PYRENE TRIMERS SYNTHESIS

Py₃Man



Py₃Man was synthesized on the Applied Biosystems 394 DNA synthesizer using CPG-PyODMT as solid support. A standard cyanoethyl phosphoramidite coupling protocol, for the 1 μ mol synthesis (“trityl-on” mode), was followed.

Compounds **4** and **6** were dissolved in 1,2-dichloroethane and ACN, respectively, to yield 0.1M solutions.

The coupling yields, per single steps of synthesis, were between 95% and 100% (monitoring by “trityl assay”). After synthesis, the cleavage of the Py₃Man from the support was achieved by treatment with MeNH₂ (33% in EtOH) + NH₃ (25-30% in H₂O)

50/50 for 15 min at RT, then for 15 min at 65 °C. In this conditions, mannose was deprotected as well.

Then, the suspension was centrifuged and the supernatant was lyophilized. The crude was dissolved in 2mL of solution made with TEAA 0.05 M pH=7/ACN 8:2 and purified by reverse-phase HPLC (Lichrospher 100 RP-18 250x4mm column), using:

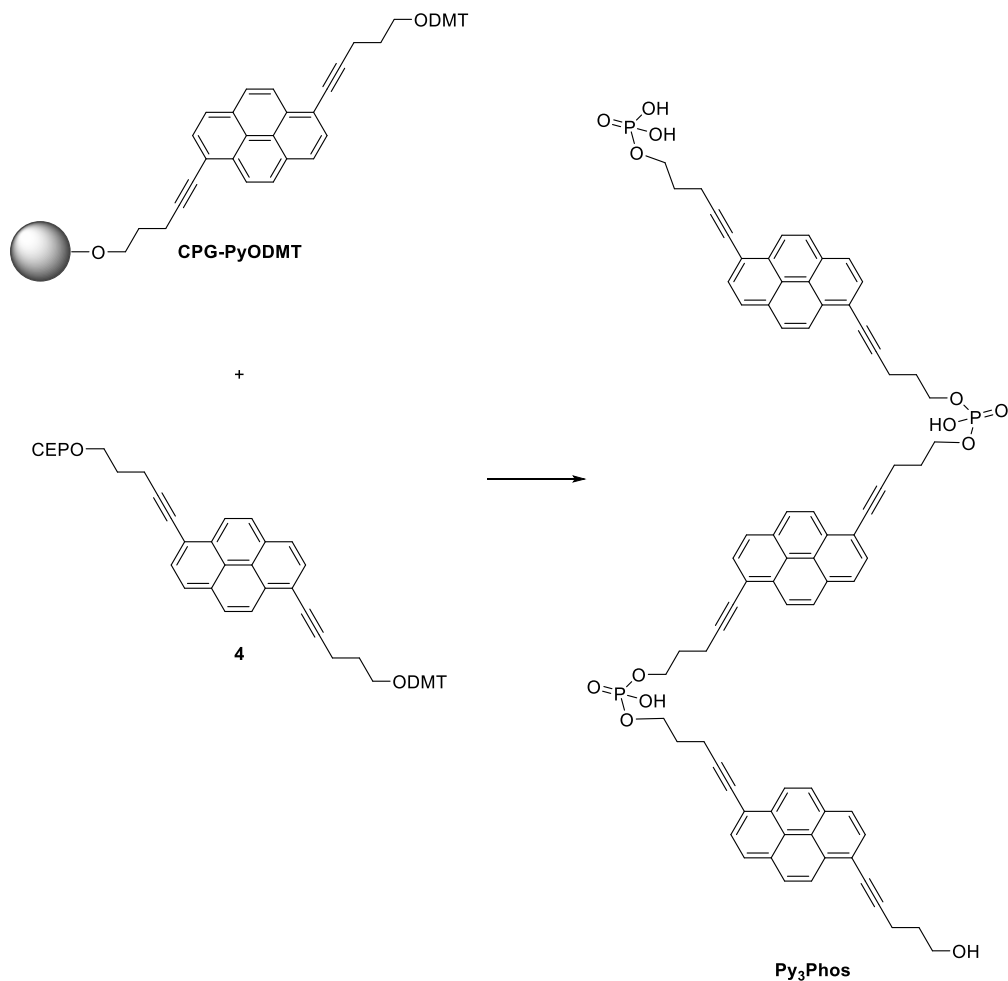
- Solvent A triethylammonium acetate (TEEA) 0.05M pH=7
- Solvent B HPLC grade ACN.

The program used was: 1 ml/min; T = 50°C; B[%] (tR [min]) = 0 (0); 35 (2); 65 (16); 80 (18); 100 (22); 100 (30). The retention time of the product was 12 minutes.

The identity of the compound was confirmed by ESI mass spectrometry. The samples were measured in negative ion mode in MeOH.

HR-MS (NSI): calc. m/z for [C₈₄H₇₅O₁₈P₃] 1464.42, found: 487.1321 (z=3)

The purified compound was dissolved in 2 mL of MeOH (this represents the stock solution). A small aliquot of stock solution was diluting, measuring the absorbance at 365nm. The concentration was determined using $\epsilon_{365} = 35000 \text{ cm}^{-1}\text{M}^{-1}$ per single pyrene unit.

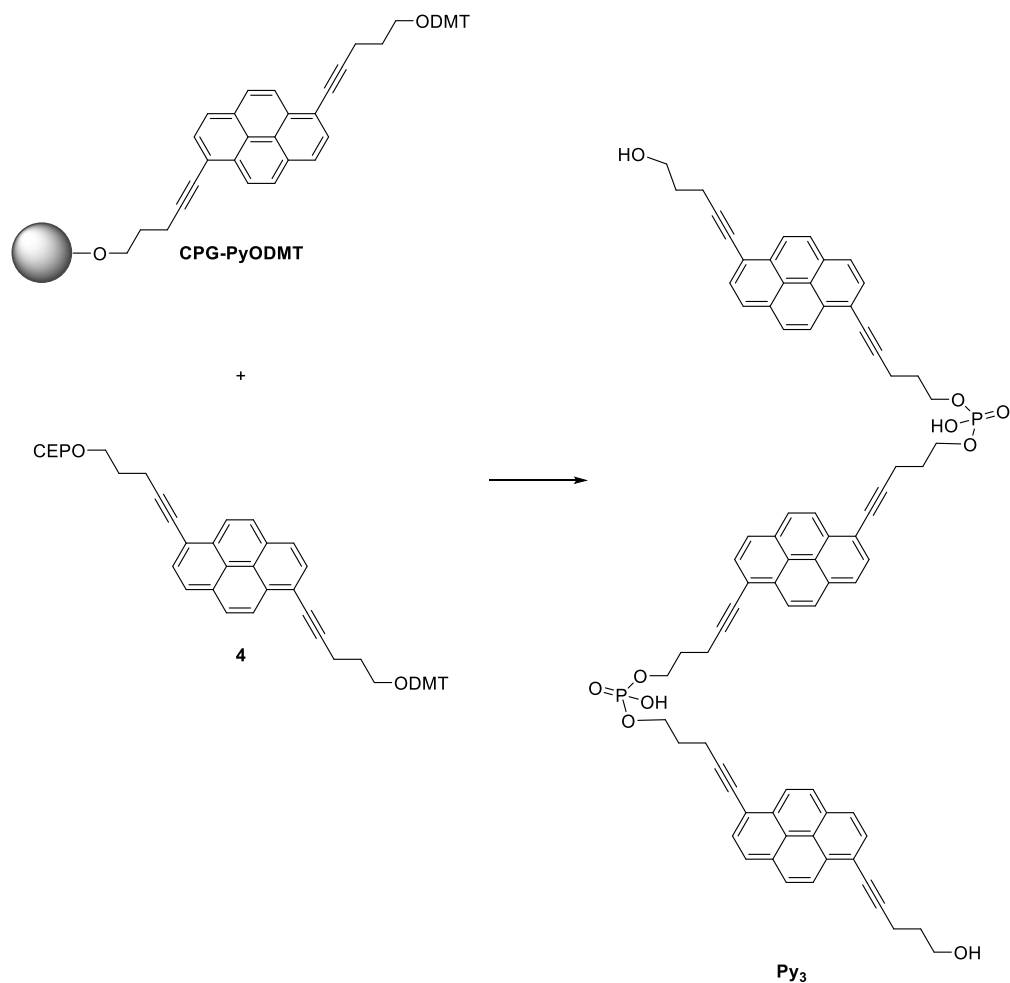
Py₃Phos

Py₃Phos was found in one of the fraction for purification of Py₃Man.

The identity of the compound was confirmed by ESI mass spectrometry, measured in negative ion mode in MeOH.

HR-MS (NSI): calc. m/z for [C₇₈H₆₅O₁₃P₃] 1302.36, found: 433.1135 ($z=3$)

The purified compound was dissolved in 2 mL of MeOH (this represents the stock solution). A small aliquot of stock solution was diluting, measuring the absorbance at 365nm. The concentration was determined using $\epsilon_{365} = 35000 \text{ cm}^{-1}\text{M}^{-1}$ per single pyrene unit.

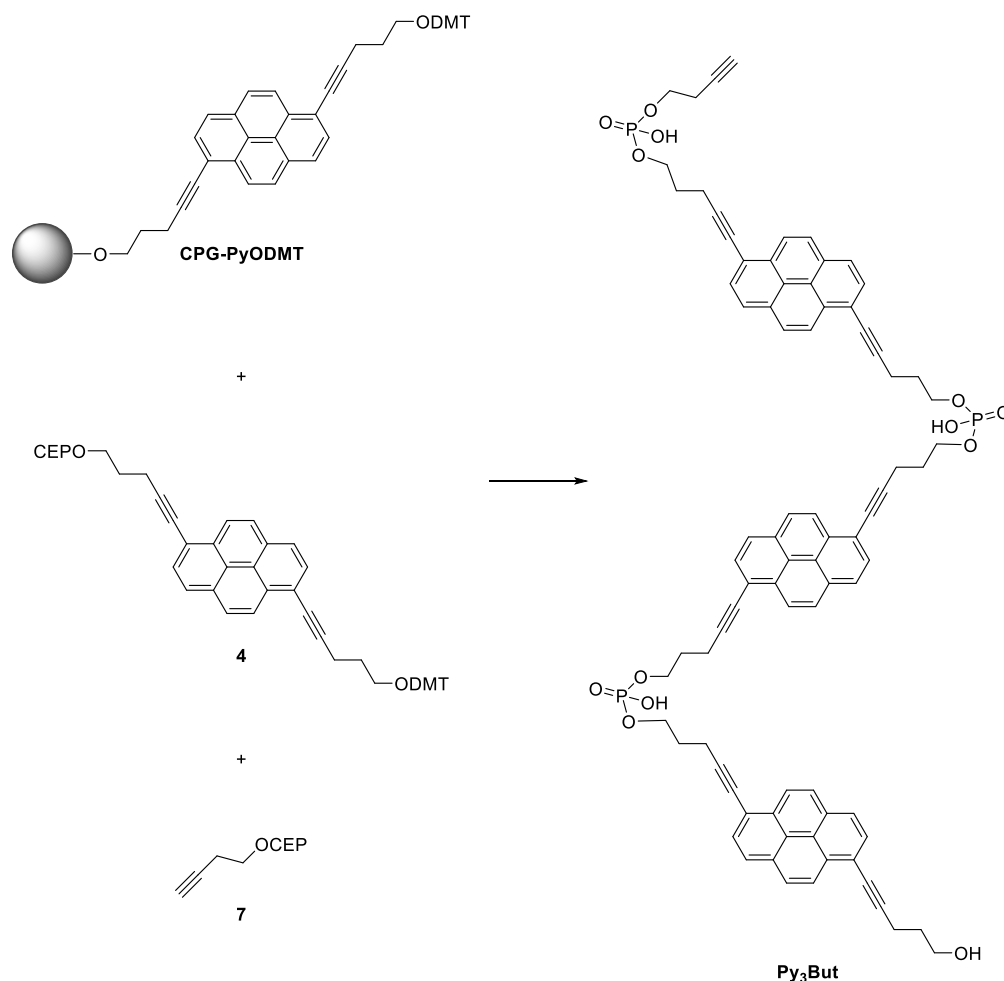
Py₃

Py₃ was synthesized according to ref.⁹³

The identity of the compound was confirmed by ESI mass spectrometry, measured in negative ion mode in MeOH.

HR-MS (NSI): calc. m/z for $[C_{78}H_{64}O_{10}P_2]$ 1222.40, found: 610.1906 ($z=2$)

The purified compound was dissolved in 2 mL of MeOH (this represents the stock solution). A small aliquot of stock solution was diluting, measuring the absorbance at 365nm. The concentration was determined using $\epsilon_{365} = 35000 \text{ cm}^{-1}\text{M}^{-1}$ per single pyrene unit.

Py₃But

Py₃But was synthesized on the Applied Biosystems 394 DNA synthesizer using CPG-PyODMT as solid support. A standard cyanoethyl phosphoramidite coupling protocol for the 1 μmol synthesis (“trityl-on” mode) was followed.

Compounds **4** and **7** were dissolved in 1,2-dichloroethane and ACN, respectively, to yield 0,1 M solutions.

The coupling yields per single steps, of synthesis, were between 95% and 100% (monitoring by “trityl assay”). After synthesis, the cleavage of the Py₃But from the support was achieved by treatment with MeNH₂ (33% in EtOH) + NH₃ (25-30% in H₂O) 50/50 for 15 min at RT, then for 15 min at 65°C.

Then, the suspension was centrifuged and the supernatant was lyophilized. The crude was dissolved in 2 mL of solution made with TEAA 0.05 M pH=7/ACN 8:2 and purified by reverse-phase HPLC (Lichrospher 100 RP-18 250x4mm column), using:

- Solvent A triethylammonium acetate (TEEA) 0.05 M pH=7
- Solvent B HPLC grade ACN.

The program used was: 1 ml/min; T = 50°C; B[%] (tR [min]) = 20 (0); 35 (2); 65 (16); 80 (18); 100 (22); 100 (27); 20 (30).

The identity of the compound was confirmed by ESI mass spectrometry. The samples were measured in negative ion mode in MeOH.

HR-MS (NSI): calc. m/z for [C₈₂H₆₉O₁₃P₃] 1354.40, found: 450.4550 (z=3)

The purified compound was dissolved in 2 mL of MeOH (this represents the stock solution). A small aliquot of stock solution was diluting, measuring the absorbance at 365nm. The concentration was determined using $\epsilon_{365} = 35000 \text{ cm}^{-1}\text{M}^{-1}$ per single pyrene unit.

Oligomers Identification

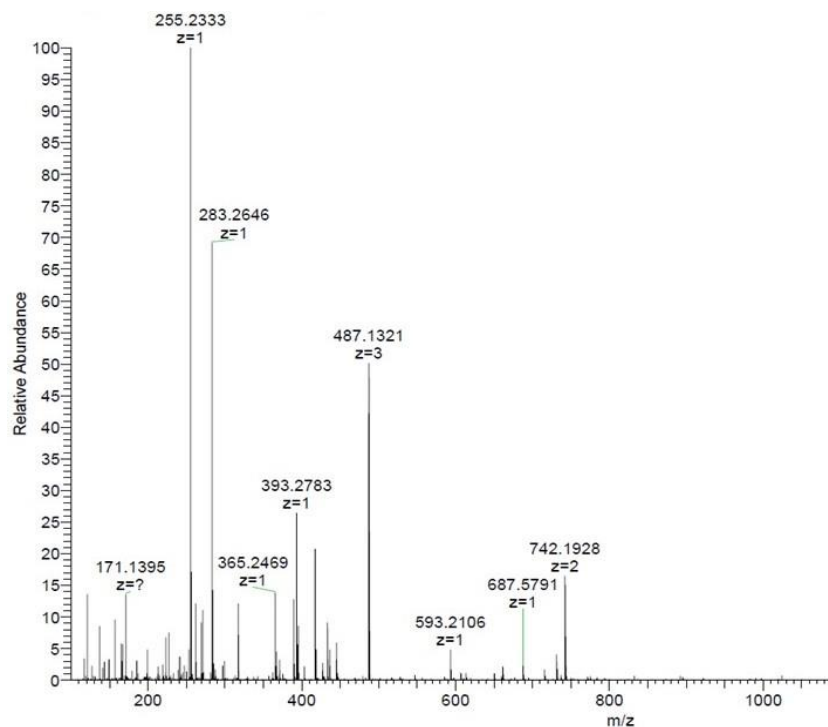
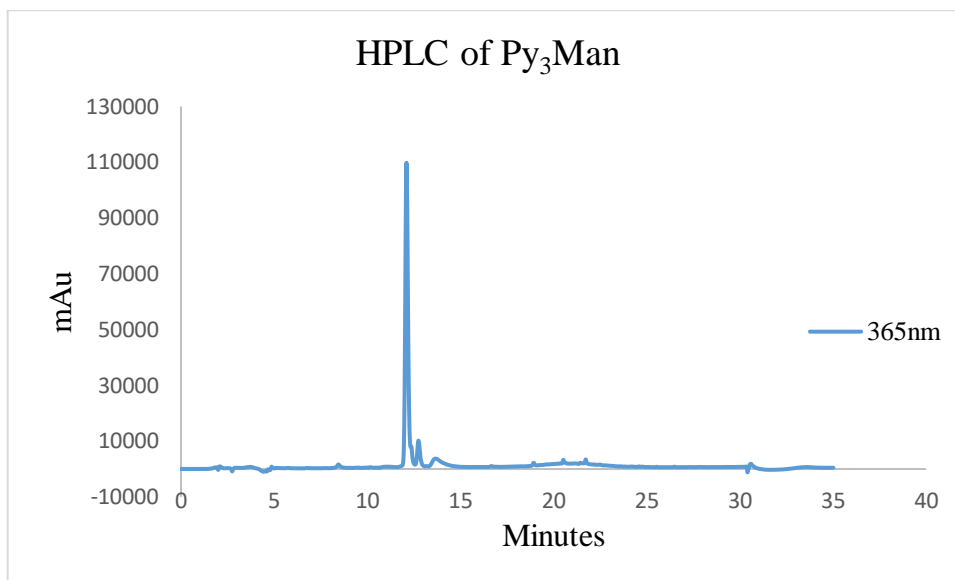


Figure 5.5 HPLC trace (top) of Py₃Man with 12 minutes as retention time. Mass spectrum (bottom) of Py₃Man.

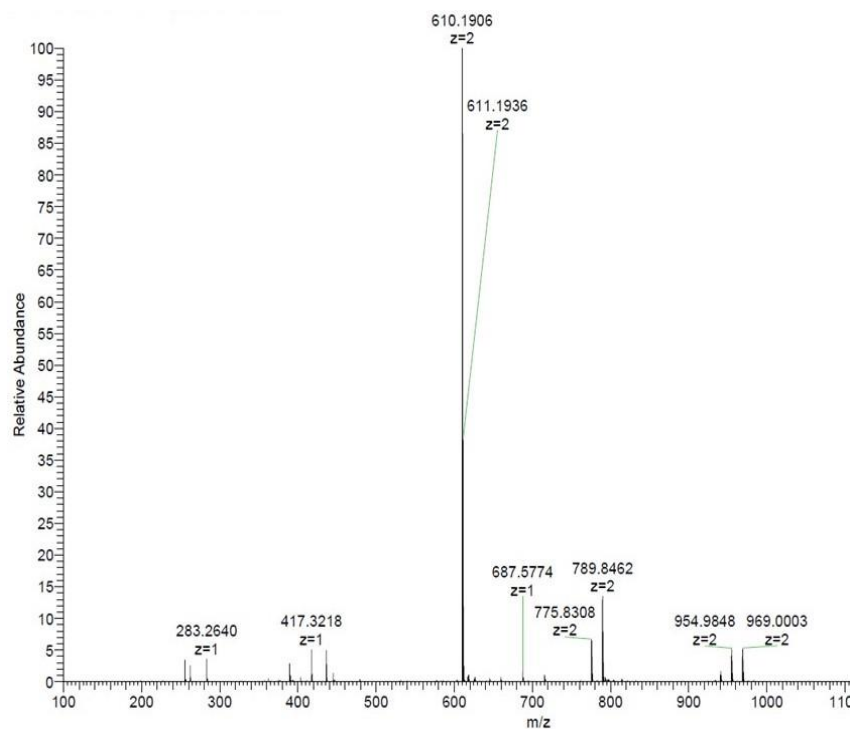
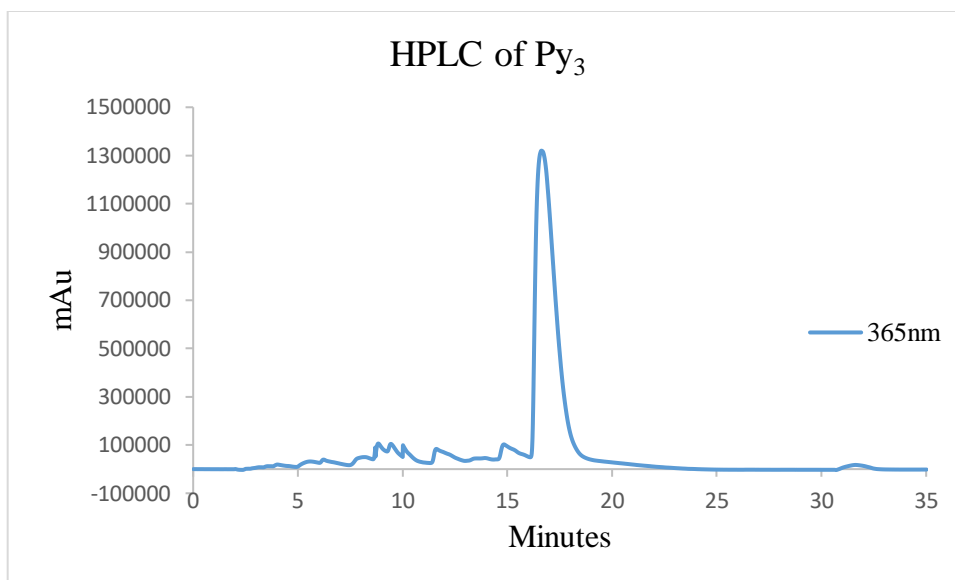


Figure 5.8 HPLC trace (top) of Py_3 with 16 minutes as retention time. Mass spectrum (bottom) of Py_3 .

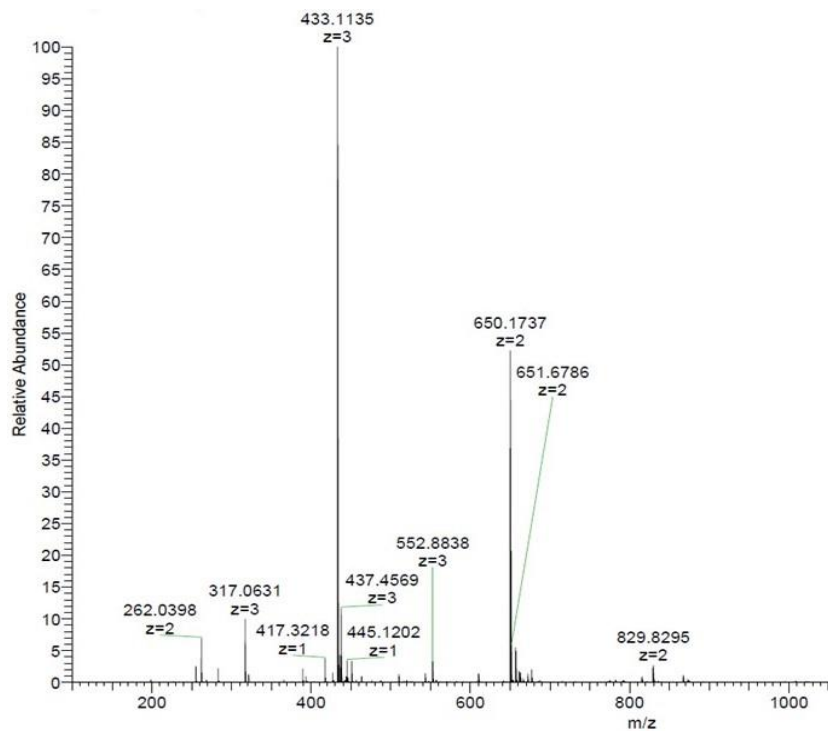


Figure 5.7 HPLC trace (top) of Py₃Phos with 5 minutes as retention time. Mass spectrum (bottom) of Py₃Phos.

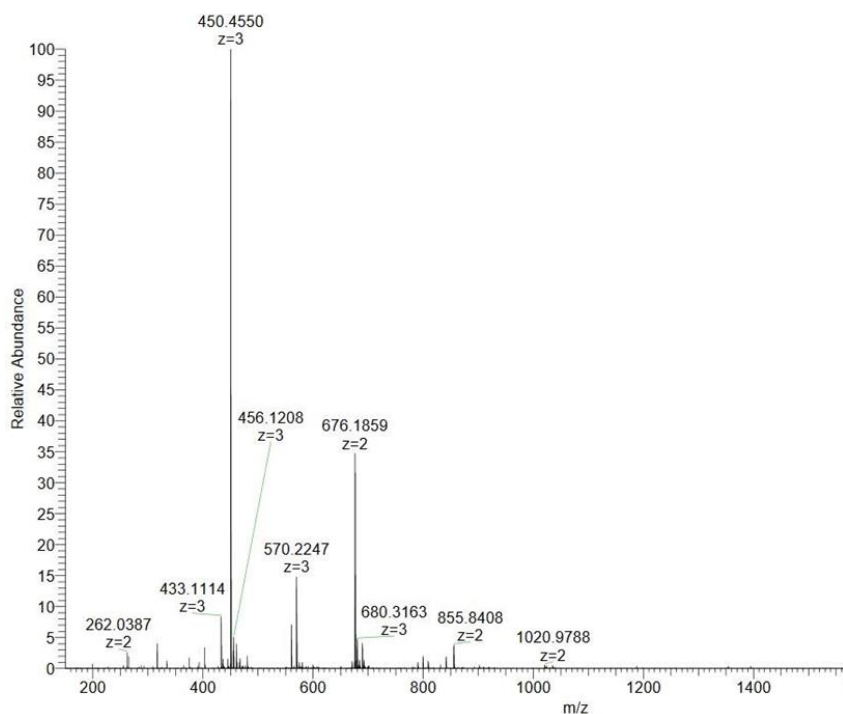
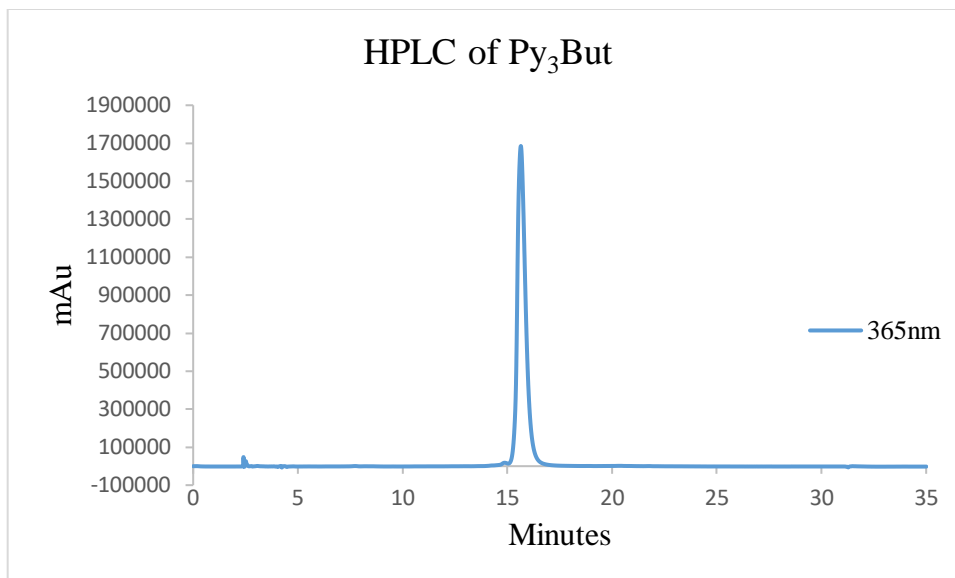


Figure 5.6 HPLC trace (top) of Py₃But with 15.5 minutes as retention time. Mass spectrum (bottom) of Py₃But.

PREPARATION OF AuNP¹¹³

A solution of 4% HAuCl₄ in 1 mL of MilliQ water was prepared. Then, in another flask, to 375 μ L of this solution, 500 μ L of 0.2 M K₂CO₃ was added and the mixture was diluted up to 100 mL with water. The mixture was left under stirring in an ice-cold bath for about 5 minutes.

Meanwhile, 0.5 mg/mL of NaBH₄ aqueous solution was prepared. The latter was added in five aliquots, of 1 mL, to HAuCl₄/K₂CO₃ mixture under rapid stirring for additional 5 minutes in an ice-cold bath. A change of color, from purple to dark red/orange, occurred. Then, this solution was moved in several plastic tubes of 1.5 mL each and centrifuged at 1.2×10^4 rpm for 10 minutes (this procedure was done because the centrifuge used only worked with plastic tubes of 1.5 mL). After that, the supernatant was collected in two volumes of 50 mL (the two were used in the same way in the next steps).

In one of them, 20 mg of bis(p-sulfonatophenyl)phenylphosphine (BSPP) were added and the mixture was shaken overnight at rt.

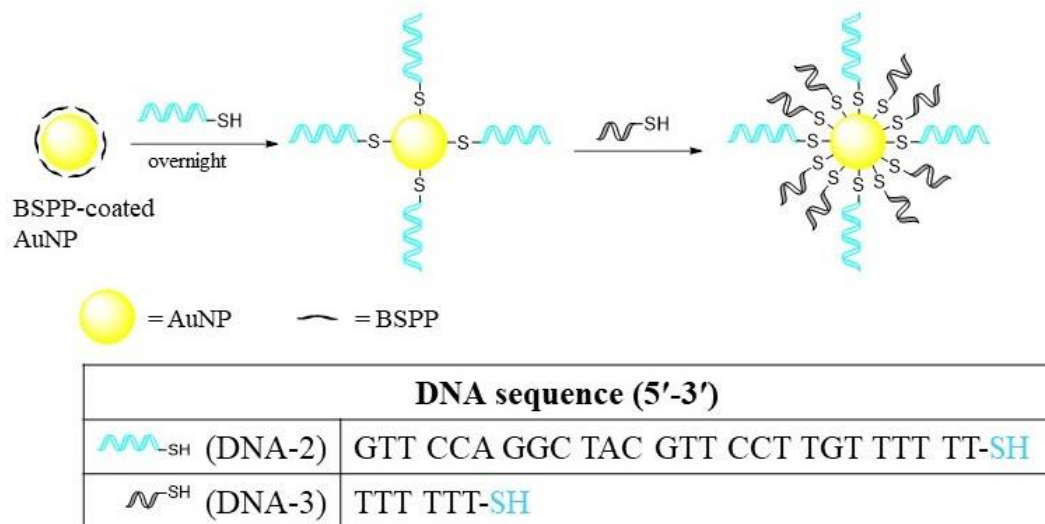
Then, to this solution, solid NaCl was slowly added (shaking after every addition) until a change of color occurred, turning in light purple.

Again, this solution was moved in plastic tubes of 1.5 mL and centrifuge for 30 minutes at 3×10^3 rpm. Then, the supernatant was carefully removed and the precipitate (AuNP) was resuspended in 0.5 mL (using the plastic tube of 1.5 mL) of BSPP aqueous solution at a concentration of 250 mg/mL. In this last step, in every tube the amount of precipitate was too little. So, in order to have a more concentrate AuNP solution, 0.5 mL of BSPP aqueous solution were poured in a tube containing the precipitate. Then, this mixture was moved in another tube containing other precipitate, and so on. This operation led to obtain a total of six tubes with AuNP in 0.5 mL of BSPP solution. To each of them, 0.5 mL of MeOH were added and the mixture was again centrifuged for 30 minutes at 1.2×10^4 rpm. At this point, the supernatant was removed and the precipitate was again resuspended in 0.5 mL of BPSS (250 mg/mL).

The concentration of AuNP-BSPP was calculated by measuring the absorbance at 520nm ($\epsilon_{520} = 9.3 \times 10^6 \text{ M}^{-1} \text{ cm}^{-1}$).¹¹⁷

As depicted in chapter 4, these AuNP-BSPP were covered by 3'-thiol modified DNA strands and polyethylene glycol (PEG) derivatives.

AuNP covered by DNA strand



Scheme 5.1 Schematic representation of preparation of AuNP covered by DNA-2 and DNA-3 strands

As depicted in **Scheme 5.1** (and as already discussed in chapter 4), commercially available DNA-2 and DNA-3 strands are used for covering AuNP.

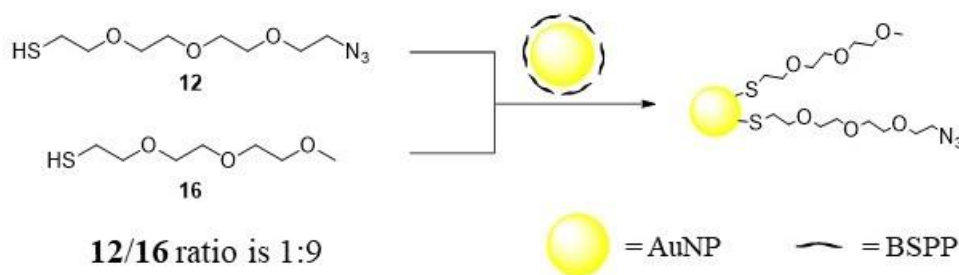
In a first step, 0.5 mL of a solution, containing 1 μM of AuNP-BSPP and 17 μM of DNA-2 strand, was prepared and shaken overnight at rt.

Then, the solution was centrifuged for 30 minutes at 1.2×10^4 rpm and then the supernatant was carefully removed.

The precipitated was redissolved in 0.5 mL water solution of DNA-3 strand at 100 μM leaving it in the fridge for 3 hours.

Then the concentration of AuNP, covered with DNA strands, was calculated by measuring the absorbance (as depicted above).

AuNP covered by PEG derivatives



Scheme 5.2 Schematic representation of AuNP covered by PEG derivatives

The preparation of AuNP covered by PEG is similar to the one used for AuNP covered with DNA.

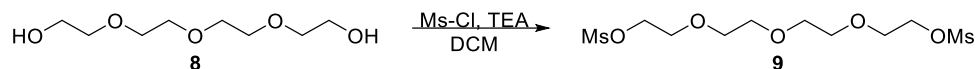
After the synthesis of **12** and **16**, a stock solution containing both compounds was prepared. In particular, the concentration of **12** was 10mM and that of **16** was 90 mM, for a total of 100 mM with a ratio of 1:9. This solution was diluted 10 times obtaining 10mM of **12/16** in a ratio 1:9.

Then, in a volume of 200 μ L, AuNP-BSPP and PEG derivatives mixture were added with a concentration of 1 μ M and 500 μ M (AuNP-BSPP and PEG derivatives respectively). This solution was shaken overnight at rt. Then, it was centrifuged at 1.2×10^4 rpm for 30 minutes, then the supernatant was removed and the precipitate redissolved in 500 μ L of water.

The concentration of AuNP, covered with PEGs, was calculated by measuring the absorbance (as depicted above). Yield

SYNTHETIC PROCEDURES OF POLYETHYLENE GLYCOL DERIVATIVES¹¹⁴

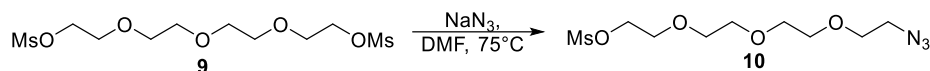
Synthesis of 9



The commercially available compound **8** (2 g, 10.297 mmol) and TEA (7.2 mL, 51.845 mmol, 5 eq) were dissolved in anhydrous DCM (50 mL) at 0°C under argon; then, methanesulfonyl chloride (Ms-Cl) (2 mL, 25.743 mmol, 2.5 eq) was added and the solution was slowly warmed up to rt, leaving it under stirring overnight. Then, TLC showed the reaction was complete. The solution was washed, once with 10% citric acid solution and twice with brine, dried with Na₂SO₄.

The crude product was used for the next step with any further purification. $R_f = 0.85$ (DCM/MeOH 9:1). Based on ref.¹¹⁴

Synthesis of 10



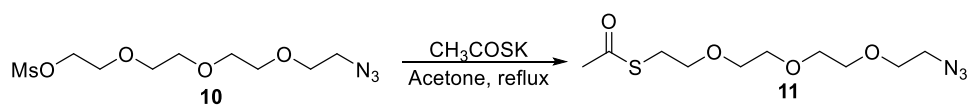
Compound **9** (from the previous step) was dissolved in DMF (15mL) at rt under argon. Then, NaN₃ (670 mg, 10.297 mmol, 1eq) was added and the solution was warmed up to 75°C and stirred overnight. Then, water was added, the crude product was extracted with EtOAc, dried with Na₂SO₄ and purified over column chromatography (Hex/EtOAc 3:7), obtaining 950 mg (26%, over two steps) of pure as pale yellow oil. $R_f = 0.7$ (EtOAc).

¹H NMR (300 MHz, DMSO-*d*₆) δ 4.35–4.26 (m, 2H), 3.72–3.64 (m, 2H), 3.60 (t, 2H), 3.55 (bp, 8H), 3.39 (t, $J = 5.6, 4.2$ Hz, 2H), 3.17 (s, 3H).

¹³C NMR (75 MHz, DMSO) δ 71.0, 70.5, 70.3, 70.2, 70.1, 69.8, 69.7, 69.4, 68.8, 62.4, 50.5, 44.0, 37.3.

HR-MS (NSI): calc. m/z for [C₉H₁₉N₃O₆S] 297. 10 [M+Na]⁺, found: 320.0879.

Synthesis of 11

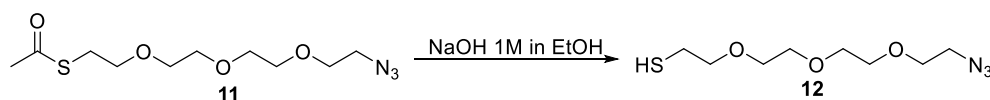


Compound **10** (930 mg, 3.128 mmol) is dissolved in acetone (20 mL) under argon. After 20 minutes, potassium thioacetate (CH_3COSK) (429 mg, 3.754 mmol, 1.2 eq) is added and the solution is warmed up to reflux and stirred overnight. Then, the solvent is removed under vacuum, the crude is dissolved in DCM and washed with brine, dried with Na_2SO_4 and purified over column chromatography (Hex/EtOAc 3:7), leading to 696 mg (80%) of pure as a pale yellow oil. $R_f = 0.4$ (Hex/EtOAc 3:7).

^1H NMR (300 MHz, $\text{DMSO}-d_6$) δ 3.64–3.58 (m, 2H), 3.55 (bp, 4H), 3.52–3.47 (m, 6H), 3.43–3.34 (m, 2H), 3.01 (t, $J = 6.5$ Hz, 2H), 2.33 (s, 3H).

^{13}C NMR (75 MHz, DMSO) δ 195.5, 70.3, 70.2, 70.2, 70.1, 70.0, 69.7, 69.4, 50.5, 31.0, 28.8.

Synthesis of **12**



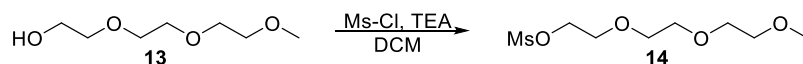
Before the reaction started, the solutions of NaOH 1M in EtOH and HCl 1 M in water were prepared and purged with argon.

Compound **11** (696 mg, 2.596 mmol) was dissolved in 30 mL of dry EtOH under argon for 30 minutes. Then, 2.6 mL of NaOH solution (2.6 mmol, 1eq) were transferred to the mixture with **11**, for 40 minutes. After that, 5.2 mL of HCl solution (5.2 mmol, 2 eq) were transferred to the reaction mixture, leaving the reaction for addition 15 minutes. Once the reaction was complete, the mixture was extracted with DCM, dried with NaSO_4 obtaining 490 mg (80%) of product as colorless oil, which was used in the next step with any further purification.

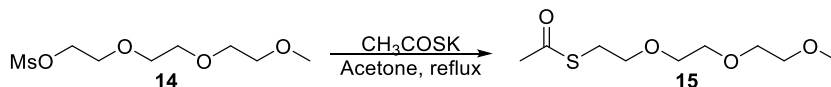
^1H NMR (300 MHz, $\text{DMSO}-d_6$) δ 3.64–3.58 (m, 2H), 3.57–3.46 (m, 10H), 3.43–3.34 (m, 2H), 2.69–2.55 (m, 2H), 2.24 (t, $J = 8.1$ Hz, 1H).

^{13}C NMR (75 MHz, DMSO) δ 72.7, 70.3, 70.3, 70.2, 70.2, 70.1, 69.9, 69.8, 69.1, 50.5, 40.8, 40.6, 40.3, 40.0, 39.7, 39.5, 39.2, 38.4, 23.9.

HR-MS (NSI): calc. m/z for $[\text{C}_8\text{H}_{17}\text{N}_3\text{O}_3\text{S}]$ 258.10 $[\text{M}+\text{Na}]^+$, found: 258.0883.

Synthesis of 14

Same procedure for synthesis of **9**. Ms-Cl and TEA were used in 1.2 eq and 2.5 eq respectively. The crude was used for the next step with any further purification.

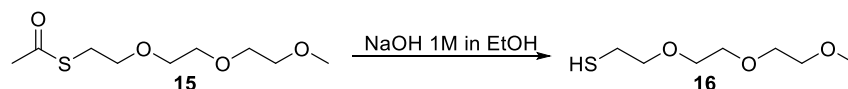
Synthesis of 15

Same procedure for synthesis of **11**. The pure (82%) was obtained as pale yellow oil. $R_f = 0.6$ (Hex/EtOAc 1:1).

$^1\text{H NMR}$ (300 MHz, $\text{DMSO-}d_6$) δ 3.55–3.46 (m, 8H), 3.47–3.38 (m, 2H), 3.24 (s, 3H), 3.01 (t, $J = 6.5$ Hz, 2H), 2.33 (s, 3H).

$^{13}\text{C NMR}$ (75 MHz, DMSO) δ 195.6, 71.8, 70.2, 70.1, 70.0, 69.4, 58.5, 31.0, 28.7.

HR-MS (NSI): calc. m/z for $[\text{C}_9\text{H}_{18}\text{O}_4\text{S}]$ 245.09 $[\text{M}+\text{Na}]^+$, found: 245.0829.

Synthesis of 16

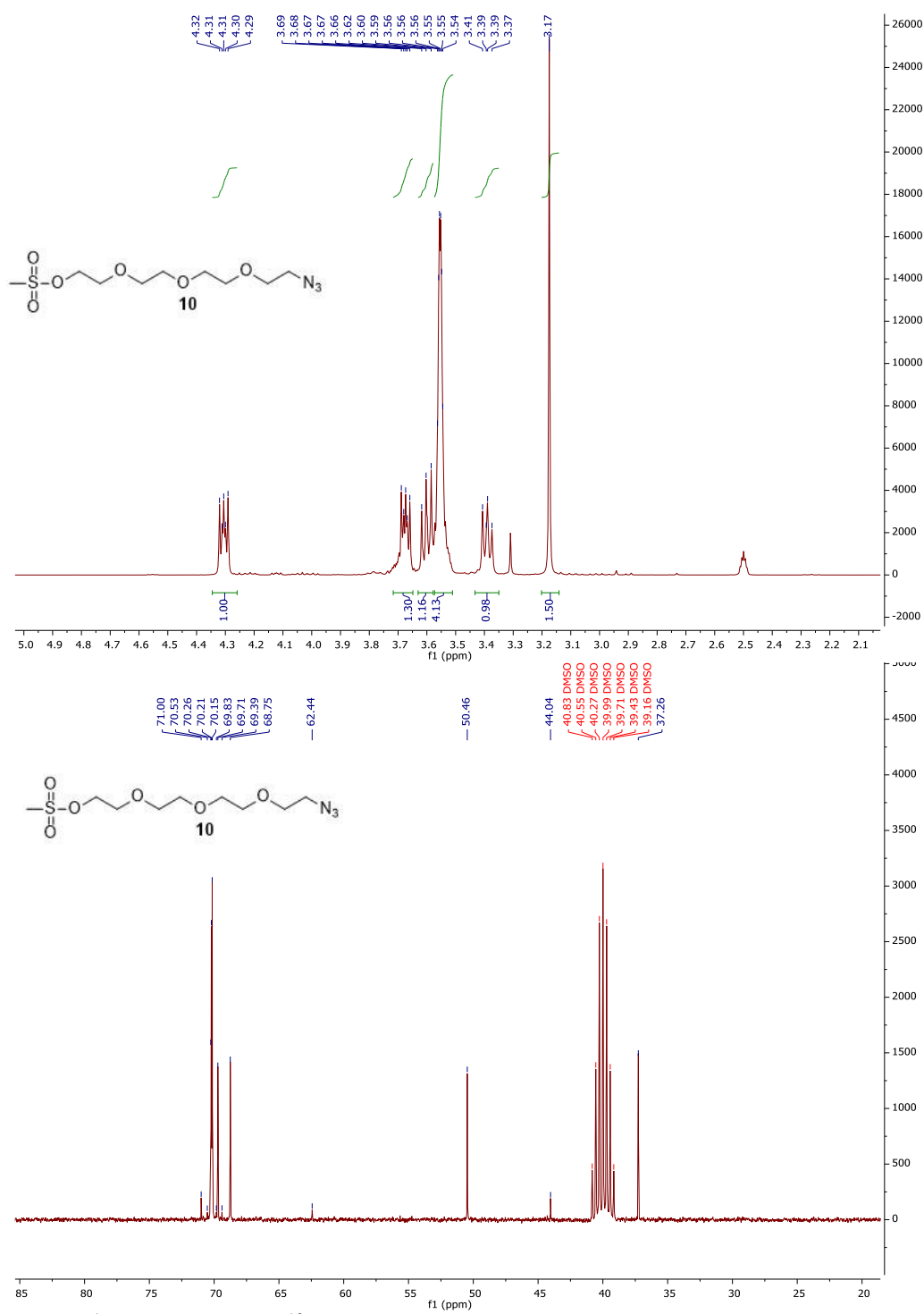
Same procedure for synthesis of **12**. The pure (80%) was obtained as colorless oil.

$^1\text{H NMR}$ (300 MHz, $\text{DMSO-}d_6$) δ 3.56–3.49 (m, 8H), 3.46–3.39 (m, 2H), 3.24 (s, 3H), 2.62 (dt, $J = 8.0, 6.7$ Hz, 2H), 2.26 (t, $J = 8.0$ Hz, 1H).

$^{13}\text{C NMR}$ (75 MHz, DMSO) δ 72.7, 71.8, 70.2, 70.1, 69.9, 58.5, 23.9.

HR-MS (NSI): calc. m/z for $[\text{C}_7\text{H}_{13}\text{O}_3\text{S}]$ 203.08 $[\text{M}+\text{Na}]^+$, found: 203.0723.

NMR SPECTRA

Figure 5.9 ^1H NMR (top) and ^{13}C NMR (bottom) of compound **10**

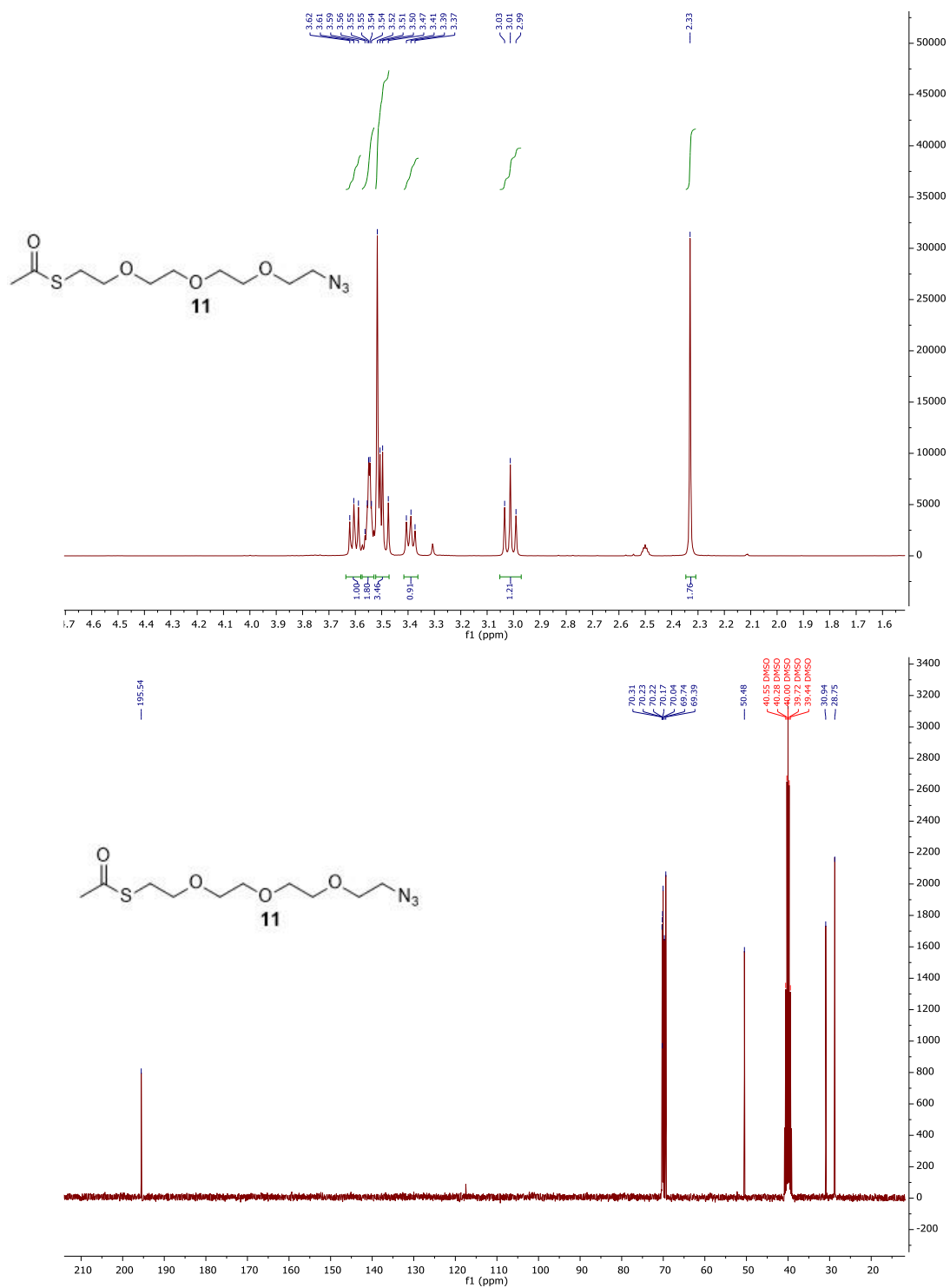


Figure 5.10 ^1H NMR (top) and ^{13}C NMR (bottom) of compound **11**

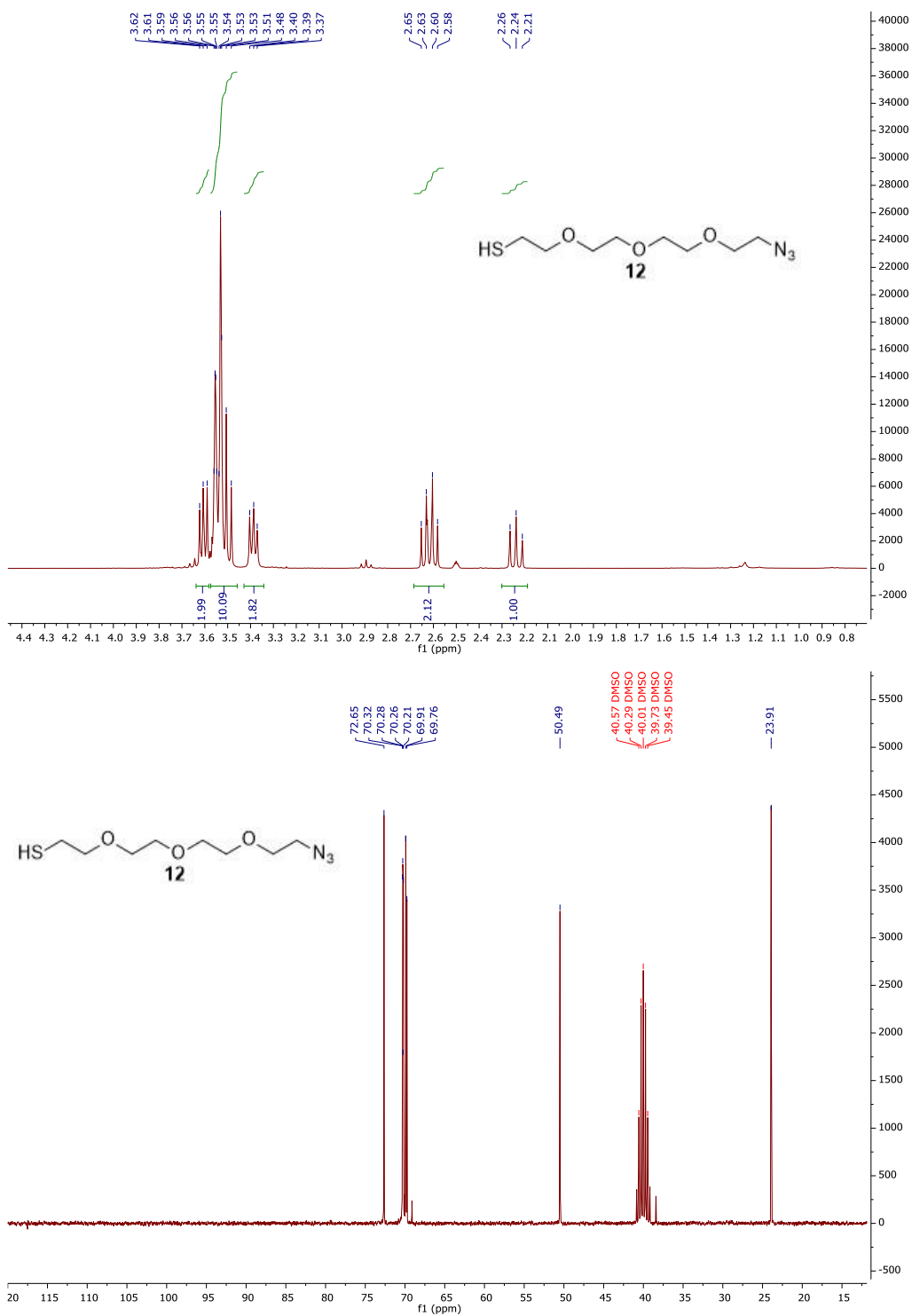


Figure 5.11 $^1\text{H NMR}$ (top) and $^{13}\text{C NMR}$ (bottom) of compound **12**

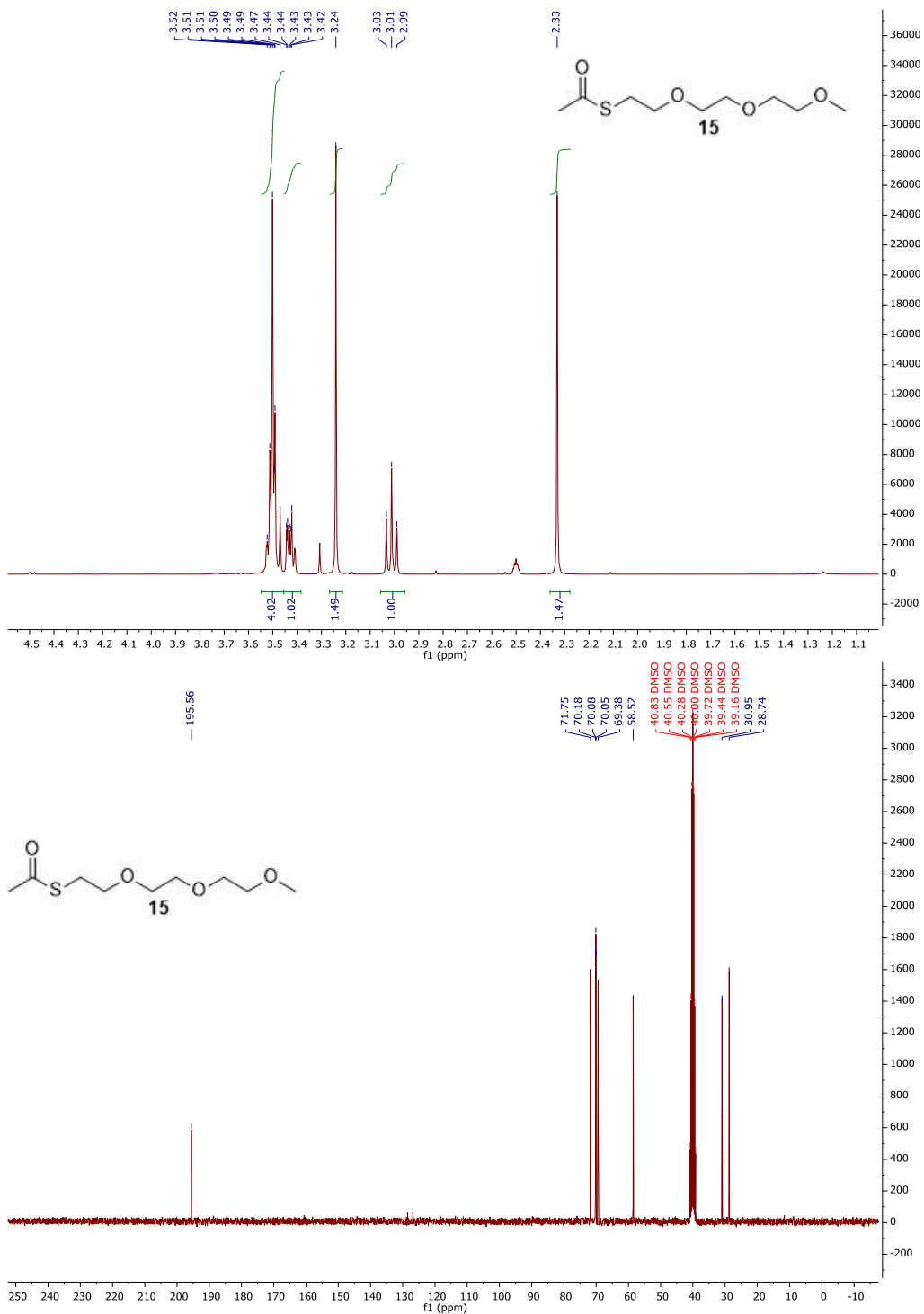


Figure 5.12 ¹H NMR (top) and ¹³C NMR (bottom) of compound 15

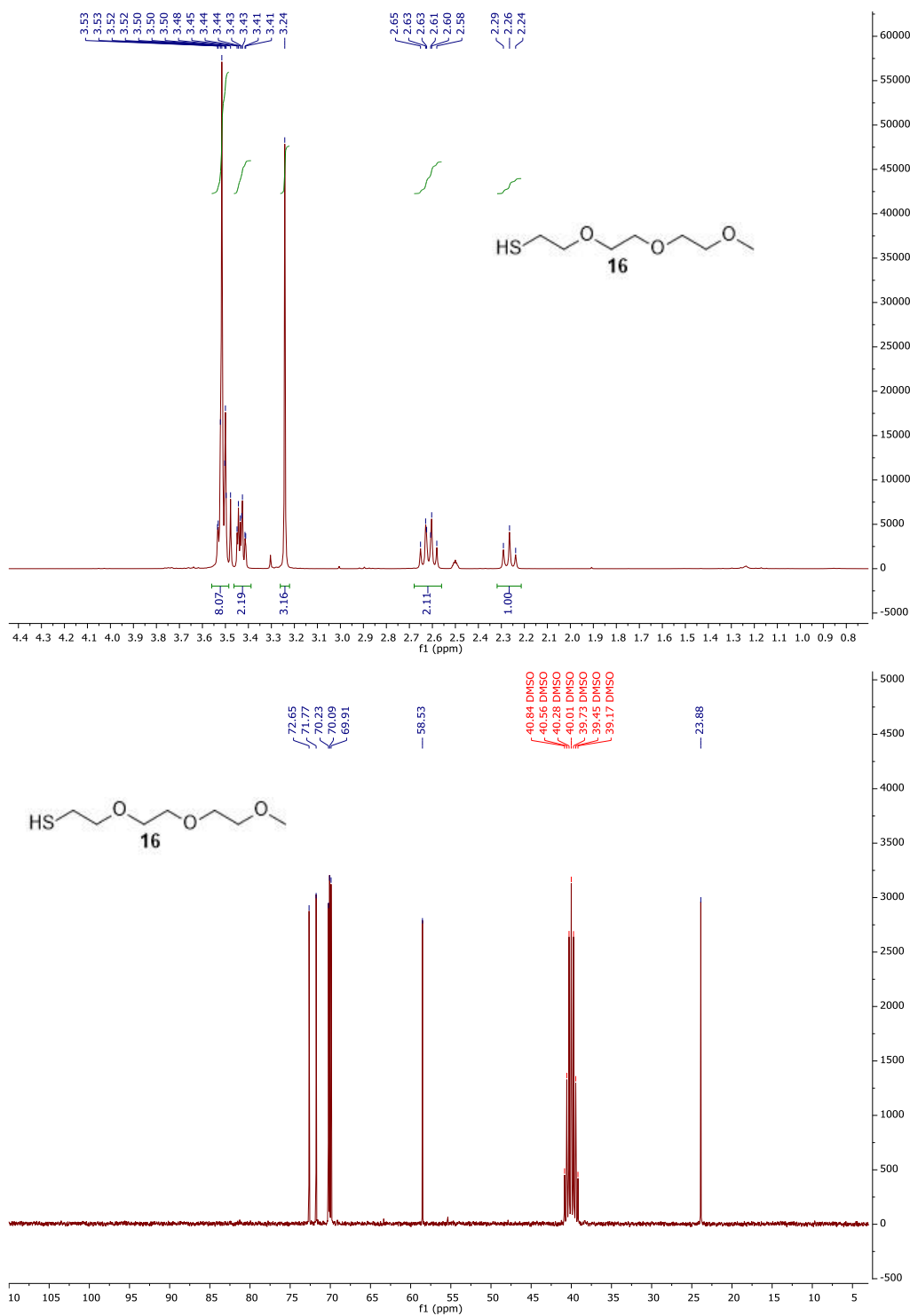


Figure 5.13 ¹H NMR (top) and ¹³C NMR (bottom) of compound 16

Part B

ABSTRACT

Most proteins that enter the secretory pathway are glycosylated, that is, a carbohydrate component (glycan) is covalently linked to the protein. The synthesis of the glycan structures and their post-translational attachment to the proteins requires many steps, and any defects in this complex machinery lead to genetic lethal diseases.

While the synthesis of the glycans starts on the cytosolic face of the ER, the final assembly takes place on the luminal side. The translocation from one side to another does not occur spontaneously, but it is probably facilitated by the presence of a class of protein known as **scramblases**. So far, their molecular structure and how they promote the translocation are still unknown.

Our research group is involved in finding answers to these questions: **what is the identity of such proteins and how do they work?** This work is part of an interdisciplinary research project funded by the SNF (Sinergia project).

More specifically, our goal was to synthesize suitable molecular probes that help to identify and study potential scramblase candidates. The structure of the probes resemble the natural substrates, consisting of a sugar moiety linked via phosphate/pyrophosphate to a long isoprenoid chain.

In here, the synthesis of a mimic of a natural isoprenoid chain is described. The analogue consist in an *S*-Citronellol coupled to dodecyl alkyl chain linked to a NBD fluorescent tag, which will be used as a convenient method for scramblases assay: the tests are able to discriminate between vesicles lacking and/or possessing the appropriate scramblases.

CHAPTER 1

1 INTRODUCTION

Glycoproteins (**Figure 1.1**) are an important class of compounds, essential for both prokaryotes and eukaryotes life, since they carry out many functions in cells: embryonic development, cell–cell recognition, cell adhesion, immune functions and pathogen identification. Some examples are collagens, immunoglobulins lectins, mucins and others.¹¹⁸

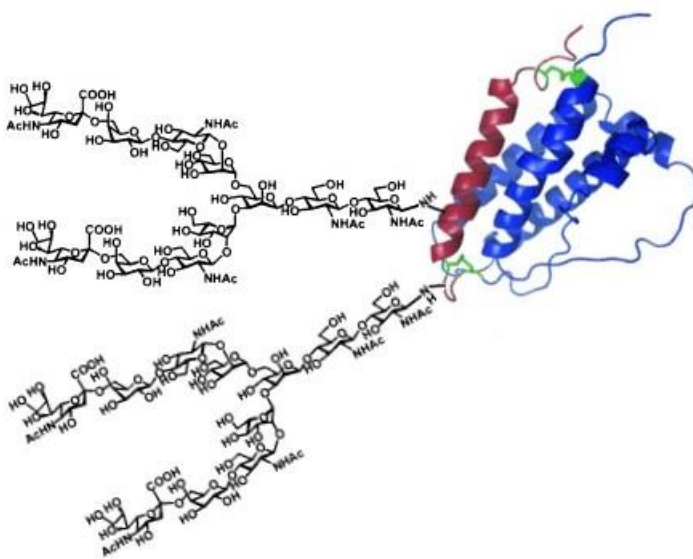


Figure 1.1 example of a glycoprotein structure. Adapted from¹¹⁹

Their synthesis occurs mainly in the Endoplasmic Reticulum (ER) and Golgi apparatus, often as a series of subsequent enzymatic reactions.

The Glycoproteins are described as compounds formed by a carbohydrate component (glycan) covalently linked to a peptide or a protein, via a glycosidic bond.¹²⁰

Sugar moieties, found in glycoproteins, can be mannose (Man), galactose (Gal) and glucose (Glc), or derivatives of such: N-acetylgalactosamine (GalNAc) N-acetylglucosamine (GlcNAc) and N-acetylneuraminic acid (sialic acid).¹²¹

These glycans are linked to proteins as either monosaccharide or oligosaccharide, as either linear or branched structure containing the sugars mentioned above.

The presence of hydrophilic and polar carbohydrates can chemically and structurally change the characteristics of a protein. These sugars are often necessary in order for proteins to work properly and for example to be specifically recognized by other components inside the cell.

1.1 BIOSYNTHESIS OF DOLICHOL

Polyisoprenoid alcohols are membrane lipid, present in every cell, from archaea to eukaryotes.¹²³

In particular, dolichol is a long-chain isoprenoid alcohol (polyisoprenoid) and functions as a carrier for the carbohydrates, which are linked to proteins in the process of glycosylation (for example, N-glycosylation and O-mannosylation).

The assembly of glycans takes place in the endoplasmic reticulum of all eukaryotic cells (as described in the next sessions). The structure of dolichol is shown in **Figure 1.2**. Comparing it to a typical polyprenol, α -isoprenoid residue of the dolichol is hydrogenated.^{122,123}

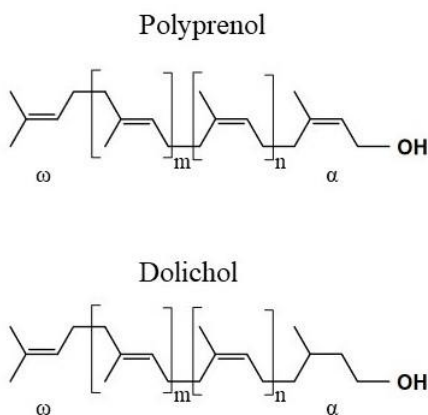


Figure 1.2 Difference between polyprenol and dolichol chains: in dolichol, the α -isoprenoid residue is a single bond. The length of the structure can be different, with n isoprenoids residues in cis configuration and m in trans. Adapted from¹²²

In particular, polyprenols are found in bacteria and photosynthetic tissues, while dolichols are present in mammalian tissues and yeast cells.¹²²

Several mechanisms, for biosynthesis of dolichol, were proposed and the most accepted one was suggested by Ekström *et al.* in 1984.¹²⁴

De novo synthesis of dolichol starts from isopentenyl pyrophosphate (IPP), which links to dimethylallyl pyrophosphate (DMAPP), with formation of geranyl pyrophosphate (GPP).

This biosynthetic step is catalyzed by the enzyme farnesyl pyrophosphate synthase (FDPS). Then, this is followed by an additional step, to give farnesyl pyrophosphate (FPP).

Other IPP units are added, step by step, to FPP in *cis*-configuration, via *cis*-prenyl transferases (DHDDS), until the formation of a long polyprenoid, embedded in the ER membrane, is completed.

The pyrophosphate moiety, of this chain, is located on the cytosolic face of the ER.

At this or stage of the synthesis, the pyrophosphate group is cleaved by an unknown phosphatase, the double bond in α is reduced by steroid 5- α reductase 3 (SRD5A3).

Finally, a phosphate is enzymatically linked from cytidine triphosphate (CTP) to the hydroxyl group of the dolichol, by dolichol specific kinase (DOLK), leading to dolichol phosphate (Dol-P) (**Figure 1.3a**).^{123,125}

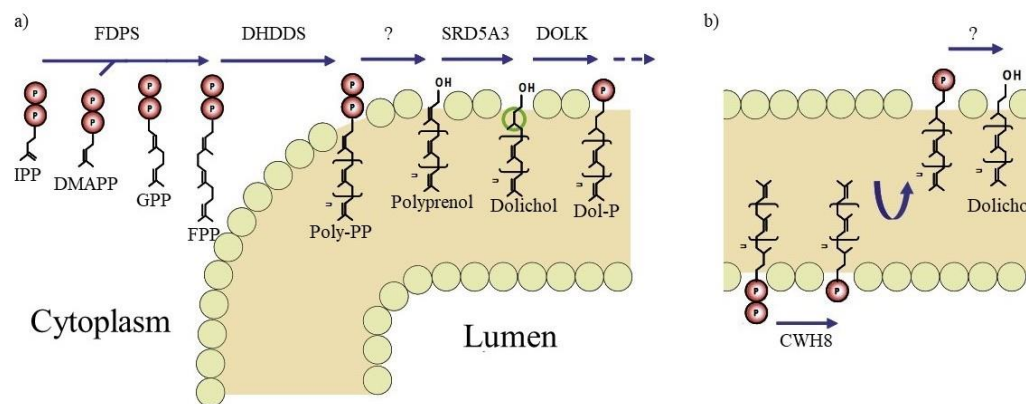


Figure 1.3 on ER membrane: a) *De novo* dolichol biosynthesis after a few catalyzed steps, leading to Dol-P, which acts as carrier of glycosylation; b) After glycan structure is linked to the growing protein, dolichol is reused for a new glycosylation step. Adapted from¹²⁵ and partially from¹²³

Once the dolichol is synthesized, it can act as carrier of glycosylation in the lumen of the ER; some sugar moieties are linked to Dol-P as phosphate derivatives, leading to a Dol-PP-glycan.

Once the glycan architecture is formed, it is cleaved from dolichol and transferred to the growing protein.

The resulting Dol-PP is converted to Dol-P (by pyrophosphatase CWH8); the latter is flipped to the cytosolic face of the ER and can be reused for a new glycan assembly (**Figure 1.3b**).¹²⁵

1.2 O-GLYCOPROTEINS

O-linked glycoproteins are a class of compounds where sugars are bound to the hydroxyl group of the side chain of threonine (Thr) and serine (Ser) residues, of a protein.¹²⁶

Examples of sugars found in humans include fucose, xylose, Glc, Man, GlcNAc and GalNAc. The latter is involved in the synthesis of a very important class of proteins in humans: mucin. There are different types of mucins, depending on the sugar directly linked to GalNAc moiety (see below).¹²⁷ These glycoproteins are very important because they are associated to many cell processes like cellular regeneration, signaling, adhesion, apoptosis, regulation in solute transport, receptors for commensal and pathogenic microbes and for leukocyte targeting, etc.¹²⁸

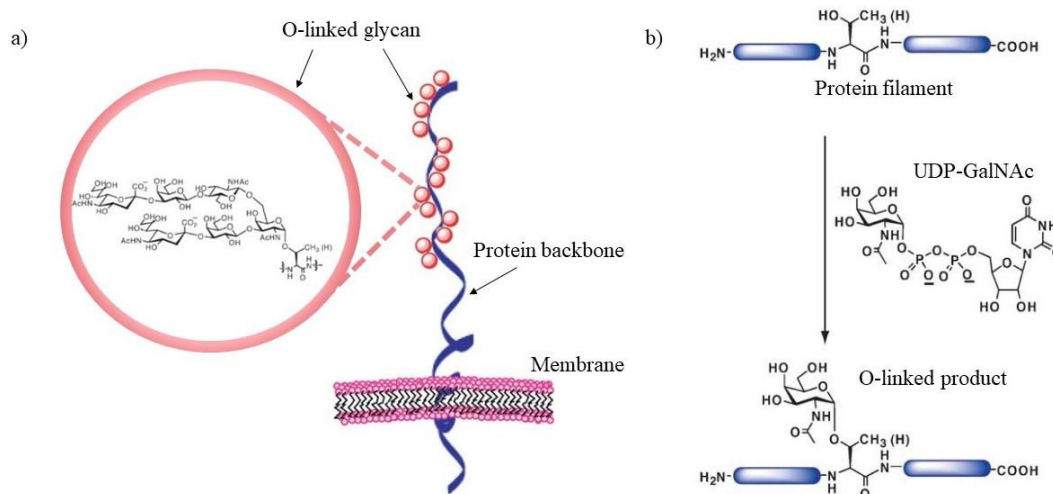


Figure 1.4 a) Membrane-bound mucin: protein backbone (blue ribbon) O-linked to glycan architecture (red-pink sphere); b) GalNAc is enzymatically cleaved from UDP-GalNAc and linked to the OH group of Ser or Thr. O-linked glycosylation. Adapted from¹²⁹

Their biosynthesis occurs in the Golgi apparatus, where the O-link formation between GalNAc and the hydroxyl group of Ser/Thr happens (**Figure 1.4a**).

The glycan moiety is provided by uridine-diphosphate-N-acetylgalactosamine (UDP-GalNAc), which is enzymatically cleaved and linked to Ser or Thr (**Figure 1.4b**).

After this first addition, other glycans are attached leading to a formation of a more complex oligosaccharide structure.

A failure in the assembly of this glycan architecture is associated to some diseases. For example, changes in mucin glycan structures can lead to an immunity reduction, leading to hematologic disorders and cancer in patients affected by Wiskott-Aldrich syndrome.¹³⁰

The synthesis of some O-glycoproteins starts in the ER and is then completed in the Golgi apparatus, like the O-mannosylation (**Figure 1.5**).

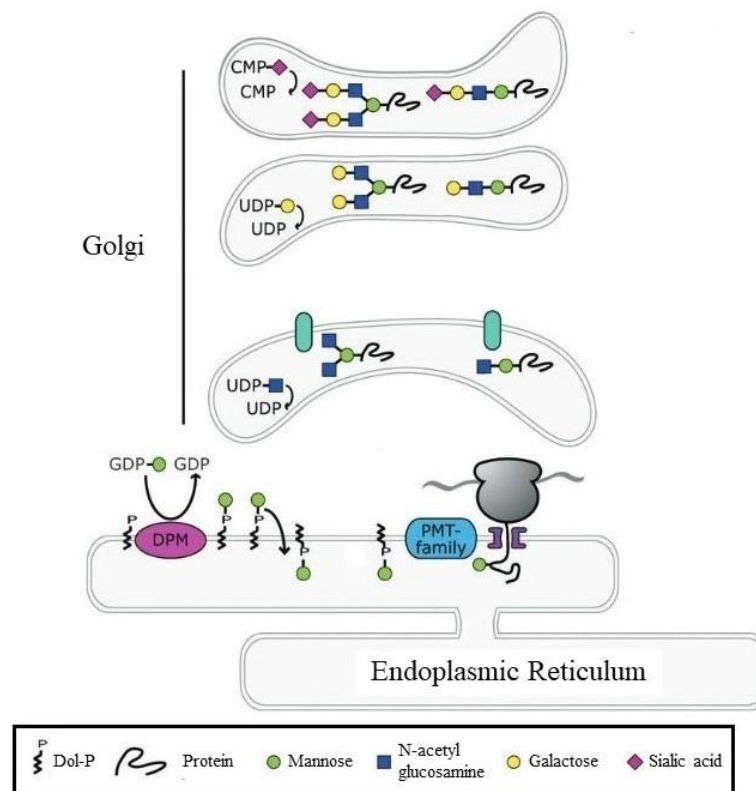


Figure 1.5 Dol-P-Man synthesis catalyzed by DPM, subsequent flipping in the ER lumen and O-link formation to the protein (PMT-family is a family of Dolichyl-phosphate-mannose-protein mannosyltransferases). The addition of other sugars occur in the Golgi apparatus. Adapted from¹³²

The synthesis is initiated in the ER and the mannosyl group is provided by dolichol phosphate β-D-mannose (Dol-P-Man). The precursor of the Dol-P-Man is guanosine diphosphate mannose (GDP-Man).

Dolichol phosphate β-D-mannosyltransferase (DPM) converts GDP-Man to Dol-P-Man.

Dol-P-Man, synthesized on the cytosolic face of the ER, is flipped in the ER lumen, where Dol-P-Man:protein O-mannosyltransferases (PMT-family) catalyze the O-link formation of the mannosyl moiety in Dol-P-Man to a serine or threonine residue of the protein entering the secretory pathway.

Then, the O-mannosyl protein is translocated to the Golgi apparatus, where further additions of glycans take place, leading to the elongation of the growing structure.

The complete biosynthetic pathway of such glycoproteins, however, is still subject to ongoing research, in order to fully understand these processes in mammalian.^{131,132}

1.3 N-GLYCOPROTEINS

N-linked glycoproteins are structures where glycans are linked to, typically, an amide nitrogen of an asparagine (Asn) residue, as a result of post-translational modification (PTM), leading to an increase of solubility and stability, and contributing to the folding process of the nascent polypeptide.¹³³

In this class of glycoproteins, the sugar is bound to an asparagine (Asn) residue of the protein, with a sequence Asn-X-Ser/Thr, where X can be any amino acid except proline. N-linked glycoproteins have many important roles, like cell-cell recognition, signal transduction, cellular growth, cell differentiation and programmed cell death.

Because of the importance of this type of modification, it is of no surprise that anomalous N-glycoprotein architectures are found in severe diseases, like breast, lung and prostate cancer. This is why, a method, which is able to identify diseases associated to anomalous N-glycoproteins, can be used for diagnosis, prognosis and a treatment prediction.¹³⁴

Furthermore, they are also involved in cellular immune response; in fact, N-glycosylated surface proteins of leucocytes, influence some of their biological activities, for example membrane orientation, folding, trafficking to the cell surface, ligand binding.¹³⁵

The synthesis of N-linked glycoproteins begins on the cytosolic face of the ER (**Figure 1.6**). Here, assembly of the first 7 glycans (GlcNAc₂Man₅), which are then transferred to Dol-PP leading to Dol-PP-GlcNAc₂Man₅ formation. This step is catalyzed by cytosolic glycosyltransferases (cytosolic GTs).

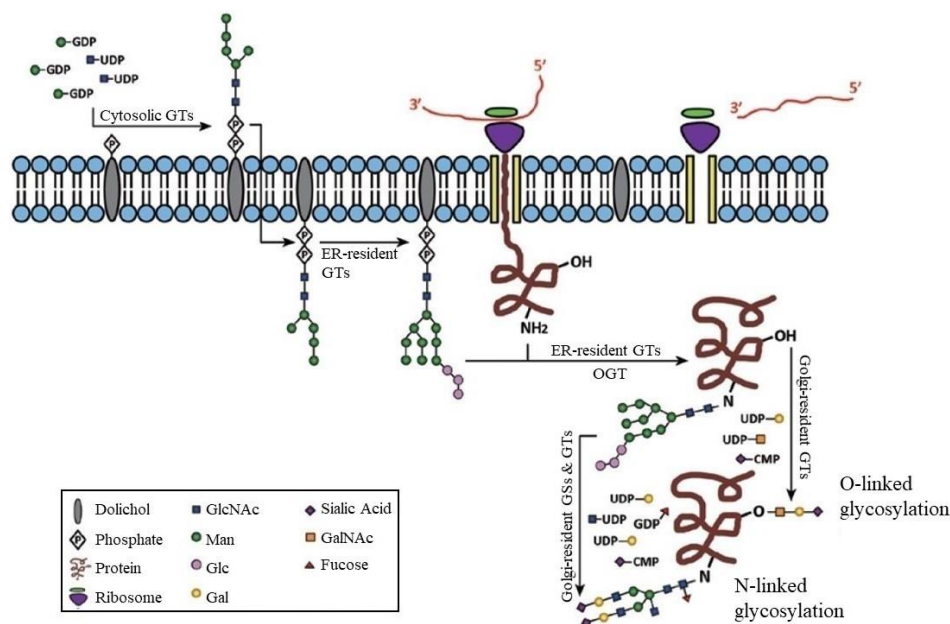


Figure 1.6 N-linked glycoprotein formation. The synthesis starts on the cytosolic face of ER, where cytosolic GTs catalyze the formation of Dol-PP-GlcNAc₂Man₅. Then, the latter is translocated in luminal side of ER, where additional sugars are catalytically (by ER-resident GTs) linked leading to Dol-PP-GlcNAc₂Man₉Glc₃. The latter is transferred in Golgi apparatus for protein maturation. On the same protein, it is possible to have O-glycosylation. Adapted from¹³⁷

Dol-PP-GlcNAc₂Man₅ is transferred from the cytosolic to the luminal side of the ER, where 7 additional sugar units are linked to give the branched structure of Dol-PP-GlcNAc₂Man₉Glc₃.

The precursors of the individual sugar units are uridine diphosphate GlcNAc (UDP-GlcNAc) for N-acetyl glucosamine, guanosine diphosphate Man (GDP-Man) for mannose and uridine diphosphate Glc (UDP-Glc) for glucose.

Glycans bond formation is mediated by a class of enzymes, ER-resident glycosyltransferases (ER-resident GTs), known as oligo glycosyltransferases (OGT), which remain in the lumen of the ER.

The last step is the transfer of this block of glycans, from Dol-PP to an Asn residue of a protein inside the ER, via an N-linked GlcNAc unit.^{136,137}

After these first modifications in ER, this new N-linked glycoprotein is introduced in Golgi apparatus and subjected to further modifications that lead to the final protein maturation.¹³⁸

1.4 GLYCOSYLPHOSPHATIDYLINOSITOL (GPI) ANCHOR

GPIs (**Figure 1.7**) are glycolipid structures added to a C-terminus of proteins in many eukaryotic cells. They are anchored on cell membrane and play an important role in signal transduction, cellular communication, immune response, etc.¹³⁹

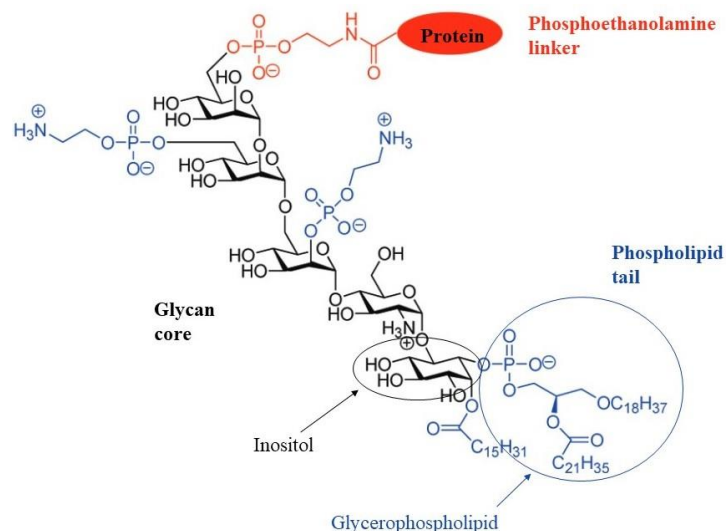


Figure 1.7 The three domains of GPI: phospholipid tail (blue), glycan core (black) and phosphoethanolamine linker (red). In circle, inositol moiety (for glycan core) and glycerolphospholipid (for phospholipid tail) are shown. Adapted from¹³⁹

They consist of three domains: 1) phosphatidylinositol, which is made by a phosphate linked to a glycerol holding two lipid chains and an inositol moiety linked to sugars in order to form a 2) glycan core; the latter is bound to a C-terminus amino acid of a protein via a 3) phosphoethanolamine linker.¹³⁹

The epithet “anchor” is due to the fact that the lipid chains are embedded into the ER membrane and the proteins on the “other side” of the GPI are sort of attached/anchored to it.¹⁴⁰ GPI biosynthesis starts on the cytosolic face of the ER, with the first addition of GlcNAc to phosphatidylinositol (PI) anchored in the ER membrane, via GPI-GlcNAc transferase, generating the intermediate GlcNAc-PI (**Figure 1.8**).

GlcNAc-PI is de-acetylated by GlcNAc-PI deacetylase, leading to glucosamine-PI (GlcN-PI). This structure is translocated to the luminal side of the ER and additional sugars are attached: three mannose residues, from Dol-P-Man, are added to this growing structure via a glycosylphosphatidylinositol-mannosyltransferases (GPI-MT1, GPI-MT2 and GPI-MT3 for the three mannoses, respectively).

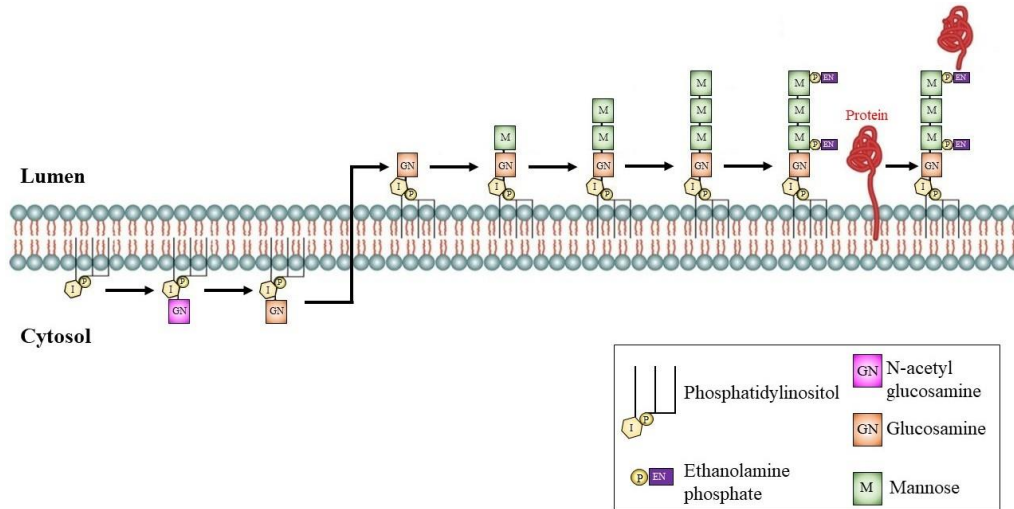


Figure 1.8 GPI synthesis in the ER; each step is catalyzed by the proper enzyme. The synthesis starts from cytosolic face of ER, with the addition of GlcNAc to PI with formation of GlcNAc-PI. Then the de-acetylation of the latter leads to GlcN-PI. This is translocated to the luminal face of ER, with the addition of three mannose residues. EthN-P is linked to the last sugar and then attached to the C-terminus of a newly synthesized protein. Adapted from¹⁴²

At this point, ethanolamine phosphate (EthN-P) is linked to the last sugar, which is, then, attached to the C-terminus of a newly synthesized protein, via an amide bond, by GPI-transamidase (GPIT).^{141,142}

In order to be recognized by GPIT, GPI must have, at least, one EthN-P residue and the recognition is the strongest when this residue is bound to the first mannose of the GPI glycan.¹⁴³

1.5 ENDOPLASMIC RETICULUM (ER)

The “machine”, where glycans are synthesized (N-glycoproteins and GPI anchors) or at least their synthesis starts (O-glycoproteins), is the Endoplasmic Reticulum (ER). Despite of its role in the glycoproteins synthesis, it is also responsible for proteins transport and folding, lipid and steroid synthesis, carbohydrate metabolism and calcium ions storage.¹⁴⁴

The ER represents the largest organelle in the cell and some domains can be built-up from nuclear envelope (NE) and a system which constitutes the peripheral ER, made up by flat sheets (or cisternae) and tubules.¹⁴⁴

In short, peripheral ER is a network of sheets and tubules spread all over the cytoplasm.¹⁴⁵

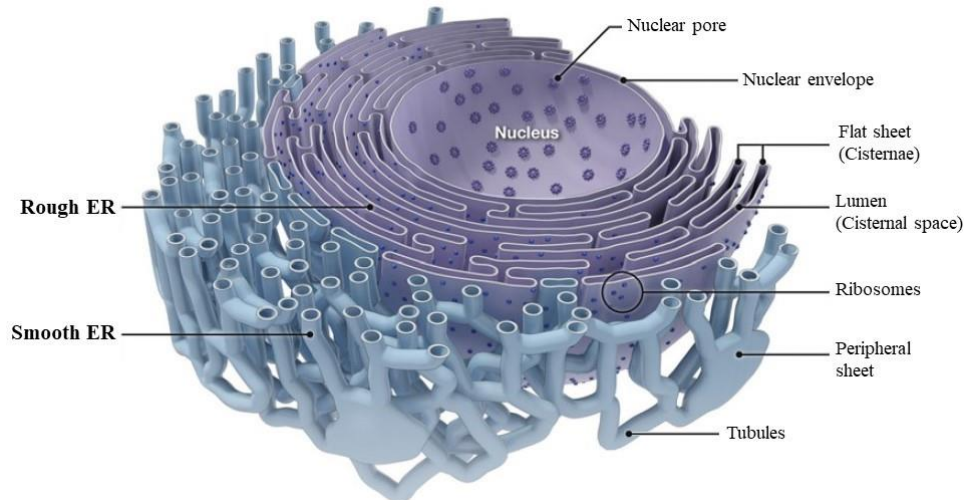


Figure 1.9 A schematic representation of ER. Adapted from¹⁴⁶

As shown in **Figure 1.9**, the structure of ER is a continuous membrane, which starts with the NE. That is formed by two lipid bilayers and it contains many nuclear pores, which allow the passage of material between nucleus and cytoplasm. Moreover, it is possible to define two areas: an inner and an outer nuclear membrane; the latter shares a common lumen (cisternal space) with the cisternae (flat sheets) of the peripheral ER.

The cisternae are studded with many ribosomes appearing like a “rough” surface, hence the name rough ER.

Rough ER is designated to the biosynthesis, folding, post-translational modifications, for secreted and integral membrane proteins¹⁴⁴ (like some N-glycoproteins).

The tubular area is named Smooth ER, because of the absence of ribosomes and it is specialized for lipid synthesis and delivery, calcium signaling, sites of contact for other organelles and carbohydrate metabolism.¹⁴⁶

The ER structures are shaped by several proteins and, in particular, reticulons family are well studied. They are found at the curved edges of ER sheets and in tubules.

The level of this reticulons defines the tubulars structure and their abundance. In fact, the formation of long tubules, at the expense of sheets, is due to the overexpression of some isoform of these proteins; but their depletion, and their capability to bend membranes, reduces the numbers of tubules, leading to a formation of peripheral sheets.^{144,146}

CHAPTER 2

1 FLIPPING ACROSS MEMBRANES

As already depicted in the last chapter, the assembly of the glycan, as well as the post-translational attachment to the proteins, involves many steps.

The biosynthetic route is essential to eukaryotes and archaea organisms and requires a complex enzymatic machinery. Any defect in the synthesis of the glycan structure and the attachment to proteins, leads to a large family of genetic diseases, which are classified as Congenital Disorders of Glycosylation (CDG).¹⁴⁷

In order to sustain cellular life, polar lipids must be translocated across both plasma membrane and in the other organelle membranes in eukaryotes and the bacterial cytoplasmic membrane.^{148,149}

This translocation, from one side to another does not occur spontaneously, because it requires an energetic cost. For this reason, cells have some membrane protein, which accelerate this flipping.¹⁴⁸

These proteins can be split in three categories: flippases, floppases, and scramblases.¹⁵⁰

The flippases catalyze the transport from outer to inner side of the membranes, whereas floppases supports this translocation in the reverse direction. Both of them uses energy from hydrolysis of ATP. As an example of these two can be mentioned P4-ATPases as flippase and ATP-binding cassette (ABC) as floppase.¹⁵¹

On the other hand, scramblases are ATP-independent protein and they are responsible for a bidirectional movement across membrane.¹⁵⁰ An example of scramblase is rhodopsin.¹⁵²

These scramblases are required in the endoplasmic reticulum (and bacterial cytoplasmic membrane) for a variety of glycosylation pathways.¹⁵²

As already described in the previous section, the synthesis of glycans begins on the cytosolic face of the ER, then continuous on the luminal side. The translocation of the

glycan precursor does not occur spontaneously, but it is facilitated by scramblases, as ATP-independent translocator (**Figure 2.1**).^{153,154}

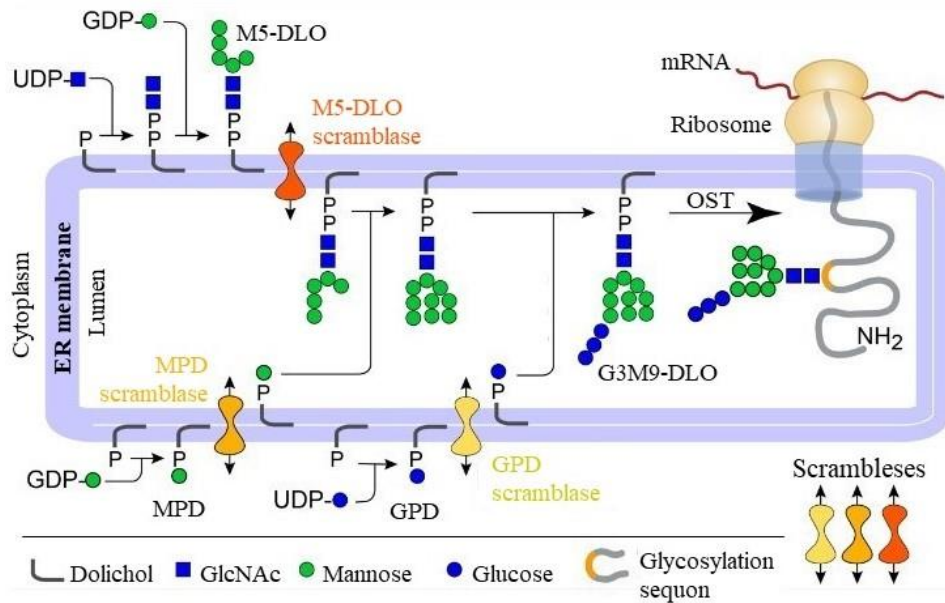


Figure 2.1 Scramblases catalyze the “flipping” of the glycan precursors (MPD, M5-DLO and GPD) from cytosolic face to luminal side. Once the assembly of the glycan is completed, OST catalyzes the link of the complex carbohydrate structure to the protein that is been translated. Adapted from¹⁵⁵

It has been hypothesized the existence of three distinct scramblases, which have shown their ability to discriminate between different isomers of glycolipid substrates.^{155,156}

As already discussed for N-linked glycoproteins, there is the formation of Dol-PP-GlcNAc₂Man₅ (M5-DLO) on the cytosolic face of the ER. Additional glycans are added on the luminal side and the translocation is catalyzed by one of the scramblases, in this case M5-DLO scramblase.

In the lumen, M5-DLO is extended to Dol-PP-GlcNAc₂Man₉ (M9-DLO) with the addition of further mannose units, then to Dol-PP-GlcNAc₂Man₉Glc₃ (G3M9-DLO) after three glucose residues are attached.

Finally, G3M9-DLO is linked to the amide nitrogen of an asparagine via the oligosaccharyltransferase (OST).

Precursors of mannose and glucose are GDP-Man and UDP-Glc respectively; these two, on the cytoplasmic face, are first linked to a Dol-P leading to formation of Dol-P-Man

(MPD) and Dol-P-Glc (GPD); then these latter two are flipped in the lumen by their specific scramblases: MPD scramblase and GPD scramblase.¹⁵⁵

There are clear evidence about the existence of scramblases (at least in case of the ER), but their molecular structure, and so their mechanism, is still unknown.¹⁵⁷

Shed light on comprehension about the nature, and how they work, of this particular class of proteins is a major challenge in cell and structural biology.

2 SINERGIA

To accomplish this goal an interdisciplinary team was assembled. A collaboration between three groups, who bring their expertise: Prof. Dr. Anant Menon (Weill Cornell Medicine, New York, USA); Prof. Dr. Peter Bütikofer (Institute of Biochemistry and Molecular Medicine, University of Bern, Switzerland); Prof. Dr. Robert Häner (Department of Chemistry and Biochemistry, University of Bern, Switzerland).

This interdisciplinary team is supported by the SNSF (Swiss National Science Foundation), who has financed this project **Sinergia**.¹⁵⁸

With the Sinergia project, the SNSF wants to promote promising areas of research where a synergistic approach is needed to address complex and innovative scientific issues.

Accordingly, Sinergia supports interdisciplinary, multidisciplinary and unidisciplinary projects initiated by cooperating research teams, in which innovative research is planned. As a rule, all Sinergia applicants must be established researchers conducting their research in Switzerland.

If three or more candidates are involved, one of them may be based at a research institute abroad if his/her expertise are indispensable, i.e. not available in Switzerland (2+1, 3+1).

The duration of the grant is up to 4 years.¹⁵⁹

3 GOAL OF THE SINERGIA PROJECT

The aim of this Sinergia project is the identification, and the study, of the scramblases involved in the translocation of the glycan in the ER.

In particular, the efforts are oriented to the study of scramblases responsible for flipping of M5-DLO, MPD and GPD (**Figure 2.2**).

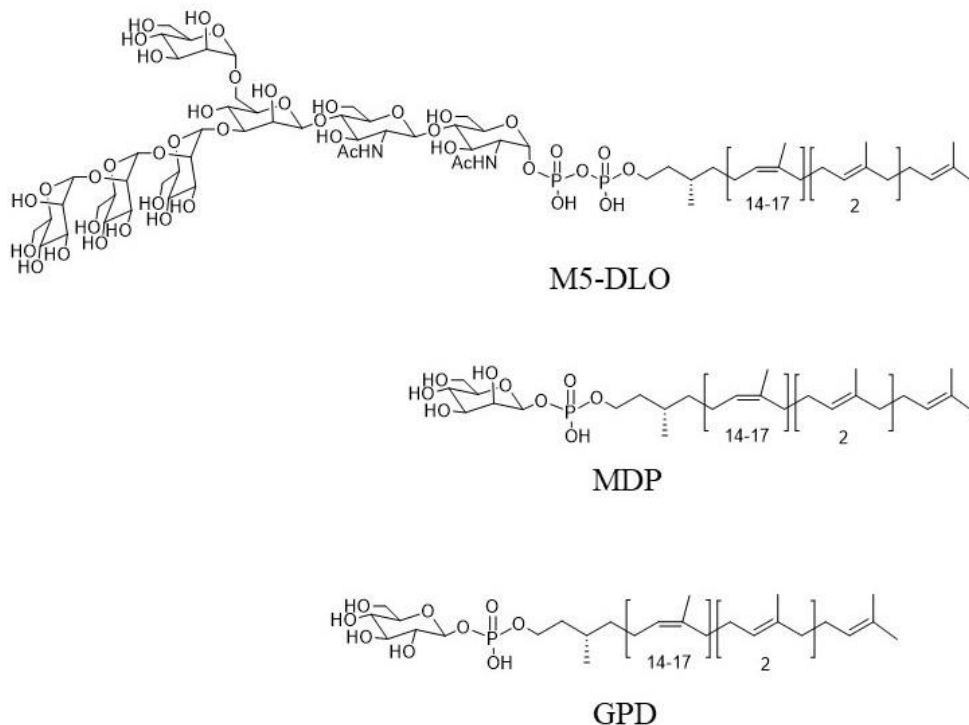


Figure 2.2 Chemical structures of M5-DLO (Dol-PP-GlcNAc₂Man₅) and MPD (Dol-P-Man) and GPD (Dol-P-Glc). At the moment, we are only focused on synthesis of M5-DLO and MPD analogues, since GDP represents the source of glucose residues, which are linked to M9-DLO (leading to G3-M9-DLO) in the luminal side of ER.¹⁵⁵

The groups of Bütikofer and Menon are in charge of the biochemical experiments of this Sinergia project, while our group carry out the chemical synthesis of probes used for the studies about scramblases.

The idea is to synthesize molecular probes that mimic the natural substrates, in order to be recognized by potential scramblases candidates, thus, allowing their isolation and characterization.

In order to simplify the synthetic paths, M5-DLO derivatives contain only chitobiose (GlcNAc₂) as sugar moiety, since as suggested by previous studies, it can be translocated across the membrane, being recognized by the enzymes involved.^{160,161}

About the dolichol chain, its synthesis is very demanding because it requires many steps, exceeding the time frame of the Sinergia. For this reason, a shorter derivative was prepared, made up by the *S*-Citronellol (Cit) linked to a dodecyl chain, obtaining the corresponding product Cit-Dod.

The two analogs synthesized are both of them tail-labeled: one containing a photoclickable group and the other a fluorescent tag (**Figure 2.3**).

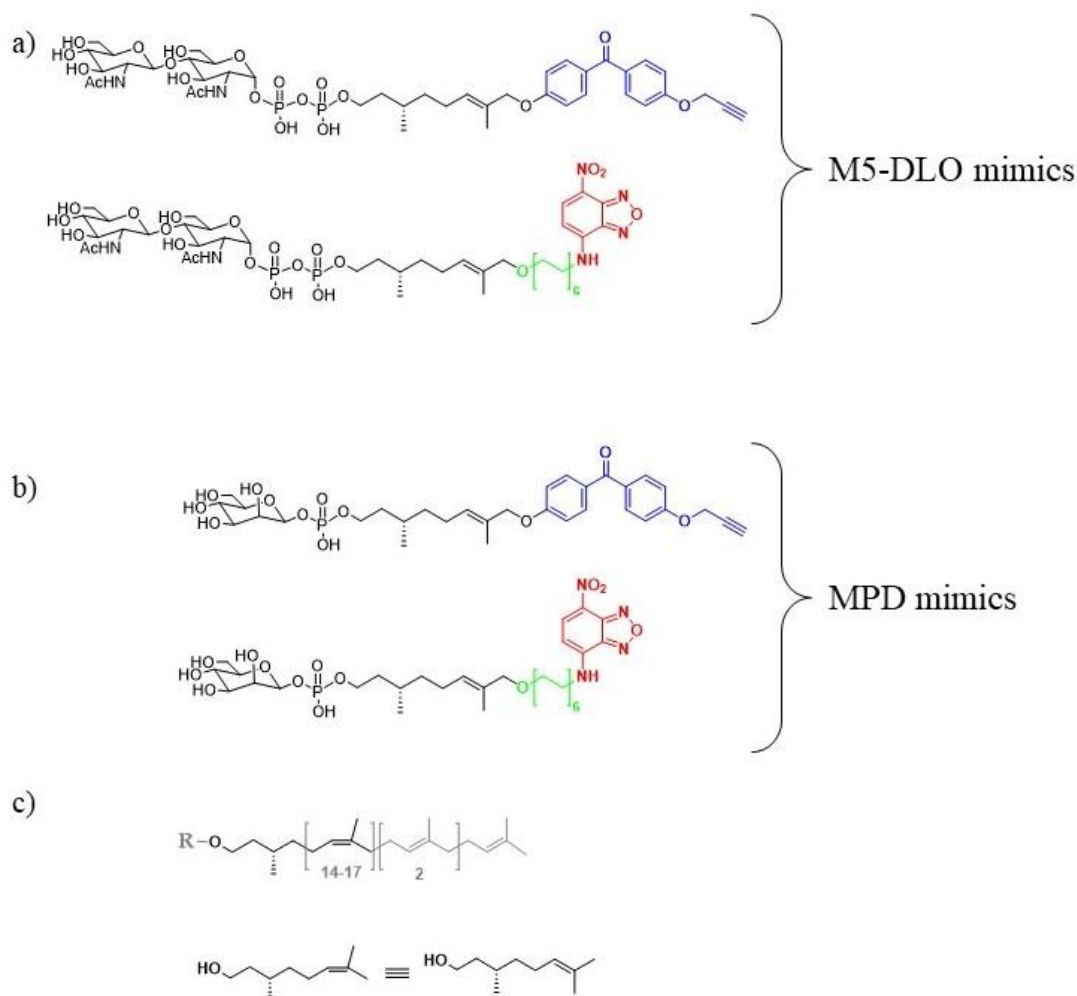


Figure 2.3 Probes used as mimic of natural structures. a) M5-DLO mimics: GlcNAc₂ is linked (top) Cit-BP and to Cit-Dod-NBD (bottom) through a pyrophosphate group. b) MPD mimics: mannose is linked to Cit-BP (top) and Cit-Dod-NBD (bottom), via phosphate bridge. In Cit-BP, BP is blue colored, whereas in Cit-Dod-NBD, Dod is green and NBD is red. c) *S*-Citronellol moiety in the dolichol chain. In figure, “R” can be either PP-GlcNAc₂ or P-Man.

These two molecules are used for two different strategies (see below for the details). In particular, the photoclickable probe is photocrosslinked to its target, upon UV-irradiation. In this way, the scramblase candidates can be “fished” out and identified by mass spectrometry.

Instead, the fluorescent probe is a convenient method for scramblases assay: the tests are able to discriminate between vesicles lacking and/or possessing the appropriate scramblases.¹⁵⁸

The photoclickable probes (top in **Figure 2.3a** and **Figure 2.3b**) are formed by an *S*-Citronellol coupled to benzophenone bearing a propargyl group (BP), with formation of Cit-BP.

Cit-BP is linked to sugars via either a pyrophosphate bridge (for a M5-DLO mimic) or a phosphate (like in the case of a MPD mimic).

Also here, previous studies have showed that a structure with these features is recognized by enzymes involved in the dolichol pathway.¹⁶²

The fluorescent probes (bottom in **Figure 2.3a** and **Figure 2.3b**) are made by a *S*-citronellol coupled to a dodecyl alkyl chain linked to 7-nitrobenzofurazan (NBD, the fluorescent tag), via an amino group (Cit-Dod-NBD).

Cit-Dod-NBD is linked to sugars for preparation of M5-DLO and MPD mimics, depending if it is linked to sugar moieties, through a pyrophosphate or a phosphate group. Finally, *S*-citronellol is a C₁₀ monoterpene molecule, which corresponds to the α -saturated isoprenoid group of the dolichol chain (**Figure 2.3c**)

It has been proved that *S*-citronellol, linked to a glycosyl phosphate, can be used as a dolichol analogue for a transbilayer movement in the ER membrane.^{163,164}

3.1 STRATEGIES FOR THE IDENTIFICATION

The approach with the photoclickable probe uses Cit-BP as dolichol analogue linked to either PP-GlcNAc₂ or P-Man (**Figure 2.4**). The analogue will be incubated with microsomes or a crude mixture of ER membrane proteins (Step 1).

The probe can bind to the scramblases. Then, the system will be UV irradiated, with the radical formation of the benzophenone, leading to a covalent bond with the protein target (Step 2). More in particular, irradiation generates a triplet ketyl biradical, which reacts with the functional groups of proteins.¹⁶⁵ Several approaches have already used benzophenone linked to short isoprenols in order to be inserted into proteins after photoirradiation at 365nm.¹⁶² Activation at this wavelength does not cause many damages to proteins.¹⁶⁶

The process continues (Step3), dissolving the adduct in (sodium dodecyl sulfate); then, the propargyl group on benzophenone reacts, via click chemistry, with azide-biotin in order to form a permanent bond between biotin and the probe covalently linked to the

target (Step 4). The next step is to use a streptavidin resin (Step 5), for capturing the adduct. Streptavidin is a tetrameric protein, which shows high affinity with biotin, and is able to bind up to four molecules.¹⁶⁷

At this point, the resin will be washed (Step 6) and the bound proteins will be subjected to trypsinolysis (Step 7).

Finally, the resulting peptides will be analyzed at mass spectrometry for protein identification.¹⁶⁸

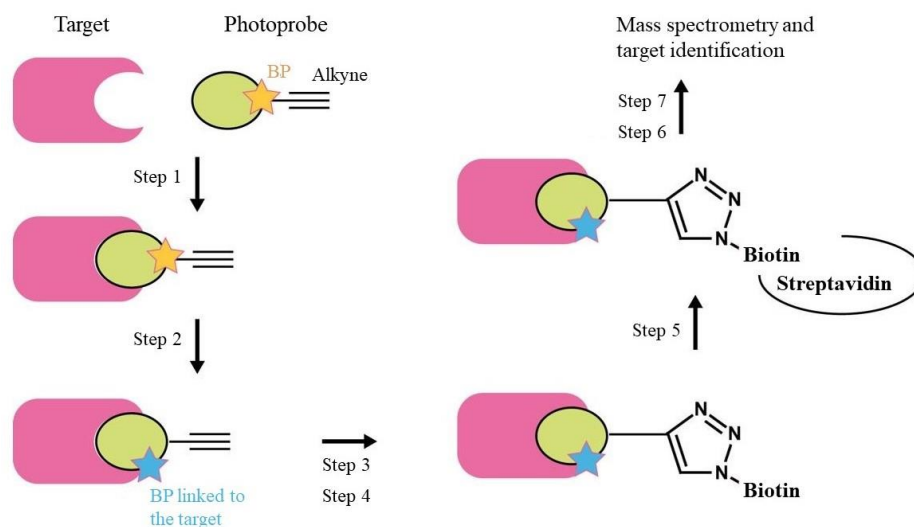


Figure 2.4 General procedure for protein identification via click chemistry. Step 1: photoclickable probe binds to the target (BP = benzophenone); Step 2: covalent bond with the target, after UV irradiation; Step 3: SDS dissolution; Step 4: click chemistry with azide-biotin; Step 5: the adduct is captured by streptavidin on resin; Step 6: washing of the final structure; Step 7: trypsinolysis with peptides formation, which will be analyzed to mass spectrometry for proteins identification. Adapted from¹⁶⁸

The fluorescence-based approach uses Cit-Dod-NBD as dolichol analogue, linked to either PP-GlcNAc₂ or P-Man.

This method is based on previous studies and requires the incorporation of the probes in pre-existing membranes.¹⁶⁹ The fluorescence assays using the NBD tag is described in **Figure 2.5**.

Phosphate and pyrophosphate, due to their polarity, are located towards the aqueous environment, while the isoprenoid chain remains within the hydrophobic fatty acid chains.¹⁷⁰ NBD localizes at the membrane-water interface.^{171,172}

The fluorescent probe will be symmetrically reconstituted into larger unilamellar vesicles, lacking a scramblase or possessing an appropriate one.¹⁵³

All the vesicles will be treated with impermeant reductant dithionite, which reduces NBD in its non-fluorescent amino form: ABD (4-amino benzofurazan).

In this way, only 50% of NBD will be reduced (with loss of fluorescence) in vesicles with no scramblases, because the half was in the outer leaflet and exposed to dithionite; those in the inner leaflet will be protected from reduction.

Instead, in vesicles with scramblases all NBD will be reduced, because scramblases will flip the probe from the inner to the outer leaflet (and vice versa), leading to a reduction of all fluorescent tags, resulting in 100% loss of fluorescence.¹⁶⁸

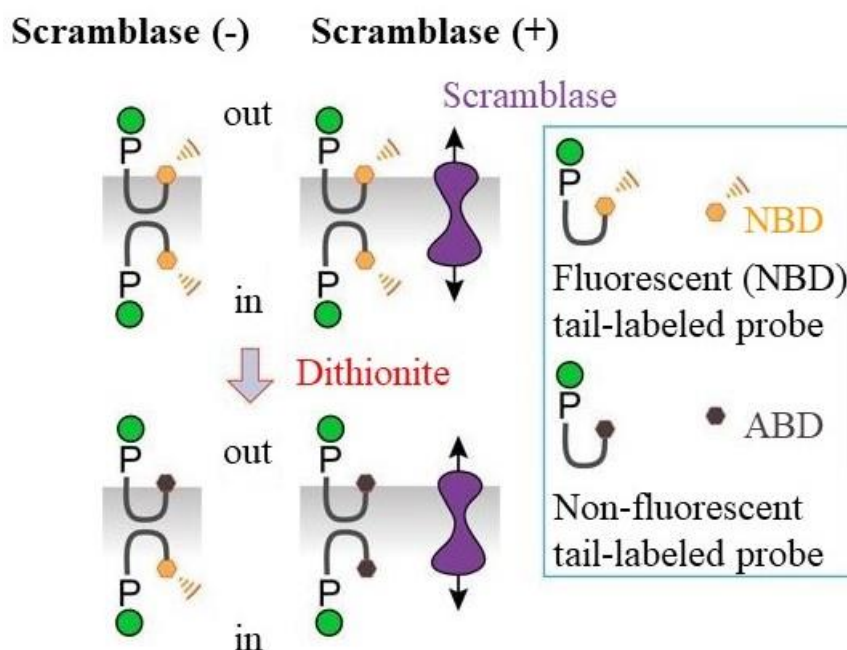


Figure 2.5 NBD-labeled probe reconstituted into unilamellar vesicles. Treating vesicles with no scramblases (Scramblase (-), on the left) with dithionite, only half show a loss of fluorescence; on the other hand, for vesicle with scramblases (Scramblase (+), on the right), the treatment with dithionite causes 100% loss of fluorescence. Adapted from¹⁶⁸

This method will be used for measuring the MPD, M5-DIO and GlcN-PI scramblase activity in synthetic lipid vesicles. In this way, the scramblases functions to specific proteins will be assigned. Then, these tests will be validates *in vivo*.¹⁵⁸

4 AIM OF THE THESIS

As a part of this Sinergia project (see above), my work aimed for the synthesis of a NBD-labeled dolichol chain mimic (**Figure 2.6**).

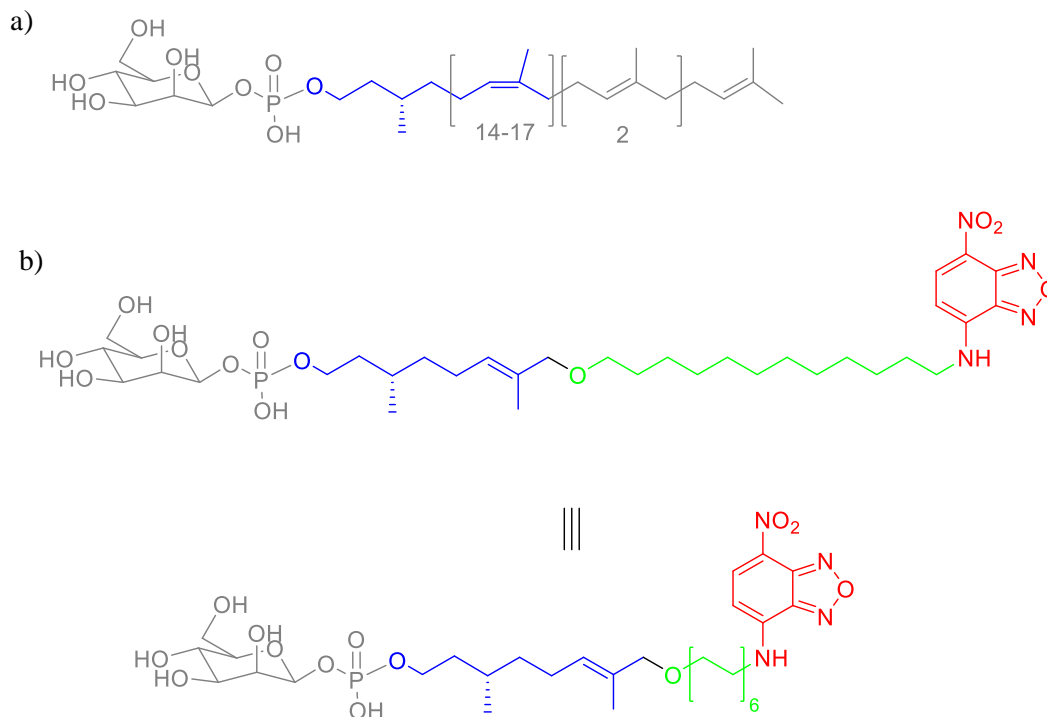


Figure 2.6 Comparison between a) natural dolichol structure and b) dolichol mimic probe synthesized for the Sinergia project: the *S*-citronellol moiety is linked to dodecyl alkyl chain, which bears the NBD tag via an amino group.

Naturally occurring dolichol is a long polyisoprenoid chain and its synthesis is very challenging.

S-citronellol is a valid short-chain analogue as previous results showed^{163,164} and it could be directly coupled to NBD.

But in order to accommodate for better positioning of the NBD fluorophore in close proximity of the membrane-water interface, a dodecyl alkyl chain was introduced as linker between *S*-citronellol and the fluorescent tag.

Since *S*-Citronellol (like dolichol) remains within the lipid bilayer,^{163,164,170} we thought to increase the length of the lipidic moiety of the probe.

In this way, due to the flexibility of the chain, the tail likely rolls up in order to allow NBD to accommodate on the membrane-water interface.

The analogue synthesized in this thesis was Cit-Dod-NBD linked to P-Man. The detailed synthetic steps for the synthesis of the probe are described in the next section.

This will be used for the identification of the MPD scramblase activity.

CHAPTER 3

1 SYNTHESIS OF A DOLICHOL MIMIC

This part of the thesis is focused on the synthesis of a dolichol mimic (**Cit-Dol-NBD**), with a terminal NBD group (or fluorophore) as fluorescent tag (as described in chapter 2).

In the beginning, it was thought to synthesize the dolichol analogue (**Figure 3.1**) using the phosphoramidite synthesis with DNA synthesizer (see part A: chapter 2).

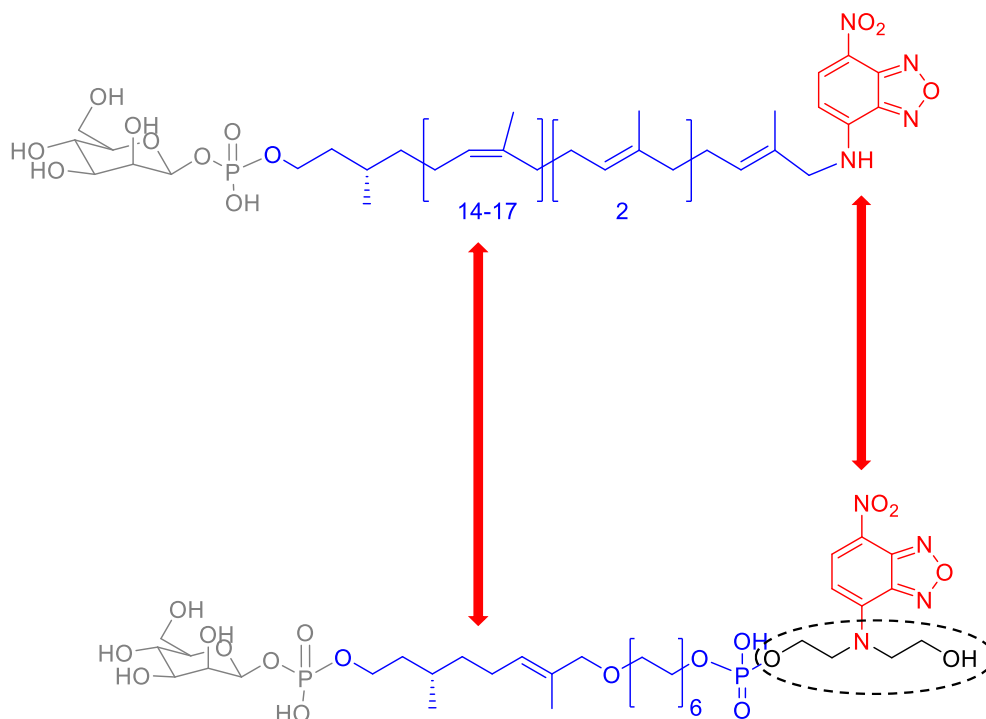


Figure 3.1 Comparison between: a) natural MPD derivative bearing NBD, with dolichol (blue) linked to a mannose via phosphate (grey) and NBD (red); b) synthesis of the (supposed) MPD mimick (blue) linked to both mannose (grey) and NBD (red) via phosphate bridge. NBD is bound to phosphate thanks to diethanolamine (black circle).

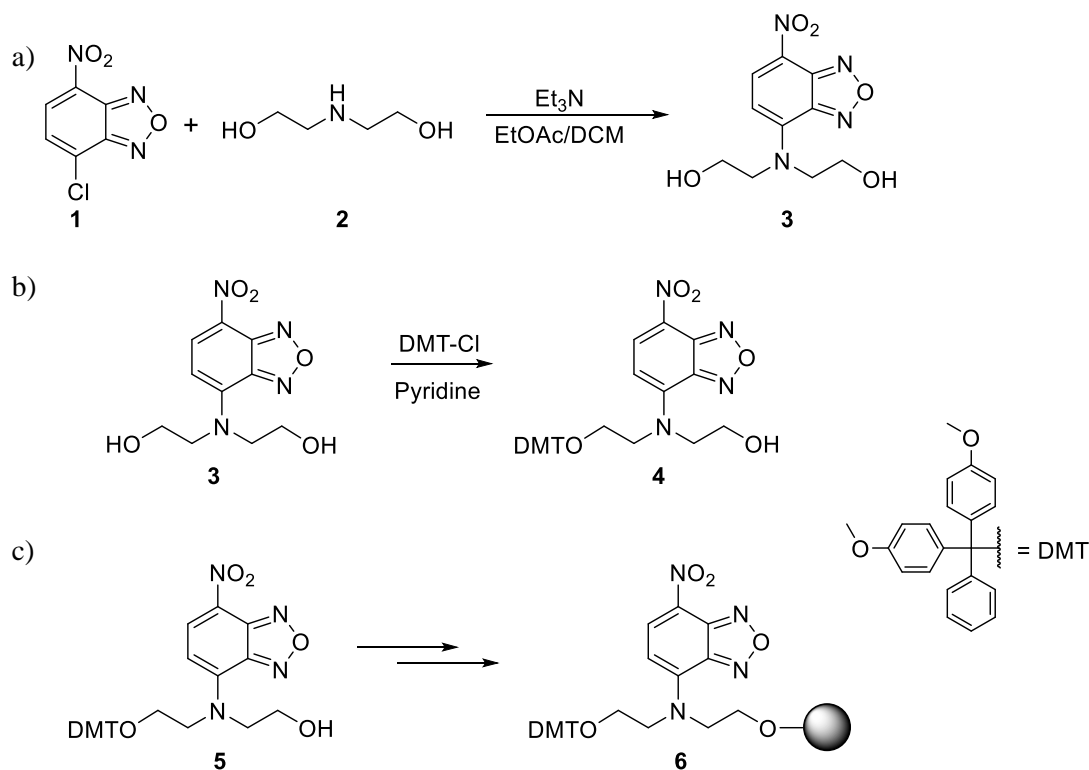
Using this method, NBD is not directly linked to the dolichol mimick structure via an amino group, but through a phosphate bridge. We thought that in this way, due to the

polarity of phosphate, it is preferable for NBD to be positioned in close proximity to the membrane-water interface.

As shown in **Figure 3.1**, NBD is linked to the amino functional group of diethanolamine. The latter serves two purposes: one of the two hydroxyl groups is linked to the phosphate, whereas the other OH-group is connected to the CPG solid support during the solid-phase synthesis on a DNA synthesizer using phosphoramidite chemistry.

2 USE OF DNA SYNTHESIZER

As already mentioned above, synthesis of the MPD mimic with the use of a DNA synthesizer starts with a NBD linked to a solid support. The synthetic routes are depicted in (**Scheme 3.1**).



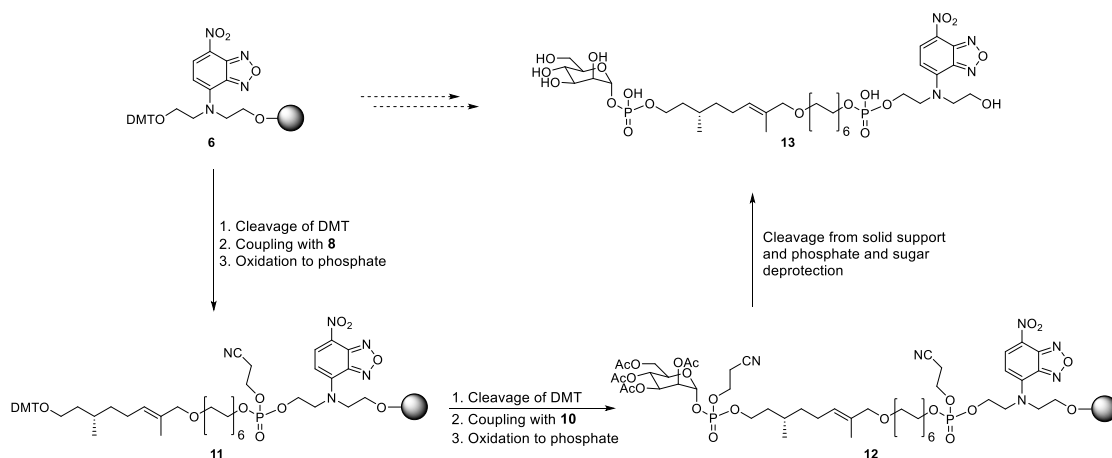
Scheme 3.1 Synthetic steps for formation of NBD N-linked to diethanolamine. The synthesis starts (a) with reaction between NBD-Cl (**1**) and ethanolamine. Then (b), one of the two OHs is protected with DMT with formation of **5**, while the other OH is linked to a CPG solid support (grey sphere), obtaining **6**.

Then, phosphorus (III) is oxidized to phosphate and the reaction cycle starts over with the removal of the DMT and subsequent coupling with **10**, followed by phosphorus oxidation, leading to **12**.

The protocol used, for the cleavage from solid support, was one of those employed in our group for phosphoramidite synthesis.

This regards the treatment with a 2M solution of ammonia (NH₃) in methanol (MeOH), overnight. The condition from solid support cleavage is able to deprotect both the two phosphates and the hydroxyl groups of the sugar (**Scheme 3.4**).

Then, the suspension was centrifuged and the supernatant was separated from the solid support and lyophilized overnight. The crude product was purified by HPLC and the mass was checked with mass spectrometry (MS).



Scheme 3.4 Schematic representation of the hypothetical synthesis of MPD mimic (**13**), with the use of a DNA synthesizer. The synthesis starts from **6**, and had to lead to formation of **13**, after several automated solid-phase synthesis steps.

Unfortunately, this strategy did not work and after several attempt, the product was not found. It is not sure at which stage the approach failed.

We think that this method did not work, probably, for problems due to the nature of NBD: in fact, it showed a low stability in a basic environment.

This was verified by the treatment of compound **3** with the same conditions, which should cleave and deprotect the target compound **12** (NH₃ in MeOH, 2M, overnight).

After this treatment, the solution was checked with TLC (using Hexane/EtOAc 1:1 as eluent), showing the formation of a second spot, which means **3** was turning in another

unknown product. Keeping the reaction longer in this condition, after 48 hours, all of compound **3** was completely converted into the unknown product.

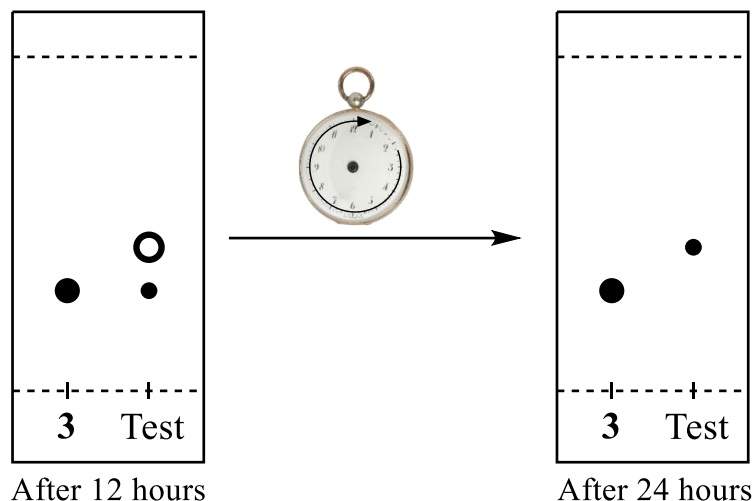


Figure 3.2 TLC plates of **6** in a solution of NH_3 (2M) in methanol (indicated with “Test”, while **3** represents compound **3** before the treatment). After 12 hours there is the formation of a second spot (TLC plate on the left). The lower spot (compound **3**) disappears completely after 48 hours (TLC plate on the right).

The results above were confirmed by recording a ^1H -NMR spectrum (**Figure 3.3**). The comparison of the spectrum of compound **3** before the treatment (**Figure 3.3a**) with NH_3 (2M) in MeOH and the spectrum of the reaction after 12 hours (**Figure 3.3b**) reveals the formation of a side-product.

In the spectrum before the treatment there is the presence of only five signals: the chemical shifts of the two aromatic protons are at 8.44ppm and 6.57ppm, while the aliphatic protons are at 4.14ppm and 3.77ppm and the protons of the -OHs at 5.00ppm.

When **3** was left in this solution of NH_3 methanol, the NMR shows the presence of additional peaks, shifted upfield.

Only the one at 8.47ppm (**Figure 3.3b**) has a different shape (here, it is a triplet while in **Figure 3.3a**, it was a doublet), but most likely this is due to an overlapping between the signals of two different species. The identity of this new compound was not determined, but it was concluded that NBD is not stable for a prolonged time under the tested conditions. Because the removal of protecting group approach relies on the use of basic conditions, further trials based on the same or similar approach were discontinued.

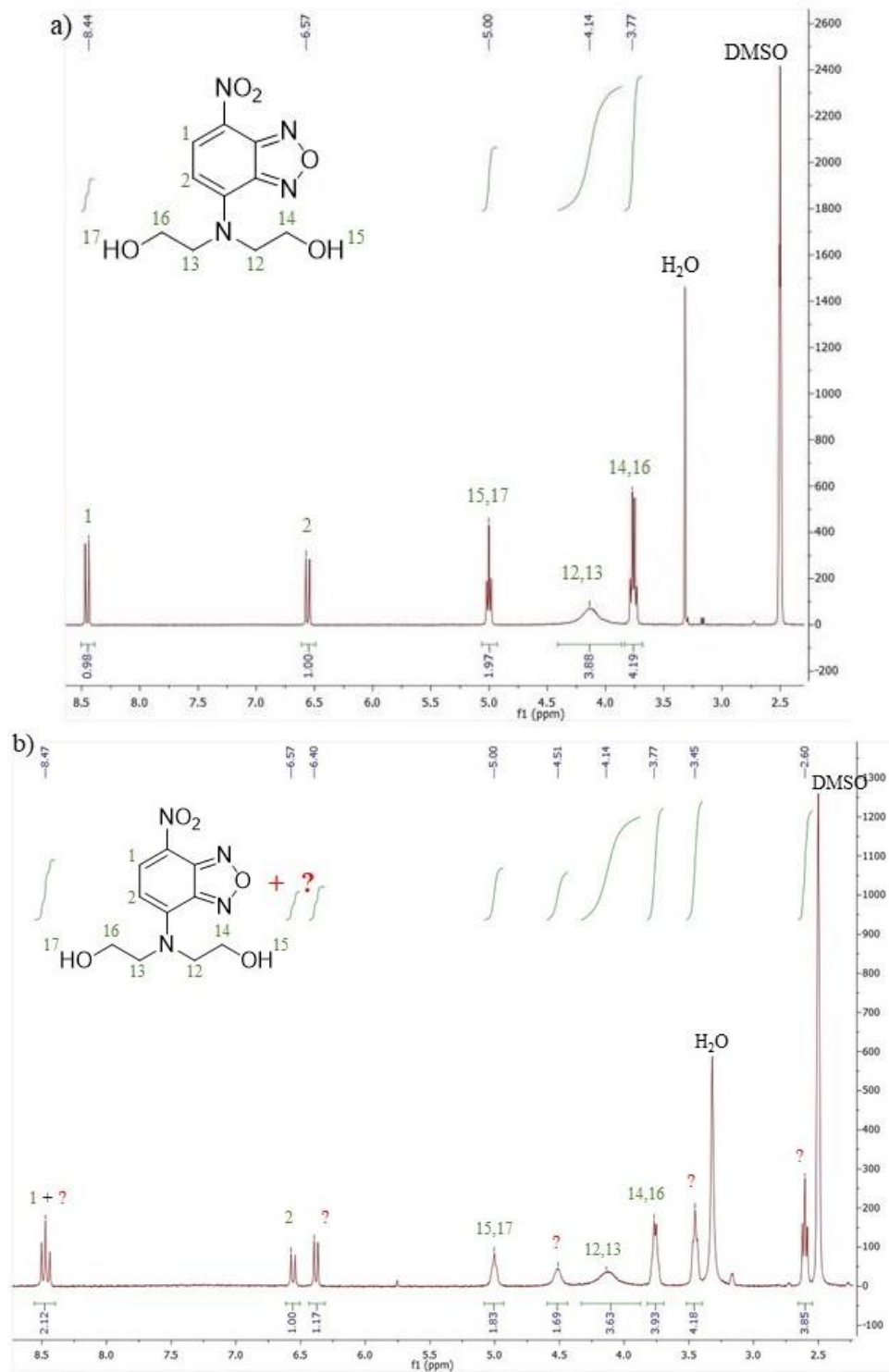


Figure 3.3 ^1H NMR comparison between: a) compound **3** before treatment with NH_3 (2M) in methanol and b) compound **3** after 12 hours of treatment. The solvent used for the NMR measurements was DMSO-d_6 .

3 SYNTHESIS IN SOLUTION

Based on the findings described above, the synthesis of a fluorescent MPD analog was changed from solid-phase to in-solution. In this approach, the NBD is linked directly to the alkyl chain of the dodecyl linker (**Figure 3.4**).

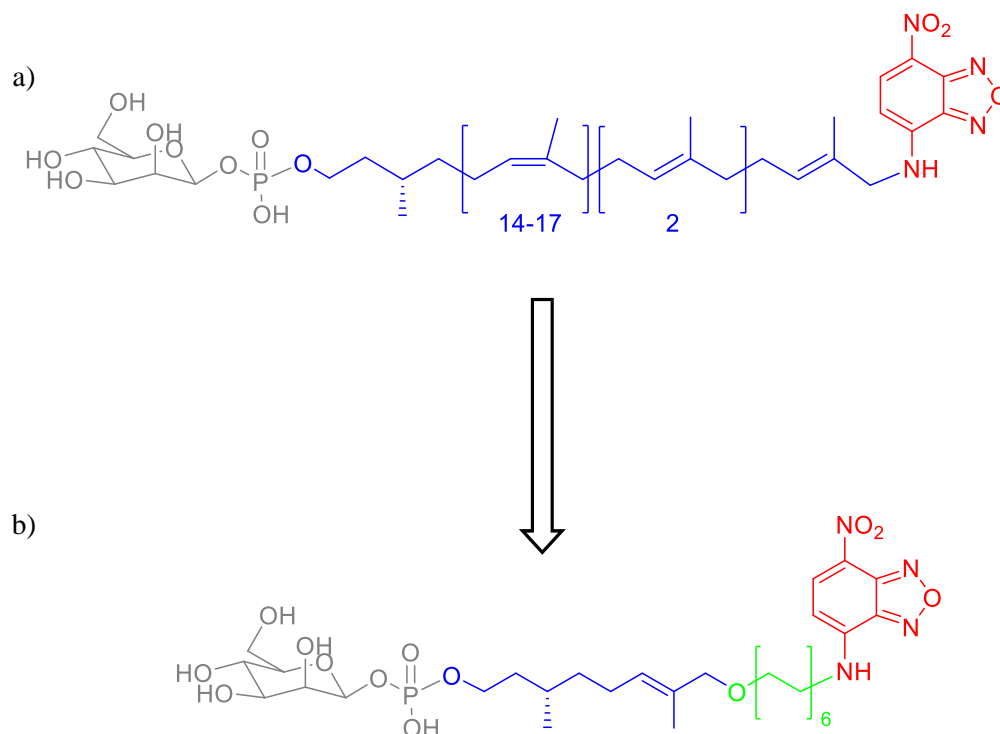


Figure 3.4 Comparison between natural MPD derivative linked to NBD (a) and the fluorescent MPD analogue (b) (synthesized in solution). In b, Citronellol (blue) is linked to a dodecyl chain (green), bound to NBD (red).

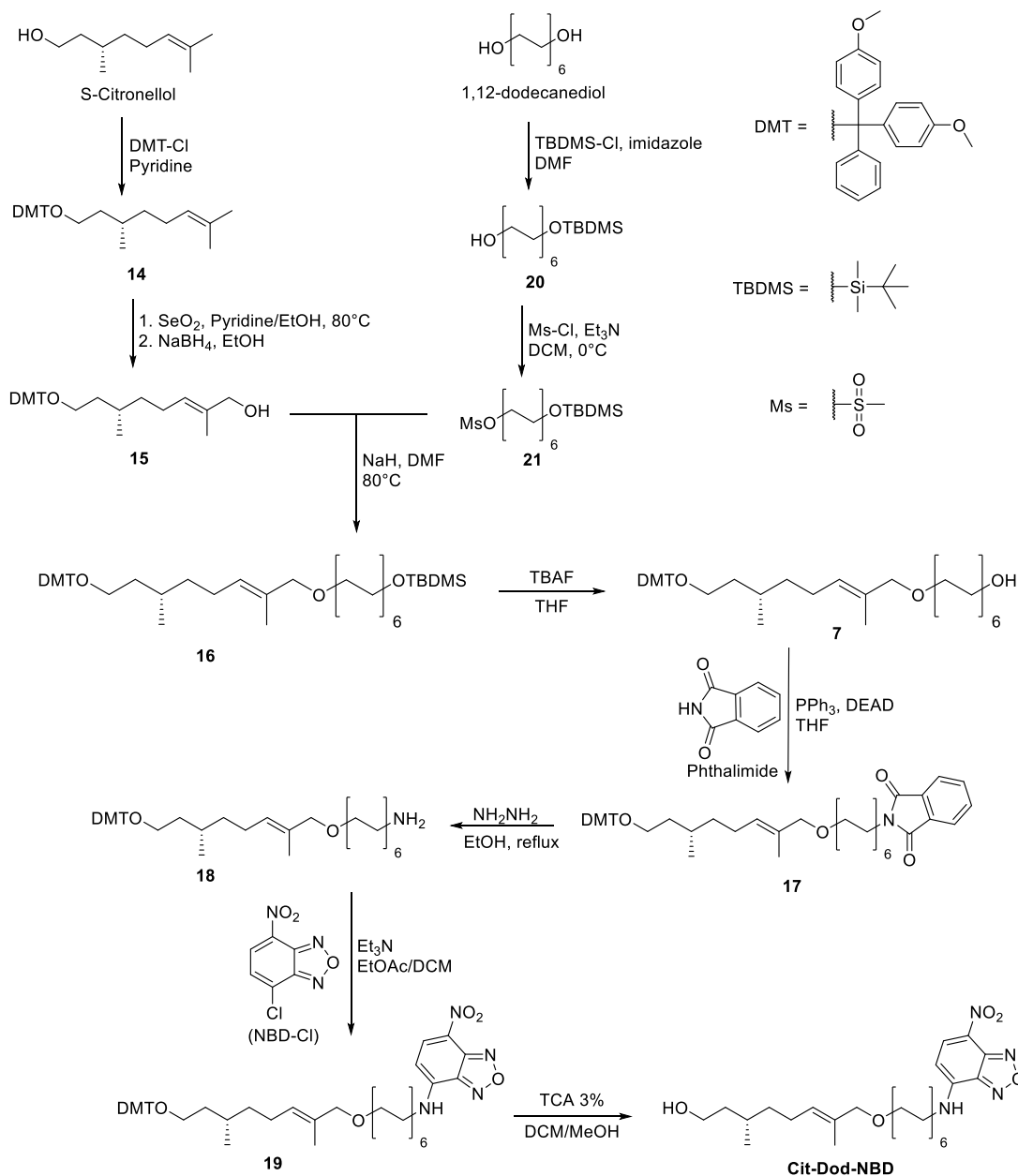
The goal of this part of the thesis was focused on the preparation of a dolichol mimic structure linked to NBD (leading to **Cit-Dod-NBD**).

The purpose of **Cit-Dod-NBD** is to be coupled to the mannose derivative (**10**), via a phosphate group, leading to **β -Man-Cit-Dod-NBD**. The latter is synthesized by Dr. Markus Probst (Häner group, DCB, University of Bern, Switzerland, 2018).

In **Scheme 3.5**, all the reaction steps for the synthesis of **Cit-Dod-NBD** are shown. The procedure starts with the protection of *S*-citronellol with DMT (obtaining **14**), followed by an allylic oxidation to afford **15**. In parallel, the synthesis of **20** is obtained by a monoprotection reaction of 1,12-dodecanediol with a silyl protecting group. In the next step, the free OH is converted into a mesylate, which is a better leaving group, obtaining

21. Then, the two compounds **15** and **21** are coupled through a Williamson ether synthesis, leading to **16**.

The next step of the synthetic procedure is a desilylation reaction of **16** and the corresponding OH (in **7**) is converted into an amino group.



Scheme 3.5 Reaction scheme for the synthesis of **Cit-Dol-NBD**.

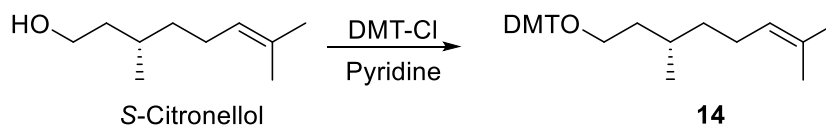
The compound **7** has been mentioned above. In here, the reaction steps, which lead to the synthesis are described.

This is made via phthalimide substitution, with the formation of **17**. Then, the phthalimide moiety is reduced to an amino group, to give **18**.

Finally, the amino functional group in **18** is coupled to NBD (using NBD-Cl) with the formation of **19**, which is subjected to treatment with TCA 3% in DCM/MeOH (dichloromethane/methanol), for DMT cleavage and formation of **Cit-Dod-NBD**.

3.1 SYNTHETIC STEPS

The first reaction was the protection of *S*-citronellol with DMT in pyridine with the formation of **14** (Scheme 3.6).



Scheme 3.6 Reaction scheme of the DMT protection of *S*-citronellol.

In order to make the coupling of **14** with 1,12-dodecanediol, a functional group on **14** was introduced.

Performing a Riley oxidation¹⁷⁴ leads to an allylic oxidation with the use of SeO₂. The latter is an oxidizing agent used in many organic reactions.¹⁷⁵

The general mechanism of the reaction is depicted in **Figure 3.5**.

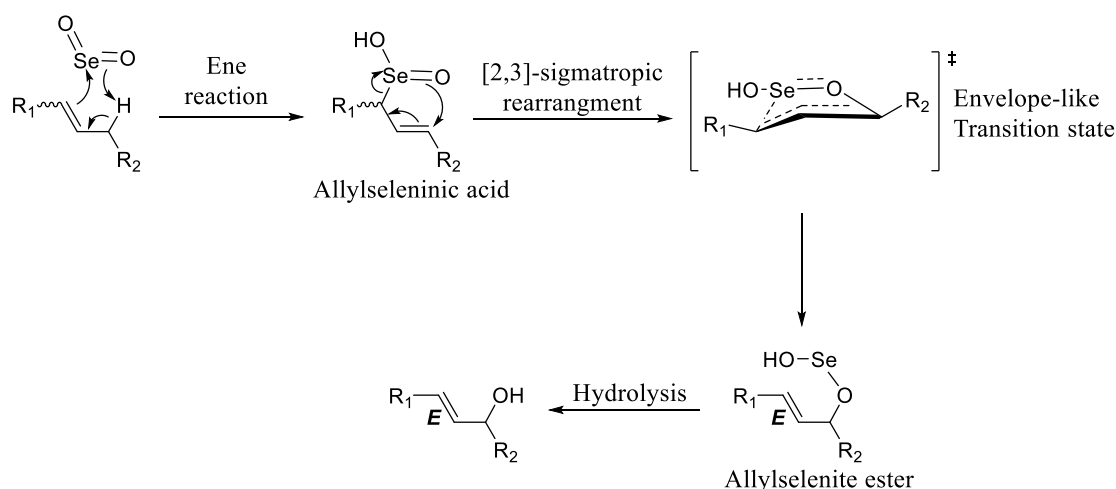


Figure 3.5 Reaction mechanism of the allylic addition of a hydroxyl group to an alkyl chain. The double bond is in *E*-configuration. Taken from ref.¹⁷⁶

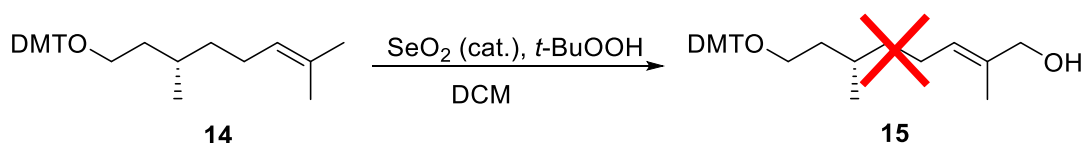
This oxidation starts via an ene reaction between the olefin (electron rich) and the selenium center (electron poor), with the formation of the allylselenenic acid. The latter

rearranges through a [2,3]-sigmatropic rearrangement, which leads to an allylselenite ester.

The subsequent hydrolysis generates the allyl alcohol as the reaction product.^{175,176}

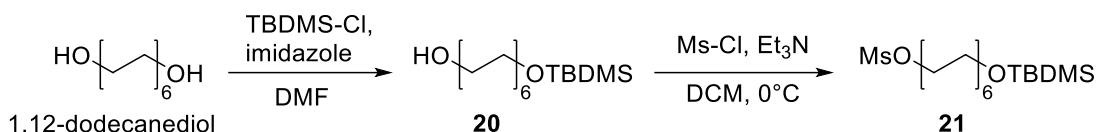
This kind of reactions show a high selectivity for the *E*-configuration due to the fact that the rearrangement proceeds through an envelope-like transition state (TS).¹⁷⁶

In the beginning, this synthesis was made using a catalytic amount of SeO₂ in the presence of *tert*-butyl hydroperoxide (*t*-BuOOH) in DCM, according to ref.¹⁷⁵ (**Scheme 3.7**). The role of *t*-BuOOH was to regenerate SeO₂.¹⁷⁵



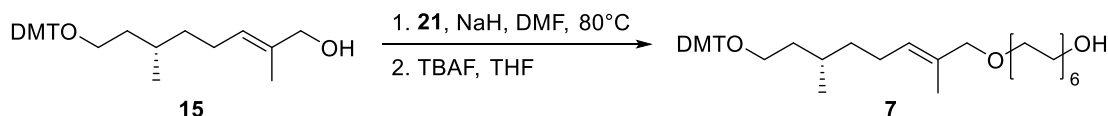
Once the OH functional group was added to the protected citronellol, the next reaction was the coupling with the dodecyl alkyl chain derivative (**21**).

The precursor of **21** is 1,12-dodecanediol, which undergoes monoprotection of one of the two hydroxyl groups, using *t*-butyldimethylsilyl (TBDMS) as protecting group. The “other” OH was converted into a mesylate (MsO⁻), which is a better leaving group for the coupling reaction with **15** (**Scheme 3.9**).



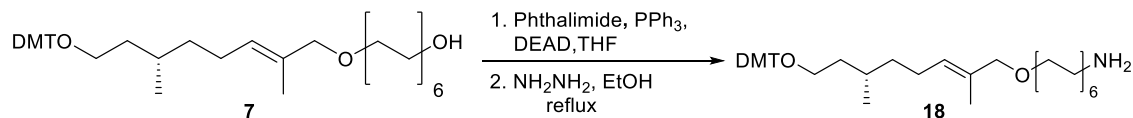
Scheme 3.9 Reaction scheme (2 steps) for the synthesis of **21** starting from 1,12-dodecanediol.

The compound **21** is coupled to **15** in a Williamson ether synthesis with the formation of **16**, followed by desilylation, using tetra-*N*-butylammonium fluoride (TBAF), which leads to **7** (**Scheme 3.10**).



Scheme 3.10 Reaction scheme for the preparation of **7**. It is a two steps reaction: the first is the coupling via Williamson ether procedure, leading to **16** (see **Scheme 3.5**). Then, a second step is a desilylation with the use of TBAF resulting in **7**.

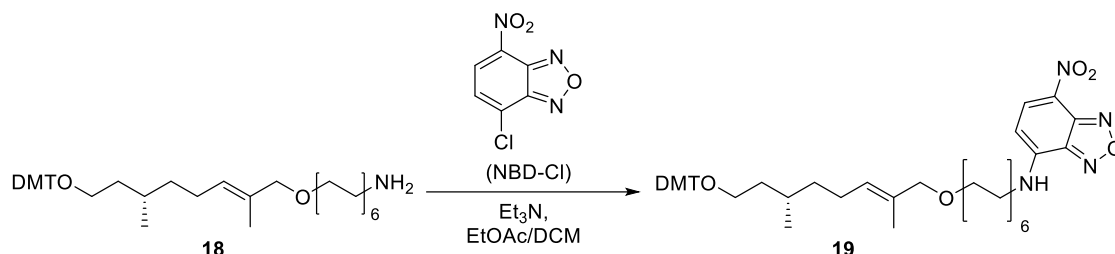
In order to link NBD to the tail of this alkyl chain, the (free) OH is converted into an amino function. First, the hydroxyl group was substituted with a phthalimide, under Mitsunobu conditions. Then, phthalimide is reduced to an amino function with the use of hydrazine (NH₂NH₂) (**Scheme 3.11**).



Scheme 3.11 Synthesis of **18**. The hydroxyl group of **7** is substituted by phthalimide, obtaining **17** (see **Scheme 3.5**). Then, reduction of the phthalimide with hydrazine affords **18**.

The coupling with NBD is depicted in **Scheme 3.12**. NBD (7-nitrobenzoxadiazole) is widely used, in the biochemical, physicochemical and material sciences, as fluorescent probe. It shows a fluorescence quantum yield that is very sensitive to changes in the local environment and polarity.¹⁷⁷

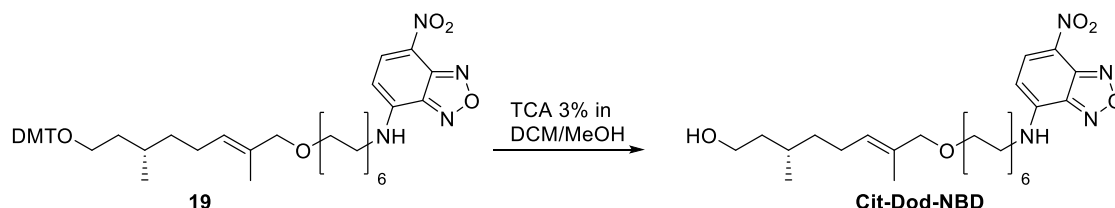
This sensitivity, to the surrounding environment, is due to the presence of electron donating and electron withdrawing groups (amino and nitro groups, respectively) linked to the opposite positions of the aromatic ring.¹⁷⁸



Scheme 3.12 Reaction scheme of the NBD coupling with **18**, and the formation of **19**.

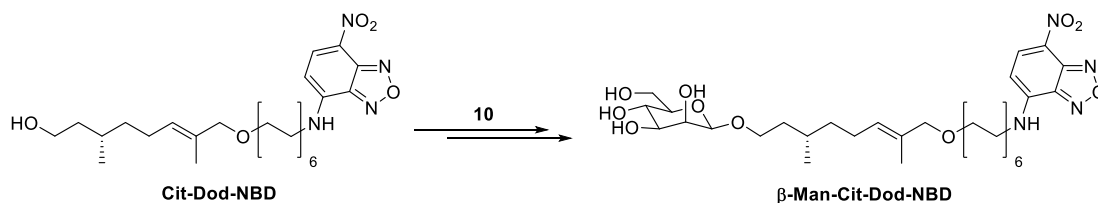
The reaction is rather simple: **18** and NBD-Cl were dissolved in a mixture of ethyl acetate (EtOAc) and DCM, followed by the addition of triethylamine (Et₃N) leading to a deep-red oil **19**, which shows a very strong fluorescence when in solution.

Finally, the last step is the removal of DMT with a solution of trichloroacetic acid (TCA) (3% in DCM/MeOH), and then the formation of **Cit-Dod-NBD** (**Scheme 3.13**).



Scheme 3.13 DMT deprotection with a solution of 3% of TCA in a mixture of DCM/MeOH.

The compound **Cit-Dod-NBD** is the dolichol mimic, which is then coupled to the mannose (see compound **10**, **Scheme 3.3**). This reaction was carried out by Dr. Markus Probst (Department of Chemistry and Biochemistry, University of Bern, 2018) as part of the Sinergia project (see Chapter 2), for the formation of **β-Man-Cit-Dod-NBD**.



Scheme 3.14 Reaction scheme for the coupling of **Cit-Dod-NBD** with **10** for the preparation of **β-Man-Cit-Dod-NBD** as described in ref.¹⁷³

The synthesis of **Cit-Dod-NBD** has been described. After the coupling with the compound **10**, the product (as described in **Scheme 3.14**) was shipped to Prof. Dr. Anant Menon (professor of biochemistry, Weill Cornell Medicine, New York, USA).

There, it will be used as probe for the identification of MPD scramblase activity.

CHAPTER 4

CONCLUSIONS

The synthesis of **Cit-Dod-NBD**, as a mimic of a dolichol structure, has been described. The natural molecule is much longer than the analogue synthesized here, and its preparation requires many steps and it would be very demanding.

For this reason, a short derivative was synthesized, by coupling the *S*-Citronellol (Cit) to a dodecyl chain (Dod) linked to a NBD as fluorescent tag.

Actually, *S*-Citronellol could be directly linked to the NBD, because, as described in chapter 2, it represents a valid short-chain analogue.

But, since NBD had to be positioned in proximity of the membrane-water interface, a dodecyl chain was introduced. In this way, *S*-Citronellol and dodecyl can remain in the lipid bilayer, while the NBD tag will face towards the membrane-water interface.

In the beginning, the phosphoramidite synthesis with a DNA synthesizer was thought to be a straightforward method to synthesize molecular probes, but unfortunately the attempt failed due to reagents that were not compatible with our building blocks and the target structure was not obtained.

Studies made on a derivative of NBD (**3**) in a solution used for the cleavage from the solid support (NH₃ 2M in MeOH), showed some changes in the structure of the fluorescent tag. So, most likely degradation of the NBD occurred during the cleavage step. For this reason, the structure was synthesized in solution, leading to **Cit-Dod-NBD**. The latter was coupled to a mannose through a phosphate bridge by Dr. Markus Probst (Department of Chemistry and Biochemistry, University of Bern).

The product of this coupling was shipped to Prof. Dr. Anant Menon (Weill Cornell Medicine, New York, USA) for the biological experiments.

CHAPTER 5

EXPERIMENTAL SECTION

Abbreviations

DCM	Dichloromethane
DEAD	Diethyl azodicarboxylate
DMF	Dimethylformamide
EtOAc	Ethyl acetate
EtOH	Ethanol
Hex	Hexane
MeOH	Methanol
Na ₂ SO ₄	Sodium sulfate
PPh ₃	Triphenylphosphine
TBDMS-	<i>tert</i> -butyldimethylsilyl
TCA	Trichloroacetic acid
TEA	Triethylamine
THF	Tetrahydrofuran

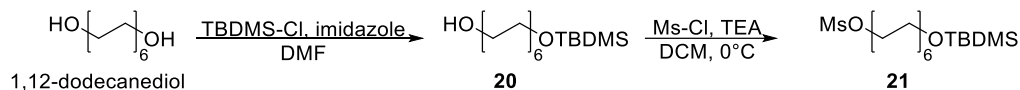
Then, water was added and the crude was extracted with DCM. The organic phase was dried with Na₂SO₄ and purified over column chromatography, leading to 580 mg (55%) of product **15** as yellow oil. R_f = 0.2 (Hex/EtOAc 8:2).

¹H NMR (400 MHz, DMSO-*d*₆) δ 7.38–7.20 (m, 9H), 6.88 (d, *J* = 8.9 Hz, 4H), 5.28 (t, *J* = 7.7 Hz, 1H), 4.62 (t, *J* = 5.6 Hz, 1H), 3.77 (d, *J* = 5.3 Hz, 2H), 3.72 (s, 6H), 3.02–2.94 (m, 2H), 1.97–1.91 (m, 2H), 1.64–1.54 (m, 2H), 1.52 (s, 3H), 1.41–1.30 (m, 1H), 1.29–1.18 (m, 2H), 1.11–1.06 (m, 1H), 0.76 (d, *J* = 6.4 Hz, 3H).

¹³C NMR (101 MHz, DMSO) δ 158.45, 145.74, 136.56, 136.54, 135.68, 130.03, 128.21, 128.11, 127.01, 124.07, 113.56, 85.68, 66.97, 61.35, 55.46, 36.86, 36.80, 29.42, 24.84, 19.95, 13.93.

HR-MS (NSI): calc. *m/z* for [C₃₁H₃₈O₄Na] 497.28 [M+Na]⁺, found: 497.27

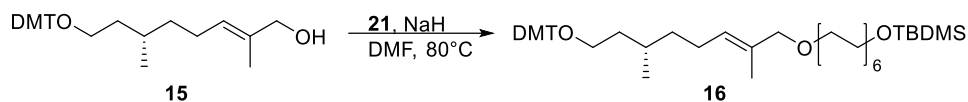
Synthesis of **21**



To a solution of 1,12-dodecanediol (1g, 4.942 mmol) in DMF (15 mL), *tert*-butyldimethylsilyl chloride (TBDMS-Cl) (745 mg, 4.942 mmol, 1eq) and imidazole (594 mg, 9.884 mmol, 2 eq) were added, under argon at rt. The solution is left under stirring for 4 hours. Then, EtOAc was added and the mixture was washed two times with water. The organic phase is dried with Na₂SO₄ and purified over column chromatography (Hex/EtOAc 8:2) obtaining 750 mg (48%) of **20** as a transparent oil. This reaction is taken from ref.¹⁷⁹ R_f = 0.8 (Hex/EtOAc 8:2).

¹H NMR (300 MHz, DMSO-*d*₆) δ 4.30 (t, *J* = 5.2 Hz, 1H), 3.56 (t, *J* = 6.3 Hz, 2H), 3.36 (q, *J* = 6.5, 5.1 Hz, 2H), 1.48 – 1.35 (m, 4H), 1.24 (s, 16H), 0.86 (s, 9H), 0.02 (s, 6H).

Then, **20** (750 mg, 2.369 mmol) was dissolved in DCM (10 mL) at 0°C under argon; after 15 minutes, TEA (1.650 mL, 11.845mmol, 5eq) was added, followed by methanesulfonyl chloride (Ms-Cl) (0.37 mL, 4.738 mmol, 2 eq) and the mixture was warmed slowly up to rt and left under stirring for 1 hour. Then, the solution was extracted with brine and the organic phase was dried with Na₂SO₄ and evaporated. The oil (**21**) was used in the next step without any further purification.

Synthesis of **16**

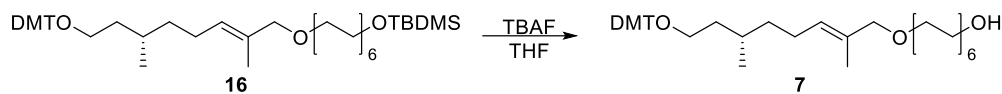
In a round-bottom flask, **15** (937 mg, 1.974 mmol) was dissolved in DMF (10 mL) under argon at rt, followed, after 20 minutes, by addition of NaH (60% dispersed in mineral oil, 237 mg, 5.922 mmol, 3 eq). The mixture was left under stirring for 30 minutes.

Meanwhile, in another flask, **21** (935 mg, 2.369 mmol, 1.2 eq) was dissolved in DMF (3 mL) under argon at rt. After 15 minutes, the latter was moved via cannula in the flask with **15**, the resulting solution was warmed up to 80°C leaving it under stirring for 4 hours. Then, water was added and the mixture was washed with EtOAc. The organic phase was dried with Na₂SO₄ and purified over column chromatography (Hex/EtOAc 85:15) leading to 943 mg of pure **16** as a pale yellow oil (62%) over two steps. R_f = 0.6 (Hex/EtOAc 8:2).

¹H NMR (300 MHz, DMSO-d₆) δ 7.38–7.21 (m, 9H), 6.87 (d, J = 8.3 Hz, 5H), 5.29 (t, J = 6.9 Hz, 1H), 3.73 (s, 8H), 3.58–3.52 (m, 2H), 3.23 (t, J = 6.6 Hz, 2H), 3.00–2.93 (m, 2H), 1.96–1.85 (m, 2H), 1.61–1.55 (m, 2H), 1.52 (d, J = 4.4 Hz, 3H), 1.48–1.35 (m, 5H), 1.24 (bp, 19H), 1.08 (t, J = 7.0 Hz, 3H), 0.85 (s, 9H), 0.76 (d, J = 6.3 Hz, 3H), 0.00 (s, 6H).

¹³C NMR (75 MHz, DMSO) δ 158.4, 145.7, 136.6, 130.0, 128.2, 128.1, 113.6, 85.7, 68.4, 55.46, 40.8, 40.6, 40.3, 40.0, 39.7, 39.5, 39.2, 36.7, 32.7, 29.3, 26.3, 26.2, 25.7, 25.7, 20.0, 18.4, 13.7, -4.8.

HR-MS (NSI): calc. m/z for [C₄₉H₇₆O₅Si] 795.55 [M+Na]⁺; found: 795.54

Synthesis of **7**

Compound **16** (943 mg, 1.220 mmol) was dissolved in THF (10 mL) under argon at rt. Then, tetrabutylammonium fluoride (TBAF) (462 mg, 1.464 mmol, 1.2 eq) was added, leaving the solution under stirring for 6 hours. Then the solvent was evaporated and the oil was dissolved in DCM and washed with brine. The organic phase was dried with

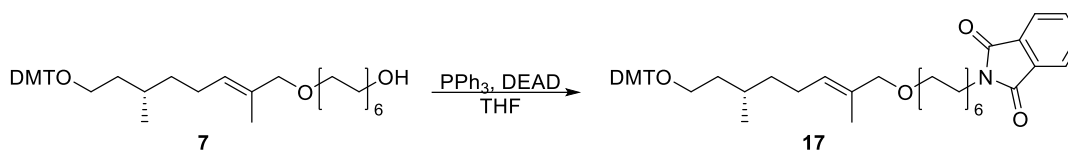
Na_2SO_4 and purified over column chromatography, obtaining 603 mg (75%) of pure **7** as a yellow oil. $R_f = 0.2$ (Hex/EtOAc 8:2).

^1H NMR (300 MHz, DMSO- d_6) δ 7.41–7.21 (m, 9H), 6.87 (d, $J = 8.9$ Hz, 4H), 5.30 (t, $J = 6.9$ Hz, 1H), 4.30 (t, $J = 5.1$ Hz, 1H), 3.73 (s, 8H), 3.39–3.34 (m, 2H), 3.23 (t, $J = 6.4$ Hz, 2H), 2.97 (bp, 2H), 1.97–1.92 (m, 2H), 1.63–1.55 (m, 2H), 1.53 (s, 3H), 1.43–1.34 (m, 5H), 1.22 (bp, 19H), 1.10 (t, $J = 4.6$ Hz, 1H), 0.76 (d, $J = 6.3$ Hz, 3H).

^{13}C NMR (75 MHz, DMSO- d_6) δ 158.4, 145.7, 136.5, 130.0, 128.2, 128.1, 117.5, 113.6, 85.7, 61.19, 55.5, 36.6, 33.0, 29.6, 29.5, 26.0, 19.9.

HR-MS (NSI): calc. m/z for $[\text{C}_{43}\text{H}_{62}\text{O}_5]$ 681.46 $[\text{M}+\text{Na}]^+$; found: 681.49

Synthesis of **17**

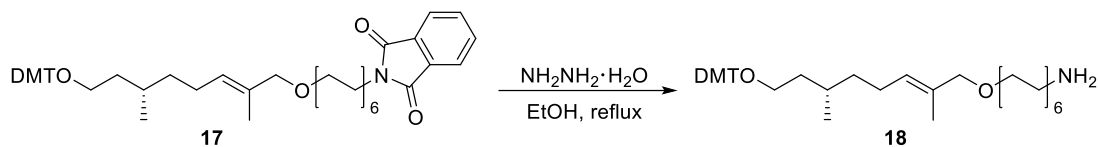


Compound **7** (1.070 g, 1.573 mmol) was dissolved in THF (40 mL) with PPh_3 (670 mg, 2.517 mmol, 1.6 eq) and phthalimide (347 mg, 2.359 mmol, 1.5 eq). Then, DEAD (40% in Toluene, 1.150 mL, 2.517 mmol, 1.6 eq) is added at rt under argon, leaving the mixture under stirring for 2 hours. Then, the solvent is evaporated and the oil is dissolved in EtOAc and washed with brine. The organic phase dried with Na_2SO_4 and purified over column chromatography (Hex/EtOAc 8:2) leading to 891 mg (73%) of pure **17** as a yellow oil. $R_f = 0.5$ (Hex/EtOAc 8:2).

^1H NMR (300 MHz, DMSO- d_6) δ 7.84 (d, $J = 162.3$ Hz, 5H), 7.38–7.18 (m, 9H), 6.86 (dd, $J = 613.1, 8.9$ Hz, 4H), 5.29 (t, $J = 6.9$ Hz, 1H), 3.72 (s, 8H), 3.54 (t, $J = 7.1$ Hz, 2H), 3.22 (t, $J = 6.4$ Hz, 2H), 3.03–2.85 (m, 2H), 1.98–1.86 (m, 2H), 1.60–1.49 (m, 7H), 1.49–1.38 (m, 2H), 1.27–1.16 (m, 18H), 1.10–1.03 (m, 1H), 0.74 (d, $J = 6.2$ Hz, 3H).

^{13}C NMR (75 MHz, DMSO) δ 169.7, 168.4, 158.4, 145.7, 136.5, 134.8, 133.1, 132.5, 132.1, 130.0, 128.2, 128.1, 127.4, 127.0, 123.5, 123.4, 123.4, 113.5, 85.7, 76.2, 69.1, 61.3, 55.4, 40.8, 40.6, 40.3, 40.0, 39.7, 39.5, 39.2, 37.8, 36.8, 36.6, 29.6, 29.4, 29.3, 29.2, 29.00, 28.3, 26.7, 26.2, 24.9, 19.9, 14.0.

HR-MS (NSI): calc. m/z for $[\text{C}_{43}\text{H}_{62}\text{O}_5]$ 810.48 $[\text{M}+\text{Na}]^+$, found: 810.47

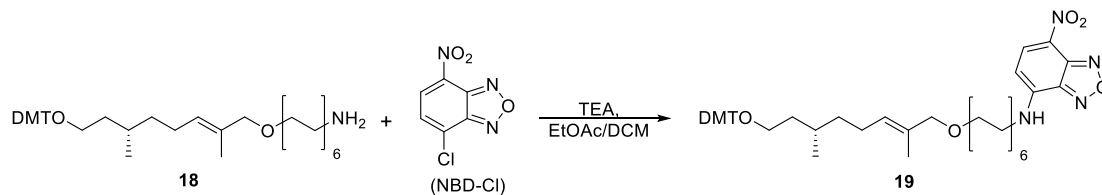
Synthesis of **18**

Compound **17** (2.44 g, 3.132 mmol) was dissolved in EtOH (50 mL) under argon at rt. After 10 minutes, hydrazine monohydrate (0.610 mL, 12.528 mmol, 4 eq) was added and the solution was warmed up to reflux and left under stirring overnight. Then, the mixture was diluted with EtOAc and washed with a Na₂CO₃ 2M solution. The organic phase with dried with Na₂SO₄ and evaporated, using the crude (**18** as white solid) (1.668 g, 80%) for the next step with no any further purification. R_f = 0.4 (DCM/MeOH 9:1).

¹H NMR (300 MHz, DMSO-d₆) δ 7.40–7.19 (m, 15H), 6.87 (d, J = 8.9 Hz, 7H), 5.30 (t, J = 6.9 Hz, 1H), 3.72 (s, 12H), 3.35–3.18 (m, 3H), 3.04–2.89 (m, 4H), 1.99–1.85 (m, 3H), 1.65–1.50 (m, 8H), 1.43 (s, 5H), 1.22 (s, 40H), 0.92–0.83 (m, 2H), 0.74 (d, J = 4.2 Hz, 6H).

¹³C NMR (75 MHz, DMSO) δ 158.4, 145.7, 136.5, 130.0, 128.1, 127.4, 127.0, 123.2, 113.5, 85.7, 69.1, 61.4, 61.3, 55.5, 29.5, 26.9, 26.2, 24.9, 19.9, 14.1.

HR-MS (NSI): calc. m/z for [C₄₃H₆₂O₅] 657.98 [M]⁺, found: 658.48

Synthesis of **19**

Compound **18** (905 mg, 1.378 mmol) was dissolved in a mixture EtOAc/DCM (12 mL, 3:1) under argon at rt. Then, 4-Chloro-7-nitrobenzofurazan (NBD-Cl) (357 mg, 1.79 mmol, 1.3eq) was added, leaving the solution under stirring for 1 hour. After that, TEA (0.250 mL, 1.791 mmol, 1.3 eq) was added, leaving the mixture under stirring for additional 3 hours. Finally, the reaction was dilute with DCM, washed with brine, dried with Na₂SO₄ and purified over column chromatography (Hex/EtOAc 7:3) obtaining 787 mg (70%) of pure **19** as a strong red oil.

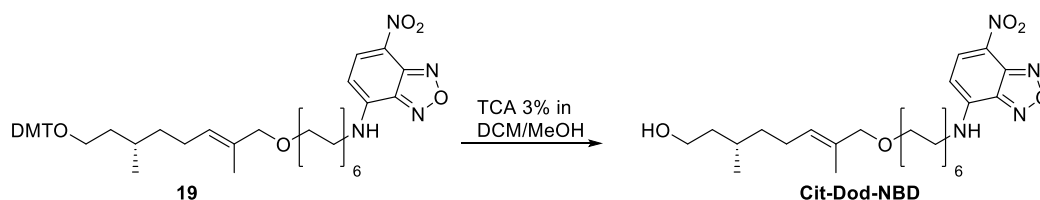
R_f = 0.7 (DCM/MeOH 9:1).

^1H NMR (300 MHz, DMSO- d_6) δ 9.55 (s, 1H), 8.50 (d, J = 9.0 Hz, 1H), 7.43–7.18 (m, 9H), 6.87 (d, J = 8.9 Hz, 4H), 6.39 (d, J = 9.0 Hz, 1H), 5.30 (t, J = 7.3 Hz, 1H), 3.73 (s, 8H), 3.52–3.40 (m, 2H), 3.23 (t, J = 6.4 Hz, 2H), 2.97 (q, J = 6.3 Hz, 2H), 1.99–1.89 (m, 2H), 1.70–1.61 (m, 2H), 1.53 (s, 3H), 1.47–1.18 (m, 24H), 0.75 (d, J = 6.2 Hz, 3H).

^{13}C NMR (75 MHz, DMSO) δ 158.3, 148.8, 140.7, 130.4, 129.4, 128.7, 128.1, 127.9, 126.9, 114.1, 113.2, 80.4, 79.7, 55.5, 40.8, 29.4, 26.9.

HR-MS (NSI): calc. m/z for $[\text{C}_{43}\text{H}_{62}\text{O}_5]$ 843.48 $[\text{M}+\text{Na}]^+$, found: 843.47

Synthesis of Cit-Dod-NBD



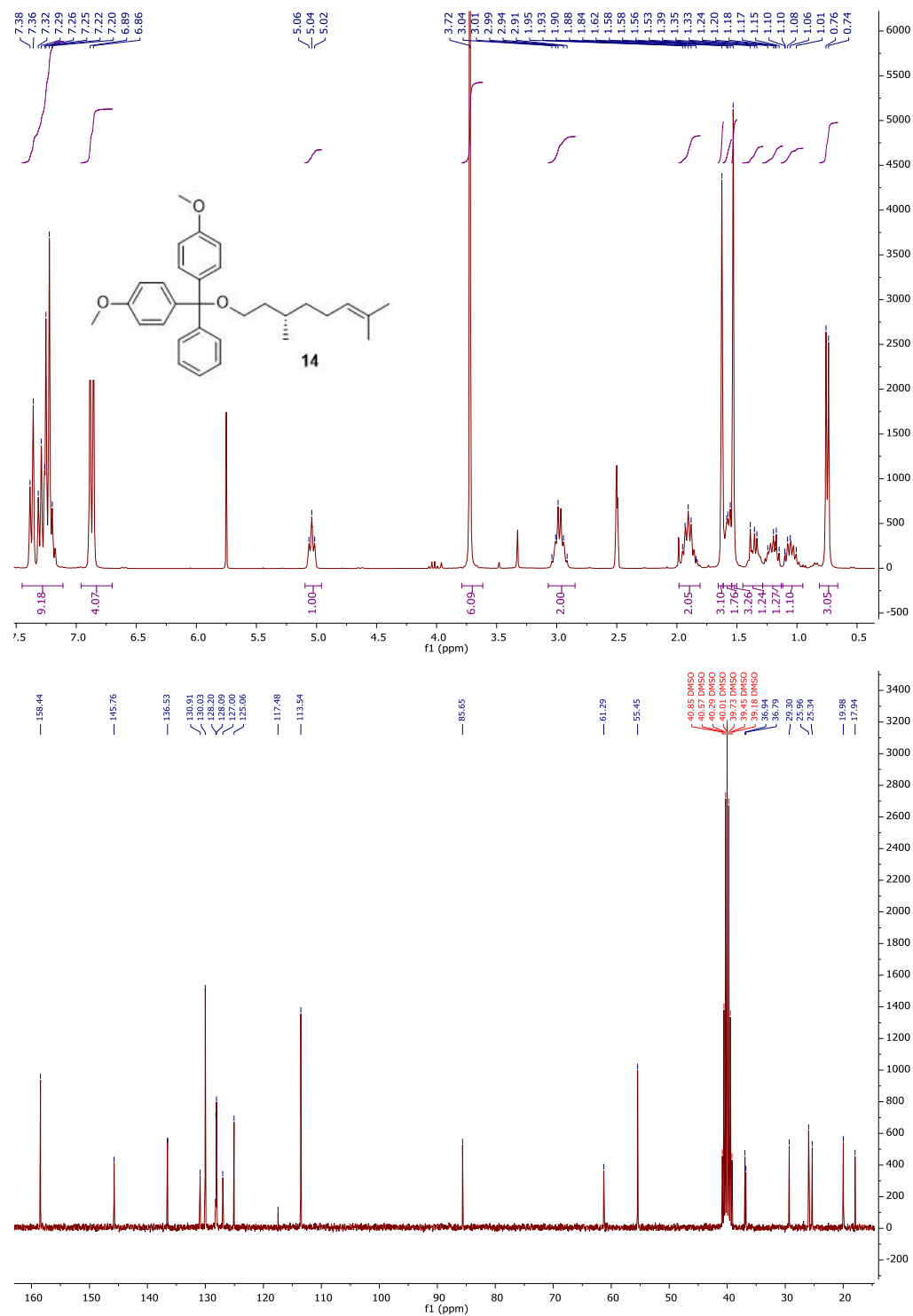
Compound **19** (787 mg, 0.964 mmol) was dissolved in 3% TCA solution in DCM/MeOH 1:1 at rt, for 2 hours under stirring. Then, the mixture was diluted in DCM and washed with brine and the organic phase is dried with Na_2SO_4 and purified over column chromatography (Hex/EtOAc 6:4) leading to 455 mg (92%) of pure **Cit-Dod-NBD** as a red oil. R_f = 0.5 (Hex/EtOAc 1:1).

^1H NMR (300 MHz, DMSO- d_6) δ 9.55 (s, 1H), 8.50 (d, J = 8.8 Hz, 1H), 6.49–6.31 (m, 1H), 5.33 (t, J = 7.2 Hz, 1H), 4.28 (t, J = 5.1 Hz, 1H), 3.73 (s, 2H), 3.59–3.36 (m, 4H), 3.26 (t, J = 6.4 Hz, 2H), 1.74–1.61 (m, 2H), 1.55 (s, 3H), 1.52–1.40 (m, 4H), 1.24 (s, 19H), 0.84 (d, J = 6.5 Hz, 3H).

^{13}C NMR (75 MHz, DMSO) δ 132.4, 127.5, 99.5, 79.7, 76.2, 69.2, 63.8, 59.2, 37.0, 33.97, 30.7, 29.6, 29.5, 29.4, 29.2, 28.8, 28.1, 26.9, 26.2, 25.0, 24.92, 19.7, 19.1, 14.1, 14.0.

HR-MS (NSI): calc. m/z for $[\text{C}_{43}\text{H}_{62}\text{O}_5]$ 518.70 $[\text{M}]^+$; found: 518.35

NMR SPECTRA

Figure 4.1 ^1H NMR (top) and ^{13}C NMR (bottom) of compound **14**.

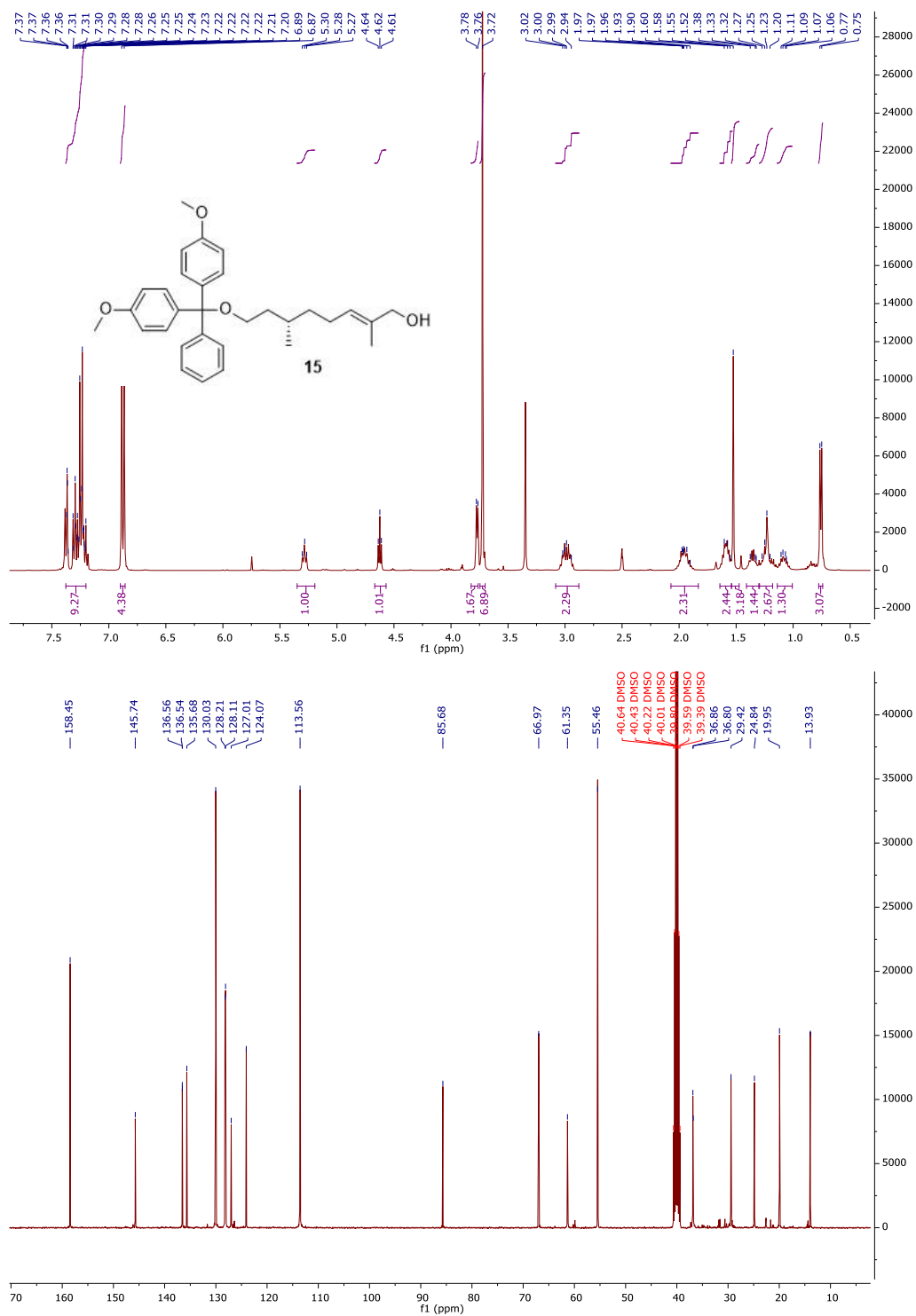


Figure 4.2 ¹H NMR (top) and ¹³C NMR (bottom) of compound 15.

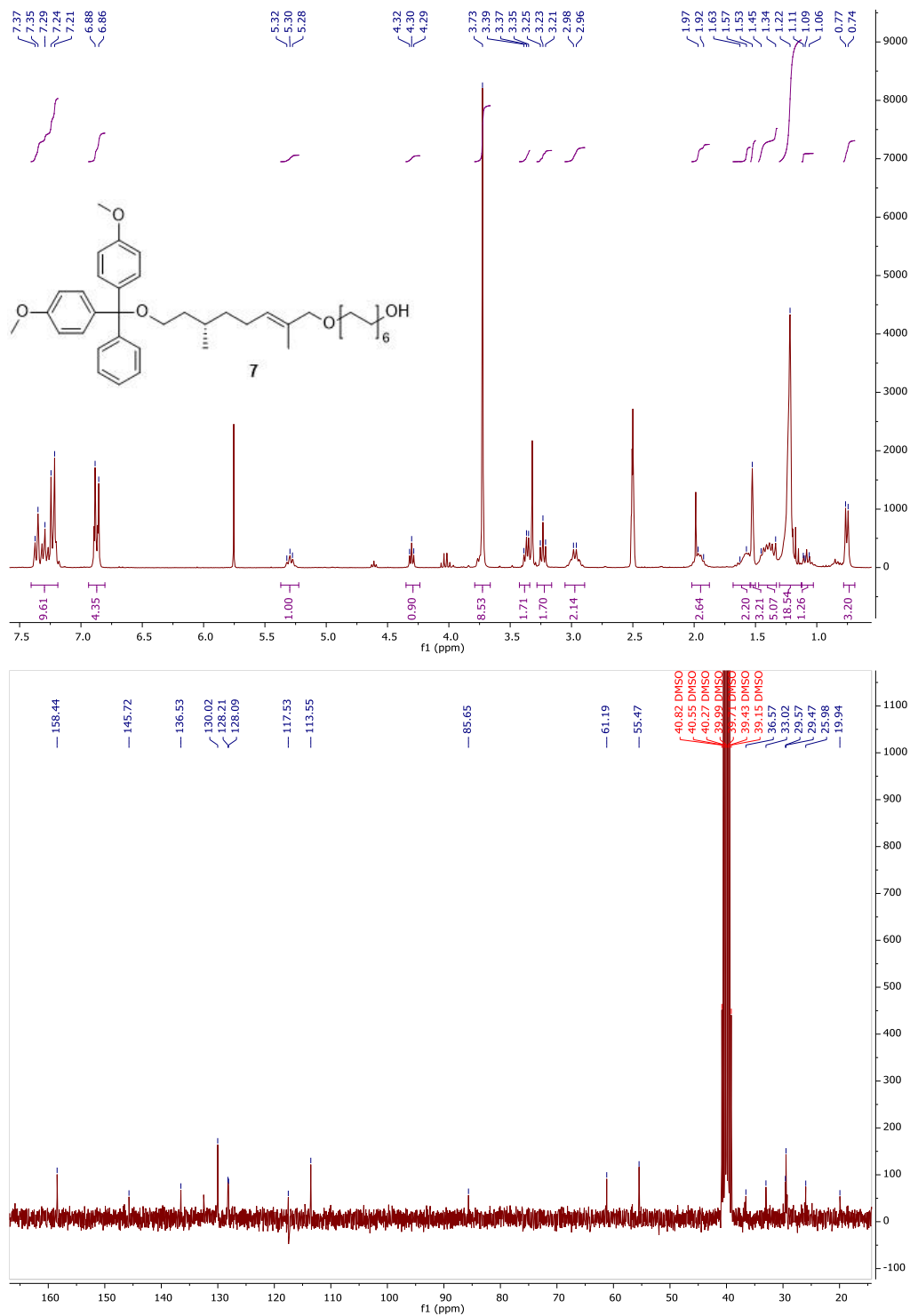


Figure 4.4 ^1H NMR (top) and ^{13}C NMR (bottom) of compound 7.

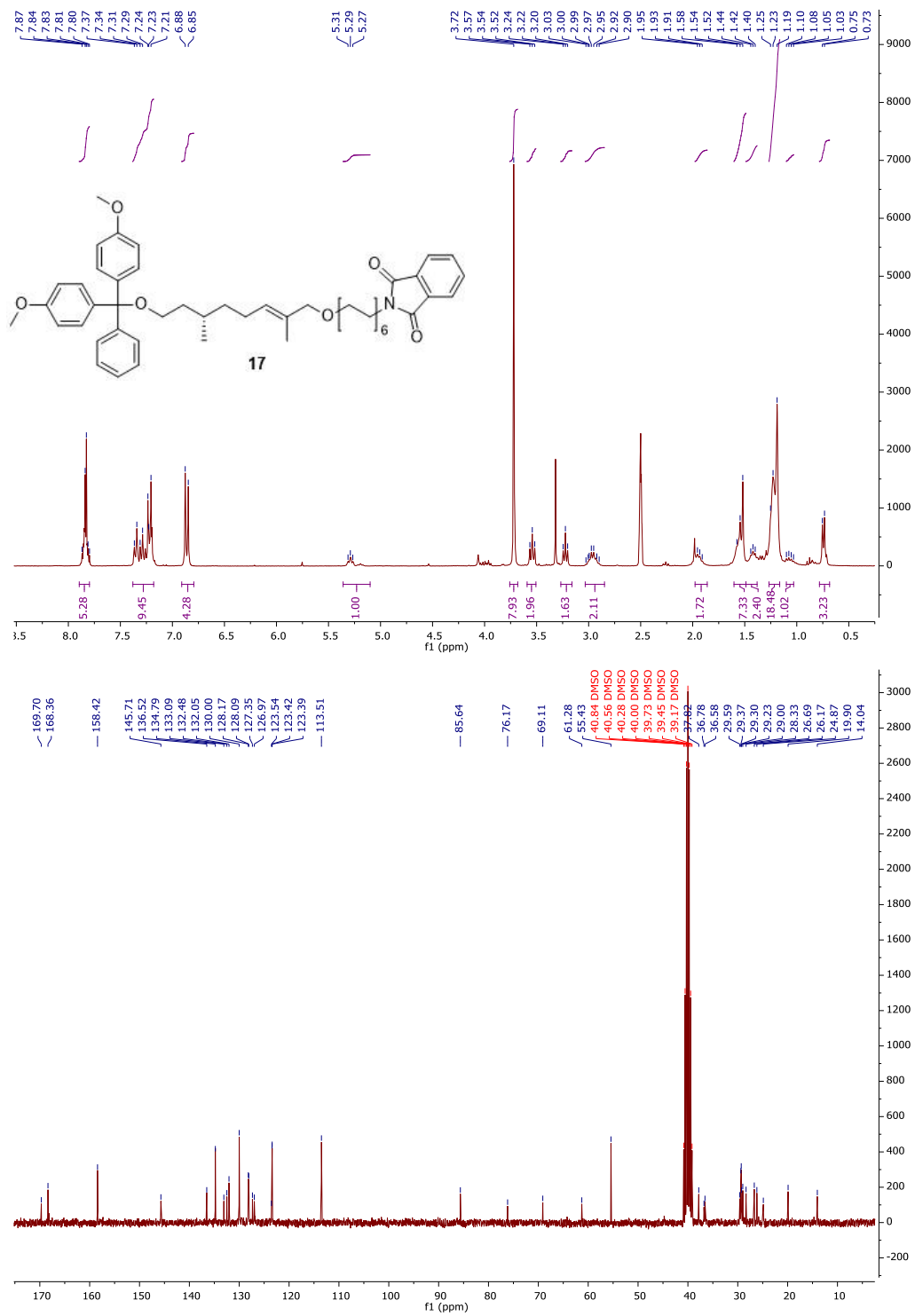


Figure 4.5 ^1H NMR (top) and ^{13}C NMR (bottom) of compound 17.

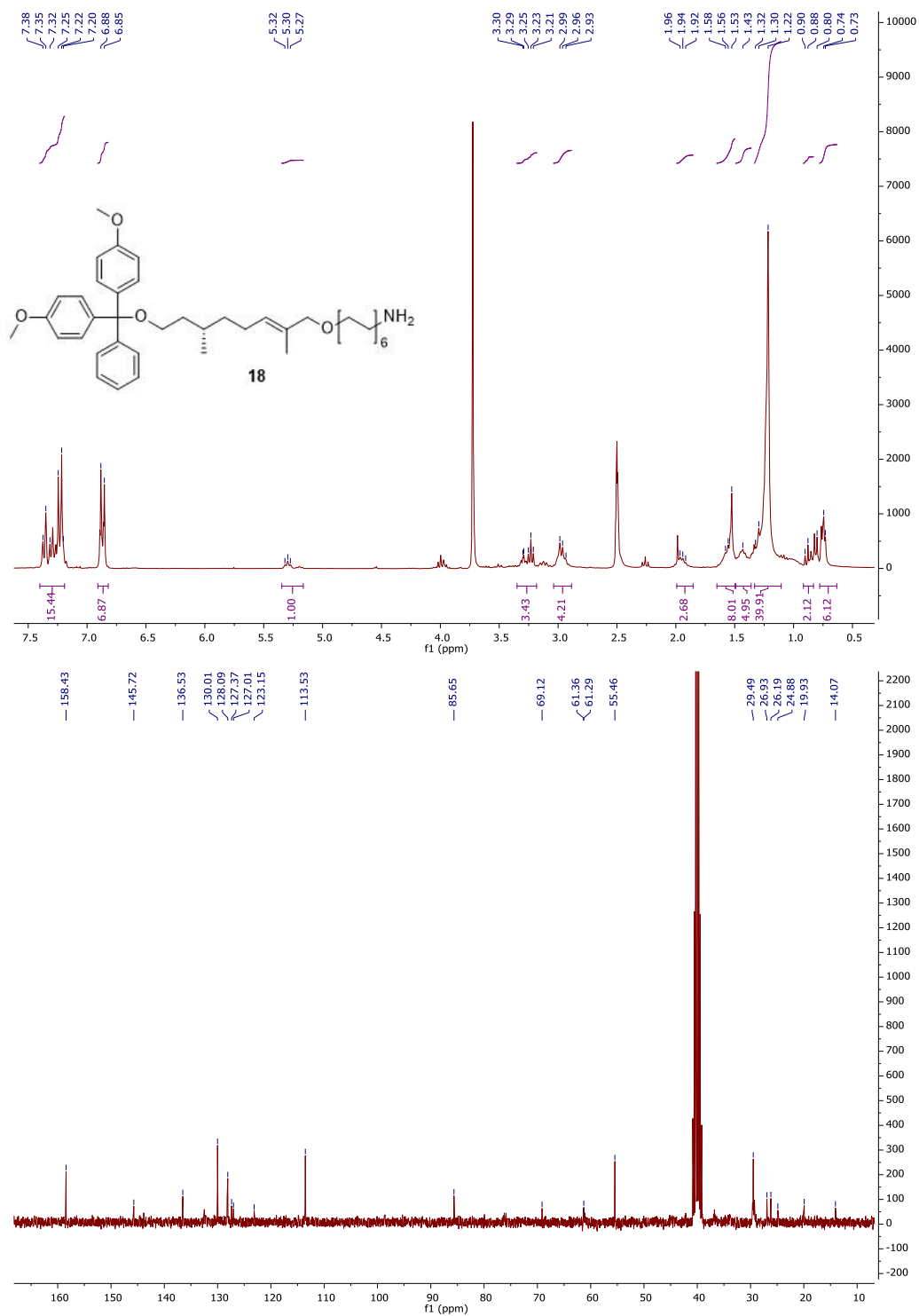


Figure 4.6 ^1H NMR (top) and ^{13}C NMR (bottom) of compound **18**.

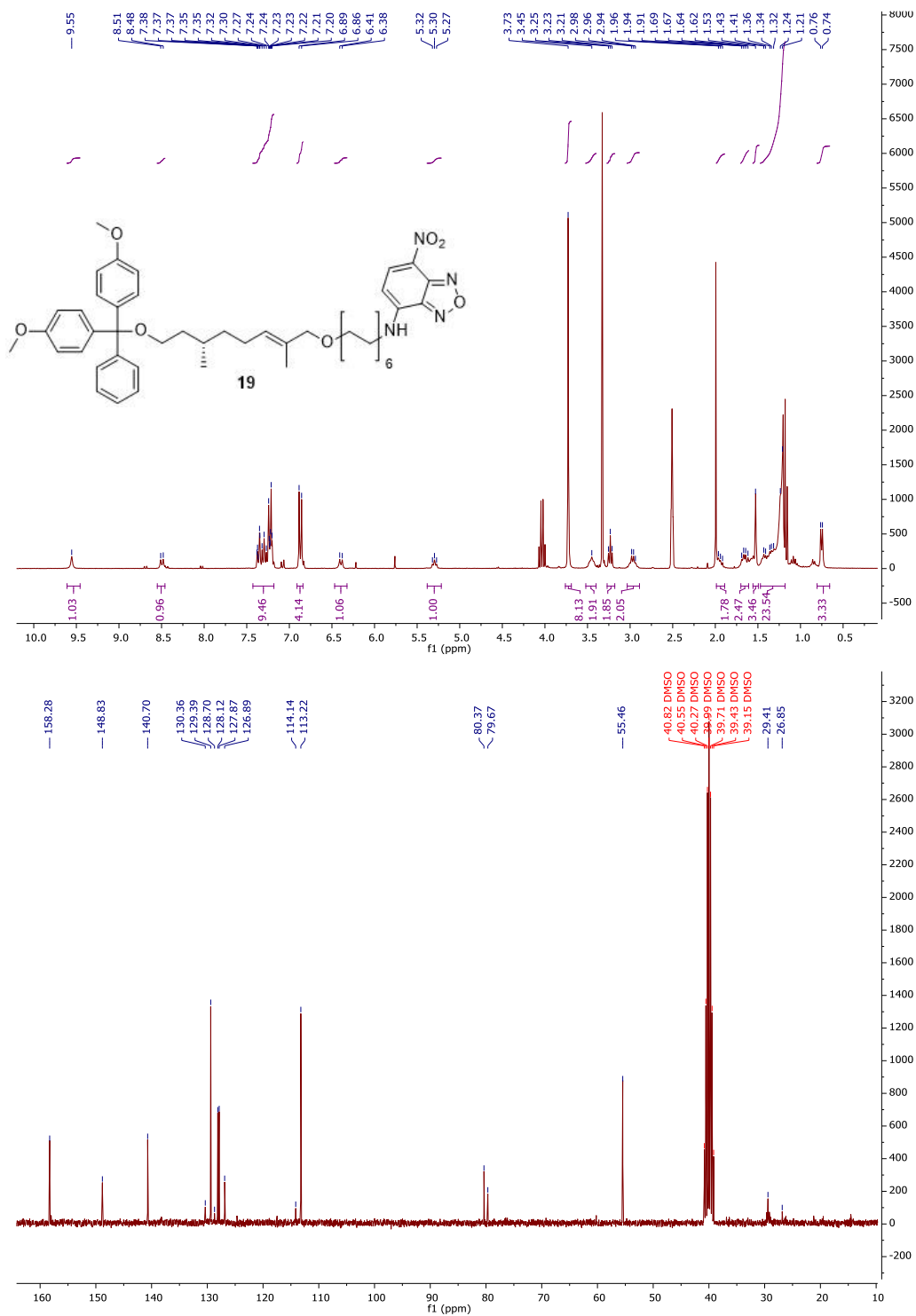


Figure 4.7 ¹H NMR (top) and ¹³C NMR (bottom) of compound 19.

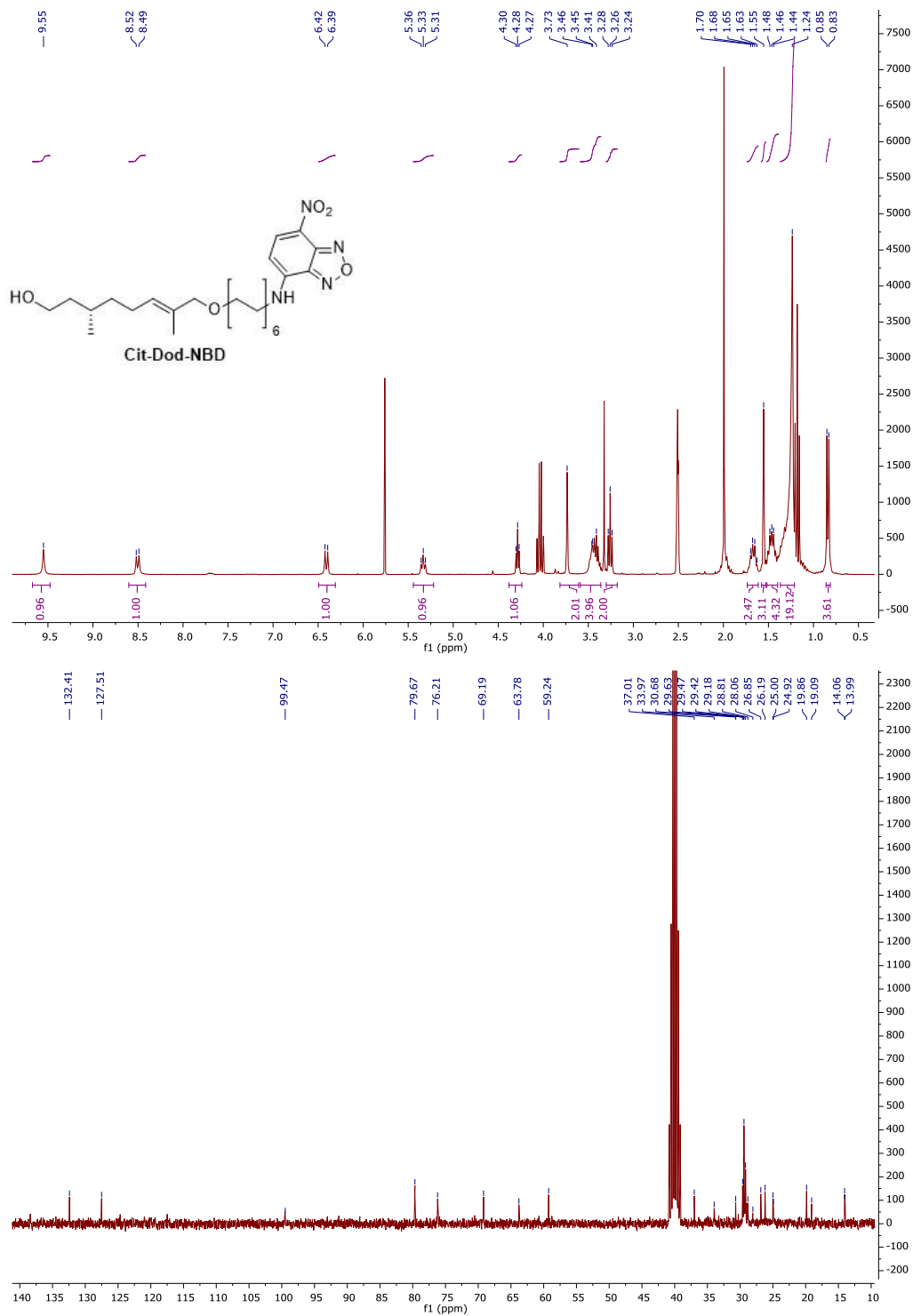


Figure 4.8 ¹H NMR (top) and ¹³C NMR (bottom) of compound Cit-Dod-NBD.

BIBLIOGRAPHY

- ¹ Lehn J.-M., *Chem. Soc. Rev.* **2007**, 36, 151-160
- ² Sommer R. D., Rheingold A. R., Goshe A. J., Bosnich B., *J. Am. Chem. Soc.*, **2001**, 123, 3940-3952
- ³ Brunsveld L., Folmer B. J. B., Meijer E. W., Sijbesma R. P., *Chem. Rev.*, **2001**, 101, 4071-4097
- ⁴ Lian Z., Qiao F., Jiang M., Wang R.-Z., Xing L.-B., Liu S., Wang S., **2019**, *Dyes and Pigments*, 171, 107774
- ⁵ Krieg E., Bastings M. M. C., Besenius P., Rybtchinski B., *Chem. Rev.*, **2016**, 116, 2414-2477
- ⁶ Abbel R. Grenier C., Pouderoijen M. J., Stouwdam J. W., Leclère P. E. L. G., Sijbesma R. P., Meijer E. W., Schenning A. P. H. J., *J. Am. Chem. Soc.*, **2009**, 131 833-843
- ⁷ Chen A. C. A., Culligan S. W., Geng Y., Chen S., H., Klubek K. P., Vaeth K. M., Tang C. W., *Adv. Mar.*, **2004**, 16, 783-787
- ⁸ Bisoyi H. K., Li Q., *Progress in Materials Science*, **2019**, 104, 1-52
- ⁹ Aida T., Meijer E. W., Stupp S. I., *Science*, **2012**, 335, 813-817
- ¹⁰ Chen Y., Kushner A. M., Williams G. A. Guan Z., *Nature Chemistry*, **2012**, 4, 467-472
- ¹¹ Liao H., Liao S., Tao X., Liu C., Wang Y., *J. Mater. Chem. C*, **2018**, 6, 12992-12999
- ¹² Burnworth M., Tang L., Kumpfer J. R., Duncan A. J., Beyer F. L., Fiore G. L., Rowan S. J., Weder C., *Nature*, **2011**, 472, 334-337
- ¹³ Herbst F., Döhler D., Michael P., Binder W. H., *Macromol. Rapid Commun.*, **2013**, 34, 203-220
- ¹⁴ Tomás H., Rodriguez J., Li Y., *Chem. Soc. Rev.*, **2012**, 41, 2193-2221
- ¹⁵ Chen J.-K., Lee D.-J., Cheng C.-C., *Acta Biomaterialia*, **2017**, 50, 476-483
- ¹⁶ Liu J., Xu J., Luo Q., Hou C., Tian R., Fu S., Yan T., Li F., Huang Z., Liu S., *Polymer Chemistry*, **2019**, 10, 3566-3570
- ¹⁷ Yang L., Tan X., Wang Z., Zhang X., *Chem. Rev.*, **2015**, 115, 7196-7239
- ¹⁸ Dong R., Zhou Y., Huang X., Zhu X., Lu Y., Shen J., **2015**, *Adv. Mater.*, 27, 498-526
- ¹⁹ de Greef T. F.A., Smulders M. M. J., Wolffs M., Schenning A. P. H. J., Sijbesma R. P., Meijer E. W., **2009**, *Chem. Rev.*, 109, 5687-5754
- ²⁰ Korevaar P. A., de Greef T. F. A., Meijer E. W., **2014**, *Chem. Mater.*, 26, 576 586
- ²¹ Smulders M. M. J, Nieuwenhuizen M. M. L., de Greef, T. F. A., van der Schoot P., Schenning A. P. H. J., Meijer E. W., **2010**, *Chem. Eur. J.*, 16, 362-367
- ²² Hartlieb M., Mansfield E. D. H., Perrier S., **2020**, *Polym. Chem.*, 11, 1083-1110
- ²³ Sorrenti A., Leira-Iglesias J., Markvoort A. J., de Greef T. F. A., Hermans T. M., **2017**, *Chem. Rev.*, 46, 5476-5490

- ²⁴ Flory P. J., **1946**, *Chem. Rev.*, 39, 137, 197
- ²⁵ Ciferri A., **2016**, *Chem. Rev.*, 116, 1353-1374
- ²⁶ Ciferri A., Crumbliss A. L., **2019**, *Frontier in Chemistry*, 7, 487
- ²⁷ Gilbert R. G., Hess M., Jenkins A. D., Jones R. G., Kratochvil P., Stepto R. F. T., **2009**, *Pure and Applied Chemistry*, 81, 779
- ²⁸ Zaho D., Moore J. S., **2003**, *Org. Biomol. Chem.*, 1, 3471-3491
- ²⁹ Gershberg J., Fennel F., Rehm T. H., Lochbrunner S., Würthner F., **2016**, *Chem. Sci.*, 7, 1729-1737
- ³⁰ Dhiman S., Sarkar A., George S. J., **2018**, *RSC Adv.*, 8, 18913-18925
- ³¹ Cai K., Xie J., Zhang D., Shi W., Yan Q., Zhao D., **2018**, *J. Am. Chem. Soc.*, 140, 5764-5773
- ³² de Greef T. F. A., Meijer E. W., **2008**, *Nature*, 453, 171-173
- ³³ Hirao T., Hisano N., Akine S., Kihara S.-I., Haino T., **2019**, *Macromolecules*, 52, 6160-6168
- ³⁴ Williams I., Williams N., **2016**, *Advanced in Physical Organic Chemistry Ed. Academic press*, ISBN: 9780128050811
- ³⁵ Ercolani G., Mandolini L., Mencarelli P., Roelens S., **1993**, *J. Am. Chem. Soc.*, 115, 3901-3908
- ³⁶ Yang Y., Urban M. W., **2018**, *Adv. Mater. Interfaces*, 5, 1800384
- ³⁷ Bentz K. C., Cohen S. M., **2018**, *Angew. Chem. Int. Ed.*, 57, 14992-15001
- ³⁸ Winter A., Schubert U. S., **2016**, *Chem. Soc. Rev.*, 45, 5311-5357
- ³⁹ Dobrawa R., Würthner F., **2005**, *J. Polym., Sci. Part A: Polym. Chem.*, 43, 4981-4995
- ⁴⁰ Tavenor N. A., Murnin M. J., Horne W. S., **2017**, *J. Am. Chem. Soc.*, 139, 2212-2215
- ⁴¹ Bode S., Bode R. K., Ehrhardt M., seifert A., Schacher F. H., Paulus R. M., Stumpf S., Sandmann B., Vitz J., Winter A., Hoepfener S., Garcia S. J., Spange S., van der Zwaag S., Hager M. D., Schuber U. S., **2013**, *Polym. Chem.*, 4, 4966-4973
- ⁴² Zheng Q., Ma Z., Gong S., **2016**, *J. Mater. Chem. A*, 4, 3324-3334
- ⁴³ Eloi J.-C., Chabanne L., Whittel G. R., Manners I., **2008**, *Materials Today*, 11, 28-36
- ⁴⁴ Zhao Y., Ma X., **2015**, *Chem. Rev.*, 115, 7794-7839
- ⁴⁵ <https://courses.lumenlearning.com/cheminter/chapter/hydrogen-bonding/>
- ⁴⁶ Marinez-Felipe A., Brebner F., Zaton D., Concellon A., Ahmadi S., Piñol M., Oriol L., **2018**, *Molecules*, 23 2778/1-2778/10
- ⁴⁷ Zimmermann S. C., Yang S. K., **2013**, *Isr. J. Chem.*, 53, 511-520
- ⁴⁸ Sijbesma R. P., Meijer E. W., **2003**, *Chem. Comm.*, 1, 5-16
- ⁴⁹ Harada A., 2012, *Supramolecular Polymer Chemistry* edited by Akira Harada, Wiley-VCH, ISBN 978-3527323210

- ⁵⁰ Brienne M. J., Gabard J., Lehn J.-M., Stibor I., **1989**, *J. Chem. Soc., Chem. Commun.*, 24, 1868-1870
- ⁵¹ Chen S., Yuan H., Chen S., Yang H., Ge Z., Zhuo H., Liu J., **2014**, *J. Mater. Chem. A*, 2, 10169-10181
- ⁵² Jiang Z.-C., Xiao Y.-Y., Kang Y., Oan M., Li B.-J., Zhang S., **2017**, *ACS Appl. Mater. Interfaces*, 9, 20276-20293
- ⁵³ Ding Y., Wang J., Song S., **2020**, *Polymers*, 12, 110/1-110/15
- ⁵⁴ Martinez C. R., Iverson B. L., **2012**, *Chem. Sci.*, 3, 2191-2201
- ⁵⁵ Riley K. E., Hobza P., **2013**, *Accounts of Chemical Research*, 46, 927-936
- ⁵⁶ Karabiyik H., Sevincek R., Karabiyik H., **2014**, *Physical Chemistry Chemical Physics*, 16, 15527-15538
- ⁵⁷ Chen T., Li M., Liu J., **2018**, *Cryst. Growth Des.*, 18, 2765-2783
- ⁵⁸ Gohlke M., Moessner R., Pollmann F., **2019**, *Physical Review B*, 100, 014206/1-014206/11
- ⁵⁹ Eleonora Stefanutti. Structural and dynamical studies on confined water. Physics [physics]. Université Pierre et Marie Curie - Paris VI; Università degli studi Roma Tre, 2017. English. NNT : 2017PA066730. tel-02406335
- ⁶⁰ Brini E., Fennell C. J., Fernandez-Serra M., Hribar-Lee B., Lukšič M., Dill K. A., **2017**, *Chem. Rev.*, 117, 12385-12414
- ⁶¹ Ball P., **2008**, *Chem. Rev.*, 108, 74-108
- ⁶² Kruse A., Dinjus E., **2007**, *J. of Supercritical Fluids*, 39, 362-380
- ⁶³ Krieg E., Basting M. M. C., Besenius P., Rybtchinski B., **2016**, *Chem. Rev.*, 116, 2414-2477
- ⁶⁴ Krieg E., Rybtchinski B., **2011**, *Chem. Eur J.*, 17, 9016-9026
- ⁶⁵ Hayakawa K. (2018) Chemistry of Polycyclic Aromatic Hydrocarbons (PAHs), Nitropolycyclic Aromatic Hydrocarbons (NPAHs) and Other Oxidative Derivatives of PAHs. In: Hayakawa K. (eds) Polycyclic Aromatic Hydrocarbons. Springer, Singapore
- ⁶⁶ Bamforth S. M., Singleton I., **2005**, *J. Chem. Technol. Biotechnol.*, 80, 723-736
- ⁶⁷ Meador J., 2008, Polycyclic Aromatic Hydrocarbons, DOI: 10.1016/B978-008045405-4.00413-4
- ⁶⁸ Delaunay W., Szűcs R., Pascal S., Mocanu A., Bouit P.-A., Nyulászi L., Hissler M., **2016**, *Dalton Trans.*, 45, 1896-1903
- ⁶⁹ Mallocci G., Cappellini G., Mulas G., Mattoni A., **2011**, *Chemical Physics*, 384, 19-27
- ⁷⁰ Pisula W., Feng X., Müllen K., **2010**, *Adv. Mater.*, 22, 3634-3649
- ⁷¹ Hoeben F. J. M., Jonkheijm P., Meijer E. W., Schenning P. H. J., **2005**, *Chem. Rev.*, 105, 1491-1546
- ⁷² Kim S.-Y., Lee J.-D., Cho Y.-J., Son M. R., Son H.-J., Cho D. W., Kang S. O., **2018**, *Phys. Chem. Chem. Phys.*, 20, 17458-17463

- ⁷³ Jelley E. E., **1936**, *Nature*, 138, 1009–1010
- ⁷⁴ Scheibe G., **1936**, *Angew. Chem.*, 49, 563
- ⁷⁵ Würthner F., Kaiser T. E., Saha-Möller C. R., **2011**, *Angew. Chem. Int. Ed.*, 50, 3376-3410
- ⁷⁶ Klymchenko A. S., **2013**, *J. Nanosci. Lett.*, 3, 21/1-21/8
- ⁷⁷ Zhai D., Xu W., Zhang L., Chang Y.-T., **2014**, *Chem. Soc. Rev.*, 43, 2402-2411
- ⁷⁸ Ostrowska K., Ceresoli D., Stadnicka K., Gryl M., Cazzaniga M., Soave R., Musielak B., Witek L. J., Goszczycki P., Grolik J., Turek A. M., **2018**, *IUCrJ*, 5, 335, 347
- ⁷⁹ Bayda M., Dumoulin F., Hug G. L., Koput J., Gorniak R., Wojcik A., **2017**, *Dalton Trans.*, 46, 1914-1926
- ⁸⁰ Fothergill J. W., Hernandez A. C., Knowlton W. B., Yurke B., Li L., **2018**, *J. Phys. Chem. A*, 122, 8989-8997
- ⁸¹ Vybornyi M., Vyborna Y., Häner R., **2019**, *Chem. Soc. Rev.*, 48, 4347-4360
- ⁸² Matteucci M. D., Caruthers M. H., **1981**, *J. Am. Chem. Soc.*, 103, 3185-3191
- ⁸³ Beaucage S. L., Caruthers M. H., **1981**, *Tetrahedron Lett.*, 22, 1859-1862
- ⁸⁴ Winiger C. B., Langenegger S. M., Khorev O., Häner R., **2014**, *Beilstein J. Org. Chem.*, 10, 1589-1595
- ⁸⁵ Bittermann H., Siegemund D., Malinovskii V. L., Häner Robert, **2008**, *J. Am. Chem. Soc.*, 130, 15285-15287
- ⁸⁶ Malinovskii V. L., Wenger D., Häner R., **2010**, *Chem. Soc. Rev.*, 39, 410-422
- ⁸⁷ Olejko L., Bald I., **2017**, *RCS Adv.*, 7, 23924-23934
- ⁸⁸ Garo F., Häner R., **2012**, *Angew. Chem. Int. Ed.*, 51, 916-919
- ⁸⁹ Probst M., Wenger D., Biner S. M., Häner R., **2012**, *Org. Biomol. Chem.*, 10, 755-759
- ⁹⁰ Probst M., Langenegger S. M., Häner R., **2014**, *Chem. Commun.*, 50, 159-161
- ⁹¹ Häner R., Garo F., Wenger D., Malinovskii V. L., **2010**, *J. Am. Chem. Soc.*, 132, 7466-7471
- ⁹² Rudnev A., V., Malinovskii V. L., Nussbaumer A. L., Mishchenko A., Häner R., Wandlowski T., **2012**, *Macromolecule*, 45 5986-5992
- ⁹³ Vybornyi M., Rudnev A. V., Langenegger S. M., Wandlowski T., Calzaferri J., Häner R., **2013**, *Angew. Chem. Int. Ed.*, 52, 11488-11493
- ⁹⁴ Figueira-Duarte T. M., Müllen K., **2011**, *Chem. Rev.*, 111, 7260-7314
- ⁹⁵ Vyborna Y., Vybornyi M., Rudnev A., Häner R., **2015**, *Angew. Chem. Int. Ed.*, 54, 7934-7938
- ⁹⁶ Vybornyi M., Rudnev A., Häner R., **2015**, *Chem. Mater.*, 27, 1426-1431
- ⁹⁷ Sonogashira K., **2002**, *Journal of Organometallic Chemistry*, 653, 46-49
- ⁹⁸ Chichilla R., Najera C., **2007**, *Chemical Reviews*, 107, 874-922

- ⁹⁹ Picca G., Probst M., Langenegger S. M., Khorev O., Bütikofer P., Menon A. K., Häner R., **2020**, *Beilstein Journal of Organic Chemistry*, 16, 1732–1739
- ¹⁰⁰ Krieg E., Bastings M. M., Besenius P., Rybtchinski B., **2016**, *Chem. Rev.*, 116, 2414-2477
- ¹⁰¹ Sorrenti A., Leira-Iglesias J., Markvoort A. J., de Greef T. F. A., Hermans T. M., **2017**, *Chem. Soc. Rev.*, 46, 5476-5490
- ¹⁰² Yamamoto D., Uchihashi T., Kodera N., Yamashita H., Nishikori S., Ogura T., Shibata M., Ando T., **2010**, *Methods in Enzymology*, 475 (Single Molecule Tools, Part B), 541-564
- ¹⁰³ Shlyakhtenko L. S., Gall A. A., Lyubchenko Y. L., **2013**, *Methods in Molecular Biology*, 931, 295-312
- ¹⁰⁴ Product information Sigma-Aldrich: <https://www.sigmaaldrich.com/content/dam/sigmaaldrich/docs/Sigma/Datasheet/10/c5275dat.pdf>
- ¹⁰⁵ From wikipedia: Concanavalin A (https://en.wikipedia.org/wiki/Concanavalin_A)
- ¹⁰⁶ Cunningham B. A., Hemperly J. J., Hopp T. P., Edelman G. M., **1979**, *PNAS* 76, 3218-3222
- ¹⁰⁷ https://www.worldofmolecules.com/life/glutamic_acid.htm
- ¹⁰⁸ <https://www.ebi.ac.uk/chebi/searchId.do?chebiId=CHEBI:22660>
- ¹⁰⁹ Lavis, D. L.; Chao, T. Y.; Raines, R. T., **2006**, *ACS Chemical Biology*, 1, 252-260
- ¹¹⁰ Presolski S. I., Hong V. P., Finn M. G., **2011**, *Current protocols in chemical biology*, 3, 153-162
- ¹¹¹ Hong V., Presolski S. I., Ma C., Finn M. G., **2009**, *Angew. Chem. Int. Ed.*, 48, 9879-9883
- ¹¹² Hong V., Presolski S. I., Ma C., Finn M.G., **2009**, *Angew. Chem. Int. Ed. Eng.*, 48, 9879-9883
- ¹¹³ Zhang T., Chen P., Sun Y., Xing Y., Yang Y., Dong Y., Xu L., Yang Z. Liu D., **2011**, *Chem. Commun.*, 47, 5774-5776
- ¹¹⁴ Gobbo P., Novoa S., Biesinger M. C., Workentin M. S., **2013**, *Chem. Commun.*, 49, 3982-3984
- ¹¹⁵ B. Haddada M., Blanchard J., Casale S., Krafft J.-M., Vallee A., Methivier C., Bojday S., **2013**, *Gold Bulletin*, 46, 335-341
- ¹¹⁶ Bösch C. D., Langenegger S. M., Häner R., **2016**, *Angew. Chem. Int. Ed.*, 55, 9961-9664
- ¹¹⁷ Claridge S. A., Goh S. L., Fréchet J. M. J., Williams S. C., Micheel C. M., Alivisatos A. P., **2005**, *Chem. Mater.*, 17, 1628-1635
- ¹¹⁸ Larry R. Engelking, **2015**, *Textbook of Veterinary Physiological Chemistry (Third Edition)*, Chapter 20 - Glycoproteins and Glycolipids, Editor(s): Larry R. Engelking, Academic Press, Pages 130-135, ISBN 9780123919090
- ¹¹⁹ Hirano K., Macmillan D., Tezuka K., Tsuji T., Kajihara Y., **2009**, *Angew. Chem. Int. Ed.*, 48, 9557-9560

- ¹²⁰ IUPAC Commission on colloid and Surface Chemistry, **1995**, *Pure and Applied Chemistry*, 67, 1307-1375
- ¹²¹ Saraswathy N., Ramalingam P., **2011**, *Concept and techniques in genomics and proteomics*, published by Woodhead Publishing Series in Biomedicine 1st ed., pp. 213-214
- ¹²² Swiezewska E., Danikiewicz W., **2005**, *Progress in Lipid Research*, 44, 235-258
- ¹²³ Cantagrel V., Lefeber D. J., **2011**, *J. Inherit. Metab. Dis.*, 34, 859-867
- ¹²⁴ Ekström T. J., Chojnacki T., Dallner G., **1984**, *J. Biol. Chem.*, 259, 10460-10468
- ¹²⁵ Cantagrel V., Lefeber D. J., Ng B. G., Guan Z., Silhavy J. L., Bielas S. L., Lehle L., Hombauer H., Adamowicz M., Swiezewska E., De Brouwer A. P., Blümel P., Sykut-Cegielska J., Houliston S., Swistun D., Ali B. R., Dobyns W. B., Babovic-Vuksanovic D., van Bokhoven H., Wevers R. A., Raetz C. R., Freeze H. H., Morava E., Al-Gazali L., Gleeson J. G., **2010**, *Cell*, 142, 203-217
- ¹²⁶ Bergstrom K. S. B., Xia L., **2013**, *Glycobiology*, 23, 1026-1037
- ¹²⁷ Wopereis S., Lefeber D. J., Morava É., Wevers R. A., **2006**, *Clinical Chemistry*, 52, 574-600
- ¹²⁸ Pinzón Martin S., Seeberger P. H., Varón Silva D., **2019**, *Frontiers in Chemistry*, 7, 710/1-710/13
- ¹²⁹ Hang H. C., Bertozzi C. R., **2005**, *Bioorg. Med. Chem.*, 13, 5021-5034
- ¹³⁰ Tan S., Cheng P.-W., **2007**, *American Journal of Respiratory Cell and Molecular Biology*, 36, 737-745
- ¹³¹ Xu C., Ng D. T. W., **2015**, *Seminar in Cell & Developmental Biology*, 41, 129-134
- ¹³² Lommel M., Strahl S., **2009**, *Glycobiology*, 19, 816-828
- ¹³³ Tannous A., Brambilla Pisoni G., Hebert D. N., Molinari M., **2015**, *Seminar in Cell & Developmental Biology*, 41, 79-89
- ¹³⁴ Zhang H., Tian Y., **2013**, *Proteomics*, 13, 504-511
- ¹³⁵ Sriram V.; Willard C. A.; Liu J. Brutkiewicz R. R., **2008**, *Immunology*, 123, 272-281
- ¹³⁶ Bieberich E., **2014**, *Adv Neurobiol.*, 9, 47-70
- ¹³⁷ Wang Y.-C., Peterson S. E., Loring J. F., **2014**, *Cell Research*, 24, 143-160
- ¹³⁸ Fisher P., Thomas-Oates J., Wood. A. J., Ungar D., **2019**, *Frontiers in cell and developmental biology*, 7, 157/1-157/11
- ¹³⁹ Paulick M. G., Bertozzi C. R., **2008**, *Biochemistry*, 47, 6991-7000
- ¹⁴⁰ Kinoshita T., Fujita M., **2016**, *J. Lipid Res.*, 57, 6-24
- ¹⁴¹ Maeda Y. Watanabe R., Harris C. L., Hong Y., Ohishi K., Kinoshita K, Kinoshita T., **2001**, *EMBO Journal*, 20, 250-261
- ¹⁴² Rosenbaum E. E., Brehm K. S., Vasiljevic E., Gajenski A., Colley N. J., **2012**, *Visual Neuroscience*, 29, 143-156
- ¹⁴³ Vainauskas S., Menon A. K., **2006**, *Journal of Biological Chemistry*, 281, 38358-38364

- ¹⁴⁴ Schwarz D. S., Blower M. D., **2016**, *Cell. Mol. Life Sci.*, 73, 79-94
- ¹⁴⁵ English A. R., Zurek N., Voeltz G. K., **2009**, *Current Opinion in Cell Biology*, 21, 569-602
- ¹⁴⁶ Goyal U., Blackstone C., **2013**, *Biochimica et Biophysica Acta*, 1833, 2492-2498
- ¹⁴⁷ Jaeken J., Matthijs G., **2007**, *Annu. Rev. Genomics Hum. Genet.*, 8, 261-278
- ¹⁴⁸ Menon I., Huber T., Sanyal S., Banerjee S., Barré P., Canis S., Warren J. D., Hwa J., Sakmar T. P., Menon A. K., **2011**, *Curr Biol.*, 21, 149-153
- ¹⁴⁹ Sharom F. J., **2011**, *IUBMB Life*, 63, 736-746
- ¹⁵⁰ Kobayashi T., Menon A. K., **2018**, *Current Biology*, 28, R386-R391
- ¹⁵¹ Timcenko M., Lyons J. A., Janulienė D., Ulstrup J. J., Dieudonné T., Montigny C., Ash M.-R., Karlsen J. L., Bosen T., Kuhlbrandt W., Lenoir G., Moeller A., Nissen P., **2019**, *Nature*, 571, 366-370
- ¹⁵² Ernst O. P., Menon A. K., **2015**, *Photochemical & Photobiological Sciences*, 14, 1922-1931
- ¹⁵³ Menon A. K., Sanyal S., **2010**, *PNAS*, 107, 11289-11294
- ¹⁵⁴ Rush J. S., **2015**, *Lipid insights*, 8, 45-53
- ¹⁵⁵ Skrabanek L. A., Menon A. K., 2017, bioRxiv, Cell Biology, 1-17
- ¹⁵⁶ Rush J. S., van Leyen K., Ouerfelli O., Wolucka B., Waechter C. J., 1998, *Glycobiology*, 8, 1195-1205
- ¹⁵⁷ Sanyal S., Menon A. K., **2009**, *PNAS*, 106, 767-772
- ¹⁵⁸ Molecular identification of lipid transporters for protein glycosylation, *Swiss National Science Foundation (SNSF)*, Grant Number 170923. (<http://p3.snf.ch/Project-170923>)
- ¹⁵⁹ For more infos, please visit:
<http://www.snf.ch/en/funding/programmes/sinergia/Pages/default.aspx>
- ¹⁶⁰ Cueva R., Cotano C., Larriba G., **1998**, *Yeast*, 14, 773-781
- ¹⁶¹ Bengtson P., Ng B. G., Jaeken J., Matthijs G., Freeze H. H., Eklund E. A., **2016**, *J Inherit Metab Dis*, 39, 107-114
- ¹⁶² Rush J. S., Subramanian T., Subramanian K. L., Onono F. O., Waechter C. J., Spielmann H. P., **2015**, *Current Chemical Biology*, 9, 123-141
- ¹⁶³ Rush J. S., Waechter C.J., **1995**, *The Journal of Cell Biology*, 130, 529-536
- ¹⁶⁴ Rush J. S., Waechter C. J., **2004**, *Biochemistry*, 43, 7643-7652
- ¹⁶⁵ Preston G. W., Wilson A. J., **2013**, *Chem. Soc. Rev.*, 42, 3289-3301
- ¹⁶⁶ Turek T. C., Gaon I., Distefano M. D., **2001**, *J. Org. Chem.*, 66, 3253-3264
- ¹⁶⁷ Weber P. C., Ohlendorf D. H., Wendoloski J. J., Salemme F. R., **1989**, *Science*, 243, 85-88
- ¹⁶⁸ The entire process is taken from Sinergia grant proposal described in 158
- ¹⁶⁹ Sanyal S., Menon A. K., **2009**, *ACS Chem.Biol.*, 11, 895-909

- ¹⁷⁰ Kern N. R., Lee H. S., Wu E. L., Park S., Vanommeslaeghe K., MacKerell A. D. Jr, Klauda J. B., Jo S., Im W., **2014**, *Biophysical Journal*, 107, 1885-1895
- ¹⁷¹ Raghuraman H., Shrivastava S., Chattopadhyay A., **2007**, *Biochimica et Biophysica Acta*, 1768, 1258-1267
- ¹⁷² Chattopadhyay A., **2003**, *Chemistry and Physics of Lipids*, 122, 3-17
- ¹⁷³ Picca G., Probst M., Langenegger S. M., Khorev O., Bütikofer P., Menon A. K., Häner R., **2020**, *Beilstein Journal of Organic Chemistry*, 16, 1732–1739
- ¹⁷⁴ Riley H. L., Morley J. F., Friend N., **1932**, *Journal of the Chemical Society*, 1875-1883
- ¹⁷⁵ Mlochowski J., Wojtowicz-Mlochowska H., **2015**, *Molecules*, 20, 10205-10243
- ¹⁷⁶ Nakamura A., Nakada M., **2013**, *Synthesis*, 45, 1421-1451
- ¹⁷⁷ Cohen C., Damiron D., Dkhil S. B., Drockenmuller E., Restagno F., Léger L., **2012**, *Journal of Polymer Science Part A: Polymer Chemistry*, 50, 1827-1833
- ¹⁷⁸ Gentili P. L., Mugnai M., Bussotti L., Righini R., Foggi P., Cicchi S., Ghini G., Viviani S., Brandi A., **2007**, *Journal of Photochemistry and Photobiology A: Chemistry*, 187, 209-221
- ¹⁷⁹ Liu D., Zhang G., Ren T., **2000**, *Tetrahedron Letters*, 42, 1007-1010

Declaration of consent

on the basis of Article 18 of the PromR Phil.-nat. 19

Name/First Name: Picca Giovanni

Registration Number: 15-136-609

Study program: Chemistry and Molecular Sciences

Bachelor

Master

Dissertation

Title of the thesis:

Preparation of Mannose-derived 2D Supramolecular Polymers and Synthesis of Mannose/Dolichol mimics for Scramblase identification

Supervisor:

Prof. Dr. Robert Häner

I declare herewith that this thesis is my own work and that I have not used any sources other than those stated. I have indicated the adoption of quotations as well as thoughts taken from other authors as such in the thesis. I am aware that the Senate pursuant to Article 36 paragraph 1 litera r of the University Act of September 5th, 1996 and Article 69 of the University Statute of June 7th, 2011 is authorized to revoke the doctoral degree awarded on the basis of this thesis.

For the purposes of evaluation and verification of compliance with the declaration of originality and the regulations governing plagiarism, I hereby grant the University of Bern the right to process my personal data and to perform the acts of use this requires, in particular, to reproduce the written thesis and to store it permanently in a database, and to use said database, or to make said database available, to enable comparison with theses submitted by others.

Place/Date

Signature

Curriculum Vitae

Personal Information

First name, Name	Giovanni Picca
Date of birth	19 July 1987
Hometown	Teverola, Itlay
Email address	giovanni.picca87@gmail.com
Phone Number	+41766996875

Education

2015-2020	Ph.D student in R. Häner's research group, University of Bern, Switzerland
2011-2014	Master studies in Chemical Science in the University of Naples Federico II
2006–2011	Bachelor studies in Chemical Science in the University of Naples Federico II

Publications

G. Picca, M. Probst, S.M. Langenegger, O. Khorev, P. Bütikofer, A.K. Menon, R. Häner, **2020**, Non-enzymatic Synthesis of Anomerically Pure, Mannosyl-based Molecular Probes for Scramblase Identification Studies, *Beilstein J. Org. Chem.*, 16, 1732-1739